



8-1-2006

Design, Integration and Control of Proton Exchange Membrane Electrolyzer for Wind Based Renewable Energy Applications

Kevin W. Harrison

Follow this and additional works at: <https://commons.und.edu/theses>

Recommended Citation

Harrison, Kevin W., "Design, Integration and Control of Proton Exchange Membrane Electrolyzer for Wind Based Renewable Energy Applications" (2006). *Theses and Dissertations*. 3002.
<https://commons.und.edu/theses/3002>

This Dissertation is brought to you for free and open access by the Theses, Dissertations, and Senior Projects at UND Scholarly Commons. It has been accepted for inclusion in Theses and Dissertations by an authorized administrator of UND Scholarly Commons. For more information, please contact und.common@library.und.edu.

DESIGN, INTEGRATION AND CONTROL OF PROTON EXCHANGE MEMBRANE
ELECTROLYZER FOR WIND BASED RENEWABLE ENERGY APPLICATIONS

by

Kevin W. Harrison

Associates in Arts and Science, Monroe Community College, 1992

Bachelor of Science, University of Rochester, 1995

Master of Science, University of North Dakota, 2002

A Dissertation

Submitted to the Graduate Faculty

of the

University of North Dakota

in partial fulfillment of the requirements

for degree of

Doctor of Philosophy

Grand Forks, North Dakota

August

2006

This dissertation, submitted by Kevin W. Harrison in partial fulfillment of the requirements for the Degree of Doctor of Philosophy from the University of North Dakota, has been read by the Faculty Advisory Committee under whom the work has been done and is hereby approved.

Harri Schfer
(Chairperson)

Michael D. Mouna

John Erjavec

Mary Alice Kurek

Janaki Zehi

Robert W. Thresher

This dissertation meets the standards for appearance, conforms to the style and format requirements of the Graduate School of the University of North Dakota, and is hereby approved.

Joseph D. Benoit
Dean of the Graduate School

August 2, 2006
Date

PERMISSION


Title Design, Integration and Control of Proton Exchange
 Membrane Electrolyzer for Wind Based Renewable Energy
 Applications

Department Electrical Engineering

Degree Doctor of Philosophy

In presenting this dissertation in partial fulfillment of the requirements for a graduate degree from the University of North Dakota, I agree that the library of this University shall make it freely available for inspection. I further agree that permission for extensive copying for scholarly purposes may be granted by the professor who supervised my dissertation work or, in his absence, by the chairperson of the department or the dean of the Graduate School. It is understood that any copying or publication or other use of this dissertation or part thereof for financial gain shall not be allowed without my written permission. It is also understood that due recognition shall be given to me and to the University of North Dakota in any scholarly use which may be made of any material in my dissertation.

Signature



Date

July 27, 2006

TABLE OF CONTENTS

LIST OF FIGURES	ix
LIST OF TABLES	xv
ACKNOWLEDGMENTS	xvi
ABSTRACT	xviii
CHAPTER	
1. INTRODUCTION	1
Variable Renewable Sources	3
Myth Clarification	3
Environmental Imperative	4
Research Motivation	7
Relevance	10
Research Objective	11
2. HYDROGEN	13
Properties	14
Flammability Limits	16
Electrolysis	16
Alkaline	17
Proton Exchange Membrane	17
3. COMMERCIAL ELECTROLYZER TESTING	19

NREL Test Facility.....	19
Safety.....	20
Data Acquisition.....	22
Instrumentation.....	24
Modes of Operation.....	27
Grid Only.....	27
PV Only.....	28
PV and Grid.....	28
System Testing	29
External Power Supplies	29
Baseline	31
Complex Waveform	33
PV.....	35
PV Simulation	36
Wind Turbine.....	37
Conclusions	41
4. UND SYSTEM DESIGN	43
Motivation	43
Data Acquisition.....	44
Safety	47
Emergency Stop	47
Circuit Protection	47
CG1	47

	CG2	49
	Interlock Loop	51
	Chiller	51
	Power Supplies	52
	Water System	54
	Hydrogen System	57
	Electrolyzer Operation Reference	59
5.	DEW POINT CONTROL	66
	Introduction	66
	System Design	68
	Proposed Experimental System	70
	Theory of Operation	71
	Modeling	73
	TEC Stage 1	76
	TEC Stage 2	76
	Energy Analysis	77
	Desiccant	78
	Thermoelectric	79
	Acknowledgments	80
6.	RESULTS	81
	Operational Temperature Trials	82
	High Temperature Trials	85
	Coefficients	87

	Anode Exchange Current Density.....	89
	Cathode Exchange Current Density.....	89
	Conductivity.....	90
	Efficiency Trials.....	91
	Warm Up.....	91
	Results.....	95
7.	PEM ELECTROLYSIS MODELING.....	99
	Introduction.....	99
	Methodology.....	101
	First Principals.....	102
	Overpotential.....	105
	Activation.....	105
	Ohmic.....	106
	Concentration.....	107
	IV Characteristic.....	107
8.	CONCLUSIONS AND RECOMMENDATIONS.....	110
	UND System.....	112
	Dew Point Control.....	113
	Future Work.....	115
	NREL Test Facility.....	115
	Dew Point Control.....	116
	Hydrogen Diffusion.....	117
	Mass and Energy Balance.....	117

DI Water	118
Impact of Variable Power	118
Electrochemical Compression.....	118
Remaining System Issues.....	119
Back Pressure Regulator	119
Desiccant Tubes.....	119
Dew Point Sensor.....	120
Vent Valve	120

APPENDICES

A	Wiring Diagrams	123
B	Plumbing Diagrams	165
C	Facility Layout.....	181
D	Model Code	188

LIST OF REFERENCES.....	194
-------------------------	-----

LIST OF FIGURES

Figure	Page
1. Carbon dioxide levels for the past 400,000 years. Graph reproduced by author using data from [13].	4
2. PEM cell components and reaction showing the positive anode and negative cathode electrodes.	18
3. Proton Energy System's HOGEN 40RE.	20
4. Internal components of HOGEN 40RE.	26
5. NREL's energy sources directly coupled to electrolyzer.	27
6. Sample current step waveform from external power supplies and resulting hydrogen mass flow from HOGEN 40RE.	29
7. Frequency attenuation of Xantrex XDC power supplies in current mode from 5 – 25 Hz.	34
8. Stack current and voltage waveforms during 5 Hz complex waveform testing.	34
9. One-hour run in PVO mode showing stack current (top), voltage (middle), and resulting hydrogen production (bottom).	36
10. Stack current (top), voltage (middle), and hydrogen flow rate (bottom) during a portion of the PV simulation.	37
11. Six-pulse, line frequency phase controlled converter.	39
12. Electrolyzer/wind turbine power electronics interface.	40
13. System efficiency across range of operating current of HOGEN 40RE. Trials included are baseline, frequency, PVO, and PVsim.	42
14. Instrument rack with power supplies, data acquisition, electronic load and other important devices.	45
15. Two-line diagram showing relay logic to respond to 10% LFL signal from combustible gas detector (CG2).	50

16.	Interlock loop wiring diagram showing the devices that can interrupt the loop causing PS1 to remove power from the electrolyzer stack.	53
17.	UND water system block diagram.	55
18.	External and DI water loops components and flow.	56
19.	Hydrogen system components from stack to storage.	58
20.	Typical thermoelectric device configured to cool the cold plate on top.	69
21.	Dew point control experimental system design.	71
22.	Detailed CPA showing the cold plate, TEC and water-cooled heat sink.	73
23.	Manufacturer's performance curves for heat pumping capacity versus current for various ΔT	78
24.	Current sweep waveform and stack incoming and exiting DI water temperatures for 20°C trial.	82
25.	IV characteristic curves at constant cathode pressure (170 psig) at temperatures from 6.8 – 33.6°C.	83
26.	IV characteristic curves at constant cathode pressure (90 psig) at temperatures from 9.0 – 32.4°C.	84
27.	IV characteristic curves at constant cathode pressure (0 psig) at temperatures from 9.0 – 29.6°C.	84
28.	High temperature IV characteristic curves between 35 – 70°C at constant cathode pressure of ~ 150 psig.	85
29.	IV characteristic curves at constant temperature (~ 25°C) at cathode pressures of 0 and 168 psig.	87
30.	Anode exchange current density ($i_{a,o}$) experimental results.	89
31.	Cathode exchange current density ($i_{c,o}$) experimental results.	90
32.	Conductivity (σ) fitted linearly to experimental results.	91
33.	Hydrogen system pressure variations during 30-minute warm-up trial with stack current at 70 A.	92
34.	Temperature cycling of system DI water.	93

35.	Analog signal from combustible gas detector (CG1) monitoring the oxygen phase separator gas mixture.	94
36.	System efficiency summary with NREL HOGEN 40 data (♦) and UND system data (●).	98
37.	Experimental IV curve with model for 10°C and 50°C.	108
38.	10°C data and model showing contribution of the overpotential terms.	109
39.	Debris found in hydrogen phase separator that could be partially blocking the vent orifice at shutdown.	121
40.	Fundamental components of system monitoring, control and power to PEM stack.	124
41.	Power enclosure (PE) power supply, terminal and fuse wiring.	125
42.	Power enclosure (PE) buffer module (BM) mounting board (MB) wiring.	126
43.	Sensor enclosure (SE) buffer module (BM) mounting board (MB) wiring.	127
44.	Sensor and power enclosure devices.	128
45.	Power enclosure (PE) electromechanical relay (EMR) wiring.	129
46.	Interlock loop wiring showing user and program lines of PS1.	130
47.	Sensor enclosure (SE) terminal, current and voltage sensor wiring.	131
48.	Sensor enclosure (SE) terminal wiring continued.	132
49.	Chiller heater extension wiring to CH Flg 1 to accommodate 2 kW heater relocation.	133
50.	External water loop solenoid valves CH Flg3.	134
51.	Flow, temperature and pressure sensor cable wiring and configuration.	135
52.	Analog input cable Flange1 (Flg 1) wiring from power enclosure to instrument rack.	136
53.	Cable 1 (Cbl 1) carrying digital input and output signals from power enclosure to instrument rack.	137
54.	Chiller external contacts and flow switch wiring as part of the interlock loop.	138

55.	Plug and flange 6 (Plg/Flg 6) wiring assembly. Analog input signals from power enclosure (PE) to instrument rack and internal flange wiring of power enclosure (PE).....	139
56.	Analog input cable wiring Cable 6 (Cbl 6).	140
57.	Resistivity 1 sensor (RS1) wiring from sensor enclosure (SE) to oxygen phase separator (O2phSep).....	141
58.	Resistivity 2 sensor (RS2) wiring from sensor enclosure (SE) to oxygen phase separator (O2phSep).....	142
59.	Plug and flange 9 wiring assembly (Plg/Flg 9).	143
60.	Oxygen phase separator (O2phSep) temperature sensors (T1, T3) wiring and configuration (Cbl 9A).	144
61.	Pressure (P3), temperature (T6), and dew point (DP1) sensor wiring (Cbl 9B,C and Dev 9B).	145
62.	Temperature (T4), combustible gas detector (CG1) and electrolyzer hydrogen flow (F2) wiring and configuration (Cbl 9D).....	146
63.	Electrolyzer voltage and current (V1, I1) and fuel cell voltage and current (V2, I2) wiring (Plg9E P/S, Cbl 9E).	147
64.	Electrolyzer and fuel cell hall-effect current transducers and voltage device wiring (Plg 9E S/P).	148
65.	Hydrogen phase separator (H2phSep) level sense wiring and float orientation (Flg/Plg 13, Cbl 2).....	149
66.	Oxygen phase separator (O2phSep) level sense, hydrogen phase separator and humidity bottle device wiring (Plg13 – 15).	150
67.	Oxygen phase separator (O2phSep) level sense wiring and float orientation (Flg/Plg/Cbl 14).	151
68.	Humidity bottle flange device wiring (Flg/Plg/Cbl 15).	152
69.	Flange and plug wiring for level sense and humidity bottle (Flg/Plg 16).....	153
70.	Flange and plug wiring of solenoid valves (Flg/Plg 17).	154
71.	External water pump and solenoid valves. Hydrogen phase separator and desiccant solenoid valves and ambient temperature (T8) wiring (Cbl 17A, B)..	155

93.	Desiccant plumbing components.	178
94.	Oxygen phase separator specification to manufacturer.....	179
95.	External reservoir (Res 1) specification to manufacturer.....	180
96.	Detailed hood dimensions and views.	182
97.	Top view Upson 360A showing structural components with hood	183
98.	Upson 360A top view floor plan with descriptions.	184
99.	Upson 360A north wall enclosures and cylinder cabinet.....	185
100.	Upson 360A south wall with desk, instrument rack and canopy hood.	186
101.	Upson 360A east wall canopy hood, instrument rack, cylinder cabinet and major component locations.....	187

LIST OF TABLES

Table	Page
1. HHV's and LHV's of common fuels, kJ g^{-1}	15
2. Comparing hydrogen properties with other fuels. Based on LHV and 1 atm, 25°C for gases.....	15
3. Baseline system efficiencies of HOGEN 40.	32
4. System efficiency of HOGEN 40 with 15 A peak	33
5. Summary of system efficiency of PVO and PVsim trials.	37
6. Explanation of symbols.....	74
7. Governing equations for thermoelectric analysis and gas dehumidification	75
8. Results of baseline calculation for HOGEN 40 as designed.....	75
9. Condition of humid hydrogen at inlet of Stage 1 CPA.	76
10. Condition of hydrogen gas at the exit of Stage 1.	77
11. Condition of hydrogen gas at the exit of Stage 2.	77
12. TEC-based dew point control.....	79
13. Efficiency trial matrix and resulting average system variables.....	95
14. System efficiencies for baseline testing of UND system.	96
15. Typical HOGEN 40 system efficiency data.....	97
16. Constants for heat capacities of gases in ideal state and liquid water.	109

ACKNOWLEDGMENTS

I would like to express my deepest gratitude to Dr. Michael Mann for encouraging me to attend the University of North Dakota, providing much of my funding until our proposal was accepted and for his untiring general and technical support throughout all of my work. Thank you to Dr. Robert Thresher and Dr. Edward Muljadi for providing much of the required technical insight, direction and encouragement. I would also like to thank Dr. Hossein Salehfar, Dr. Marcellin Zahui and Dr. Mary Kweit for their patience, editing and support of my work.

I would like to acknowledge Brad Stevens, Troy Simonsen and Chad Wocken of the Energy & Environmental Research Center for providing me with research assistantships, technical assistance and valuable feedback. I would like to recognize the following people who contributed their time, effort and expertise that made my internships at the National Renewable Energy Laboratory productive: Ben Kroposki, Johanna Levene, Christopher Pink, Lynnae Boyd, Sue Hock, Dr. George Sverdrup, Dr. John Turner, Lee Jay Fingersh and Jason Cotrell.

I am, of course, grateful for Kimberly Ruliffson for her support and who brought considerable writing and editing skills to this report. I would like to acknowledge George Fazekas and Jeremy Toal for their continued friendship and expert advice. Thank you and best of luck to Andrew Peters, Christian Biaku and Nilesh Dale as they inherit and

run the system I designed and complete their research. I deeply appreciate Dave Popke and Joe Miller for sharing their considerable practical experience. Thank you to the UND electricians and various other trades who worked diligently to construct the new lab area in Upson II room 360A. I greatly appreciate the daily contributions of the support staff who contributed to this project from behind the scenes: Barbara Westensee, Patricia Moe, Frederick Gietzen, Kay Olesen, Cadence Youngberg and Stacey Burge.

Thank you to my immediate family whom appear to have unlimited belief in me and to whom this work is dedicated to. I would also like to recognize the generosity of Johnnie Beth and Ray Ruliffson and Kathy and Albert Gale who accepted me into their homes and lives during my frequent relocations. I also appreciate Brian, Clinton, Justin and Kevin Gale for providing some 'gentle' persuasion to keep me focused.

The work presented in this dissertation was carried out at the Departments of Electrical and Chemical Engineering in the School of Engineering and Mines at the University of North Dakota. The work was financed by a U.S. Department of Energy, and a North Dakota Experimental Program to Stimulate Competitive Research (ND EPSCoR) grant, which is gratefully acknowledged.

DEDICATION

To My Loving Parents:

Who have always allowed me to learn by doing even when it monopolized garage space or was not the most aesthetically pleasing prototype.

Who taught me to work hard, question everything, and remain skeptical without becoming narrow-minded.

Who remain supportive regardless of the number of setbacks along the way.

To My Wonderful Sisters:

Who have provided insight and guidance into matters more valuable than the trivia I return.

Who have always believed in and covered for me.

Who continually provide enough encouragement to keep me focused on my dreams.

ABSTRACT

This research endeavor began with the design and construction of a new hydrogen test facility at the National Renewable Energy Laboratory (NREL). To improve the electrical link of wind-based electrolysis the characterization of a proton exchange membrane (PEM) electrolyzer under varying input power was performed at NREL's new test facility. The commercially available electrolyzer from Proton Energy Systems (PES) was characterized using constant direct current (DC), sinusoidally varying DC, photovoltaics and variable magnitude and frequency energy from a 10 kW wind turbine.

At rated stack current and $\sim 40^{\circ}\text{C}$ the system efficiency of the commercial electrolyzer was measured to be 55%. At lower stack current it was shown that commercial electrolyzer system efficiency falls because of the continuous hydrogen purge ($\sim 0.1 \text{ Nm}^3 \text{ hr}^{-1}$) used to maintain the hydrogen desiccant drying system. A novel thermoelectric-based dew point controller is designed and modeled to reduce the penalty to renewable sources because they do not always operate at 100% of rated stack current. It is predicted that the thermoelectric design when operated 100% of the time at full current to the thermoelectric modules would consume 3.1 kWh kg^{-1} of hydrogen. Using the higher heating value of hydrogen and a stack efficiency of 60% to produce the hydrogen that is continuously vented, the desiccant system consumes about 5.7 kWh kg^{-1} .

Design of the UND electrolyzer sub-systems responsible for all aspects of water,

power to the stack, and hydrogen conditioning enables more flexible and precise experimental data to be obtained than from an off-the-shelf system. Current-voltage (IV) characteristic curves were obtained on the UND system at temperatures between 7 -- 70°C. The anode and cathode exchange current densities are fitted to $2.0 \text{ E-06 } e^{0.043T}$ and $0.12 e^{0.026T} \text{ A cm}^{-2}$ respectively. Stack conductivity was fitted to $0.001T + 0.03 \text{ S cm}^{-1}$. The three coefficients represent physical stack parameters and are extracted from the temperature dependent IV curves and the Butler-Volmer equation as the model using the Levenberg-Marquardt nonlinear curve fitting algorithm.

The characterization, dew point controller and modeling work will enable improved efficiency, cost reductions and better modeling of the wind to electrolysis system.

1 CHAPTER

INTRODUCTION

“I believe that water will one day be employed as fuel, that hydrogen and oxygen which constitute it, used singly or together, will furnish an inexhaustible source of heat and light, of an intensity of which coal is not capable... I believe, then, that when the deposits of coal are exhausted we shall heat and warm ourselves with water. Water will be the coal of the future.” Jules Verne, ca. 1870, *The Mysterious Island* [1].

Jules Verne appears to be one of the earliest people to recognize, or at least articulate, the idea of splitting water to produce hydrogen (H_2) and oxygen (O_2) in order to satisfy the energy requirements of society. Hydrogen gas was first isolated by Henry Cavendish in 1766 and later recognized as a constituent of water by Lavoisier in 1783 [2]. The production of hydrogen and oxygen by the electrolytic decomposition of water has been practiced since the year 1800, when the process was first discovered by Nicholson and Carlisle [3]. Since then, the idea of society using hydrogen as a primary energy carrier has been explored and refined.

In the late 1920's and the early 1930's a German inventor, Rudolf A. Erren, recognized and worked towards producing hydrogen from off-peak electricity and modifying the internal combustion engine to run on hydrogen [4]. Erren's primary objective was to eliminate pollution from the automobile and reduce oil imports. In the 1970's Derek Gregory appears to have been one of the leading advocates in creating the case for a hydrogen-based economy [2, 4, 5]. The literature suggests that the term

“hydrogen economy” may have been coined by H. R. Linden , one of Gregory’s colleagues at the Institute of Gas Technology, in 1971 [2]. Gregory points to hydrogen’s environmental benefits and recognizes that, while fossil-fuels are inexpensive, requiring the atmosphere to assimilate the by-products of their combustion is not without consequence.

Still today, the electrolytic production of hydrogen using renewable sources is the only way to produce large quantities of hydrogen without emitting the traditional by-products of burning fossil-fuels or suffering from the hazards associated with nuclear fission. The electrolysis of water is an electrochemical reaction requiring no moving parts, making it one of the simplest and most reliable ways to produce very pure hydrogen. The primary disadvantage of electrolysis is the requirement of high-quality energy needed to disassociate the gas, namely electricity. Electricity is a convenient energy carrier as it can be transported to loads relatively easily. However, locating and constructing new transmission and distribution power lines is challenging and expensive. The cost of transporting electricity along power lines can constitute greater than 50% of the total cost at the point of end-use [6].

The potential environmental benefit of a hydrogen-based economy is hinged to a large degree on the ability to generate the gas from renewable resources in a cost-effective manner. An apparently ideal solution is to use wind-generated electricity to electrolyze water. Today, hydrogen production via electrolysis only meets the U.S. Department of Energy (DOE) goals of \$2 - \$3 per kilogram (kg) in large installations where electrolyzer capital costs are low, less than \$800 per kilowatt (kW), and those having access to inexpensive electricity, less than \$0.04 per kilowatt-hour (kWh) [7].

Electricity from large-scale wind farms in Class 4 or better resource can be generated in the range of \$0.04 – \$ 0.06 kWh⁻¹, not including the \$0.018 kWh⁻¹ federal production tax credit [8, 9]. The out-of-pocket cost of fossil-fuels, whether for electricity production or as transportation fuels, has remained relatively low; limiting the expansion of renewable forms of energy. However, if the external costs of production were taken into account the cost of coal-generated electricity would rise between \$0.03 – \$0.06 kWh⁻¹ [10]. Further limiting market penetration of renewable sources is that fossil fuels continue to receive the bulk of tax incentives here in the U.S. [11].

Variable Renewable Sources

The term “renewable” defines these technologies as driven by natural and sustainable processes which are inherently variable, not intermittent. Natural processes vary over time but are not subject to the on-off switching that, for example, a light bulb connected to a switch is subjected to. Renewable energy (RE) advocates may want to begin training themselves to describe RE as variable, not intermittent, to better describe their naturally occurring behavior. RE sources of energy can provide cost-effective, emission-free electricity with zero- or low-carbon impact making it one of the preferred methods for supplying energy to society. The large-scale wind energy facilities being installed throughout the world are a testament to the growing demand and cost-effectiveness of this RE technology.

Myth Clarification

Hydrogen is often blamed for and criminalized by opponents of transitioning to hydrogen as an energy carrier because of the 1937 Hindenburg disaster. It turns out that the coating of the Hindenburg airship was ignited by an electrical discharge. The coating

was treated with two major components of rocket fuel, aluminum and iron oxide, permitting the fire to freely engulf the surface of the vessel. It turns out that 35 of the 37 people who died in the disaster, perished from jumping or falling from the airship to the ground. Only two of the victims died of burns, and these were from the burning airship coating and on-board diesel fuel [12].

Environmental Imperative

Humans have embarked on an unprecedented experiment with the earth's climate. Every year, larger percentages of the growing global population seek to improve their standard of living by burning ever-increasing quantities of fossil fuels. Oil, coal, and natural gas have powered cars, trucks, power plants, and factories, causing a relatively recent and dramatic buildup of greenhouse gases in the atmosphere, most notably carbon dioxide (CO₂).

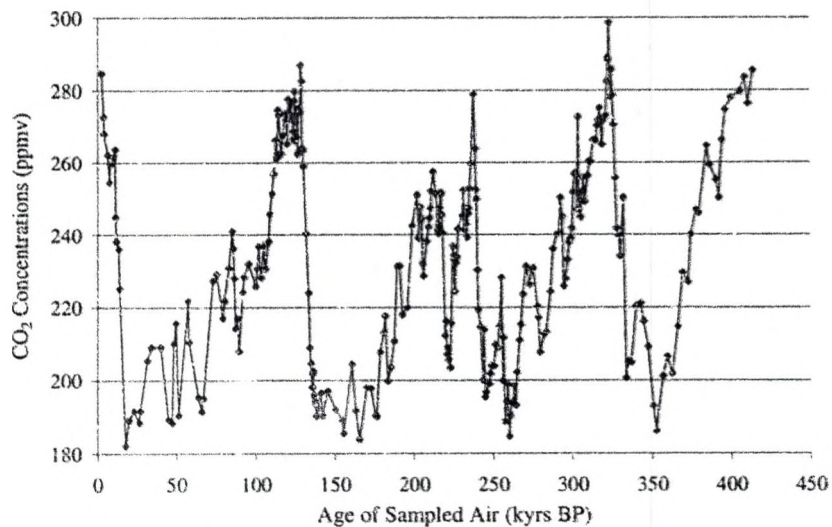


Figure 1. Carbon dioxide levels for the past 400,000 years. Graph reproduced by author using data from [13].

The anthropogenic buildup of heat-trapping gases is intensifying the earth's natural greenhouse effect, causing average global temperatures to rise at an increasing rate. We appear to be entering into a period of abrupt swings in climate partially due to buildup of human-released CO₂ in the atmosphere. Most alarming is not the fact that the climate is changing but rather the rate at which the buildup of CO₂ is occurring.

Ice core samples from Vostok, Antarctic, look back over 400,000 years before present (BP) at atmospheric CO₂ levels by examining the composition of air bubbles trapped in the polar ice buried over 3623 m (11,886 ft) deep [13]. Figure 1 shows that the range of CO₂ concentrations over this time period have been relatively stable, cycling between about 180 and 300 parts per million by volume (ppmv). Although not seen on Figure 1, today the CO₂ concentration stands at an unprecedented 380 ppmv and is rising at an increasing rate.

Two simple irrefutable facts remain that 1) the earth is heating up in part due to the burning of fossil fuels, releasing their main by-product, CO₂, and 2) nearly all reputable scientists studying the global climate change understand that it is a serious emergency. Although the changes in CO₂ concentration and, therefore, temperature are happening more quickly than previously recorded, the changes seen today still span a lifetime and are therefore unrecognized as a significant problem by the general population.

Denials by government, fossil fuel-funded researchers and the fossil fuel industry themselves cloud the debate with misinformation further delaying action. The changes to our climate are occurring at a rate faster than the adaptation time of society and the ecosystems that the planet relies on to survive. It is widely accepted by the scientific

community that anthropogenic greenhouse gases have accelerated and are responsible for at least half of the 20th century warming trend. They go on to refute the claims of skeptics by noting that the changes seen are not entirely due to increases in solar radiation, orbital shift, or long-term shifts in ocean circulation [14].

It may seem reassuring that there is no shortage of fossil fuels in the immediate future. So, why be concerned? The danger is not in running out of energy sources but in the atmosphere's ability to absorb the by-products of burning these carbon-rich fuels. A popular statistic reveals that the United States holds 5% of the world's population but consumes 25% of the world's energy. Making things worse, the United States essentially dismisses the other 163 countries that ratified the Kyoto Protocol, which aims at reducing greenhouse-gas emissions. While not perfect, the Kyoto Protocol is an international and legally binding agreement to reduce greenhouse gases emissions world wide, which took effect on February 16, 2005 [15].

This environmental imperative requires us to quickly come to terms with the actual costs (i.e., including the incidental harm or externalities) of energy use. Only then will the economic reality of energy consumption be realized and renewable sources of energy expand through market forces. That is not to say that fossil fuels like oil, natural gas, and coal do not have a future in helping to meet this growing demand. It should go without saying that all new sources of CO₂ should be sequestered, however, researching a safe and economical way of storing the gas is in its infancy. According to a report from the Clean Air Task Force, fine particulates of 2.5 micrometer (μm) released from coal-fired power plants are responsible for the deaths of roughly 30,000 Americans every year [16].

Hydrogen energy systems, based on RE sources, have been proposed as a means to increase energy independence, improve domestic economies, and reduce greenhouse gas and other harmful emissions from stationary and mobile fossil-fueled sources. Hydrogen production from wind energy, while not economically competitive today with other forms of hydrogen production like steam methane reforming (SMR), is positioned to become the preferred method when environmental, social, and economic factors are weighed. Considering the rapid progress in electric power industry deregulation and rapid improvement in wind, electrolyzer, and fuel cell technology, stand-alone renewable-resource distributed power generation is becoming a potential candidate for providing reliable power to customers and fuel for transportation.

Powering millions of hydrogen internal combustion engines and fuel cell vehicles with hydrogen generated with traditional fossil fuel sources (without CO₂/Carbon sequestration) is merely transferring the pollution from the tailpipe to the stack pipe. The environmental gains hoped for (and actually required by much of the rest of the industrialized world) by the transition to a hydrogen economy can only be achieved when renewable sources are ramped up to produce an increasing amount of the hydrogen gas.

Research Motivation

Electrolyzer manufacturers in North America are Proton Energy Systems (PES) (<http://www.protonenergy.com/>), Hydrogenics Corporation (<http://www.hydrogenics.com/>), Teledyne Energy Systems (<http://www.teledyne.com/>), and Avalance (<http://www.avalance.com/>). Power electronics (PE) inside these commercial electrolyzers are designed for grid-connected operation and represent a significant portion of the overall system cost [17]. The power electronics convert

alternating current (AC) from the grid to direct current (DC) power required by the electrolysis cell stack. In addition to the DC requirements of the stack, the system also consumes additional AC power for the balance of plant or ancillary losses. All of these commercial systems are self-contained and it is relatively straightforward to perform basic performance testing on them. PES offers a version of their mid-sized electrolyzer (S series) that is designed for connection to photovoltaic (PV) panels in addition to having the standard AC to DC converter for utility operation [18]. The additional power electronics, incorporating maximum power point tracking (MPPT), converts all available DC power from the PV array to run the electrolysis stack. This system appears to be one of the first to incorporate dedicated PE to interface with a PV source.

Today, the majority of wind to hydrogen demonstration projects are focused on installing commercially available electrolyzers and powering them from the AC power from wind turbines [19-21]. In these projects the AC from the wind turbines is sent out onto the grid and the electrolyzers tied into the grid achieving a loose coupling of source and load. Scheduling the power to the electrolyzer, based on an output signal from the wind turbines, is relatively straightforward in this case.

Capital costs of electrolysis equipment range from just under \$1000 kW⁻¹ for the largest alkaline systems to over \$10,000 kW⁻¹ for small proton exchange membrane (PEM) electrolyzers [22, 23]. Merely taking an off-the-shelf wind turbine with its own PE and commercial electrolyzer with its own PE reduces overall energy transfer from the wind to hydrogen system. The potential exists to characterize electrolyzer performance under varying input power and design a single PE package and intelligent controller to achieve direct coupling between the stack and wind turbine output. This topology would

not only eliminate the redundancy of power electronics that exists in the wind turbine and electrolyzer but also achieve gains in system cost and robustness. Characterizing the system demands of renewable energy sources and the requirements of the hydrogen producing stack appears to have synergistic benefits. Ultimately, the detailed understanding of both systems and design of the directly coupled wind to electrolysis would reduce the cost of renewably generated hydrogen.

On the turbine side, variable-speed wind turbines (which will soon be the norm as a result of enhanced energy capture relative to constant-speed machines) rely on power electronics to convert the variable frequency, variable voltage AC produced at the generator to DC. Small turbines used in battery-charging applications stop here; however, larger turbines used to connect to the grid must then convert the DC back to AC at grid frequency: 60 Hertz (Hz). It is important to note that because of the economies of scale, it is the large wind turbines that are achieving highly competitive energy costs and will likely be the device of choice in large-scale wind-to-hydrogen operation.

The small wind-to-hydrogen systems (< 20 kW) being studied today are systems incorporating a common DC bus fixed with a battery bank to which the wind turbine and electrolyzer as well as fuel cells and PV panels are connected. Typically, the wind turbine is of the battery-charging type, which requires connection to a constant voltage DC bus (hence, the battery bank) and incorporates power electronics to convert wild AC to DC and to regulate power output. The electrolyzer stack accepts DC power input but the system would also include power electronics to regulate power input and possibly convert DC at one voltage level to another.

There are a number of weaknesses with this configuration, namely a redundancy of power electronics leading to increased cost and potential for failure. The inability to match wind turbine power output to electrolyzer power requirements because of separate power electronic controllers ultimately results in reduced energy capture. Furthermore, one goal of testing the direct coupling of an electrolyzer with a wind turbine is to determine the effect of the fluctuating power output of a wind turbine on stack performance and system operation.

Relevance

While hydrogen production via electrolysis is not a new technology, it is a challenge to get detailed technical information to aid in developing models of manufacturer's equipment. This research combines theoretical analysis and experimental work to extract system parameters from the data to aid in understanding system performance and the development of mathematical models.

The electrolyzer system design is the main focus of this research. Reproducing the current – voltage (IV) characteristic data from the system at NREL will represent success of this design. The HOGEN 40RE[®] electrolyzer from Proton Energy Systems was evaluated at the NREL facility. The stack integrated into the HOGEN electrolyzer is the same stack at the heart of the UND system. Additional control of certain variables like DI water (DIW) temperature will allow the determination of stack parameters otherwise unattainable.

Reproduction of IV characteristic data and stack efficiency data are the basis of the modeling effort of this dissertation and provide verification that the designed system is performing satisfactorily. IV data from the stack at NREL were taken and the

resulting coefficients and basic electrochemical model developed as a result of this research.

Research Objective

Renewable electrolysis can help overcome one of the key barriers to realizing a hydrogen-based economy by replacing the carbon-intensive one that exists today. There is an excellent opportunity for research in renewable hydrogen production both in terms of understanding the operation of the electrolyzer under variable sources and optimizing, in terms of efficiency, cost, and robustness, the link between a renewable source and electrolyzer stack. This research involves the design and installation of a test facility to enable the characterization and experimental testing of a directly coupled wind to hydrogen system. In addition to the design and construction of the facility, initial testing to verify electrolyzer performance, modeling of the PEM electrolyzer, and a novel gas dehumidification model and experimental setup are also vital parts of this research.

Taking lessons learned from a hydrogen test facility at the National Renewable Energy Laboratory (NREL) a new facility at the University of North Dakota (UND) was designed and built to enhance the testing capabilities existing at NREL. Initial testing at NREL focused on determining the baseline performance of a PEM electrolyzer. The UND facility used these data to verify the operation of the electrolyzer system that was built around the same 6 kW stack at the heart of the commercial electrolyzer from Proton Energy Systems. It was determined that in order to perform detailed studies of electrolyzer components and to quantify the influence of varying energy to the stack, the system would have to be built from the stack up. PES agreed to supply the PEM electrolysis stack and desiccant drying system to UND to allow the electrolyzer system to

be built. Understanding the system performance under varying conditions will allow the development of shared power electronics between the wind turbine and electrolyzer. This will ultimately replace the two separate power electronics interfaces with a single package. Furthermore, the single point of control will allow the matching of wind turbine and electrolyzer electrical characteristics, thereby increasing the energy capture of the wind turbine. Finally, this solution will eliminate the need for a constant voltage DC bus and provide a true test of electrolyzer operation under fluctuating power input conditions.

The U.S. Department of Energy (DOE) is focusing a significant effort to create cost-effective production and delivery technologies that are viable within the next 20 years. DOE awarded UND \$470,000 over three years to characterize, model, and study the systemic integration of renewable electrolysis and fuel cells. This work is sponsored by DOE's Experimental Program to Stimulate Competitive Research (EPSCoR): Building EPSCoR – State/National Laboratory Partnerships under grant No. DE-FG02-04-ER46115. Funding has also been provided by the North Dakota Department of Commerce Division of Community Services and UND. NREL's Center for Electric and Hydrogen Technologies and Systems and National Wind Technology Center (NWTC) are collaborating partners in this research. NREL's new facility, dedicated to testing hydrogen-based equipment, is located at the Distributed Energy Resources Test Facility located at the NWTC near Boulder, Colorado.

2 CHAPTER HYDROGEN

Hydrogen (H) is the simplest of atoms, consisting of one proton and one electron. However, hydrogen as a fuel (H_2), like other flammable gases such as natural gas, demands proper handling to avoid unwanted flammable or explosive environments. Hydrogen is not a primary source of energy, rather it is an energy carrier much like electricity. Therefore, hydrogen requires energy to extract it from substances like natural gas, water (H_2O), coal, or any other fossil fuel. Today, SMR is the cheapest and most widely used process to obtain hydrogen gas constituting roughly 50% of the global production of the gas [24]. SMR, like hydrogen production from all fossil fuels, suffers from supply issues, the inevitable rising costs and climate-altering carbon-based pollution. The reforming process generates CO_2 as well as carbon monoxide (CO), which is poisonous to humans because the oxygen-transporting hemoglobin has 200 times the affinity to CO than O_2 [25]. Electrolysis, on the other hand, currently supplies roughly 4% of the world's hydrogen.

Hydrogen has long been part of the society's energy supply as sources have incrementally increased in percent of hydrogen starting from wood, coal, oil and natural gas (primarily methane, CH_4), methanol (CH_3OH), propane (C_3H_8), butane (C_4H_{10}), and heavier hydrogen-carbon chains contained in gasoline. Light and heavy fossil fuels are made up of chains of carbon surrounded by hydrogen atoms; thus the name hydrocarbons. It seems logical that ultimately our energy supply might be composed of

pure hydrogen. However, the gas suffers from low energy density when not bonded in carbon chains making it difficult to store large amounts in volumes that society has grown accustomed to. In the transportation sector, hydrogen storage is an obstacle as larger fuel tanks would be the consequence to realize a minimum 300 mile range for a vehicle between refueling [26].

Properties

Each fuel is limited to a fixed amount of energy it can release when it reacts with oxygen. Every fuel has been experimentally tested to determine the amount of energy it can release and is reported as the fuel's higher heating value (HHV) and lower heating value (LHV). The difference between the two values is the latent heat of vaporization of water, and the LHV assumes this energy is not recovered [27]. In other words, LHV's neglect the energy in the water vapor formed by the combustion of hydrogen in the fuel because it may be impractical to recover the energy released when water condenses. This heat of vaporization typically represents about 10% of the energy content.

It is often confusing to know which heating value to use when dealing with similar processes such as electrolysis and fuel cells. The appropriate heating value depends on the phase of the water in the reaction products. When water is in liquid form, the HHV is used; if water vapor (or steam) is formed in the reaction, then the LHV would be appropriate. An important distinction is that water is produced in the form of vapor in a fuel cell as well as in a combustion reaction and, therefore, the LHV represents the amount of energy available to do work. Table 1 shows both the LHV and the HHV for common fuels. Table 2 compares the same fuels as above and reports their energy density, which is the amount of energy for a given volume. Hydrogen suffers

volumetrically in this category as it takes a larger volume to store an equivalent amount of energy as gasoline.

Table 1. HHV's and LHV's of common fuels, kJ g^{-1} .

Fuel	HHV, 25°C, 1 atm	LHV, 25°C, 1 atm
Hydrogen	141.9	119.9
Methane	55.5	50.0
Gasoline	47.5	44.5
Diesel	44.8	42.5
Methanol	20.0	18.1

Table 2. Comparing hydrogen properties with other fuels. Based on LHV and 1 atm, 25°C for gases.

	Hydrogen	Methane	Gasoline	Diesel	Methanol
Density, kg m^{-3}	0.0898	0.71	702	855	799
Energy density, MJ m^{-3}	10.8	32.6	31,240	36,340	14,500
Energy density, kWh m^{-3}	3.0	9.1	8680	10,090	4030
Energy, kWh kg^{-1}	33.3	12.8	12.4	11.8	5.0

*Energy density = LHV * density (ρ), and the conversion factor is 1 kWh = 3.6 MJ.

As atoms, hydrogen (H) is very reactive and prefers to join into molecular pairs (H_2), forming a gas which behaves much like any other fuel, for example, natural gas. The hydrogen molecule can be further described as orthohydrogen if the atoms are both spinning in the same direction and parahydrogen if they are spinning in opposite directions. At room temperature, the majority (75%) is orthohydrogen, and the difference only becomes important at cryogenic temperatures where orthohydrogen becomes unstable [27]. Hydrogen becomes a liquid below its boiling point of -253°C (20 K) at atmospheric pressure. The density (mass/volume) of air at sea level is 1.225 kg m^{-3} , and

hydrogen is $0.08988 \text{ kg m}^{-3}$, making it 13.6 times lighter than air. This is an important safety consideration in that a hydrogen leak will dissipate quickly.

Flammability Limits

The lower flammability limit (LFL) of these fuels represents the minimum concentration required below which the mixture is too lean to support combustion [28]. Another important safety consideration is the flammability range of fuel. Hydrogen has a wide flammability range of (4% – 75%) while gasoline is (1% – 7%) when mixed with air at standard temperature (25°C) and pressure (1 atm). Hydrogen in oxygen has slightly different flammability range (4% – 85%). Gasoline can only be ignited once the liquid fuel is vaporized and only in the proper fuel/air mixture. Safety systems typically employ sensors that provide warning and alarm signals at certain percentages (for example 10% and 20%) of the LFL to avoid environments where a combustible gas would reach an unsafe and flammable concentration.

Electrolysis

Electrolysis is defined as splitting apart with an electric current. Hydrogen as an energy carrier and potential fuel is attractive because it can be produced by splitting water. In addition, the readily available electrolyzer can be used in a home or business where off-peak or surplus electricity could be used to make the environmentally preferred gas. Electrolysis was first demonstrated in 1800 by William Nicholson and Sir Anthony Carlisle and has found a variety of niche markets ever since. Two electrolyzer technologies, alkaline and PEM, exist at the commercial level with solid oxide electrolysis in the research phase.

Alkaline

The alkaline electrolyzer is a well-established technology that employs an aqueous solution of water and typically 25 – 30 wt.% potassium hydroxide (KOH), however, sodium hydroxide (NaOH) and sodium chloride (NaCl) can also be used. The liquid electrolyte enables the conduction of ions between the electrodes and is not consumed in the reaction but does need to be replenished occasionally. These systems are run at current densities in the range of 100 – 300 mA cm⁻². The reactions for the alkaline anode and cathode are shown in Eqns. 2-1 and 2-2, respectively.



Proton Exchange Membrane

PEM electrolysis (PEME) is also referred to as solid polymer electrolyte (SPE) or polymer electrolyte membrane (also, PEM), but all represent a system that incorporates a solid proton-conducting membrane which is not electrically conductive. The membrane serves a dual purpose, as the gas separation device and ion (proton) conductor. High-purity deionized (DI) water is required in PEM-based electrolysis, and PEM electrolyzer manufacturer PES requires a minimum of 1 MΩ - cm resistive water and would prefer higher. DI water is introduced at the anode of the cells, and a potential is applied across the cell to dissociate the water. The protons (H⁺) are pulled through the membrane under the influence of an electric field and rejoin with electrons being supplied by the power source at the cathode to form hydrogen, H₂, gas [29]. PEM electrolyzers are typically operated at roughly an order of magnitude higher current density than their alkaline

counterparts but will suffer from lower efficiency at the higher level. PEM also holds other advantages over alkaline including the ability to maintain a differential pressure across the anode (oxygen) and cathode (hydrogen) sides of the membrane to reduce the compression stages for high-pressure storage. Finally, without any additional purification of either technology PEME, generates purer hydrogen product gas than alkaline. The PEM anode and cathode reactions are described in Eqns. 2-3 and 2-4, respectively, and shown in Figure 2.

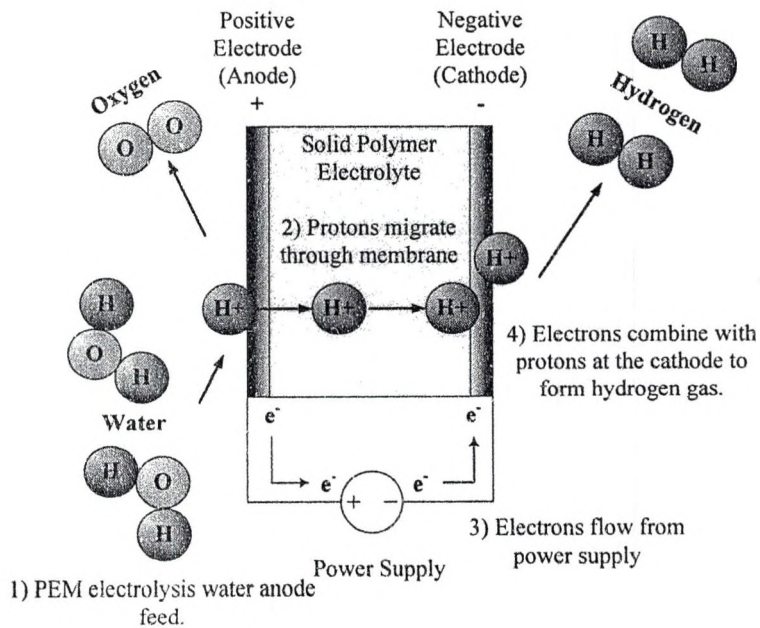


Figure 2. PEM cell components and reaction showing the positive anode and negative cathode electrodes.

3 CHAPTER

COMMERCIAL ELECTROLYZER TESTING

“Although the benefits of the hydrogen economy are still years away, our biggest challenges from a sustainability standpoint are here today”, said Mike Nicklas, Past Chair of the American Solar Energy Society, during his opening comments at the first Renewable Hydrogen Forum in Washington, D.C., in April 2003 [30].

NREL Test Facility

The NREL facility was designed and built from 2003 to 2004 to enable the testing of hydrogen-based electrolyzer and fuel cell equipment coupled with renewable sources of energy. This chapter, taken primarily from a NREL technical report currently in press [31], details the initial PEM electrolyzer testing conducted at NREL’s hydrogen test facility located at the NWTC. The UND electrolyzer and fuel cell test bed, detailed in Chapter 4, is based on lessons learned during the NREL facility construction, system instrumentation and initial testing explained in this chapter. The UND system was designed to enhance and complement the testing capabilities of the NREL facility.

The first testing completed at the NREL facility was the characterization of a HOGEN 40RE PEM electrolyzer from Proton Energy Systems, Wallingford, Connecticut. The HOGEN 40 stack is rated to produce 40 standard cubic feet (1.05 Nm^3) at 200 psig (13.8 atm) of dry (less than 5 ppm) hydrogen gas per hour. The PEM stack consists of 20 series connected cells, each cell having an active area of 0.093 ft^2 (86.4 cm^2). At rated current (140 A) results in a maximum current density of 1.6 A cm^{-2} .

The HOGEN 40RE is the renewable energy version which has additional power electronics mounted in a “ side-cart ” to accept energy from a PV array via two DC disconnects also located in the side-cart. The energy from the PV array passes through the DC/DC power converter and then applied to the stack for electrolysis only. The DC/DC buck converter accepts input DC voltage range of 60 – 200 Vdc and steps it down to the 30 – 40 Vdc required by the PEM stack. The energy from the PV array is passed directly to the stack while the AC utility connection maintains the ancillary system loads. The PEM electrolyzer with optional RE power electronics is a commercially available S-series production model. The optional side-cart is shown on the HOGEN 40RE in Figure 3.

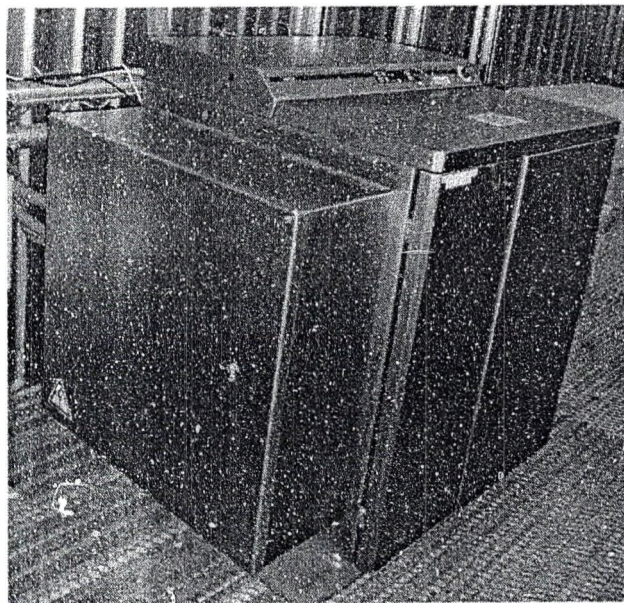


Figure 3. Proton Energy System's HOGEN 40RE.

Safety

NREL's hydrogen test facility is constructed from a 40-foot-long shipping container and divided into three rooms.

1. Battery Storage
2. Control Room
3. Test Bay

The 20-foot-long test bay was designed to Class I Div. II standards to accommodate hazardous environments. However, the HOGEN 40RE is designed with internal ventilation fan and hydrogen detection and does not require a room suited for hazardous environments to operate safely. Hydrogen detectors monitor the facilities test bay and are wired to relays that automatically initiate system shutdown. Relay logic routes power to an emergency fan if the level of hydrogen reaches 10% of the LFL of hydrogen gas in air. At 20% LFL a separate set of relays trips the main AC breaker on the back of the electrolyzer, energizes a blue emergency beacon, and locks the system out until a manual reset button is depressed by the operator.

A summary of the facility's hydrogen-related safety systems include the following:

- During all equipment operations an exhaust fan in the test bay and amber beacon on the outside of the facility are running. Both devices are software-controlled and operate while the electrolyzer is in operation.
- Two hydrogen detectors are located in the test bay. Both detectors are calibrated every six months, have two trip points at 10% and 20% of the LFL of hydrogen in air and are wired in parallel to additional relay logic to drive system shutdown
- The 10% LFL trip point initiates a controlled (i.e., software-driven) shutdown of the system and turns on a second emergency exhaust fan. The second exhaust fan is driven by relays and will operate regardless of the state of the software.

- Regardless of the state of the control software, the hydrogen detectors 20% LFL trip point initiates a hard shutdown of the equipment. The hard shutdown consists of dry contacts in both detectors wired through relay logic to trip the AC breaker of the electrolyzer.
- If the 20% LFL is reached, the system is locked out by a latching relay until manually reset by the operator.
- If the system is locked-out and the test bay is determined to be safe the safe operating procedure (SOP) instructs operators to use a handheld combustible gas detector to find and repair the source of leak before returning the system to operation. While this 20% LFL alarm relay is latched, a blue beacon is running on the outside of the facility to notify personnel that the system is shutdown and an elevated level of hydrogen was reached in the test bay.
- Control software archives both alarms and other hardware events in a log file, and visual alerts on the user interface provide feedback to the operator. A software-controlled audible alarm in the control room is activated in both the 10% and 20% alarm case, with a higher frequency signal for the 20% level.
- Heat detection and fire pull-boxes are integrated into main fire alarm system. The separation wall between test bay and control room has a 2-hour fire rating, and the door from the control room is rated for 1 hour.

Data Acquisition

All analog and digital input/output signals are acquired or emanate at the data acquisition (DAQ) system. Software, written in LabView[®], monitors and controls system operation using analog output (AO), digital input/output (DI, DO), and samples analog

input (AI) signals from a host of sensors. The major components of the data acquisition system can be referenced by visiting the National Instruments (NI) website at <http://www.ni.com/>.

Major components of the DAQ system include the following:

- PCI-6036E multifunction DAQ device – 16 bit, 16 single-ended (or eight differential) AI, two AO, 200 kS s⁻¹ and eight digital input/output (I/O).
- Signal conditioning extensions for Instrumentation (SCXI) 12-slot chassis (SCXI-1001).
- SCXI-1102C – 32-differential channel AI module. Each channel has a three-pole, low-pass filter with a 10 kHz cutoff frequency. A SCXI-1308 terminal board attached to the front of the module contains 249 Ω resistors to accept the 4 – 20 mA AI sensor signals.
- SCXI-1162HV – 32-channel high-voltage (HV) DI module. The optically isolated module can accept a wide range of AC or DC digital inputs. A SCXI-1326 shielded terminal block connects to the module to access each channel.
- SCXI-1163 – 32-channel DO module. Each channel is optically isolated and provides a low voltage (0 or +5 V) to control external devices. A SCXI-1326 shielded terminal block connects to the module to access each channel.
- SCXI-1180 feed-through panel provides access to the two AO's of the PCI-6036E card. A SCXI-1302 shielded terminal block connects to the module to access the pins of the DAQ card.

The PCI-6036E card is installed in the computer and connected to the SCXI-1001 12-slot chassis via a 50-pin cable. The SCXI modules mounted in the chassis interface to

analog sensors and devices via the front-mounted screw-terminal blocks. External to the SCXI system, buffer modules interface low-level signals from the DO module to control higher-power devices like fans and mechanical relays.

Instrumentation

All analog sensors have 4 – 20 mA output signals connected to the SCXI-1102C AI module. The SCXI-1308 terminal block on the front of the 1102C module contains 249 Ω resistors resulting in a 1 – 5 V signal. The software contains two user-selectable sample rates (low and high) for the AI channels. Both the high- and low-speed data are written to separate files with the low-speed data either averaged or decimated from the high-speed samples. The time-stamped samples are saved in the rows and sensor channels are in the columns and are saved in a comma-delimited file format. Voltage and Hall-effect current transducers are both direct-acting and produce an output signal directly proportional to the input. Power required by the additional sensors, instrumentation and DAQ system does not contribute to stack or system efficiency calculations shown in subsequent sections.

Sensors were integrated into the electrolyzer to monitor the following electrolyzer parameters:

- Multifunction sensor monitors AC input voltage and current and outputs four user-programmable signals. A 100:5 A current transformer and voltage pick-off are fed to the sensor to determine the rms current and voltage. Other parameters such as active and apparent power are calculated within the sensor and are available as user programmable output signals.
- Input voltage and current to the DC/DC power converter.

- Output current from the DC/DC power converter (i.e., PV array contribution to stack current).
- Voltage and current of the PEM Stack.
- All ancillary power (rms) used by the system (i.e., valves, pumps, controller, sensors, and fan).
- DI water flow, temperature, and pressure to stack.
- DI water temperature and pressure after the PEM stack.
- DI water resistivity prior to system mixed-bed filter.
- Hydrogen product mass flow at electrolyzer output.
- Hydrogen system pressure inside electrolyzer.

Figure 4 shows the major water and hydrogen components inside the HOGEN 40RE which includes the “ heart ” of the system: the PEM stack in front center. The compartment behind these systems (not viewable) contains the AC/DC power converter, ventilation fan, 24 Vdc power supply, system controller, radiator, and control relays. A side compartment to the left of these systems (not viewable) contains the optional (RE version, Figure 3) DC/DC power converter and DC disconnects used to interconnect to a PV array. To monitor system performance the additional instrumentation, listed above, were directly installed into the electrolyzer’s water plumbing and hydrogen gas tubing. The combustible gas detector (Figure 4, upper right) monitors hydrogen levels in this compartment and the oxygen phase separator.

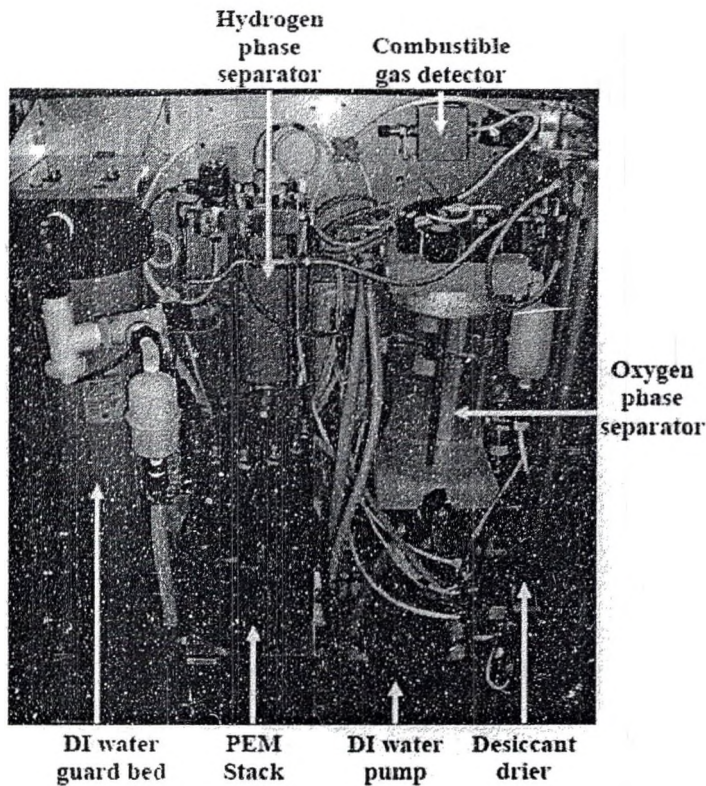


Figure 4. Internal components of HOGEN 40RE.

Figure 5 is simplified to show the various energy input devices that are interfaced to the electrolyzer. Each of the three inputs (power supplies, wind turbine, and PV array) are tested individually by physically moving conductors and by configuring the DC bus at NREL's Hybrid Power Test Bed (HPTB). During PV testing the array is wired to the system's DC disconnects which are closed when the electrolyzer's controller has verified critical system parameters, such as water flow to the stack. When conducting testing with the external power supplies or the wind turbine they are also wired through the electrolyzer's DC disconnects, but the DC/DC power converter is bypassed, resulting in a direct connection to the PEM stack. A shunt-trip circuit breaker protects the stack by physically disconnecting any source that exceeds 155 A for more than 2 seconds.

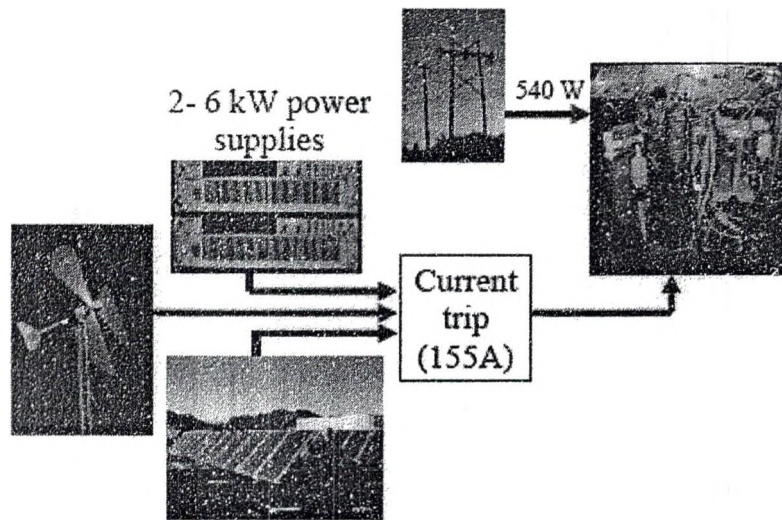


Figure 5. NREL's energy sources directly coupled to electrolyzer.

Modes of Operation

In all three input modes of operation the AC grid provides power to the system's ancillary loads which include the ventilation fan (~240 W), 24 Vdc power supply, water pump, solenoid valves, sensors, and the main controller board. The unit has a manual AC disconnect to remove AC utility power, and the system controller activates DC disconnects (RE version only) to control incoming DC power from the PV array.

Grid Only

The electrolyzer can operate in one of three input modes. The factory default operating mode is grid only (GO) where the unit is powered from 190 – 240 Vac, single-phase, 60 Hz power source. NREL operates the unit at 208 Vac resulting in 35 A at full-load, resulting in 7.2 kW. In this mode all power needed for stack and ancillary power is derived from the AC utility grid [32]. The onboard AC/DC converter rectifies and filters

the DC required by the stack while the 24 Vdc power supply provides power for the ancillary devices. At the beginning of life, full current (140 A) and stack DI water temperature at roughly 35°C the stack voltage is approximately 40 V.

PV Only

In PV only (PVO) mode both the AC grid and PV source are interfaced with the electrolyzer. The DC/DC power converter consumes a small amount of the PV energy to operate, with all the remaining applied directly to the stack. The DC/DC converter typically operates at about 92% efficiency. In this mode of operation all ancillary power requirements are still provided by the AC grid connection. Future modifications will enable the electrolyzer to operate grid independent [32].

PV and Grid

In PV grid (PVG) mode both the AC grid and PV source are interfaced with the electrolyzer. The DC/DC converter provides as much power as possible for electrolysis with the AC/DC power converter making up the difference to maintain the desired hydrogen production. If, for instance, the PV array is producing 2 kW and hydrogen demand is such that 4 kW is required then the AC grid will provide the remaining 2 kW for electrolysis [32].

The electrolyzer can be run in one of two output modes (tank filler or load follower). In tank filler mode, the controller applies full current to the stack until the product pressure transducer reaches the pressure set-point (200 psig, 13.8 barg) and then enters idle more. In idle, the system monitors tank pressure and maintains the system to allow electrolysis to begin once tank pressure falls below a given hysteresis below set-point. In tank filler mode the stack current is either fully on or off.

If the electrolyzer is connected to a process that requires a continual draw of hydrogen at a variable rate, the electrolyzer can be run in load follower mode where the controller will monitor demand through pressure feedback and adjust current to the stack accordingly [32].

System Testing

External Power Supplies

The system-controlled internal DC disconnects, typically used to isolate the unit's DC/DC converter from the external PV array, was utilized to provide a safe means of introducing the externally generated current waveforms from the power supplies directly to the PEM stack. During the stack characterization, the system was run in PVO mode with the external power supplies providing current to the stack, bypassing the systems DC/DC converter.

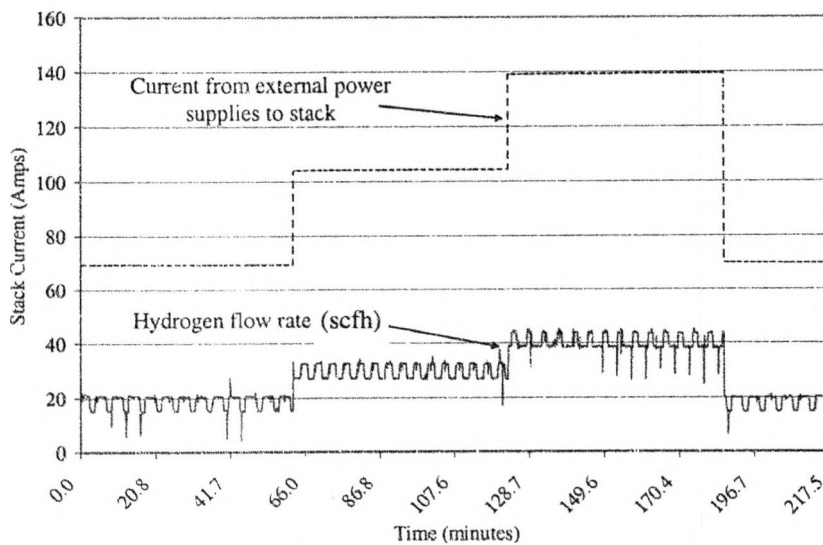


Figure 6. Sample current step waveform from external power supplies and resulting hydrogen mass flow from HOGEN 40RE.

Figure 6 shows the step currents from the power supplies and the resulting hydrogen flow in standard cubic feet per hour (scfh) from the system. Hydrogen production ripple is caused by the internal hydrogen phase separator pumping down the accumulated water and desiccant drying tube crossover. These system functions cause a drop in system pressure resulting in varying hydrogen production output. A more detailed explanation is provided in the Chapter 6.

The system efficiency is calculated using Eqn. 3-1 which includes both the ancillary losses plus the stack energy. During the power supply testing, the stack is powered by external supplies to enable accurate control of input current waveforms. To take into account the efficiency of the external power supplies, the manufacturer's owners manual was referenced and an average efficiency of 89 % was used [33]. During actual testing of the PV array the efficiency of the onboard DC/DC power converter was determined using the current and voltage transducers which were added to monitor the input energy from the PV array and the energy to the stack.

$$\text{System Efficiency} = \frac{\text{HHV} \left(\frac{\text{kWh}}{\text{kg}} \right)}{\left(\frac{\text{Stack Input Energy (kWh)}}{\text{Power Supply Efficiency}} \right) + \text{Ancillary Losses (kWh)}} \times \text{Hydrogen Produced (kg)} \quad 3-1$$

$$\text{Stack Efficiency} = \frac{\text{Ideal Stack Potential}}{\text{Actual Stack Potential}} \quad 3-2$$

The HHV of hydrogen is 39 kWh kg⁻¹ and the ideal stack potential is a function of temperature and pressure. All efficiencies are referenced to the HHV of hydrogen. The minimum amount of energy that must be consumed to split water into hydrogen and oxygen is known as the heat of formation (enthalpy) and corresponds to the HHV of

hydrogen. The ideal stack potential in Eqn. 3-2 is defined in greater detail in Chapter 7 that covers modeling stack parameters.

$$\text{Energy} = \frac{1}{3600} \int \text{Power} \, dt \sim \frac{1}{3600} \sum_i^n \frac{P_i + P_{i-1}}{2} (t_i - t_{i-1}) \quad 3-3$$

Using Eqn. 3-3, stack and ancillary energy are calculated with samples (P_i) from the DAQ system and the time stamp (t_i) associated with each measurement. The hydrogen mass flow meter output signal is calibrated in scfh and is also integrated using the discrete samples and the associated time stamp with Eqn. 3-3. Hydrogen gas directly from the stack is saturated with water vapor, making a mass flow measurement to find the quantity of hydrogen produced (kg) difficult. It is worth noting that part of the H_2 product gas is used to regenerate the desiccant drying beds, and that loss is not measured by the hydrogen mass flow sensor at the system output. Chapter 5 covers the desiccant drying system in detail and an alternative method of dehumidifying the product gas is presented to improve system efficiency. The constant in front of the integral of Eqn. 3-3 converts sub-second sampled data into hours.

Baseline

Prior to the baseline testing the electrolyzer was run for 1 hour as a warm-up period and then each current level was run for 1 hour. RS232 communication and an AO signal are interfaced with the power supplies to provide the desired current. The two 100 A power supplies are run in current mode in a master/slave configuration. The master accepts a 0 – 10 V signal from a DAQ AO channel and combined supply current between 0 – 200 A to the stack.

Table 3. Baseline system efficiencies of HOGEN 40.

Stack Current Amp	System Efficiency %	System Temperature °C
35.2	27.4	29.2
69.4	50.3	29.0
104.5	54.4	34.7
139.6	54.7	42.7
139.7	55.3	40.5
104.7	52.1	42.8
70.1	44.6	39.3
35.3	21.3	35.6

The system was operated at four different current levels (35, 70, 105, and 140 A) to establish baseline performance. These levels correspond to 25%, 50%, 75% and 100% of the rated current of the stack. Table 3 shows the system efficiencies and DI water temperature for the HOGEN 40 system for these baseline trials. The system temperatures are averaged DI water temperatures during the trials. Higher system temperatures should result in higher system efficiency. The temperature data of Table 3 is not reliable because the commercial HOGEN 40 does not control water temperature. The design of the UND system (Chapter 4) includes water temperature control and results (Chapter 6) in higher temperatures leading to higher stack efficiencies.

It is worth repeating that the system efficiency is different than the stack efficiency. The system efficiency (Eqn. 3-1) uses the higher heating value of hydrogen (39 kWh kg^{-1}), the energy consumed by the stack (kWh), efficiency of the DC power supplies and the balance of plant ancillary losses (kWh). During the baseline testing the DC/DC power converter was physically bypassed and the electrolyzer was run in PVO to enable the external power supplies to provide power directly to the stack.

Complex Waveform

The 1-hour warm-up run contained no ripple, and each subsequent trial was run for 30 minutes with the resulting system efficiencies shown in Table 4. It is shown that presenting a complex waveform (AC + DC offset) consisting of a 15 A peak sinusoidal waveform riding on a DC offset of 140 A does not appear to impact performance.

Table 4. System efficiency of HOGEN 40 with 15 A peak sinusoid plus 140 A DC offset.

Stack Current Amp	Frequency Hz	System Efficiency %	System Temperature °C
139.9	0	54.2	43.7
140.5	5	53.3	49.0
140.5	10	53.2	49.4
140.5	15	52.9	48.8
140.5	20	53.2	48.3
140.5	25	53.1	47.8
140.4	25	53.7	46.1
140.4	20	53.8	46.0
140.3	15	53.8	45.4
139.5	10	54.2	45.4
140.2	5	54.0	44.3

The programmable power supplies source power to the stack in current rather than voltage mode. Because of the frequency attenuation of the power supplies in current mode (Figure 7) frequencies greater than 25 Hz were not practical. Calculations based on the frequency response of the power supplies were made to generate nearly constant peak waveforms between the frequencies 1 – 25 Hz.

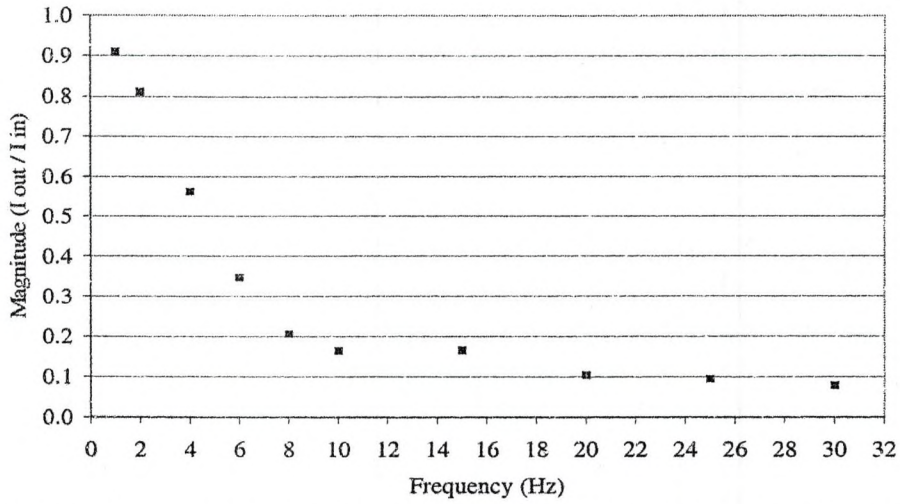


Figure 7. Frequency attenuation of Xantrex XDC power supplies in current mode from 5 – 25 Hz.

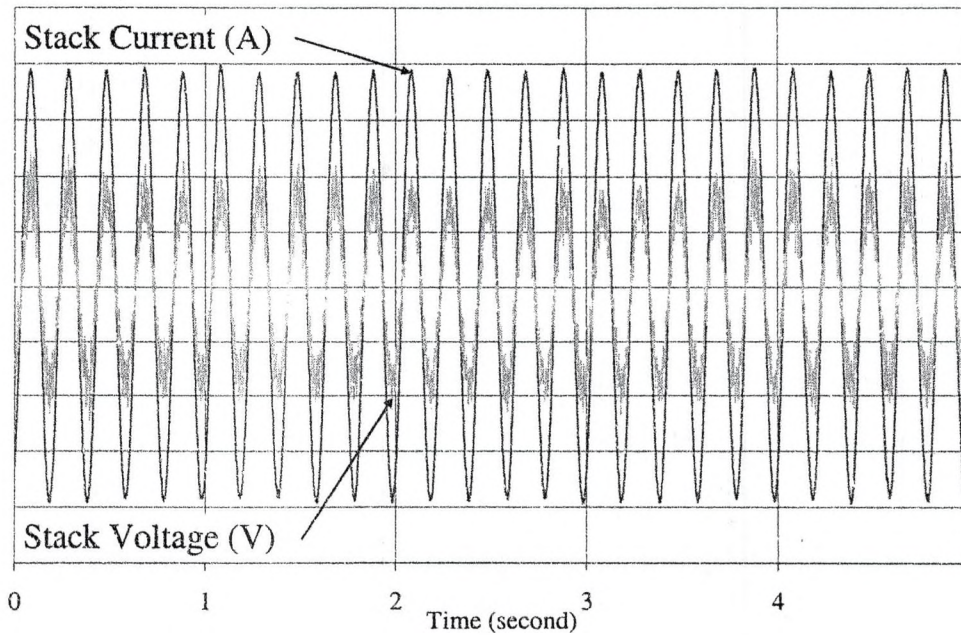


Figure 8. Stack current and voltage waveforms during 5 Hz complex waveform testing.

The complex waveform testing revealed that the electrolyzer PEM stack appears to behave like a purely resistive load, with no phase shift between the voltage and current measurements (Figure 8). This means that electrically speaking, the electrolyzer exhibits no inductive or capacitive effects; although having cells stacked like plates of a capacitor might indicate otherwise. The other interesting conclusion is that current ripple on a DC offset seems to have little or no effect on system efficiency during these trials. A more accurate means of determining the impedance of the stack cells could be accomplished by performing electrochemical impedance spectroscopy.

PV

As mentioned earlier, the HOGEN 40RE contains a DC/DC power converter which enables the interconnection of the electrolyzer with a PV array. The additional power converter contains MPPT to optimize the operating point and consumes some of the PV energy to power itself. This testing utilized NREL's 5 kW PV array which was configured to provide a maximum of 5280 W at 131.2 V and 40.1 A under full-sun conditions. The DC/DC converter has a programmable input range which was set to accept 60 to 200 VDC with the output current applied directly to the stack. Open circuit voltage for the 48-panel PV array was 164.8 V.

Figure 9 shows a 1-hour test of the electrolyzer in PVO mode with the PV array providing all of the energy for electrolysis. The high frequency current waveform is a result of the MPPT of the DC/DC power converter. The sampling rate during this trial was 100 samples per second ($S s^{-1}$). During this test the DC/DC power converter was presented with 3.64 kWh of energy from the PV array and delivered 3.32 kWh to the

stack, resulting in an efficiency of 91.2%. Variations in the output current from the DC/DC converter (Figure 9, top) are the result of clouds passing over the PV array.

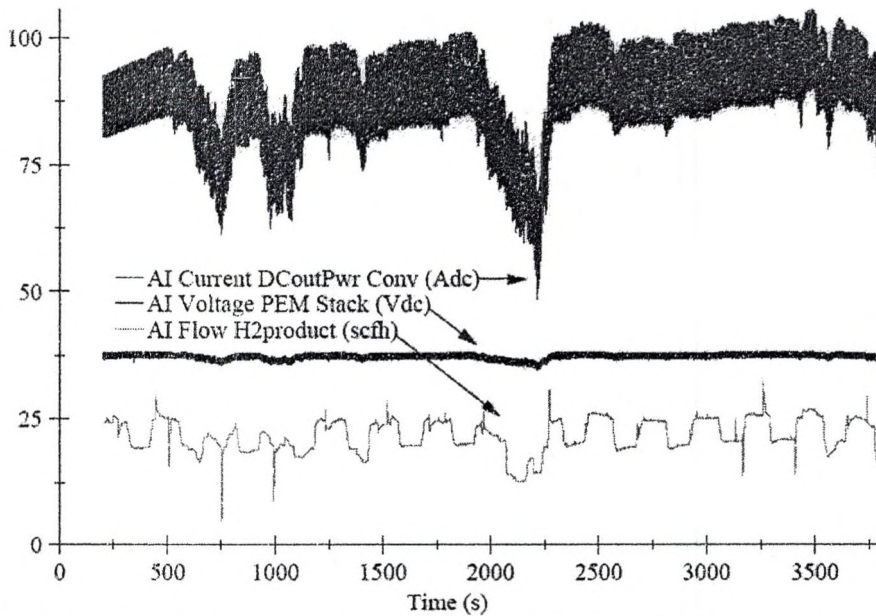


Figure 9. One-hour run in PVO mode showing stack current (top), voltage (middle), and resulting hydrogen production (bottom).

PV Simulation

Figure 10 shows the varying stack current during a portion of a PV simulation (PVsim) trial. Stack current was copied from an actual PV test and a comma-delimited file was created for the trial. The software reads the file and controls the power supplies which supplied current to the stack directly. In other words, the power supplies were not supplying power to the DC/DC power converter like the actual PVO test. The software updated the power supply current to the stack once per second resulting in the lower resolution data of Figure 10.

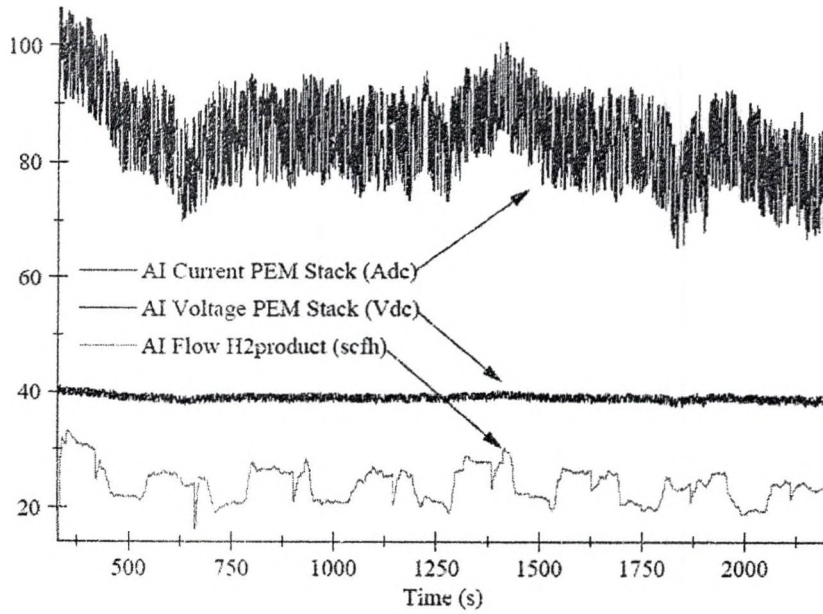


Figure 10. Stack current (top), voltage (middle), and hydrogen flow rate (bottom) during a portion of the PV simulation.

Table 5 shows the PVsim trial results. The difference in the system efficiency between the actual PV test (PVO) and the PV simulation (PVsim) may be the result of the slightly higher temperature that the trial was conducted at. However, these efficiencies are comparable with the baseline efficiencies from earlier (Table 3).

Table 5. Summary of system efficiency of PVO and PVsim trials.

Mode	Stack Current Amps	System Efficiency %	System Temperature °C
PVO	88.6	52.1	36.3
PVsim	88.8	52.6	37.7

Wind Turbine

As a proof of concept and feasibility study, an of-the-shelf wind turbine package was modified and connected directly to the PEM stack. Being a variable speed PMG, the output power, voltage, and frequency scale with available wind energy. The values for

frequency and voltage are based on historical operating values at NREL's NWTC test site. Unlike the PV testing which utilized the DC/DC power converter provided in the HOGEN 40RE, this wind turbine testing was conducted more like the baseline power supply testing. The wind turbine testing had the electrolyzer in PVO mode and energy from the wind turbine's power converter was connected directly to the stack.

The wind turbine used for this project is a readily available commercial product and has the following electrical specifications:

- Direct drive permanent magnet generator (PMG)
- 10 kW maximum power output
- Inverted generator configuration with an outer rotation field and stationary armature
- Variable, wind-based output energy
- Voltage range: 120 – 270 V for low and high wind speeds, respectively
- Frequency range: 50 – 130 Hz for low and high wind speeds, respectively

The wind turbine system includes a device to convert the variable voltage, variable frequency AC from the turbine to a regulated DC. This power electronics interface (also called a VCS10) is designed for battery charging operations, but was modified to also accommodate powering the HOGEN 40 PEM stack. The PE interface is a voltage controlled device that regulates output based on DC bus voltage. The input and output settings of the interface were modified from the factory settings to accommodate the following circuit parameters:

- Input voltage range: 120 – 273 Vac

- Input frequency range: 50 – 131 Hz
- Output voltage: 32 – 42 Vdc

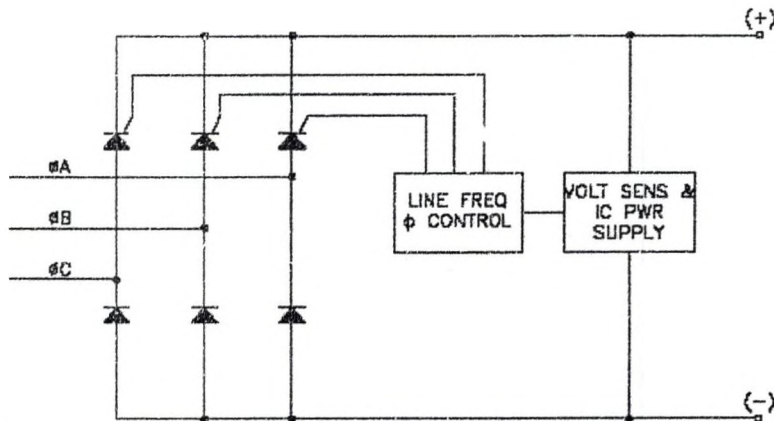


Figure 11. Six-pulse, line frequency phase controlled converter.

Figure 11 shows the topology for this application. It is similar to a three-phase rectifier, except it uses controlled silicon controlled rectifiers (SCR's) to provide some level of voltage regulation. The circuit, which is known as a six-pulse, line-frequency phase-controlled converter, is widely used and is commonly found in poly-phase supplied battery chargers.

A three-phase step-down transformer (166:52 V) is included with the package. It is necessary to efficiently accomplish the conversion from the wind turbine output (nominally 230 Vac) to the electrolyzer input (30 – 40 Vdc). The scale of the transformation was based on the ability to make the converter and make its controls as simple as possible. This means the nominal input voltage to the converter should be such that if it was just a six-pulse rectifier, its output voltage would be slightly higher than the necessary voltage. That way, the converter can control DC bus voltage by reducing the duty cycle of its SCR's. The average output voltage of a simple six-pulse rectifier can be calculated as in Eqn. 3-4.

$$V_{DCavg} = \frac{3\sqrt{2}}{\pi} V_{ACin}$$

3-4

Therefore, for a 60 Vdc nominal output (unregulated), the input should be 44 Vac. This results in a transformer turns ratio requirement of approximately 4. The VCS10 also requires power for its controls. To facilitate the ability to perform a controlled startup and shutdown, its integrated control (IC) circuitry should have power before startup begins and after shutdown terminates. Thus control power must be independent from the power produced from the PE interface. In the current configuration, the control power is taken from the DC (battery) side. The battery also not only provides the necessary control power, it acts as a sink to any transients occurring on the PEM stack supply.

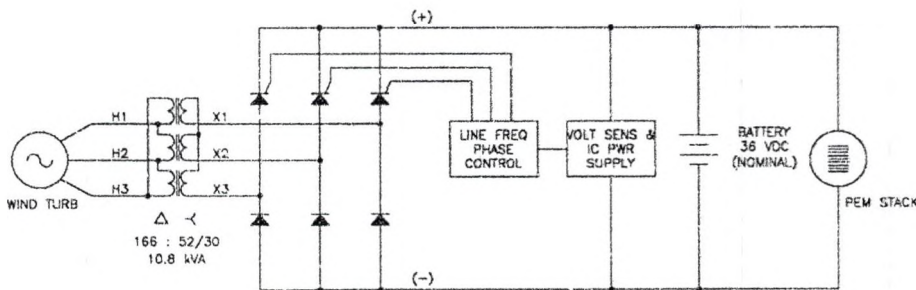


Figure 12. Electrolyzer/wind turbine power electronics interface.

Figure 12 depicts the basic topology of the electrolyzer/wind turbine power electronics interface. The system voltage will be controlled using line frequency phase control. As available wind energy is increased, the triggering duty cycle of the SCR's is modified to achieve a higher amount of input energy to the stack and battery. Trial runs of the interface were conducted by connecting a resistive load bank in place of the PEM stack. The operation of the interface was evaluated as well as the potential effects of its

output on the PEM stack. Initial runs consisted of a 2.75 Ω resistive load connected to the battery and interface system. Bus voltage was set to 38 Vdc nominally.

Conclusions

The objectives of the testing conducted at NREL's facility were to experimentally characterize the performance of the HOGEN 40RE PEM electrolyzer based on varying input power. Characterizing the electrolyzer performance with variable input power and under various load conditions showed that the PEM electrolyzer can perform adequately under all input power conditions.

Baseline and the complex waveform system efficiencies are in good agreement when comparing similar current ranges. During the complex waveform testing, 15 A peak sinusoidal currents were superimposed on a 140 A DC offset keeping the average current at 140 A. The stack current and voltage were in phase which suggests that the stack behaves like a purely resistive load. Efficiencies under these varying current trials show that the system performance does not appear to be jeopardized by the inherent varying inputs of PV and wind systems. The efficiency of the DC/DC power converter during the PV array testing was in the range of 91% – 93%. The PV simulation testing was conducted using the external power supplies providing current directly to the stack, not through the DC/DC power converter. The power supplies updated the current to the stack once per second with the values read from the file.

Based on the characterization testing, a power electronics interface was designed using modified stock components from the wind turbine manufacturer. The tests results showed that the net capture of available wind energy from the modified stock power electronic interface actually decreases as wind speeds go up, making this arrangement of

hydrogen production inefficient and inappropriate. Future research will examine optimizing the power electronic interface to capture the maximum energy from the wind turbine for use in producing hydrogen.

Figure 13 is a summary plot of the characterization testing from baseline to PV. The decreasing system efficiencies at lower currents were not anticipated. However, insight into the HOGEN 40's desiccant drying system revealed that a constant flow of dry hydrogen product gas is used to maintain the two-tube drying system. Proton Energy Systems explained that at full current and 200 psig, roughly 10% of the dry hydrogen product is constantly used to maintain the desiccant of the opposite tube. This fact handicaps renewably integrated energy sources because of their natural varying nature.

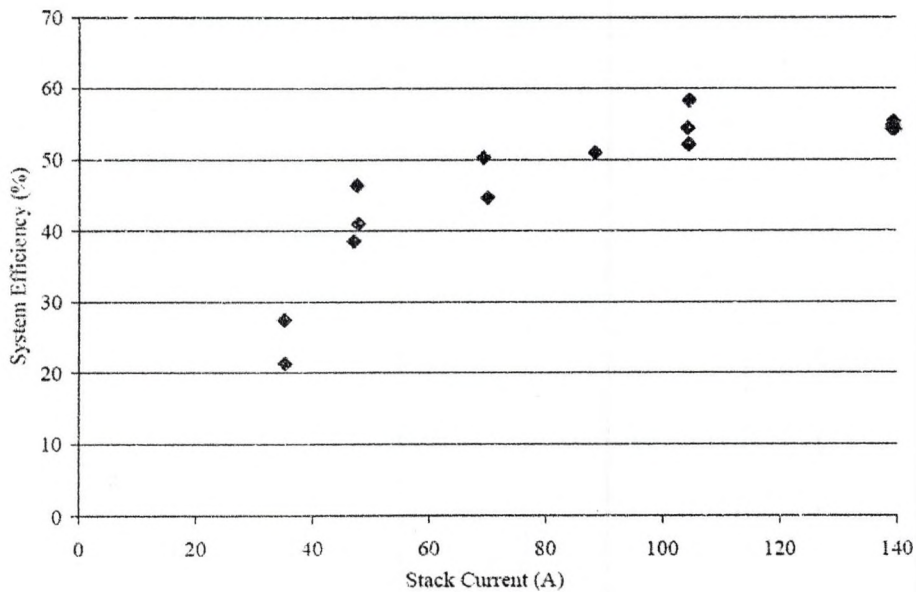


Figure 13. System efficiency across range of operating current of HOGEN 40RE. Trials included are baseline, frequency, PVO, and PVsim.

4 CHAPTER

UND SYSTEM DESIGN

Motivation

The HOGEN 40RE at NREL, as described in Chapter 3, was instrumented with additional sensors to monitor variables of interest. The internal plumbing of the off-the-shelf system was modified to accommodate the additional temperature, pressure, flow and water quality sensors. However, critical system variables were not adjustable as they are closely monitored by the electrolyzer's on-board controller and would shut down operation when outside the tolerances. Strict tolerances on water flow, water temperature, water resistivity, hydrogen system pressure and stack current did not allow for system testing outside of these limits. It is recognized that these safety tolerances exist to maintain performance within PES design specifications. It was determined, however, that the UND system would be designed to safely test variables of interest outside the commercial unit's tolerances.

The main focus of this chapter and dissertation was to design the test facility and PEM electrolyzer to enable detailed experimentation. The UND electrolyzer design enabled the team to operate and test the system outside of the limits of the PES commercial electrolyzer or any other existing PEM electrolyzer system. Based on the previous work done at NREL, PES agreed to sell the UND team a HOGEN 40 PEM stack, hydrogen water-phase separator and desiccant drying system. These basic components allowed for the UND design to operate closely to their commercial unit and

verified with the data taken at NREL (Chapter 3). The PEM stack consists of 20 series-connected cells, each cell having an active area of 0.093 ft^2 (86.4 cm^2). At 140 A, this results in a maximum current density of 1.6 A cm^{-2} . The hydrogen phase separator removes most of the entrained liquid water that accompanies the hydrogen gas from the stack cathode. The two-tube desiccant drying system will allow a side-by-side comparison with the novel drying approach discussed in Chapter 5. The goal of the new drying system is to improve system efficiency by eliminating the venting of dry hydrogen product.

Data Acquisition

The system monitoring and control hardware are based on a National Instruments PCI-6024E 12-bit card. The card is interfaced to a SCXI-1000 4-slot chassis via a SCXI-1149 cable assembly where (currently) three modules are installed (Figure 14).

Slot 1 of the chassis contains an SCXI-1102C analog input module. Slot 2 contains an SCXI-1162HV digital input module. Slot 4 contains an SCXI-1163 digital output module. All three modules contain 32 channels. Slot 3 will ultimately be filled with an additional SCXI-1102C analog input module intended to monitor individual cell voltages. External to the chassis is an SCXI-1180 feed-through panel to allow access to the E-series card analog output channels.

The digital input module consists of 32 optically isolated, wide range, AC or DC digital inputs. The optical isolation provides electrical isolation to common-mode voltages up to 450 V (AC or DC). However, there is no isolation between the four signals of the same bank. The digital input module logic level will report a high state + 2 to +240 Vdc and 10 to 240 Vac (50 – 60 Hz). A low logic level is reported with voltages

less than +1 V. The modules have termination blocks (SCXI-1326) mounted on the front which contain screw terminals for easy connection to device wiring.

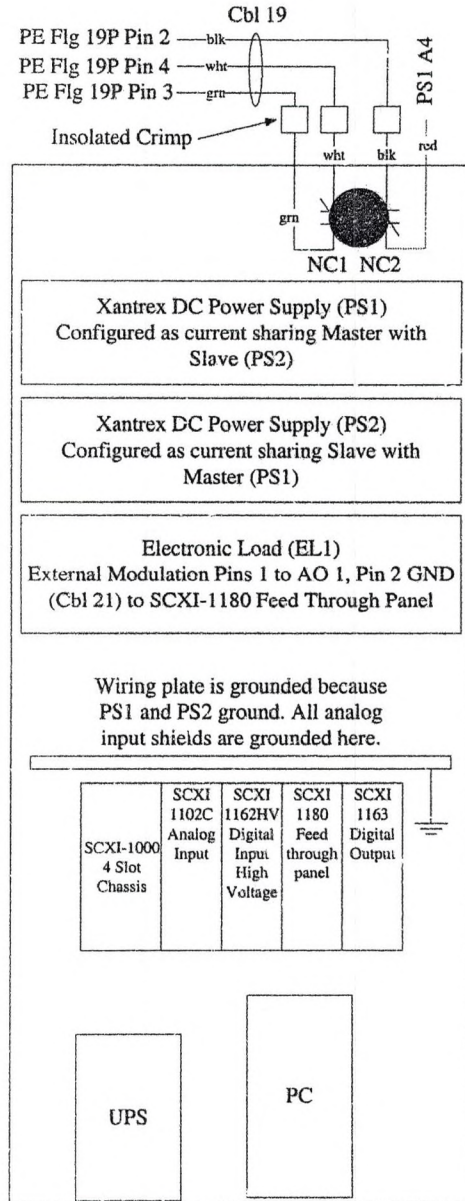


Figure 14. Instrument rack with power supplies, data acquisition, electronic load and other important devices.

The digital input and output modules are broken into eight optically isolated ports (or banks) of four channels each. Each port requires an isolated (i.e., separate) ground,

and in the case of the digital output module, each bank also requires 5 V (V_{cc}). V_{cc} represents the power connection of each port in the module. Each port of the modules is referenced to its particular ground and, in the case of the output module, V_{cc} . Therefore, for any port of outputs to work, a V_{cc} and a ground must be connected to that particular port. V_{cc} should be $5\text{ V} \pm 0.5\text{ V}$ above the ground for every given port. High voltages ($>42\text{ V}_{rms}$) are not present, which avoids the need to connect safety earth ground to the strain relief tab inside the terminal blocks. Each channel of the digital output module is an open-collector output with $4.7\text{ k}\Omega$ pull-up resistors capable of sinking 12 mA. The supply voltage (V_{cc}) should never exceed 7 V and requires 60 – 80 mA per port.

There is one exception to the wiring of the digital input module that needs to be understood. In order to monitor the state of the Interlock Loop, Channel 31 was wired to PS1 across User Line Pins A4 and A5 [33]. PS1 is the master supply controlling the current to the electrolyzer stack and is wired to turn its output off in any event that opens the Interlock Loop. For the power supplies to be on, continuity is required across Pins A4 and A5. Analog Programming Pins B1 (GND) and B2 (12 V) are jumpered to A5 and A4, respectively. When the Interlock Loop is opened, 12 V appears across A4 and A5 to turn the power supply outputs off. When all of the Interlock Loop contacts are closed, the A4 is shorted to A5 which enables the units. To monitor this event, a digital input Channel 31 is wired to Pin A4 of PS1, and Port 7 of the digital input module is grounded with the power supply ground (GND). PS1 B1 (GND) appears to be connected to earth ground through the supply. Therefore, this port is isolated from Ports 0 – 6 to keep the overall DC common isolated from earth ground.

Safety

Emergency Stop

The instrument rack (Figure 14) also includes a manual emergency stop (E-stop) with two NC contacts. E-Stop NC2 contacts are wired into the series-connected interlock loop to turn power supply output off, which, in turn, removes power to electrolyzer stack. NC1 removes power from emergency stop relay (PE EMR5). EMR5, the E-stop relay, interrupts power to the hydrogen-phase separator (H2phSep) vent valve. When the system is running and the E-stop is depressed, the pressurized hydrogen system is vented through NO solenoid valve (SV3) mounted in the H2phSep (Appendix B, Figure 90).

Circuit Protection

When DC voltage is disconnected from a solenoid valve or pump, the coil reacts by generating its own voltage, resulting in an inductive “ spike ” or back electromotive force (EMF). Depending on the size of the coil and the number of amp-turns it contains, this generated voltage can be very high. In order to suppress this back EMF and protect other sensitive components in the electronic system, a diode is reversed biased across the solenoid coils. Since the diode only conducts in one direction the polarity of the coil must be maintained so as not to burn out the diode and eliminate the protection it is meant to provide. In the majority of solenoid valves, the diodes are connected to the switchable voltage at the buffer module I/O terminals (Appendix A, Figure 42).

CGI

Hydrogen is the simplest, lightest and smallest of all gas molecules and is, therefore, more difficult to contain than other gases. Two combustible gas detectors

(CG1 and CG2) and a handheld “sniffer” are integral parts to the safety system of this system.

- The handheld unit is intended to be used whenever there is a change to the hydrogen system tubing, a hydrogen leak detected by the combustible gas detectors or if the system sits dormant for more than a month.

CG1 signal is % of the LFL of hydrogen in air, however, the display on the detector reads % LEL. CG1 is the combustible gas detector monitoring the oxygen-phase separator (O2phSep) from Port F. A needle valve, connected to Port F, is opened about ¼ turn to allow the detector to sample a small stream of the oxygen gas mixture. The remaining gas exits the reservoir through Port G via a 1/3 psig check valve (CV1). The ½ in. diameter (ID) tubing from the needle valve on Port F must be positioned about 0.125 in. away from the protective filter of CG1 located at the bottom of the sensor. When draining the O2phSep using the manual valve on Port J, verify that the needle valve on Port F is opened sufficiently to provide a vent for the tank. More importantly, verify that the same needle valve is returned to its ¼ turn open position again during operation. Otherwise, the oxygen will take the path of least resistance through the needle valve and vent the oxygen into the canopy hood and not through CV1 of port G.

CG1 was programmed (see owner’s manual) to provide latching alarms at 50% and 60% of the LFL of hydrogen. These alarm signals are wired to digital inputs of the data acquisition system. Digital input 10 (DI10) is high if the detector encounters a fault within itself; DI11 is the 50% LFL alarm, and DI12 is the 60% LFL alarm. CG1 signals are monitored and handled by the software only and are not hardwired to shut down the

system unlike the sensor signals from CG2. The AI signal from CG1 is sampled along with the rest of the AI channels and archived in the high- and low-speed data files.

CG2

CG2 is mounted in the canopy hood which is suspended above the test bed to monitor the surrounding air. Like CG1, it has two alarm levels: one at 10% and one at 20% of the LFL of hydrogen in air. The 10% alarm is a transistor-transistor logic (TTL) signal of +5 V with no alarm present and 0 V if the 10% LFL is reached. That TTL signal is wired to a Buffer Module 1 (BM1) which in turn drives Electromechanical Relay 1 (EMR1). The BM used for CG2 is in Position 0 on Mounting Board 1 of the power enclosure (PE). When CG2 senses 10% LFL, BM1 (6311) is energized with the low CG2 control signal which in turn energizes EMR1. In other words, under normal conditions where the air under the canopy hood is below the 10% LFL, the TTL signal is high (5 V), and EMR1 is off. The two-line wiring diagram showing CG2 and associated hydrogen relay safety logic appears in Figure 15.

CG2 has dry contacts for the 20% LFL alarm which is monitored only by the control software. For the system to become operational, EMR2 needs to be energized and is designated the System Health relay. For the system to be seen as “healthy” by the software, EMR2 must be on. One pole, of the two-pole relay, is wired in the series connected interlock loop described in the next section. The interlock loop enables (or disables) the main power supplies (PS1, PS2) used for electrolysis based (in part) on the state of this EMR2. The normally open (NO) relay contacts of System Health EMR2 are wired in series with other interlock devices that are designated the Interlock Loop. PS1 and PS2 need the Interlock Loop to be continuous for their outputs to be on. In the event

any of the interlock devices interrupt (or “ break ”) the loop, the power supplies outputs are automatically turned off by internal logic of the power supplies.

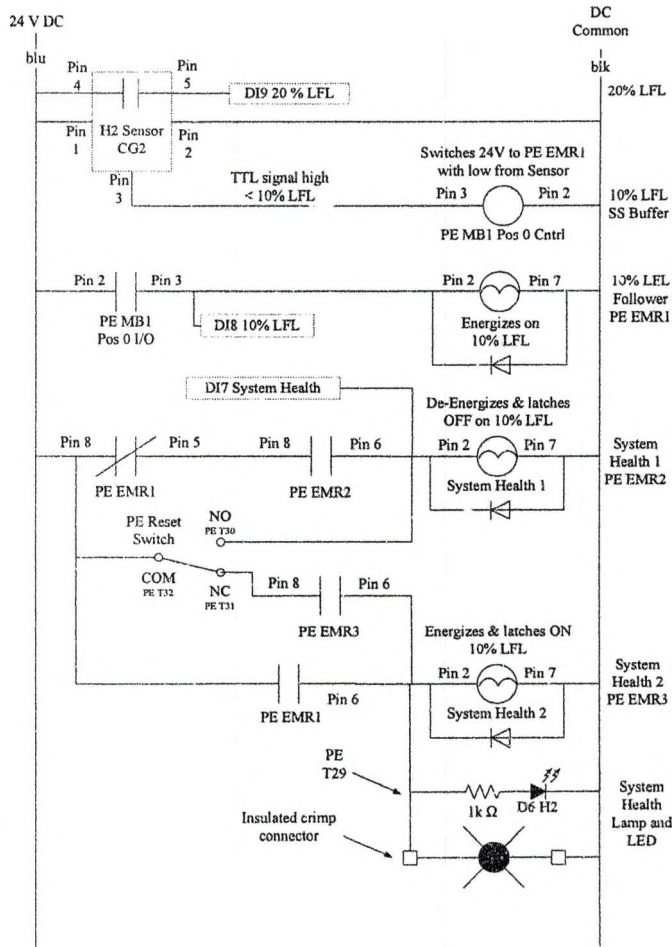


Figure 15. Two-line diagram showing relay logic to respond to 10% LFL signal from combustible gas detector (CG2).

The software monitors the state of the System Health relay on DI7 and will prompt the user when this signal is low (i.e., unhealthy). The other digital input monitoring points for CG2 10% and 20% LFL alarms are also shown in Figure 15.

In the event CG2 senses a 10% LFL condition while the system is operating, the control software will sense the alarm and shut down the system. However, CG2 also

drives EMR1 which, in turn, deenergizes System Health EMR2, which interrupts the Interlock Loop, disabling PS1 and PS2 power output.

At 10% LFL, the relay logic will automatically latch off the System Health EMR2 until the manual reset button is pressed. The manual reset button is located on the PE door. In addition, at 10% LFL, the blue beacon on the SE and the blue light emitting diode (LED) on the door will be latched on. As soon as EMR1 energizes, based on the state of CG2 10% TTL signal being low, EMR2 is latched off, and EMR3 is latched on. The NO contacts of EMR3 are responsible for powering the beacon and LED. These indicator lights are only energized in the event of a 10% LFL condition sensed by CG2.

Interlock Loop

On initial power up of the PE and SE, System Health EMR2 will be off. Pressing the manual reset button on PE will power and latch on EMR2. The Interlock Loop disables (i.e., turns off the output of PS1 and PS2) when the loop is interrupted by opening between Pins A4 and A5 (Figure 16). The software will monitor the state of the Interlock Loop on DI31 and initiate an audio alarm driven with DO14 if any of the devices open the loop. PE Plg 3P Pins 3 – 5 (corresponding Pins 4 – 6 on the Molex connector on the back of the chiller) contain the chiller relay fault contacts which are also wired into the series-connected Interlock Loop (Appendix A, Figure 54).

Chiller

When power is applied, by turning on the main circuit breaker on the back of the chiller, the unit performs a self-test and then energizes the fault relay. With main power on and running under no fault, Pins 4 and 5 of the chiller external contacts connector are shorted. External to the chiller, a separate flow switch (FS1) monitors the flow to the

PEM stack and opens when the flow drops below 1 gallon per minute (gpm). See Kodiak Recirculation Chiller Technical Manual for more details on the chiller's internal 1.5 gpm flow switch and other fault conditions. The chiller's front panel has a push button labeled "set" to set the desired temperature set point. Use the up ↑ and down ↓ arrows on the front panel to increase or decrease the set point to the level.

Power Supplies

PS1 and PS2 require 3-phase, 4-wire, 208 Vac power. Typical installation requires 25 A circuit. However, they are run in current sharing mode and, therefore, only utilized to half their rating. For this reason and that Facilities would have to bring 30 A service from a main distribution, both supplies will be fed from 20 A service. Fourth wire is safety ground which grounds the power supply chassis and the instrument rack.

The Interlock Loop state digital input (DI31) is an inverted channel. When Power Supplies 1 and 2 (PS1 and PS2) are off, the unregulated 12 V from Program Line B2 on PS1 is also off. The program views this state as a continuous loop and would allow the system to run. Once PS1 is turned on, the 12 V from B2, which is jumpered to User Line A4, and the Interlock Loop broken, the DI will be high, indicating a fault. The high state of this DI will not allow the software to proceed to the run state. In other words, for the Interlock Loop state to be continuous, all interlock contacts must be closed.

In addition to PS1 and PS2 being powered on, the following criteria must be met for the Interlock Loop to be continuous:

- System Health relay (EMR2) must be energized
- Chiller relay (EMR4) must be energized which will start the chiller
- Flow switch (FS1), at the chiller supply, closes with greater than 1 gpm

- Chiller fault relay (internal to chiller) must be closed.
- The E-stop on the instrument rack must not be depressed.

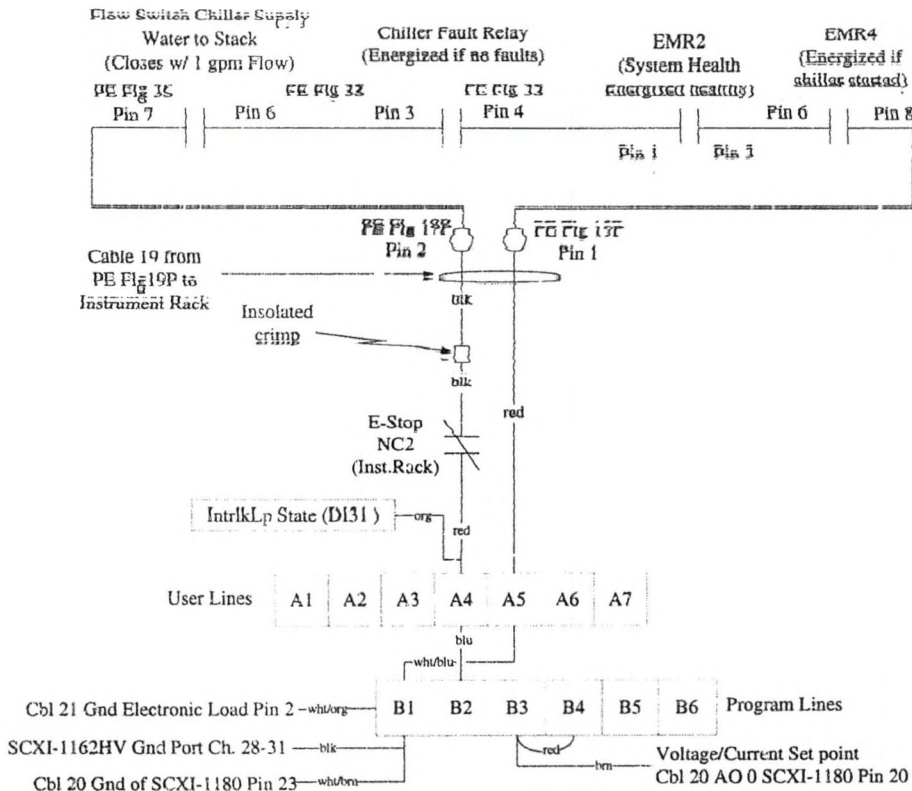


Figure 16. Interlock loop wiring diagram showing the devices that can interrupt the loop causing PS1 to remove power from the electrolyzer stack.

The purpose behind inverting the Interlock Loop (Figure 16) digital input line is that when the power supplies are off, they cannot source energy to the stack. When they are off, the Interlock Loop state appears healthy even though this is false and due to a lack of 12 V on B2 and A4. When the Interlock Loop is continuous (i.e., healthy), there is a short between A4 and A5, putting a low on the digital input but the inverted channel presents it as high. Once any of the devices open, the Interlock Loop state goes high in the hardware but the software inverts it low to indicate a problem.

Water System

PES's commercial electrolyzer contains a water pump, a mixed-bed deionization filter and a radiator in the water loop that provide the stack with conditioned (minimum Type II) DI water. The unit's onboard ventilation fan forces ambient air across the radiator to dissipate some of the stack losses into the room. The existence of the mixed-bed filter in the stack DI loop limits the operation of the system to roughly 60°C, at which point the resins used for deionization begin to break down (Personal communication with Everett Anderson, Proton Energy Systems, January 2006).

The UND system was specifically designed to allow higher-temperature testing by adding a water chiller to control and maintain stack DI water temperature. The deionizing guard bed was moved outside of the stack DI loop and utilizes an external water loop to maintain water quality at the desired level (Appendix A, Figure 87).

Figure 17 shows the major components of the DI water and oxygen handling system. Solenoid valves (SV1 and 2), mounted in the chiller, select the external reservoir when energized to purify incoming water through Filters 1 – 3 (fltr1 – 3). When SV1 and SV2 are deenergized and external water Pump (pmp1) is energized, DI water from the O2phSep (Part 150) is circulated through the carbon and mixed-bed deionization filters to maintain system water quality. This configuration allows operation at controllable resistivity levels to be presented to the stack while not limiting stack DI water temperature to greater than 60°C. Like the PES design, the UND system feeds the stack anodes with high-purity DI water as opposed to a cathode feed system. A cathode feed system could reduce the requirement of the O2phSep if the oxygen gas were simply going to be vented.

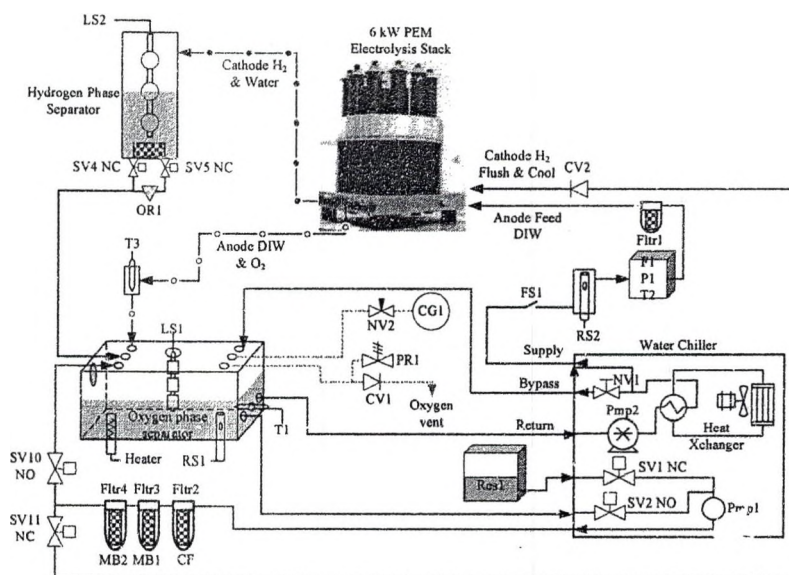


Figure 17. UND water system block diagram.

The chiller's internal water reservoir was removed, and the pump input (i.e., Return) was plumbed directly to the O2phSep port L. Internal to the chiller reservoir was a 2 kW submersion heater that was relocated into the O2phSep port I. However, because of the rigidity of the high-purity, high-temperature tubing used in the DI water loop, some short lengths of Nylon or polyvinyl chloride (PVC) tubing remain in the confined area of the chiller. The remainder of tubing in the DI water and external water loop utilize the rigid high-purity tubing to help maintain water quality during higher temperature (60 – 80°C) testing.

Figure 18 illustrates the major components, flow directions and some part numbers for the external and DI water loops. The addition of temperature control via the chiller (Part 200) allows the system to experiment at higher temperatures than allowed by the commercial system. Although the off-the-shelf chiller was ordered with the high-purity option, extensive modifications were required to accommodate the high-purity

water and PEM stack. Inside the chiller Nylon fittings were replaced with polypropylene, and all pipe dope was painstakingly cleaned from reusable parts and replaced with Teflon tape. Lessons learned from the NREL facility installation and discussion with PES warned against the use of pipe dope as it could damage the stack.

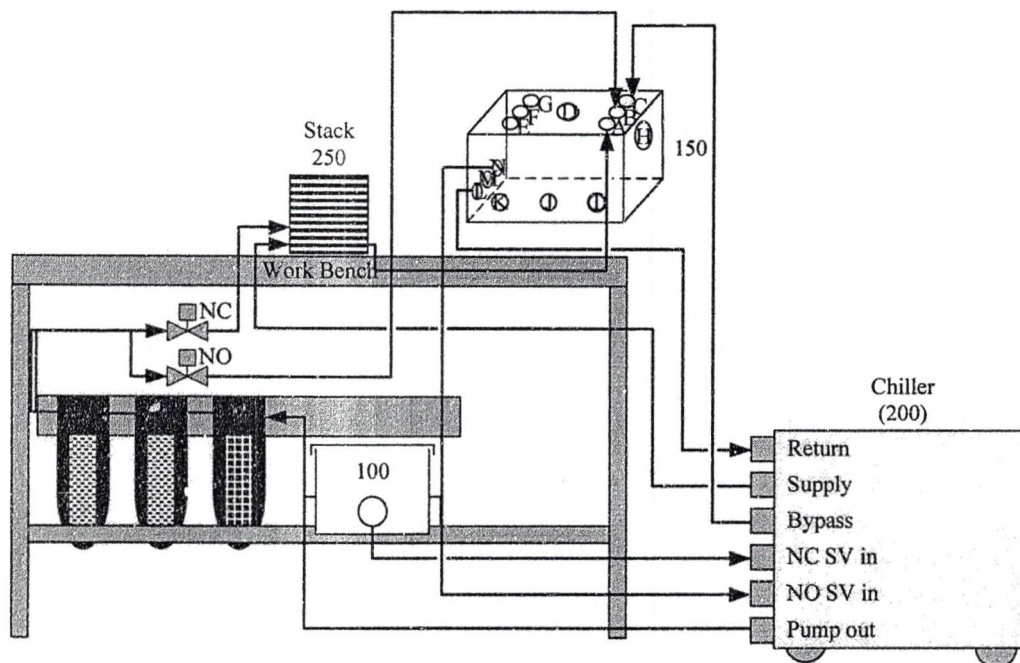


Figure 18. External and DI water loops components and flow.

The O2phSep was instrumented with temperature and resistivity sensors to monitor system performance. Appendix B provides detailed fitting drawings of the O2phSep as well as the remaining water plumbing and gas systems.

- During high temperature testing ($>60^{\circ}\text{C}$) it is important not to run the external water pump to improve water quality through the mixed-bed deionization filters.
- An external reservoir (Res1, Part 100) has a minimum level indicated on its side, and care should be taken to maintain new water at this level.

Hydrogen System

PES has tested the HOGEN 40 stack at pressures up to 400 psig. However, it has not been determined that the H2phSep can operate at higher pressures than 200 psig. The UND system incorporates a back-pressure regulator (BPR1) at the system output that is adjusted to maintain hydrogen system pressure at a desired level (Figure 19). Saturated hydrogen and liquid water emanate from the stack cathode to the H2phSep where gravity separates the majority of liquid water from the hydrogen gas. A coalescing filter (fltr5) after the H2phSep spins (or coalesces) most of the remaining liquid water from the stream. An auto drain connected to fltr5 monitors the internal water level and uses the hydrogen system pressure to recycle the captured water back into the external water reservoir.

SV's 6 and 8 are NO and select which desiccant tube will dry the hydrogen gas for a given period. The drying sequence and SV operation details are deemed proprietary to PES and are, therefore, not published in this work. SV's 7 and 9 are selected to route dry hydrogen product down the unused tube to dry the desiccant. At the top of the desiccant tubes, an orifice (OR2) "picks-off" a portion of the dry hydrogen product to dry the opposite tube. Chapter 5 outlines more of the desiccant drying details and presents an alternative method of hydrogen gas dehumidification.

Dry hydrogen product exits the desiccant drying system into the sensor stage of the process where temperature (T4), pressure (P3), dew point (DP1) and mass flow (F2) are measured. A needle valve (NV3) is opened only slightly to allow DP1 to sample the hydrogen product. NV3 is routed to the back-side of BPR1 to establish a pressure drop across the sample cell. The flow of the hydrogen product is monitored just prior to

storage using a thermally based mass flow sensor F2 (Appendix B, Figure 90). SV3 is a NO SV and is energized during operation. Any loss of power will open this valve to vent the hydrogen system through OR3.

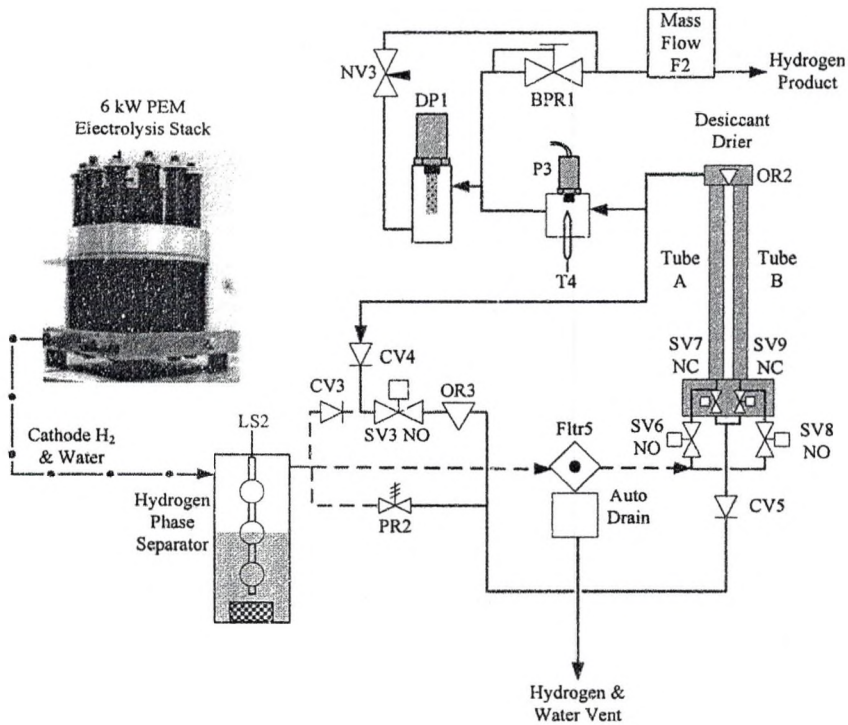


Figure 19. Hydrogen system components from stack to storage.

Internal to both the H₂phSep and O₂phSep are level sensing (LS1, LS2) floats which contain either NO or NC dry contacts. One side of the float contact is connected to 24 V and the other to a DI channel. The software monitors the water level in both reservoirs and in the case of the H₂phSep automatically drains the water through SV4 and SV5 depending on hydrogen system pressure.

Electrolyzer Operation Reference

The following steps should be followed to power up and run the system. Many of the steps, described below, contain troubleshooting steps that could aid in diagnosing system problems. The start-up steps are as follows:

1. Verify the main switch on the power enclosure is powered on. The power enclosure also powers devices in the sensor enclosure. All analog input sensors require a 30-minute warm-up before accuracy is assured.
2. Verify the SCXI-1000 chassis is powered on. If this chassis was powered off, all DO channels will be high (5 V), and devices like the external water pump (pmp1) and all solenoid valves will be on. Run the monitoring and control software to initialize all 32 channels to the appropriate state as soon as possible. Once the chassis is powered up and the software has been run, the channels will stay in the desired state, and the software program can be exited by pressing the stop button on any one of the screens.
3. Power on Power Supply 2 (slave) and then Power Supply 1 (master) in the instrument rack.
4. Verify the chiller circuit breaker on the back right of the unit is up. If the chiller is just powered up, the unit will step through its self-check, and the display on the front of the chiller will sequence numbers one through nine.
5. Verify the needle valve (NV2) on port F of the O2phSep is only opened $\frac{1}{4}$ turn from fully closed. This provides a sample of the gas to CG1 to monitor.

6. Verify the needle valve (NV3) after the dew point sensor (DP1) is only opened one-eighth of turn from fully closed. This maintains hydrogen system pressure but allows DP1 to sample the hydrogen product stream.
7. Located on the Desktop of all users of the system computer is the “ Experimental System Folder ” where the latest version of the monitoring and control software resides. Double-click on “ Data Acq SW Latest Version mmddyy.llb ”. Where the “ mmddyy ” represents the date of the latest significant changes to the software. A new window will appear with all of the program’s VI’s in it. Double-click on “ ~PS Com.vi ” to open the main VI.
8. Before running the program, navigate to the “ PS & Data Acq ” tab, and enter the desired high- and low-speed sample rate ($S s^{-1}$). High-speed sample rate of 1000 $S s^{-1}$ are sufficient to capture the slow-moving transients of this system. The low-speed sample rate can be set to anything lower than the high-speed. The sample rate of the PCI-6024E card will limit the high-speed rate. Once the software is running, any changes to these parameters are ignored.
9. Run the software by pressing the white right-pointing arrow beneath the “ Edit ” menu at the top.
10. Enter a comment that describes the trial being conducted. The comment is written to both the high- and low-speed files.
11. Select a destination for the tab-delimited high- and low-speed data files. The default folder is the experimental system folder where the software is located.
12. The file names contain the date, time and LS or HS concatenated with the high- and low-speed sample rates.

13. This example, “UND 2006 04-04 04-23-48 LS50.xls”, the file was created on April 4 at 4:23AM with the low-speed (LS) sample rate set at 50.
14. The “Electrolysis” tab contains a list of all the digital inputs and outputs. Verify that the System Health DI is on. If it is off, then either the system has just been powered up, lost power for a short period of time or there was a hydrogen leak. If the blue beacon and blue LED on the sensor enclosure are on then a hydrogen leak was detected, and the system should be leak-checked using the handheld detector as soon as the hydrogen system pressure reaches around 20 psig. If the beacon and LED are not on, then press the manual reset button on the front panel of the power enclosure. This will energize and latch on the System Health relay (EMR2) to begin closing contacts within the interlock loop.
15. Verify the O2phSep has sufficient water level (low or mid) before operating any of the manual controls. On the electrolysis tab, the external water pump (pmp1), external water solenoid valves (SV1, SV2) and chiller start can be accessed. The sensor enclosure has both resistivity monitors mounted in the front panel. Run pmp1 to circulate water from the O2phSep through the carbon filter (fltr1) and the mixed-bed deionizing filters (fltr2, flt3) to increase the water resistivity to the desired level (>1 MΩ - cm). The external solenoid valves should be off unless the operator desires water to be drawn from Res1 to raise the level of the O2phSep. The chiller can also be started to verify the interlock loop state will be high (i.e., continuous) once the system is running.
16. On the electrolysis tab, pressing the green “start” button will move the system from an off to idle state. Before entering the idle state, the software checks both

the H2phSep and O2phSep water levels and appropriate actions are initiated. In the case of the O2phSep, it requires the middle-level sense float to be made. In the event it is not, the software turns on the external solenoid valves (SV1, SV2) to pull water from the external reservoir (Res1). It then turns on the external pump (pmp1). Verify that the water level in Res1 never goes below the red " minimum " line written on the side. The software then verifies that at least the low-level sense in the H2phSep is made. If it is not, the system will pump water using the cathode flush and cool solenoid valves and the pmp1.

17. If the H2phSep is at the full level, the software will try to reduce the water level by opening SV4, which should allow some of the water to drain even though the system will not have hydrogen pressure to assist in pumping it out. If the O2phSep is at the high level, the software will prompt the user to open the manual drain valve connected to Port J. To provide a vent for this action, the needle valve (NV2) of Port F should be opened further than the ¼ turn operational set-point. Once the water level is reduced, return NV2 to its original position. NV2 must not be opened too much otherwise the oxygen gas will vent through it into the canopy hood area. The intent of NV2 is to provide a small stream of the gas mixture in the O2phSep to allow CG1 to monitor and alarm if the 50% LFL of hydrogen is reached.

18. Once the system is in the idle state, the software will automatically energize EMR4 to close contacts to the chiller. The chiller will start upon receiving these closed contacts. If the chiller does not start and EMR4 is verified to be on, the chiller may have lost its memory and require the settings to be modified.

Reference the chiller operator's manual to enter the menu on the chiller to set the external operation to NC. This enables the chiller to be operated remotely with normally closed contacts.

19. Once the chiller is running, the flow switch (FS1) at the chiller's supply port should be closed. FS1 is one of the series-connected interlocks and needs to be closed before the power supplies are enabled. When the chiller is running (i.e., EMR4 energized), FS1 is closed (>1gpm), E-stop not depressed, System Health relay (EMR2) energized, and the chiller is not faulted, the Intrlk Lp State should be high. Verify the state of this DI on the electrolysis tab. If it is not high troubleshoot the five interlocks in the loop and PS1 User and Program Lines.
20. Although the software monitors various analog inputs, the operator can view the scaled signals in the AI Graph tab. Verify that system sensors are reading appropriate levels. Prior to running, all temperatures should be relatively close to each other and reflect the ambient temperature (T8).
21. Electrolyzer stack current and voltage should be roughly zero. Stack voltage may not be fully decayed down to zero in between successive trials.
22. When the chiller is running, the DI water flow (F2) to the stack should be greater than 1 gpm.
23. Hydrogen flow at the output of the system should read approximately zero.
Reference the operator's manual to adjust the zero point using the trim-pot on the side of the sensor. Only modify the zero and only after 30 minutes of time have elapsed since powering the sensor.

24. Process messages are displayed on the electrolysis tab and indicate problems or actions the software is taking that the operator should be aware of.
25. Once in the run state, the operator can apply power to the stack using the manual controls on the PS & Data Acq tab or select a comma delimited (*.csv) file to read. The file format should have the number of seconds in Column 1 and the desired current in Column 2. The sample file "testPSdatafile.csv" should always reside in the experimental system folder. If removed, the software will prompt the operator to locate the file. The "testLoaddatafile.csv" should also reside in the same folder and have the same format with duration in Column 1 and desired load in Column 2. Reference the electronic load user's manual for details of operation modes.
26. To stop the electrolyzer, first remove all power from the power supplies, and then press the red "stop electrolyzer" button on the electrolysis tab. The system will perform a controlled shutdown. The system can remain powered up for long periods of time without jeopardizing components. A universal power supply (UPS) is located in the instrument rack to keep the SCXI-1000 chassis from losing power. If the system remains powered up and grid power is lost for longer than 30 minutes, the system will enter an undesirable state when the grid is reenergized. The SCXI-module will automatically turn on all digital outputs in the SCXI 1163 digital output module. With the power enclosure also powered up, this will result in all devices driven with a 6321 buffer module to be energized. This includes all solenoid valves except for the external water SV's (SV1, SV2) which are driven with a 6311 buffer module.

27. SV1 and SV2 are purposely driven with a 6311 BM to avoid this potential scenario, which would result in draining the external water reservoir (Res1) and running the external water pump (pmp1) without water.

5 CHAPTER DEW POINT CONTROL

Introduction

Hydrogen is a popular candidate as a future energy carrier, and electrolysis using renewable energy sources enables the full environmental benefits of the gas to be achieved. Some hydrogen applications such as fuel cells, metal storage cylinders, and power plant electric generator cooling require hydrogen gas with trace water vapor, which corresponds to a low dew point. Ballard's PEMFC module is designed for hydrogen fuel that is 99.99% pure, with no more than 0.01% contaminants, which includes water vapor [Mark Turchyn, Ballard Power Systems, personal communication, January 5, 2006]. It is unique, compared with other PEMFC's, in that it requires dry hydrogen although it has been run successfully with various levels of humidified hydrogen gas. The literature suggests that power plant electric generator cooling applications, using hydrogen gas, require a dew point between -40 and 0°C [34, 35].

Storing hydrogen gas in metal cylinders requires a low dew point to prevent water condensation inside the cylinder that could cause tank corrosion, resulting in a leak or other tank failures. Composite fiber storage cylinders are not affected by gas water content, but equipment both upstream and downstream dictates the water content of the gas to be stored. Diaphragm hydrogen compressors are designed to handle clean and dry hydrogen, but some users have used hydrogen with water vapor saturation levels as high as 50%. Although hydrogen with high levels of water vapor can be used in the

compressor, manufacturers recommend a saturation level of 10% or below to extend the operational life of the compressor. Gas/water separators are used at the compressor inlet and between compression stages in order to remove excess water from the hydrogen [Personal conversation with Tom Greco, PDC Machines Inc., January 5, 2006].

Proton Energy Systems' PEM electrolyzers incorporate an adsorption drying system to remove water vapor from the hydrogen product gas. The PES line of electrolyzers utilizes a two-tube desiccant drying system to achieve a dew point of -65°C , or less than 5 ppm water vapor, in the hydrogen product gas. Based on stack input water quality (minimum resistivity $1\text{ M}\Omega\text{-cm}$) and the gas-separating solid membrane of PEM- electrolysis, this technology is capable of producing 99.9995% pure hydrogen [36]. PEM based electrolysis is capable of maintaining a pressure differential between the anode (O_2 side) and cathode (H_2 side). The HOGEN 40 has a hydrogen delivery pressure of 1383 kPa (200 psig) while the oxygen is vented at roughly 203 kPa (15 psig).

The desiccant system of the PES HOGEN 40 is sized to run approximately 8760 hours (1 year) at full operating current density (1.6 A cm^{-2}) before it is recommended that the desiccant be replaced [Personal conversation with Everett Anderson, Director of Technology, Proton Energy Systems, January 6, 2006]. The two-tube desiccant system uses one tube at a time to dry the hydrogen from the PEM stack. At full operating current, an orifice at the top of the drying assembly diverts roughly 10% of the dried hydrogen down the opposite tube to remove the water from the adsorbent. After a predetermined amount of time, solenoid valves divert the hydrogen to the

opposite tube and the same orifice is used to regenerate the adsorbed tube with the dry hydrogen.

In this chapter, an alternative method to reduce and control the dew point of the hydrogen gas is presented. Thermoelectric coolers (TECs) are used to cool saturated hydrogen gas as it travels through a large surface area cold plate, allowing the water vapor to condense in Stage 1 and desublime in Stage 2. Two cooling stages are presented to condense and desubliminate water vapor from the hydrogen stream in an effort to achieve a theoretical dew point of -35°C .

The goal of the first stage TEC cold plate assembly is to reduce the dew point from approximately 35°C to near 5°C . Stage 1 will allow the parallel-connected TECs in the second stage to run longer at temperatures near -35°C . Pressure sensors monitor Stage 2 and switch between the parallel-connected cold plates when frozen water begins to restrict hydrogen flow within the finned cold plate. By reversing the polarity of the TEC power supply, the cold plate will be heated, causing the ice buildup to melt and be collected downstream by a coalescing filter.

System Design

Semiconductor material is used to produce thermoelectric couples that generate an electrical potential as the result of a temperature gradient. This phenomenon is known as the Seebeck effect. This process is reversible so that electrical energy across the same thermoelectric couple can produce a temperature differential, known as the Peltier effect. First observed by Jean Peltier in 1834, the Peltier effect is caused by a DC passing through the junction of two different metals [37]. The dissimilar metals or semiconductors (n-type and p-type) are connected to each other at a junction. The two

different semiconductors and junction are collectively called a couple. The current drives a transfer of heat from one junction to the other, which causes one junction to cool while the other heats. Additionally, by reversing the DC flow through the thermocouple, heat is pumped in the opposite direction as before (i.e., the hot side becomes the cold side). The heating/cooling effect can be magnified by placing many couples in series with another, creating a thermoelectric device. Figure 20 shows the detailed components of a TEC module and the DC power supply wired to cool the cold plate on top.

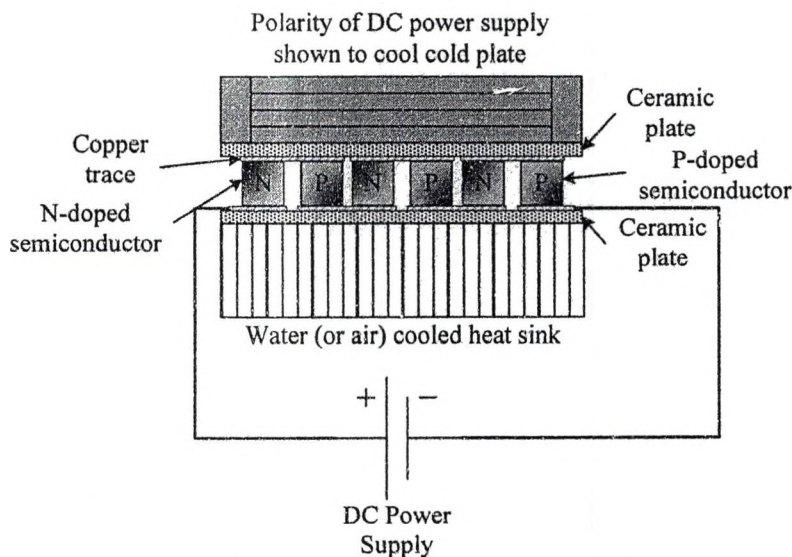


Figure 20. Typical thermoelectric device configured to cool the cold plate on top.

In order to maximize the benefits of a TEC, the heat must be removed from the hot side using a heat sink. In addition to removing the heat from the object being cooled, the heat of the TEC operation (waste heat) must also be removed. These two sources of heat require a high density of heat to be removed from the TEC surface. Using a conventional air-cooled heat sink is an option, but in order to dissipate a large number of watts from a small surface area (e.g., 90 W from 900 mm²) at typical room temperatures, the heat sink and fan become large. Water-cooled heat sinks offer compact sizing,

superior performance over air-cooled heat sinks, and are nearly silent when operating. For this reason and the readily available water source inherent to an electrolyzer system, a water-cooled heat sink was selected for this design.

Proposed Experimental System

The following describes the experimental system currently being assembled for testing at UND. It is presented here as an example of how a TEC system may be installed.

Hydrogen gas leaving a PEM stack is assumed to be fully saturated with water vapor at temperatures above ambient temperatures (20°C). To simulate the output from a PEM stack, this experimental design bubbles dry hydrogen gas from a pressure-regulated storage cylinder through a temperature controlled humidifier to fully saturate the gas. An input regulator downstream from the high-pressure H₂ cylinder and a back-pressure regulator at the output of the system will be adjusted to achieve the desired hydrogen flow rate. The humidity bottle contains a submersed heater coil to control the exit gas dew point. The entire system incorporates three cold plate assemblies (CPAs) in two stages. For this proof-of-concept testing, an operating pressure of 345 kPa (50 psig), flow rate of 1 Nm³ hr⁻¹, and saturated hydrogen gas around 35°C will be presented to the TEC-based drying system.

The CPA consists of a high-surface-area cold plate, TEC and water-cooled heat sink. Figure 21 shows the experimental system, which uses two stages of cooling to reduce and control the dew point to a calculated -35°C. Stage 1 has saturated hydrogen gas as its input and uses two 36 W TEC modules to reduce the dew point to around 5°C. Stage 2 requires two CPAs in parallel to achieve dew points below the freezing point.

Coalescing filters are located immediately downstream of each CPA to remove liquid water from the process. Temperature, pressure, dew point and mass flow sensors are used to monitor the system.

Theory of Operation

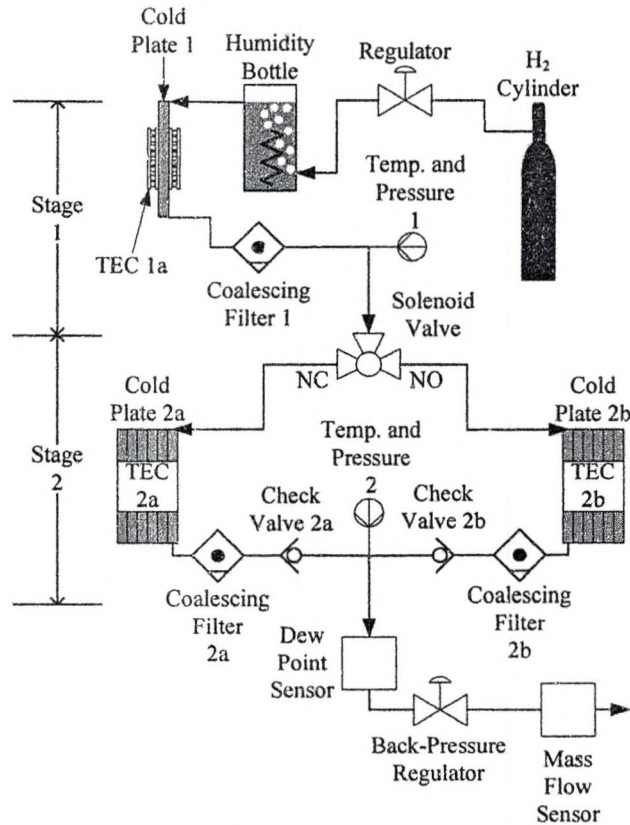


Figure 21. Dew point control experimental system design.

In Stage 1, the 35°C saturated hydrogen gas passes through Cold Plate 1 (CP1) where water vapor is condensed. The goal of Stage 1 will be to remove most of the water vapor in the hydrogen gas and allow the second stage to operate at lower temperatures for longer periods of time before switching between the parallel CPA branches. This first-stage TECs are sized to avoid freezing water in the channels of CP1 and, therefore, should be able to operate continuously in an open-loop configuration. If running open

loop (i.e., without temperature feedback) causes CP1 to freeze, then a simple on/off control scheme will be implemented to avoid freezing conditions.

The 3-way solenoid valve at the beginning of Stage 2 switches between the two parallel-connected CPAs: CPA 2a and CPA 2b (Figure 21). TEC 2a and 2b are run open loop (i.e., no temperature feedback control) to desublimates the water vapor to reduce the dew point of the exiting gas as much as possible. Temperatures well below freezing are expected in Stage 2 and condensation on the CPAs may become problematic. All TECs in the system have a sealant around the perimeter to reduce the chance of condensation shorting the module.

The hydrogen pressure is monitored at the inlet and the outlet of Stage 2. When a predetermined pressure differential is developed between Stage 2 input and output, the gas is diverted to the parallel CPA (for example, from CPA 2a to CPA 2b). Next the polarity of TEC 2a is reversed to melt the ice from the restricted CP channels. When the flow in CP 2b becomes restricted, gas flow is diverted back to CP 2a and the process repeats. Process optimization will include temperature feedback during the melting stage to avoid overheating the CP and anticipating the crossover to cool the CP in advance.

Figure 22 shows the detailed configuration of the CPA. Water-cooled heat sinks were chosen based on their exceptional ability to dissipate the high density of heat pumped/generated by TEC devices and the readily available source of water and DC electricity in an electrolysis system. This approach seemed to be a natural selection for dissipating the sensible and latent heat required to condense and desublimates water vapor from the hydrogen product and remove the waste heat of the TECs.

- At every stage in the cooling process, it is assumed that water vapor exerts a partial pressure that is equal to its saturated vapor pressure (SVP).
- The estimated minimum temperature involved in the process is -35°C ; hence the effects of the conversion of hydrogen molecules from ortho to para are neglected.
- The reference state for enthalpy is selected at 0°C where enthalpy of dry air is 0.

Table 6. Explanation of symbols

Description	Symbol	Units
Humidity ratio	W	$\frac{\text{Mass water vapor (kg)}}{\text{Mass dry hydrogen (kg)}}$
Saturated vapor pressure of water	P_s	Pascals
Molecular mass of hydrogen	M_{H_2}	g mol^{-1}
Total pressure of gas	P_T	Pascals
Total specific enthalpy of gas	h	kJ kg^{-1}
Specific enthalpy of hydrogen	h_{H_2}	kJ kg^{-1}
Specific enthalpy of water	h_v	kJ kg^{-1}
Specific heat capacity hydrogen	$C_{p\text{H}_2}$	$\text{kJ kg}^{-1} \text{K}^{-1}$
Specific heat capacity water vapor	C_{pv}	$\text{kJ kg}^{-1} \text{K}^{-1}$
Mass flow rate	m	kg sec^{-1}
Volumetric flow rate of gas	V	m^3
Pressure exerted on gas	P	atmosphere
Molecular mass	M	kg mol^{-1}
Universal gas constant	R	$0.082 \text{ m}^3 \text{ atm kmol}^{-1} \text{K}^{-1}$
Temperature of gas	T	K
Temperature of gas	t	$^{\circ}\text{C}$
Latent heat of vaporization of water	L_v	2500 kJ kg^{-1}
Latent heat of fusion of water	L_f	334 kJ kg^{-1}
Latent heat of sublimation of water	L_s	2834 kJ kg^{-1}
Molecular mass of vapor	M_v	g mol^{-1}
Sensible heat change	q_s	kJ
Heat of condensation	q_l	kJ
Heat of desublimation	q_{sb}	kJ
Enthalpy of saturated water vapor at 0°C	h_g	$2501.3 \text{ kJ kg}^{-1}$

During the process, the mass flow rate of hydrogen remains unchanged because the temperatures involved are far higher than required to condense hydrogen. However,

System operation is monitored and controlled with a computer-based data acquisition system. A LabView-based user interface will acquire and archive analog inputs and control the operation of the solenoid valve, water pump, and polarity control and operation of the TEC devices. Pressure, temperature, dew point and mass flow sensors will monitor the performance of the system.

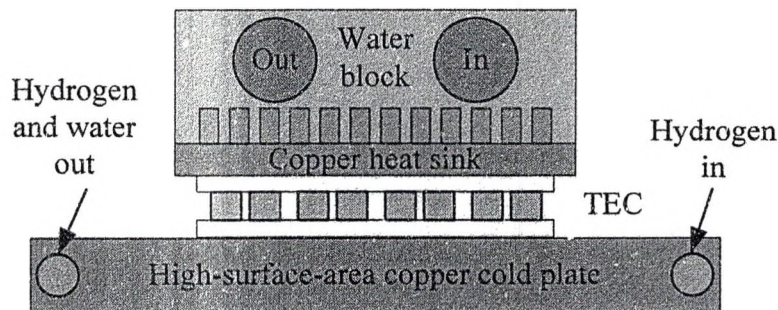


Figure 22. Detailed CPA showing the cold plate, TEC and water-cooled heat sink.

Modeling

The model of the hydrogen-conditioning process is based on the following assumptions:

- The wet hydrogen is treated as consisting of water vapor and hydrogen gas only.
- The effects of any trace gases are neglected.
- The wet gas pressure remains unchanged throughout the whole process. Cooling plates and tubing are treated as having no pressure losses.
- The temperatures and pressures involved in the process are low enough to consider hydrogen and water vapor as ideal gases.
- The process pressures do not depress the freezing point of water significantly.

Hence, water vapor below 0°C changes directly to ice.

water vapor changes phase at Stage 1 of the process. The amount of water that changes phase is computed by the change in the humidity ratio. Eqn. 5-1 in Table 7 is used to estimate the humidity ratio at this point in the process [38].

Table 7. Governing equations for thermoelectric analysis and gas dehumidification:

Description	Symbol	Equation
Humidity ratio	$W = \frac{M_v P_s}{M_{H_2} (P_T - P_s)}$	5-1
Total specific enthalpy	$h = h_{H_2} + W h_v$	5-2
Enthalpy of hydrogen	$h_{H_2} = C_{pH_2} t$	5-3
Enthalpy of water vapor	$h_v = h_g + C_{pvt}$	5-4
Sensible heat change	$q_s = M_{H_2} C_{pH_2} \Delta t$	5-5
Heat of condensation	$q_l = M_{H_2} (W_2 - W_1) L_v$	5-6
Heat of desublimation	$q_{sb} = M_{H_2} (W_2 - W_1) L_s$	5-7
SVP of water vapor above freezing	$P_s = 610.78 * \exp\left[\frac{t}{(t + 238.3)} * 17.2694\right]$	5-8
SVP of water vapor below freezing	$P_s = \exp\left[\frac{-6140.4}{(t + 273)} * 28.916\right]$	5-9
Mass flow rate	$m = \frac{1000 * P * V * M}{R * T}$	5-10

The amount of heat that the thermoelectric device needs to remove to enable the humid hydrogen to cool from one temperature to another is given by the total enthalpy change that occurs between the given temperatures. Eqns. 5-2 – 5-7 are used to estimate the enthalpy change [38]. The saturated vapor pressure of water is calculated above and below freezing with Eqns. 5-8 and 5-9, respectively [39].

Table 8. Results of baseline calculation for HOGEN 40 as designed.

Description	Number	Units
Volumetric flow rate of hydrogen output (-65°C dew pt.)	1.05	Nm ³ hr ⁻¹
Saturated vapor pressure of water at -65°C [40]	0.529	Pascal
Atmospheric pressure	101,000	Pascal
Humidity ratio of hydrogen (-65°C dew pt.)	4.7e-5	kg H ₂ O _v / kg H ₂
Percentage water vapor	0.0047	%
Percentage hydrogen	99.9953	%
Mass flow rate of hydrogen	2.39e-5	kg sec ⁻¹

The results in Table 8 are based on the parameters of the PEM HOGEN 40 electrolyzer. This electrolyzer produces $1.05 \text{ Nm}^3 \text{ hr}^{-1}$ of hydrogen at 1383 kPa (200 psig) with a -65°C dew point after desiccant drying. Table 8 estimates the mass of dry hydrogen flowing per second under these conditions. The mass flow rate of hydrogen is expected to remain constant during the process. The mass flow rate of water changes with temperature as condensation occurs. The amount of water condensing is reflected in the change in humidity ratio.

TEC Stage 1

The calculated results for TEC Stage 1 are shown in Table 9 and Table 10. It is assumed that the hydrogen will be fully saturated and at 35°C to match electrolyzer hydrogen output and TECs are 50% efficient. Our result shows 87% of the water vapor in the hydrogen gas is removed in this stage and thus requires the most energy of the two stages at 30 W.

Table 9. Condition of humid hydrogen at inlet of Stage 1 CPA.

Description	Number	Units
Temperature	35	$^\circ\text{C}$
Pressure	345,000	Pascal
Saturated vapor pressure of water vapor at 35°C	5576	Pascal
Humidity ratio of saturated hydrogen at 35°C	0.1469	$\text{kg H}_2\text{O}_v / \text{kg H}_2$
Percentage water vapor	12.81	%
Percentage hydrogen	87.18	%
Specific enthalpy of dry hydrogen at 35°C	4404	kJ kg^{-1}
Specific enthalpy of pure water vapor at 35°C	3076	kJ kg^{-1}
Total enthalpy of saturated hydrogen at 35°C	4856	kJ kg^{-1}

TEC Stage 2

Since 87% of the water vapor has been removed in Stage 1, the hydrogen is cooled again to achieve a -35°C dew point. The total enthalpy of humid hydrogen at the

inlet to the second stage is the same as the enthalpy of outlet of the first stage. It should be noted that a dew point greater than these calculations is expected experimentally because of losses in the system. These include temperature losses to ambient from the CPAs as well as water vapor recombining with the hydrogen gas between the CPA and coalescing filters.

Table 10. Condition of hydrogen gas at the exit of Stage 1.

Description	Number	Units
Temperature	5	°C
Pressure	345,000	Pascal
Saturated vapor pressure of water vapor at 5°C	871	Pascal
Humidity ratio of saturated hydrogen at 5°C	0.0226	kg H ₂ O _v / kg H ₂
Percentage water vapor	2.21	%
Percentage hydrogen	97.79	%
Specific enthalpy of pure hydrogen at 5°C	3975	kJ kg ⁻¹
Specific enthalpy of pure water vapor at 5°C	3020	kJ kg ⁻¹
Total enthalpy of saturated hydrogen at 5°C	4043	kJ kg ⁻¹
Change in enthalpy in Stage 1 (sensible + latent)	813	kJ kg ⁻¹
Total heat removal required Stage 1 cooling	19	W

Table 11. Condition of hydrogen gas at the exit of Stage 2.

Description	Number	Units
Temperature	-35	°C
Pressure	345,000	Pascal
Saturated vapor pressure of water at -35°C	22.55	Pascal
Humidity ratio of hydrogen gas at -35°C	5.8e-4	kg H ₂ O _v / kg H ₂
Rate of desublimation in Stage 2	3.5e-7	kg sec ⁻¹
Percentage water vapor	0.058	%
Percentage hydrogen	99.94	%
Specific enthalpy of pure hydrogen at -35°C	3404	kJ kg ⁻¹
Power required to transform water vapor to ice at 0°C [41]	1.1	W
Power required to cool hydrogen from 0 to -35°C	13.4	W
Power required to cool ice from 0°C to -35°C	0.02	W
Total heat removal required Stage 2 cooling	15	W

Energy Analysis

The two systems discussed consume energy to reduce the dew point of the hydrogen product gas. In the case of the desiccant system, hydrogen gas is vented after

being used to dry the desiccant in one of the two tubes. The TEC-based dew point controller uses electricity to condense and desublimates water vapor from the hydrogen gas stream. The following analysis estimates the amount of hydrogen loss of the desiccant system and converts the chemical energy contained in the loss to energy using the HHV of hydrogen (39 kWh kg^{-1}).

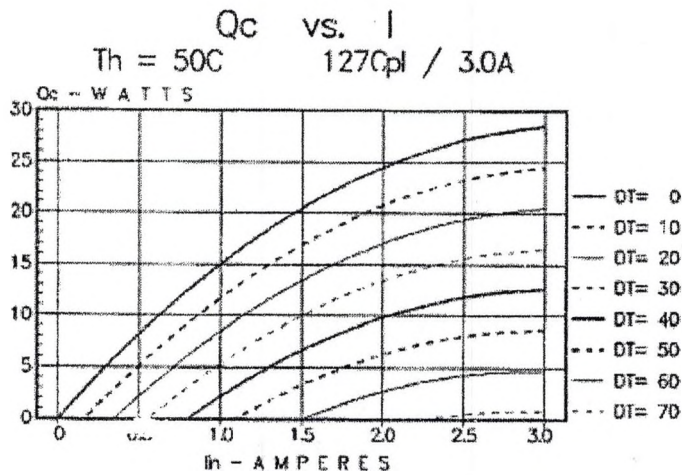


Figure 23. Manufacturer's performance curves for heat pumping capacity versus current for various ΔT .

Figure 23, taken from manufacturer's datasheet, for the 3 A modules of Stage 1 shows that a maximum of 15 W can be pumped with a hot side of 50°C . Typically, with TECs the higher the hot-side temperature, the lower heat pumping capability is. With a $\Delta T = 35^\circ\text{C}$ and a hot side approximately 25°C , heat pumping capability would be lower than 15 W.

Desiccant

The PES HOGEN 40 contains a 6 kW PEM electrolyzer stack. This commercial electrolyzer design uses the two-tube desiccant drying system to dry an estimated

1.15 Nm³ hr⁻¹ of hydrogen gas from the PEM stack. As stated earlier, PES reports that this method of drying achieves a dew point of approximately -65°C (< 5 ppm).

According to PES, at least one customer has reported that the desiccant dryer achieved the target dew point of product hydrogen gas without replacing the desiccant even though it ran continuously for a 1-year period.

The HOGEN 40 contains a back-pressure regulator at the output of the unit to maintain 1383 kPa (200 psig) hydrogen system delivery pressure. Based on the nearly constant hydrogen system pressure and fixed orifice design of the desiccant drier, 0.1 Nm³ hr⁻¹ of dry hydrogen will be consumed regardless of operating current. This impacts electrolyzer efficiency more when operating at lower current densities by consuming a larger percentage of the hydrogen product gas.

During operation, roughly 0.1 Nm³ hr⁻¹ of the dry hydrogen is consumed (i.e., vented) to maintain the desiccant drying system. Running the system for 24 hours at full current producing 1.05 Nm³ hr⁻¹ hydrogen results in 2.27 kg of H₂ per day. Therefore, the desiccant drying system vents roughly 0.2 kg of H₂ per day and, using the HHV of H₂ results in a loss of 3.4 kWh kg⁻¹ of hydrogen. With a stack efficiency of 60% at full current, the electricity needed to create the vented hydrogen is approximately 5.7 kWh kg⁻¹ of hydrogen.

Thermoelectric

Table 12. TEC-based dew point control power consumption

	Constant Operation Power (W)
TECs Stage 1	90 W
TEC Stage 2a	90 W
TEC Stage 2b	90 W

Water pump	24 W
Energy per kg	3.1 kWh kg ⁻¹ H ₂

Table 12 calculates the energy requirement per kg of hydrogen produced assuming all TECs running continuously. The TEC-based system consumes about 55% of the desiccant system when comparing the electricity used to create the hydrogen wasted in the desiccant-drying system. The TEC modules have a life expectancy exceeding 100,000 hours, making them robust components of the system. Other benefits of the TEC design would include avoiding equipment downtime, cost of replacement desiccant and labor involved to perform the maintenance.

Acknowledgments

The author would like to acknowledge Mark Turchyn (Ballard Power Systems), Everett Anderson (Proton Energy Systems) and Tom Greco (PDC Machines Inc.) who provided many of the specifications of and insight to their associated equipment referenced in this chapter. This chapter is currently being reviewed for publication in the International Journal of Hydrogen Energy.

6 CHAPTER

RESULTS

The UND experimental system was designed to allow control of system variables and enable detailed study of PEM stack performance and stack characterization for model verification (Chapter 7) and improved interfacing to renewable energy sources. The system variables capable of control are as follows:

- DI water flow rate to stack anode
- Water resistivity
- Stack current including the generation of complex (DC + AC) waveforms
- Desiccant tube drying cycle
- Hydrogen system pressure
- DI water temperature to stack anode
- Access to hydrogen stream enabling testing of alternative drying processes

The results described in the chapter represent only preliminary tests to verify the UND system with the data taken at NREL on the HOGEN 40RE system (Chapter 3). The initial testing included basic pressure testing of the system, verification of DI water quality, exercising the power supplies through the range of currents, acquiring IV characteristic curves at various (10 – 70°C) and predicting system efficiencies.

The UND system contains some of the same components used in the commercially available HOGEN 40 including:

- 20-cell, 6 kW PEM stack
- Desiccant drying system incorporating PES's solenoid valve cycling process
- Hydrogen phase separator

Operational Temperature Trials

Initial testing focused on controlling DI water temperature within the chiller manufacturer's specifications of 5 – 35°C. DI water is circulated and temperature is stabilized through the stack anode before stack current is swept from 1 – 140 A in 5 A steps every ½ second (Figure 24). The systems back pressure regulator (BPR1) maintains the hydrogen system pressure relatively constant during the current sweep.

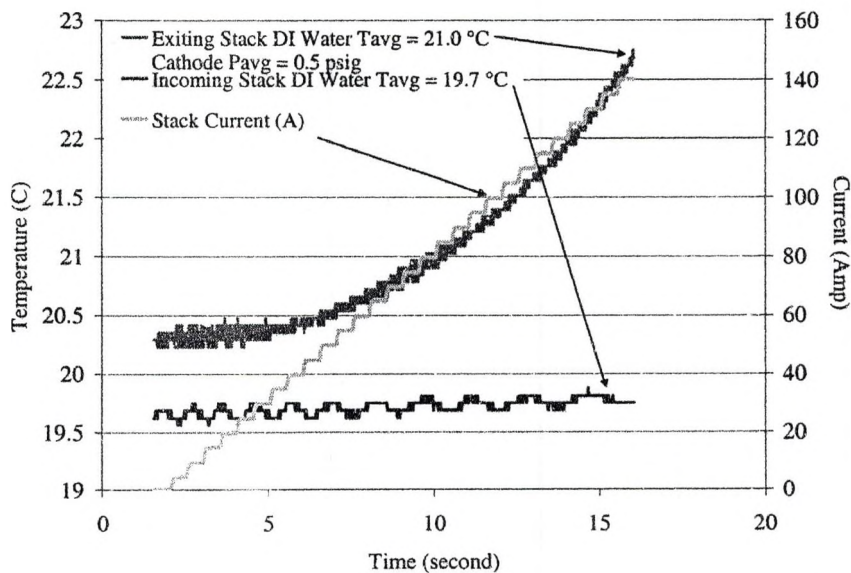


Figure 24. Current sweep waveform and stack incoming and exiting DI water temperatures for 20°C trial.

Figure 24 reveals that while anode input DIW temperature remains relatively constant at 19.7°C, the anode outlet DIW rises with current. The chiller operates in an on/off control mode to maintain water temperature within 0.1°C of the set point. In

addition, the oxygen phase separator contains roughly 10 gallons of water, helping to maintain anode inlet water temperature. Exiting DIW temperature is recorded as an average over the current sweep.

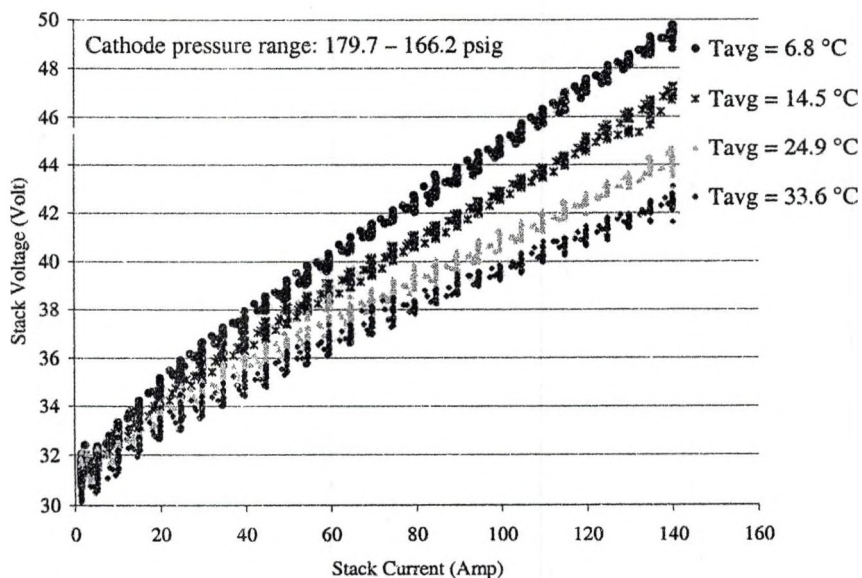


Figure 25. IV characteristic curves at constant cathode pressure (170 psig) at temperatures from 6.8 – 33.6°C.

Tests were performed at cathode pressures of ~170, 90, and 0 psig shown in Figures 25 – 27 respectively. During the trials where cathode pressure is greater than zero, stack current was set to ~ 100 A to maintain hydrogen system pressure until just before the current sweep. The 100 A maintenance current was not required at zero cathode hydrogen pressure which allowed IV curve to start from 0 V, compared to roughly 32 V in the other higher pressure cases.

Voltage decreases for a given current as temperature increases. This temperature effect can be controlled to improve stack efficiency. These IV characteristic curves are

used in Chapter 7 to extract model coefficients which represent stack parameters as a function of temperature.

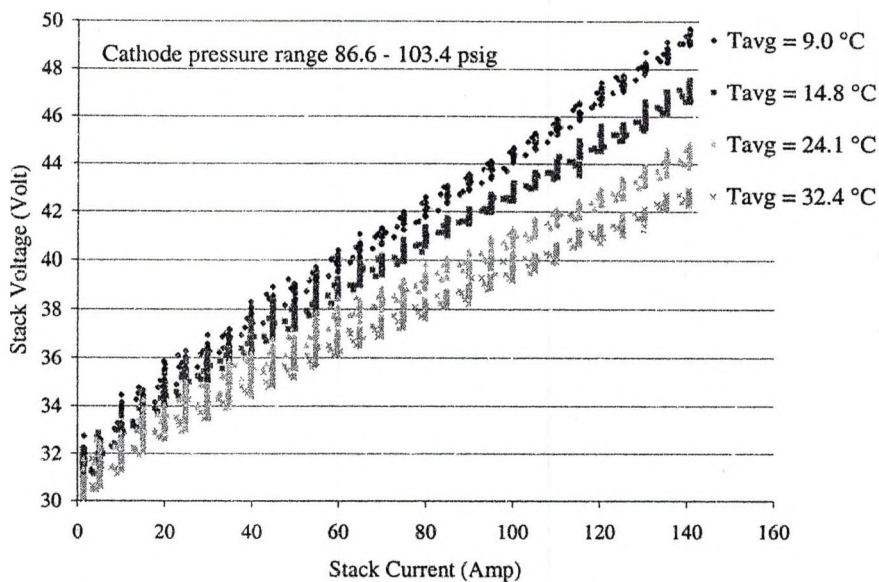


Figure 26. IV characteristic curves at constant cathode pressure (90 psig) at temperatures from 9.0 – 32.4°C.

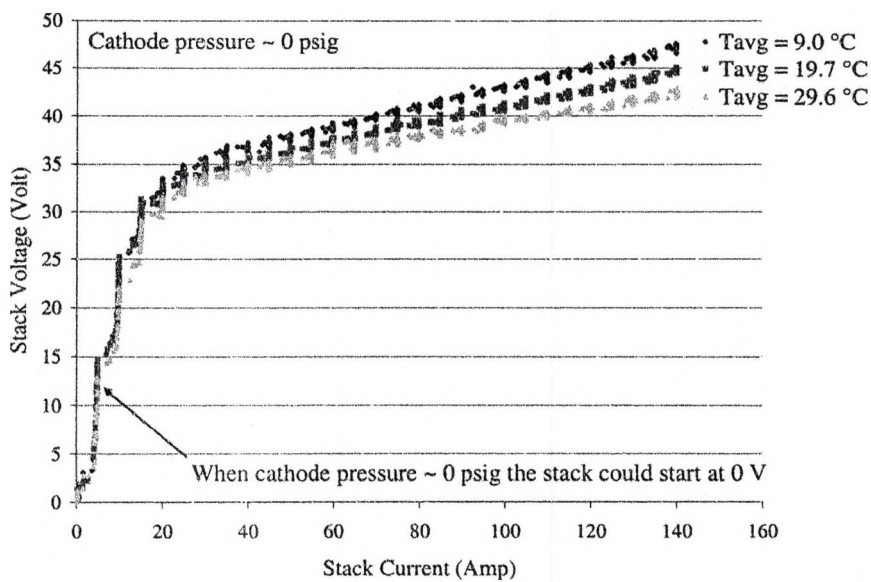


Figure 27. IV characteristic curves at constant cathode pressure (0 psig) at temperatures from 9.0 – 29.6°C.

The small step response seen when stack current is stepped from 1 A to 5A, revealed in Figure 27, is the combination of the response of the programmable power supplies running in current sharing mode and the Hall-effect current transducer monitoring stack current. The current transducers are direct acting and according to the manufacturer have a response time (to 90%) of 40 μ s. Therefore the major component of the step response is from the programmable power supplies and is in the range of 200 ms [31].

Higher Temperature Trials

The chiller installed in the UND system provides both the temperature control and water pumping of the DI water to the PEM stack anode. These higher temperature trials varied DI water temperatures between 40 – 70°C which is outside of the manufacturer’s temperature range.

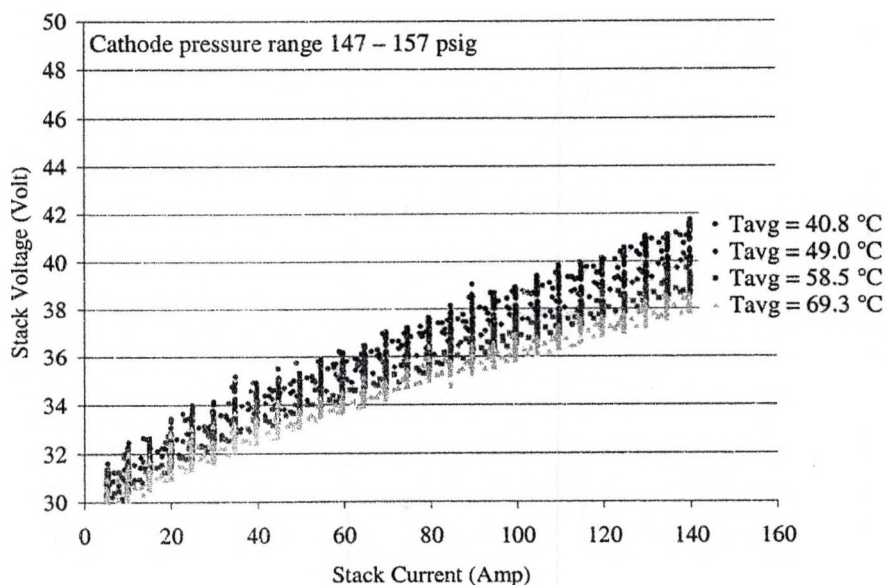


Figure 28. High temperature IV characteristic curves between 35 – 70°C at constant cathode pressure of ~ 150 psig.

Figure 28 presents the results from the higher temperature trials. Like the lower temperature trials from the previous section voltage continues to fall for a given current as temperature increases. This increases stack efficiency as activation and ohmic losses are reduced with increased temperature. The activation and ohmic losses are known as irreversible potentials and are explained in more detail in Chapter 7.

Bypassing the chiller controls with the 105 Ω fixed resistor fooled the chiller controller into thinking the water temperature was less than 35°C. The chiller was still required for the testing because the electrolyzer relies on the internal pump of the chiller to circulate the DI water. However, the fixed resistor fooled the chiller controller into thinking the water was within the temperature range and therefore did not enable the refrigeration cycle to reduce the water temperature. The chiller manufacturer warned that running with temperatures greater than 35°C could jeopardize pump seals. It was determined that these short duration high-temperature trials were acceptable but longer testing at elevated temperatures should not be conducted.

A comma-delimited (csv) file was created and contained the desired magnitude of stack current and the duration at each level. In both the low- and high-temperature tests the stack current started at 1 A then to 5 A and stepped at 5 A increments from then on with a duration of ½ second at each level. Column 1 of the file contains the duration and column 2 the stack current. The first row can contain header information and is ignored by the software reading the file.

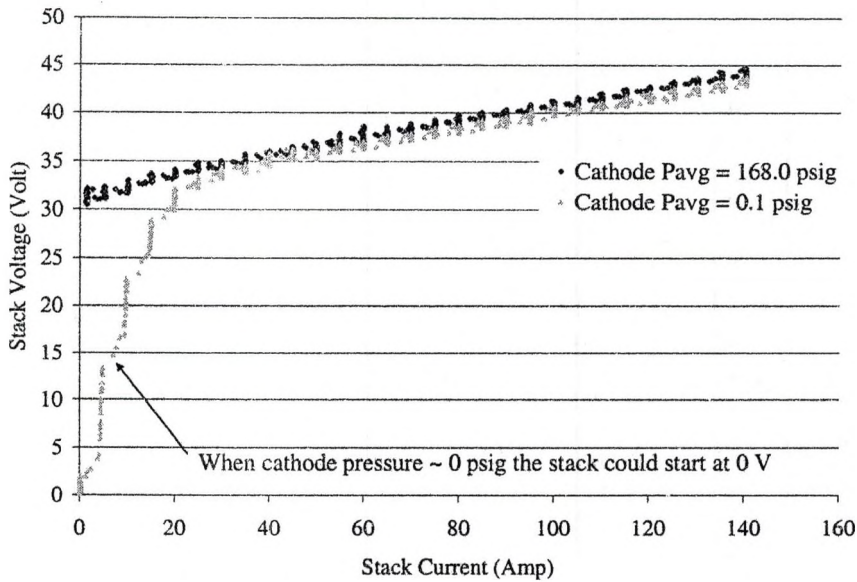


Figure 29. IV characteristic curves at constant temperature ($\sim 25^{\circ}\text{C}$) at cathode pressures of 0 and 168 psig.

Figure 29 is a plot of the IV characteristic curves in the low and high cathode pressure trials. The high- and low-pressure curves reveal a higher voltage required to electrochemically pressurize the hydrogen product. The result of the lower voltage for a given current in the low-pressure trial results in slightly higher stack efficiency. Energy is required to electrochemically pressurize the hydrogen in the high-pressure trial resulting in higher voltage, thus increase energy. The effects of pressure on stack voltage is explained by the Nernst equation and is explored further in Chapter 7.

Coefficients

The Butler-Volmer equation is used as the model to extract the three stack coefficients using the IV characteristic curves as a function of temperature. The nonlinear fit was calculated with Mathematica™, which includes an implementation of the Levenberg-Marquardt algorithm. The Butler-Volmer is used to model the data

because it predicts reaction kinetics and is described in Chapter 7 [42]. The stack IV characteristic curves from the previous sections (Figure 25 – Figure 28) were fitted to the model in Mathematica™ and the following coefficients were extracted.

- Anode exchange current density, $i_{a,o}$
- Cathode exchange current density, $i_{c,o}$
- Stack conductivity, σ

At equilibrium (i.e., no current) there exist dynamic currents, measured in amps, at each electrode and are a fundamental characteristic of electrode behavior. The anode and cathode exchange current densities can be defined as the rate of oxidation and reduction respectively. The exchange current density is a measure of the electrode's ability to transfer electrons and occurs equally in both directions resulting in no net change in composition of the electrode [43]. A large exchange current density represents *an electrode with fast kinetics where there is a lot of simultaneous electron transfer. A* small exchange current density has slow kinetics and the electron transfer rate is less. These coefficients help model and predict the overpotentials in the activation and ohmic regions of the IV characteristic curves (Chapter 7).

The anode and cathode exchange current density's were fitted exponentially as a function of temperature. Experimentally it has been determined and intuition suggests that as temperatures increase the faster a chemical reaction will proceed. Arrhenius was the first to recognize that the higher kinetic energy due to higher temperature results in lowering the activation potential [44]. Lower activation losses reduces the amount of energy for the reaction to proceed, thus increasing stack efficiency. The conductivity

coefficient was fitted linearly because it is primarily a function of current. Conductivity overpotential is shown in Chapter 7 to be a function of membrane thickness and current.

Anode Exchange Current Density

Small exchange current densities exhibited by the anode give rise to slow charge transfer which is in turn an activation-controlled process. This slow rate of reaction results in larger activation overpotential and is modeled by $2.0 \text{ E-}06 e^{0.043T}$ (A cm^{-2}). Based on the magnitudes of the anode exchange current density (Figure 30) compared with those of the cathode exchange current density (Figure 31) the activation overpotential is dominated by the anode exchange current density.

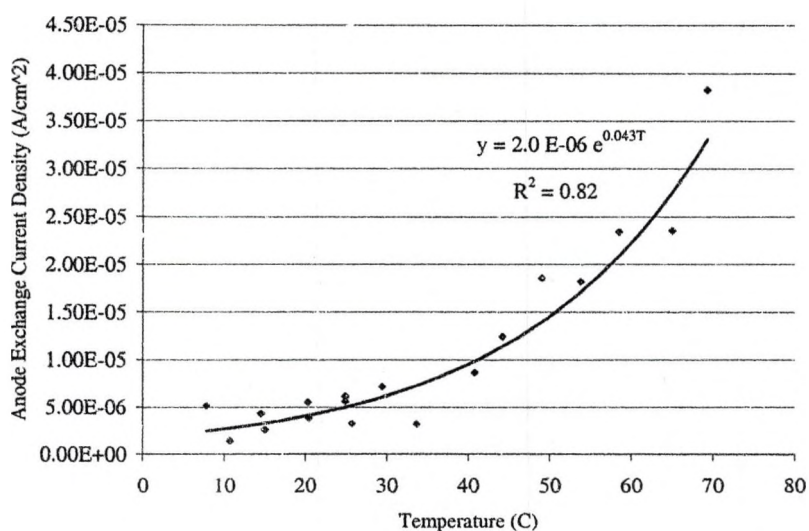


Figure 30. Anode exchange current density ($i_{a,0}$) experimental results.

Cathode Exchange Current Density

The cathode exchange current density is roughly four orders of magnitude greater than the anode exchange current density. This difference was expected and supported by Choi and Berning in [29, 45]. The anode side is therefore limiting the reaction and

dominates the activation overpotential and is modeled by $0.12 e^{0.026T}$ ($A\text{ cm}^{-2}$). Chapter 7 examines the contribution of both exchange current densities to the overall activation overpotential. It is believed that the larger variability ($R^2 = 0.69$) of the cathode exchange current density is due primarily to the way the testing was performed. The IV data from the previous sections was taken at low (~ 0 psig), medium (~ 90 psig) and high (~ 170 psig) pressure. The systems back-pressure regulator was being adjusted to obtain the various pressure data in between the current sweeps that produced the IV characteristic curves. Maintaining a single cathode pressure and performing the low- and higher-temperature testing should reduce the variability.

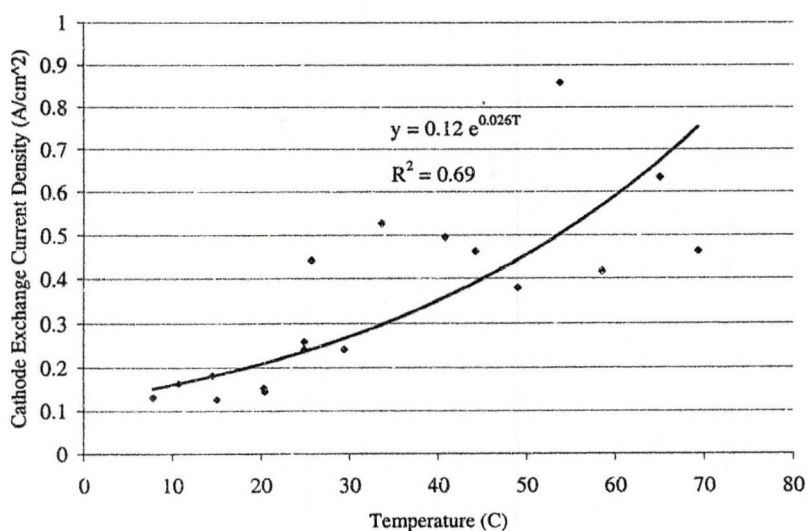


Figure 31. Cathode exchange current density ($i_{c,o}$) experimental results.

Conductivity

The final coefficient extracted (Figure 32) from this experimental data dominates in the ohmic (i.e., linear) region of the IV characteristic curves. Specifically speaking, membrane conductivity represents only the membrane's resistance to flow of protons (H^+) and is highly dependant on its thickness (ϕ) and water content. Electrical resistance

of electrodes, cell interconnects and the formation of any insulating layer on the electrode surface are all bundled under the conductivity term as is modeled linearly by $0.001T + 0.03$ ($S\ cm^{-1}$).

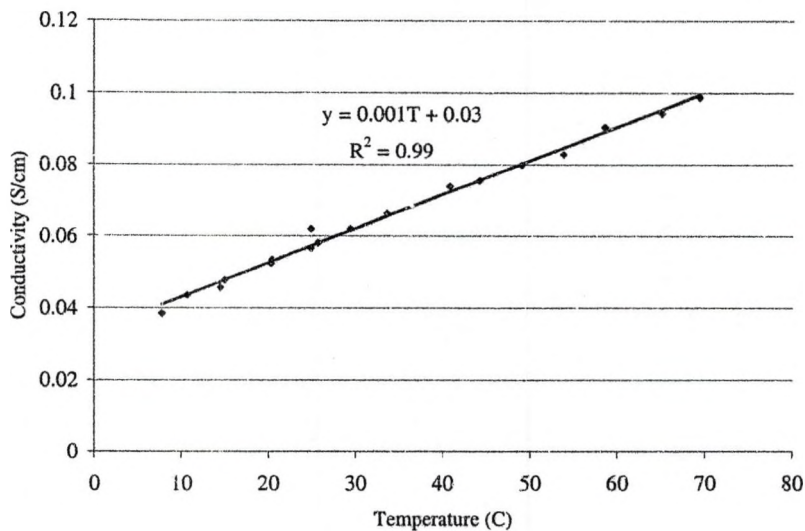


Figure 32. Conductivity (σ) fitted linearly to experimental results.

Efficiency Trials

Warm Up

Four efficiency trials were performed after a 30 minute warm-up period with stack current set at 70 A. After the warm-up period the systems back-pressure regulator (BPR1) was set at 160 psig while operating at 140 A and the locking-nut tightened and left unadjusted for the remainder of trials. The focus of these tests is to establish a baseline performance of the system. The start-up transients of the system are ignored and only steady-state data is taken once the system is allowed to run for a few minutes to reach the pressure set point.

The sample rate of the low-speed data acquisition was set at 5 S s^{-1} because of the slow moving temperatures and pressures of these steady-state constant current trials. The analysis is performed in Microsoft Excel that has a maximum row length of 65,536. The monitoring and control software has pre-set timers to disable data archiving after reaching the precise timer limit. At this sample rate, the four 30-minute trials should occupy 36,000 rows in the low-speed file which is decimated from the high-speed (1000 S s^{-1}) sampled data stream. The data acquisition system writes the data with a "txt" extension, is tab delimited and the analog input channels are in columns.

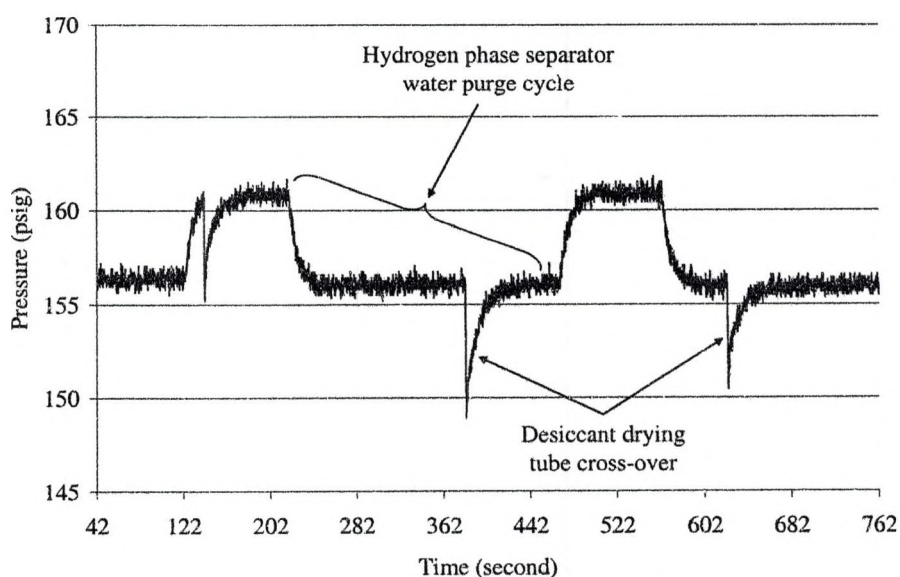


Figure 33. Hydrogen system pressure variations during 30-minute warm-up trial with stack current at 70 A.

Figure 33 shows the variations in hydrogen system pressure due to water purging cycles from the hydrogen phase separator and desiccant drying tube cross-over cycles. This sample was taken during the 30 minute warm-up trial while stack current was set at 70 A and the desired pressure set point is roughly 162 psig. System pressure was

readjusted to a nominal 160 psig at 140 A for the efficiency trials following this warm-up.

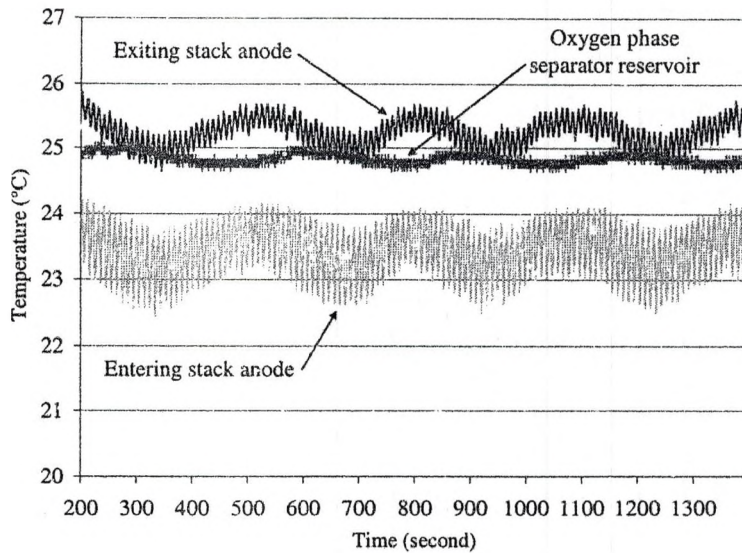


Figure 34. Temperature cycling of system DI water.

The effect of chiller temperature control can be seen in Figure 34. The chiller set-point during this warm-up trial is 25°C. The lower curve is the temperature signal from a combined pressure, temperature and flow transducer. The larger signal variability is intrinsic to the combined sensor and it is unknown whether the temperature sensing device is a resistive temperature device (RTD), thermocouple or thermistor. The 100 Ω platinum RTDs monitoring the temperature of the water/oxygen exiting the stack anode (upper curve) and the oxygen phase separator (middle curve) have less variability. The chiller's internal temperature sensor is monitoring the incoming water from the oxygen phase separator which is near the 25°C set-point. The control system of the chiller is cycling the refrigeration loop creating the sinusoidally varying temperature waveforms into and out of the stack. In addition, the chiller's control algorithm, which is based on

incoming DI water from the oxygen phase separator, is resulting in DI water entering the stack that is ~ 1.5 degrees below the set point.

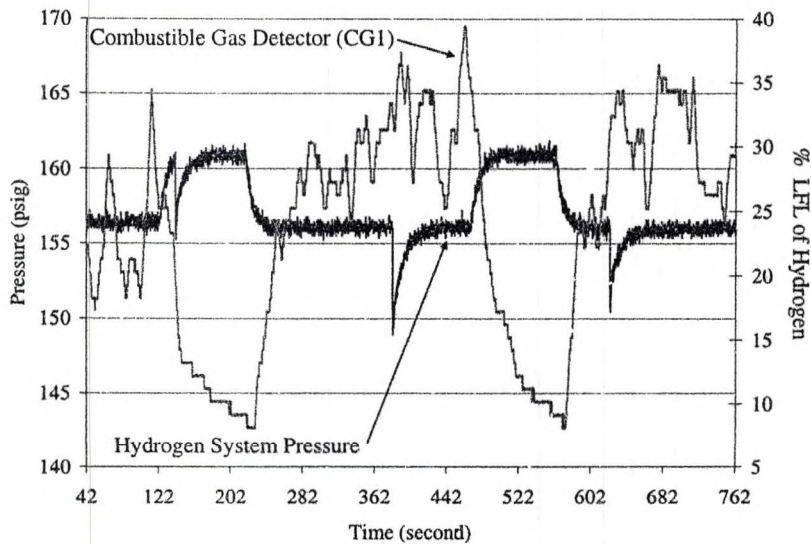


Figure 35. Analog signal from combustable gas detector (CG1) monitoring the oxygen phase separator gas mixture.

A combustable gas detector (CG1) monitors the gas makeup of the oxygen phase separator. Figure 35 shows the hydrogen content in the oxygen phase separator and the cycling that coincides with the water purge cycles of the hydrogen phase separator.

In the hydrogen phase separator high-pressure hydrogen dissolves into the water and then is subsequently released as the water is re-circulated into the oxygen phase separator reservoir. Communication with the engineering staff at PES confirms that the HOGEN 40 exhibits similar behavior [Personal communication with Everett Anderson, Proton Energy Systems, March 2006]. During this communication it was also revealed that the HOGEN 40 onboard CG detector is monitoring the exit flow of the onboard ventilation fan which tends to dilute the signal from their hydrogen phase separator.

Therefore, alarm 1 of CG1 is currently set at 50% LFL and will shutdown the system via software control if this level is reached on the UND system.

The setting of alarm 1 of CG1 to 50% LFL is higher than initially expected. For example, alarm levels for CG2 that monitors the air in the canopy hood are set at 10% and 20% of LFL. CG1 should be calibrated every six months to ensure that the sensor is accurately monitoring the oxygen phase separator gas make-up. The oxygen phase separator will always contain some hydrogen during operation which could have dangerous consequences if the LFL was reached. The amount of hydrogen loss through normal operation is much less than the amount of hydrogen lost through the desiccant process.

Results

Following the 30 minute warm-up period, four efficiency trials were conducted at 140 and 70 A with the chiller temperature set-point at 15 and 30°C respectively. Table 13 shows the trial matrix and resulting average system variables calculated after the trials. The stack DI water temperature is the temperature of the incoming water to the stack anode.

Table 13. Efficiency trial matrix and resulting average system variables

Stack Current Amp	Stack DI Water Temperature, °C	Hydrogen System Pressure, psig
69.7 (warm-up)	23.4	170.0
140.0	26.8	157.1
70.4	13.1	120.4
140.1	10.8	157.1
70.5	28.6	120.1

The system back-pressure regulator is set to a nominal 160 psig at the first 140 A trial and was not adjusted for the subsequent trials. Therefore, the system hydrogen

pressure averaged around 120 psig due to the lower current, resulting in lower hydrogen flow, of the 70 A trials.

The system efficiency calculations require integrating the stack power and hydrogen mass flow over the 30 minute trials. Equations 3-1 and 3-3 are duplicated here for convenience to show the process used to integrate the sampled stack power and hydrogen mass flow data (Eqn. 6-2) of the low-speed file to calculate system efficiency (Eqn. 6-1). The hydrogen mass flow is converted to kg by using the density 0.08988 kg Nm⁻³. In order to compare the system efficiencies of the UND system and the data taken from the HOGEN 40 installed at NREL (Chapter 3), a nominal ancillary energy term of 0.25 kWh is added to the stack energy for the 30 minute trials. This additional ancillary energy term was experimentally determined using a power transducer explained in Chapter 3.

$$\text{System Efficiency} = \frac{\text{HHV} \left(\frac{\text{kWh}}{\text{kg}} \right)}{\left(\frac{\text{Stack Input Energy (kWh)}}{\text{Power Supply Efficiency}} \right) + \text{Ancillary Losses (kWh)}} \times \text{Hydrogen Produced (kg)} \quad 6-1$$

$$\text{Energy} = \frac{1}{3600} \int \text{Power} \, dt \sim \frac{1}{3600} \sum_i^n \frac{P_i + P_{i-1}}{2} (t_i - t_{i-1}) \quad 6-2$$

where the HHV of hydrogen is 39 kWh kg⁻¹.

Table 14. System efficiencies for baseline testing of UND system.

Stack Current Amp	Stack DI Water Temperature, °C	Stack + Ancillary Energy, kWh	Hydrogen gram	System Efficiency, %
140.0	26.8	3.29	39.5	46.9
70.4	13.1	1.67	18.9	44.1
140.1	10.8	3.55	39.4	43.3
70.5	28.6	1.59	19.0	46.5

System efficiency results for the 30 minute baseline trials (Table 14) contain the correlation between increased temperature and improved efficiency. The higher temperature trials with the UND system resulted in a higher system efficiency as expected.

Table 15. Typical HOGEN 40 system efficiency data taken at NREL.

Stack Current Amp	Stack DI Water Temperature, °C	System Efficiency, %
140.3	45.4	53.8
140.5	48.3	53.2
69.4	28.0	50.3
70.1	39.3	44.6

Baseline (Table 3) and frequency waveform (Table 4) testing was conducted on the commercial HOGEN 40 in Chapter 3 with similar results shown here in Table 15. The correlation between higher temperatures leading to lower activation overpotential and higher stack efficiency is violated in the 70 A trials of Table 15. The temperature control of the UND system has verified the expected results, where higher temperatures lead to higher efficiency.

However, system efficiencies of the UND system are generally lower than the HOGEN 40 system installed at NREL (Table 15 and Figure 36) due to the lower temperatures they were run at. Higher temperature efficiency trials are required on the UND system to complete the comparison with the HOGEN 40 data taken at NREL. The UND system chiller requires modifications to run at temperatures above 35°C.

System efficiency of both the UND system and commercial HOGEN 40 decreases with decreased stack current (Figure 36). This trend is due to the desiccant systems used to dry the hydrogen product gas. Chapter 5 discussed this phenomenon in detail.

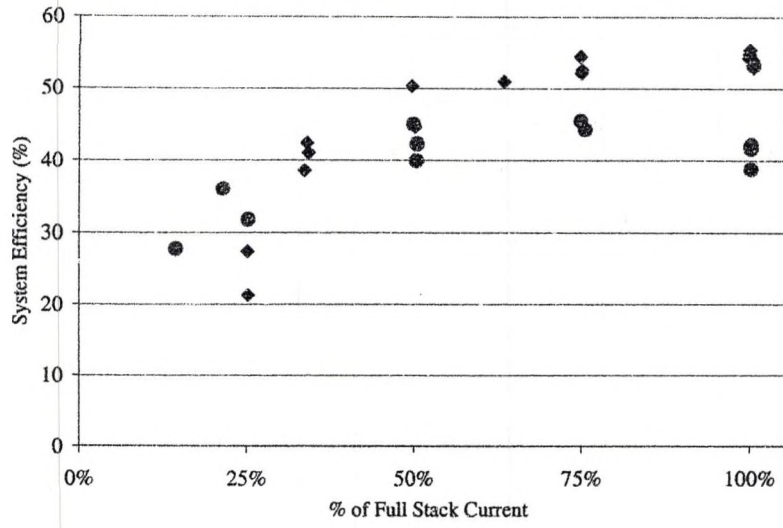


Figure 36. System efficiency summary with NREL HOGEN 40 data (◆) and UND system data (●).

7 CHAPTER

PEM ELECTROLYSIS MODELING

Introduction

This chapter is dedicated to the electrochemistry behind water electrolysis to enable the next phase of this research; namely the design of power electronics to more closely couple the energy from wind turbines to the requirements of electrolyzer stacks. The processes that affect the transport of electrons to the stack electrodes and conduction of ions through the electrolyte are explored in the hope that the experimental data obtained for these systems can be modeled easily.

The IV data gathered in Chapter 6 of this work is the basis for this modeling but will be enhanced by researches running the UND electrolyzer system to obtain more detailed stack parameters using electrochemical impedance spectroscopy (EIS). EIS requires the operation of these electrochemical cells in the linear or ohmic regions of the IV curves. Small sinusoidal waveforms are superimposed on larger currents to obtain a frequency dependent impedance response. Detailed capacitive and inductive impedance parameters can be extracted from the response and models constructed to simulate the electrochemical process.

Water electrolysis is an electrochemical reaction where water is split into hydrogen and oxygen in the presence of a catalyst and applied electric field. Energy is required to initiate the process and results in a loss known as activation overpotential. As current density increases the cell losses due to membrane, electrode, and interfacial

resistances dominate and are referred to as ohmic overpotential. The UND electrolyzer, based around PES's 20-cell HOGEN 40 stack, is not designed to operate at much higher current densities that would result in observing the third overpotential region known as transport, diffusion, or concentration overpotential. PES notes that current densities much greater than 1.6 A cm^{-2} are required before transport losses would dominate on their stack [Personal communication, Everett Anderson, Proton Energy Systems, March 2006]. For this reason concentration overpotential is neglected in this analysis. The terms overpotential, loss, and polarization are used synonymously in this chapter.

Critical PEM electrolyzer parameters like membrane conductivity, thickness, and type as well as exchange current densities are typically deemed proprietary by electrolyzer and fuel cell manufacturers. Therefore, a common practice is to determine these parameters from the open literature. Unfortunately, for the case of both the anode and cathode exchange current densities, the range of values varies dramatically from author to author because of the various operating conditions, cell construction, and stack configurations. Typical values found in the literature for the anode exchange current density range from $10^{-7} - 10^{-12} \text{ A cm}^{-2}$ [29, 45]

When comparing literature from FC models with water electrolysis work it is important to remember the differences between the system anode and cathode. This basic understanding may be trivial to most but is many times confused when switching between the two processes. The anode is always the electrode at which oxidation occurs, where electrons are lost. The cathode is defined as the electrode at which electrons enter, where reduction takes place. In electrolysis the cathode is the electrode where H_2 gas is created, in FC systems the anode is the electrode where H_2 is introduced.

Methodology

The intent of this effort is to extract important stack parameters using the experimental data of Chapter 6 to complete a temperature dependent system model. The foundation of the work is pulled from thermodynamic properties to determine the reversible potential of the reactants and products and the Butler-Volmer equation to predict the overpotentials (i.e., irreversibility) of the stack.

In Mathematica™ the anode and cathode exchange current densities and conductivity are extracted from temperature dependent IV characteristic curves of the HOGEN 40 stack over a temperature range from 7 – 70°C (Chapter 6). In the case of the exchange current densities both curves are fitted exponentially while the conductivity term is fitted linearly. These coefficients can be directly related to the physical properties of the system which is a clear advantage of this approach with respect to a simple curve-fitting method (e.g., polynomial approximation).

In this macro-level model stack current, system temperature, cathode pressure and anode pressure are required to simulate the system. Without experimental data the cathode and anode pressures can be assumed to be constant based on the electrolyzer design. In the case of the UND system the back-pressure regulator on the hydrogen output was set to ~11.0 atm (160 psig). Also, the oxygen phase separator pressure is essentially the anode pressure and is set by the cracking pressure of a 1/3 psig check valve at the gas vent port.

The model is written in Visual Basic (Appendix D) as a macro within Microsoft Excel. This approach will allow for of the model simulations to be run and then system's monitoring and control software can read the same data to power the electrolyzer

experimental system. The data are comprised of duration (seconds) in column one and the stack current (amps) in column two. Finally, the Visual Basic code outputs the predicted hydrogen flow rate which can be compared with the experimental system's mass flow rate that also reports in $\text{Nm}^3 \text{hr}^{-1}$.

First Principles

The overall reaction of the electrolysis cell (Eqn. 7-1) provides the required stoichiometric coefficients for the products and reactant used in Eqn. 7-2. The sign convention is positive for products and negative for reactants with analogous definitions for ΔB , ΔC and ΔD . Data for the constants A, B, C and D are thermodynamic properties and are reproduced from [46] in Table 16.



$$\Delta A \rightarrow A_{\text{H}_2} + \frac{1}{2}A_{\text{O}_2} - A_{\text{H}_2\text{O}} \quad 7-2$$

Table 16. Constants for heat capacities of gases in ideal state and liquid water.

	A	B	C	D
H ₂	3.249	$0.422 * 10^{-3}$	0	$0.083 * 10^5$
O ₂	3.639	$0.506 * 10^{-3}$	0	$-0.227 * 10^5$
H ₂ O	8.712	$1.25 * 10^{-3}$	$-0.18 * 10^{-6}$	0

The model uses the specific heat capacity of water and gases in the ideal state to determine the standard Gibbs free energy of reaction, ΔG° , using Eqn. 7-3.

$$\Delta G^\circ = RT \left[\frac{\Delta G_0^\circ - \Delta H_0^\circ}{RT_0} + \frac{\Delta H_0^\circ}{RT} + \frac{1}{T} \int_{T_0}^T \frac{\Delta C_p^\circ}{R} dT - \int_{T_0}^T \frac{\Delta C_p^\circ}{R} \frac{dT}{T} \right] \quad 7-3$$

where ΔH_0° and ΔG_0° are the standard enthalpy and Gibbs energy of formation of liquid water, respectively, at reference temperature T_0 . The integrals of Eqn. 7-3 take into

account the temperature dependency of the heat capacities of the products and reactants and are reduced to Eqns. 7-4 and 7-5.

$$\int_{T_0}^T \Delta C_P^\circ dT = (\Delta A)T_0(\tau - 1) + \frac{\Delta B}{2}T_0^2(\tau^2 - 1) + \frac{\Delta C}{3}T_0^3(\tau^3 - 1) + \frac{\Delta D}{T_0}\left(\frac{\tau - 1}{\tau}\right) \quad 7-4$$

$$\int_{T_0}^T \frac{\Delta C_P^\circ}{R} \frac{dT}{T} = \Delta A \ln \tau + \left[\Delta B T_0 + \left(\Delta C T_0^2 + \frac{\Delta D}{\tau^2 T_0^2} \right) \left(\frac{\tau + 1}{2} \right) \right] (\tau - 1) \quad 7-5$$

where T is the reaction temperature (K), T_0 is the reference temperature (298 K), R is the universal gas constant ($8.314 \text{ J mol}^{-1} \text{ K}^{-1}$) and $\tau \equiv \frac{T}{T_0}$.

Enthalpy is an intrinsic property of a substance and a function of temperature and pressure [46]. In practice the Gibbs free energy is the net internal energy available to do work, less work done by changes in pressure and temperature [47]. Exergy, on the other hand, is defined as the total amount of work that can be harnessed and becomes more relevant in high-temperature and high-pressure electrolysis.

At standard temperature and pressure (STP, 25°C , 1atm) Gibbs free energy of formation is defined as the point of zero energy and is used to calculate the change in energy of a system. The reversible (i.e., the minimum) voltage required to electrolyze water into hydrogen and oxygen is determined by the change of Gibbs free energy of formation between the products and reactants. The Gibbs free energy of formation is not constant; it changes with temperature and state (liquid or gas) [47].

$$E_o = -\frac{\Delta G^\circ}{zF} \quad 7-6$$

where E_o is the minimum reversible voltage of a cell, z is the number of electrons (2) taking part in the PEM electrolysis reaction of Eqn 7-1 and F is Faraday's constant (96,485 Coulomb mol⁻¹).

It has been shown in Eq. 7-3 that the Gibbs free energy will vary with temperature of the reaction [46]. The Nernst potential (V_n) of Eqn. 7-7 accounts for changes in the activity of the reaction and for nonstandard conditions.

$$V_n = E_o + \frac{RT}{2F} \ln \left(\frac{P_{H_2} P_{O_2}^{\frac{1}{2}}}{P_{H_2O}} \right) \quad 7-7$$

where P_{H_2} , P_{O_2} and P_{H_2O} represent the partial pressures of hydrogen, oxygen and water respectively.

The partial pressure of water is determined with the empirical formula from [39] and shown in Eqn. 7-8. This relationship enables the partial pressure of water to be calculated from experimental data as the temperature of the DI water into the stack anode varies. This form agrees well with the tables found in Appendix F of [46].

$$P_{H_2O} = 610.78 * \exp \left[\frac{T_c}{(T_c + 238.3)} * 17.2694 \right] \quad 7-8$$

where T_c is the temperature into the stack in °C and should not be confused with T and T_o from earlier that have units of Kelvin.

The partial pressures of hydrogen and oxygen are determined using measurements from the stack cathode and anode and Eqns. 7-9 and 7-10.

$$P_{H_2} = P_c - P_{H_2O} \quad 7-9$$

$$P_{O_2} = P_A - P_{H_2O} \quad 7-10$$

where P_C and P_A are the experimental pressures (atm) of the cathode and anode respectively.

Overpotential

Activation

Electrochemical reactions possess energy barriers which must be overcome by the reacting species. This energy barrier is called the 'activation energy' and results in activation overpotential, which are irreversible losses in the system. Activation energy is due to the transfer of charges between the electronic and the ionic conductors. The activation overpotential is the extra potential necessary to overcome the energy barrier of the rate-determining step of the reaction to a value such that the electrode reaction proceeds at a desired rate [48]. The anode (Eqn. 7-11) and cathode (Eqn. 7-12) activation overpotentials, η_A and η_C , represent irreversible losses of the PEM stack and dominate the overall overpotential at low current densities. The experimental data from Chapter 6 provide equations for both the anode and cathode exchange current densities and are duplicated here for convenience in Eqns. 7-13 and 7-14 respectively.

$$\eta_A = \frac{RT}{\alpha_a z F} \ln \left(\frac{i}{i_{a,0}} \right) \quad 7-11$$

$$\eta_C = \frac{RT}{\alpha_c z F} \ln \left(\frac{i}{i_{c,0}} \right) \quad 7-12$$

where α_a and α_c are the anode and cathode electron transfer coefficients respectively.

The electron transfer coefficient is a measure of the symmetry of the activation energy barrier and can range from zero to unity [44].

$$i_{a,o} = 2.0 * 10^{-6} e^{0.043 T_c} \quad 7-13$$

$$i_{c,o} = 0.12 e^{0.026 T_c} \quad 7-14$$

where $i_{a,o}$ and $i_{c,o}$ are the anode and cathode exchange current densities ($A\text{ cm}^{-2}$) respectively and i is the current density of the stack ($A\text{ cm}^{-2}$). These expressions are fitted from the temperature-based IV trials of Chapter 6.

As discussed in Chapter 6, the cathode exchange current density (Figure 31) is typically orders of magnitude greater than the anode exchange current density (Figure 30). The higher the exchange current density the “easier” it is for reaction to continue when current is supplied to the stack. The cathode exchange current density is thus not the limiting parameter of the activation overpotential term and is often ignored. The current density (i) normalizes the stack current (I) to the active area of the PEM stack. The stack consists of 20 series connected cells each with an active area (A) of 86.4 cm^2 .

Ohmic

Ohmic losses occur because of resistance to the flow of ions in the solid electrolyte and resistance to flow of electrons through the electrode materials. Because the ionic flow in the electrolyte obeys Ohm’s law, the ohmic losses can be expressed by Ohm’s Law. The ohmic overpotential (η_o) of Eqn. 7-15 is a function of the stack current density (i), membrane thickness (φ), and the conductivity of the stack (σ). The conductivity of the stack was extracted from experimental data of Chapter 6 (Figure 32)

and linearly fitted as a function of the temperature of DI water into the stack anode (Eqn. 7-16).

$$\eta_o = \frac{\varphi}{\sigma} i \quad 7-15$$

$$\sigma = 0.001 T_c + 0.03 \quad 7-16$$

where σ (Siemen cm^{-1}) represents the sum of membrane resistance to ion transfer and bundled electrical resistances of electrodes and interconnections within the stack. The membrane thickness (φ) for Nafion™ 117 was assumed to be $178 * 10^{-4}$ cm and the values were found to be in good comparison with the literature [49].

Concentration

The UND electrolyzer system was designed to enable performance and characterization testing of PES HOGEN 40 stack outside of the commercial unit's design specifications. PES maintains a pressure in their oxygen phase separator of roughly 15 psig to limit oxygen bubble size at the cells anode. The UND system required a lower check pressure due to the material and size of their oxygen phase separator. A check valve with a cracking pressure of 1/3 psig allows oxygen to vent out of the reservoir. This modification could result in higher mass transport losses if the system were run into the region where this overpotential becomes observable. However, according to PES, under normal operating currents (0 – 140 A) concentration losses will not be discernible in the IV characterization curves.

IV Characteristic

As the stack ages, internal polarization losses (i.e., overpotentials) increase and stack voltage will increase for a given current. As part of their ongoing work to provide

stack improvements and anticipate stack failures in the field, Proton Energy Systems monitors cell performance by continuously running (24/7) the various production stack configurations. Their data reveals that stack cells degrade at $\sim 20 \mu\text{V cell}^{-1} \text{ hour}^{-1}$ from 400 – 2000 hours to $\sim 5 \mu\text{V cell}^{-1} \text{ hour}^{-1}$ from 2000 to 14,000 hours [50]. Data taken from the manufacturer's operating manual indicate that the system is expected to dissipate 6800 BTU hour^{-1} (beginning of life) and 14,700 BTU hour^{-1} (end of life) of heat into the room.

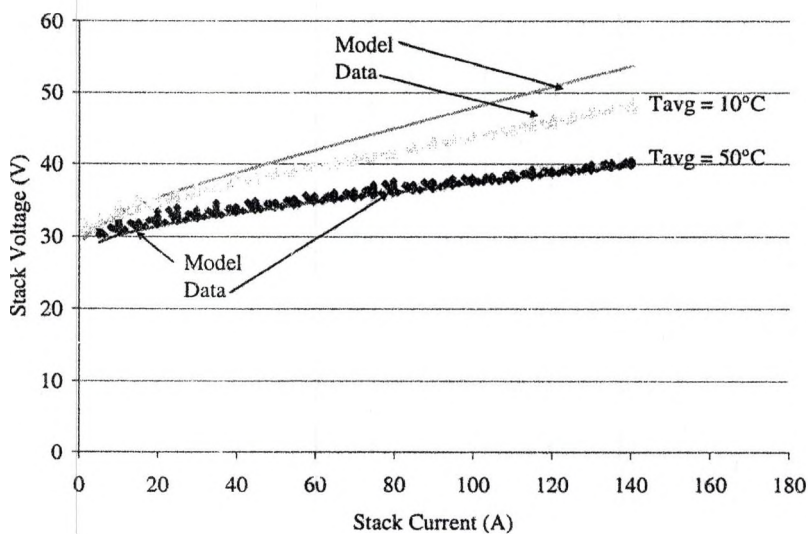


Figure 37. Experimental IV curve with model for 10°C and 50°C.

Figure 37 plots IV data at 10°C and 50°C and the resulting fitted models based on the temperature dependent anode and cathode exchange current density and conductivity. Generally, the electron transfer coefficient (α) should be a potential-dependent factor however, for this model they are assumed constant at 0.5 [29]. The 10°C the model begins to diverge after the activation overpotentials stabilize (Figure 38).

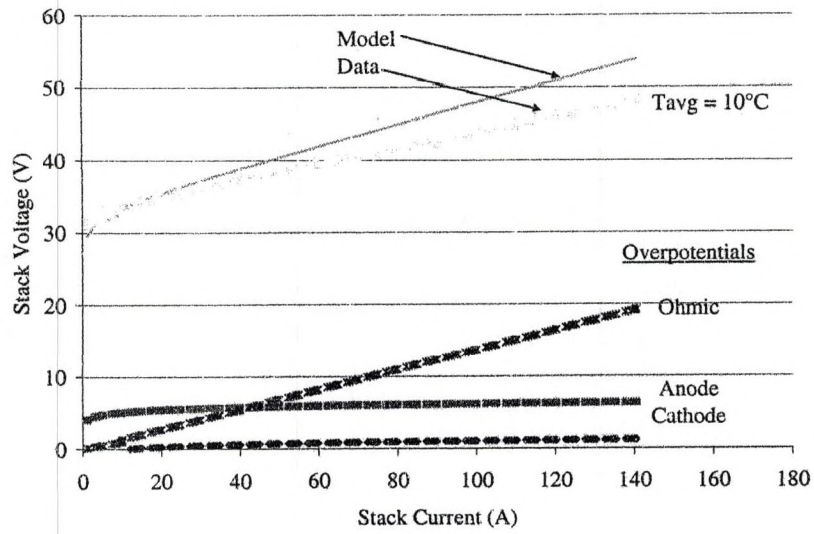


Figure 38. 10°C data and model showing contribution of the overpotential terms.

Figure 38 shows each overpotential term and the regions where they dominate. As expected, the anode term is greater than the cathode and dominates in the lower currents. The ohmic overpotential remains linear over the range of currents because of the constant IR losses associated with the conductivity coefficient, σ .

8 CHAPTER

CONCLUSIONS AND RECOMMENDATIONS

“Personally, I think that 400 years hence the power question in England may be solved somewhat as follows. The country will be covered with rows of metallic windmills working electric motors which in their turn supply current at a very high voltage to great electric mains. At suitable distances there will be great power stations where during windy weather the surplus power will be used for the electrolytic decomposition of water into hydrogen and oxygen.... In times of calm, the gases will be recombined in explosion motors working dynamos which produce electrical energy once more or more probably in oxidation cells.”, Haldane, in his talk entitled, “Daedalus or Science and the Future”, Cambridge University, 1923 [51].

There exists an opportunity to change the face of our energy consumption from one of polluting our air, water, and land to one more in harmony with the environment. The environment and the economy are often at odds for resources, but it does not have to be that way. Renewable hydrogen seems to possess the ability to transition the world’s carbon-based economy into a near-carbon-free economy. As our climate continues to beg for mercy from the choking pollution freely exhausted into the environment, it will become more apparent that continuing down this path is no longer viable. Hydrogen can be extracted from all fossil fuels as well as split from water using the electricity from RE sources. However, without sequestering the climate-altering CO₂ produced using fossil

fuels, the environmental benefits are completely lost and may be even worsened by the transition to hydrogen as an energy carrier.

If the environmental benefits of the long-term development of the hydrogen economy are to be realized, the production of hydrogen via electrolysis from RE sources will be a vital component. Today's commercially available electrolyzers are designed to use grid electricity, produce well regulated DC power to the electrolysis stack, and condition the output gas for applications different than that required by PEM fuel cells. The key element in hydrogen production from any electrical source is the electrolyzer stack which converts water and electricity into hydrogen, oxygen and heat. The electrolyzer stack is inherently a nearly constant, low-voltage, DC device requiring some form of control system and power electronics to connect it to a high-voltage, AC source of power.

The primary intent of this work is to design, build and verify a system capable of accurately varying important system variables that are normally strictly monitored and controlled by the commercial electrolyzers containing the same PEME stack. The goal of the experimental characterization of the stack, under varying conditions and power, is to enable an optimized interconnection between the stack and RE source. Such a coupled system specifically designed with the RE source in mind would reduce the overall cost of independent stand-alone systems and may eliminate the need for electrical storage components.

Electrical power provided to the electrolyzer in such a system would be controllable with excess power provided to the grid. Thus, a combined system would have more dispatch-ability than a wind-electric turbine or PV array alone. Such dispatch-

ability might be used to provide the utility with a measure of control over the renewable energy systems total output that does not exist in current renewable based, grid-connect only systems. Using a variable RE source, like wind or PV, to generate the hydrogen gas will guarantee this energy carrier will be produced with nearly zero emissions.

UND System

PES is a key enabler of this research project and ultimately of the system that was designed and built at UND. The heart of the UND system is the same 20-cell PEM electrolyzer stack that PES installs in their HOGEN 40 electrolyzer. In addition, PES provided the same hydrogen phase separator and desiccant drying system that is integrated into their commercially available HOGEN 40. Finally, PES shared some sensitive information, not shared in this paper, to enable the UND system to perform as closely to the HOGEN 40 as reasonably possible.

Taking the lessons learned from the NREL HOGEN 40 installation, facility construction, and assistance from PES, a system was designed, built and preliminary testing accomplished. The goal of the UND system is to allow control over important system variables to enable the thorough characterization and performance testing of PEM electrolysis stacks under conditions relevant to RE sources. The system variables capable of control are as follows:

- DI water flow rate to stack anode
- Water resistivity
- Stack current including the generation of complex (DC + AC) waveforms
- Desiccant tube drying cycle
- Hydrogen system pressure

- DI water temperature to stack anode
- Access to hydrogen stream enabling testing of alternative drying processes

The preliminary verifications trials focused on constant temperature IV characterization and baseline efficiency testing. Constant temperature DI water was introduced to the stack anode from 7 – 70°C while stack current was swept from 1 to 140 A. A family of IV curves were produced and stack coefficients extracted from the data. Anode and cathode exchange current densities and stack conductivity were extracted from the experimental data using the Butler-Volmer equation as the model. The Butler-Volmer equation describes electrode kinetics and gives insight into the electron transfer rate of the reaction. The anode and cathode exchange current densities (Eqns. 8-1 and 8-2 respectively) were exponentially fitted as a function of temperature and the stack conductivity (Eqn. 8-3) linearly fitted.

$$i_{a,o} = 2.0 \cdot 10^{-6} e^{0.043 T_c} \quad 8-1$$

$$i_{c,o} = 0.12 e^{0.026 T_c} \quad 8-2$$

$$\sigma = 0.001 T_c + 0.03 \quad 8-3$$

Efficiency trials were conducted while DI water temperature and stack current were held constant to verify the UND electrolyzer system against the HOGEN 40 testing performed at NREL.

Dew Point Control

One ancillary goal of this work is the analysis and comparison of the desiccant drying strategy utilized in PES commercial PEM electrolysis equipment against a thermoelectric-based design. Based on the application and required dew point control,

the TEC design may offer an alternative drying option, with the ultimate goal of improving the efficiency of the electrolyzer, thus reducing the overall cost of the produced hydrogen. It was shown that the desiccant system running with system pressure around 200 psig consumes a fixed amount of hydrogen regardless of operating current. This impacts the system efficiency more at lower current densities when hydrogen production is less. In a renewable electrolysis system, this impact on efficiency is significant because the electrolyzer is operating at low current densities as well as higher current densities due to the variability in power from the RE source.

At full operating current of ~140 A and 200 psig, the desiccant system in the HOGEN 40 electrolyzer consumes roughly $0.1 \text{ Nm}^3 \text{ hour}^{-1}$ of dried hydrogen product to maintain the desiccant beds. Thermodynamic modeling was performed to determine the appropriate sizing for the thermoelectric coolers and water-cooled heat sinks for a $1 \text{ Nm}^3 \text{ hr}^{-1}$ hydrogen flow rate to obtain a theoretical dew point of -35°C . The potential benefits and energy consumed by the thermoelectric approach is compared to the hydrogen loss of the desiccant system. The thermoelectric cooler-based system has the ability to control the dew point to match the variable flow rate of hydrogen in a renewable electrolysis system and improve the system efficiency at lower current densities. However, the PES desiccant design achieves a dew point of roughly -60°C , much lower than the TEC calculations and experimental system being developed at UND.

The two-stage cold plate and thermoelectric design may contain other operational benefits depending on the application for which the hydrogen is being produced. Ultimately, TEC design can obtain dew point control with closed-loop feedback of the TEC temperature in Stage 2 to obtain the desired dew point to match a specific

application. The TEC design uses roughly 3.1 kWh kg^{-1} of hydrogen without temperature feedback control, while the desiccant system loses roughly 3.4 kWh kg^{-1} as hydrogen loss and approximately 6.2 kWh kg^{-1} of hydrogen taking into account a PEM stack efficiency of 55 %.

Future Work

NREL Test Facility

Future work includes understanding the long-term effects of variable power inputs to the electrolyzer stack performance. The currently employed power electronics between the wind turbine and electrolyzer are not optimized. Based on the characterization of the electrolyzer, future work will also include the optimization of power electronics between the wind turbines and various electrolyzers. Evaluation of the modified power electronics, under actual wind conditions, will allow researchers to develop a control scheme for both the wind turbine and electrolyzer with extra energy available for the grid or battery storage.

As shown above, a standard off-the-shelf wind-powered battery charge controller makes an ineffective hydrogen-producing device. To optimize wind-to-hydrogen production, a PE interface that can operate beneficially with the unique characteristics of the PEM stack should be developed. If done correctly, this system could operate independently from and not require a DC bus voltage dominating battery. Independent control power could be supplied by a small power supply that turns on when sufficient wind energy is present. Simple relay logic with properly selected time delays could accomplish this task. This would continue to facilitate smooth startup and shutdown of the PE interface and would eliminate the need for the battery and its associated semi-

complex charging and maintenance requirements. DC voltage grooming could be achieved by a less expensive filter capacitor.

Dew Point Control

The dew point controller experimental system, currently being assembled at UND, will enable baseline data to be taken with the proposed TEC system and verification of the model. The cold plates are made of copper, which may become a problem during extended operation based on the purity of the water being formed by condensation and desublimation within them. Pure water extracted from the hydrogen gas may corrode the copper over time but should be sufficient for this proof of concept testing.

A closed-loop temperature control system could monitor and adjust the TEC operation to maintain a specific dew point. This level of control can be accomplished either by simple on-off operation or pulse-width modulation (PWM) of the TEC voltage. TECs run with PWM require a frequency of 1 kHz or greater to extend the life of the device. It is not recommended to control temperature by running the TECs in on-off mode as the temperature cycling reduces the life of the module.

A renewable electrolysis system could realize greater benefits with the TEC dew point controller. A closed-loop temperature controller would cycle the TEC modules to match the hydrogen flow rate to reduce the energy consumption of the system. Finally, having control over the dew point may become important when we use an electrochemical compression system to raise the final pressure of the hydrogen gas.

Hydrogen Diffusion

It is well known that PEME can operate at a significant differential pressure across the anode and cathode. In an anode water fed system this configuration gives rise to higher hydrogen diffusion across the membrane and ultimately into the oxygen phase separator. A study could include using common differential pressures (100 – 200 psig) and a given volume in the phase separator to predict the amount of hydrogen that would be present in the vessel. In addition, high-pressure hydrogen is dissolved into the water of the hydrogen phase separator that is re-circulated into the oxygen phase separator. A study could help understand and determine what level the combustible gas detector should expect to determine the appropriate % LFL to operate the system safely.

Mass and Energy Balance

The modeling effort of Chapter 7 neglected some important energy exiting the system. It is safe to presume that the oxygen in the O2phSep is completely saturated with water vapor at system operating temperatures which are normally above 20°C. The elevated temperature and saturated gas contains both sensible and latent heat as it exits the system. In addition, humid hydrogen is vented after drying the desiccant tubes containing water vapor. A detailed study could be performed to better quantify the energy contained in the exiting gases that are not accounted for in the macro-level model of Chapter 7.

It would also be interesting to predict and experimentally verify the amount of heat lost to the surrounding environment. It is said in [47] that up to 40 % of the heat generated by today's PEMFC's is radiated to the local environment. An ambient temperature sensor, located on the instrument rack of the UND system, is installed to

begin the process of quantifying this behavior. However, it is recommended that the sensor be relocated or replaced with a more accurate sensor if this testing is pursued. Determining time constants associated with temperature differences between the stack and ambient could produce an electrical model equivalent using resistors and capacitors to simulate the role of ambient temperature has on stack cooling.

DI Water

PES requires a minimum of 1 M Ω – cm (ASTM Type II) resistive water but prefers DI water with greater than 10 M Ω – cm resistivity (Type I) [36]. Alkaline electrolysis equipment does not require such pure water and an evaluation of cost impacts for this water quality could be explored.

Impact of Variable power

Complex waveforms are mathematically generated by the monitoring and control software. Sinusoidal ripple has been imposed on a DC offset during the HOGEN 40 testing at NREL to determine the impact on hydrogen production. It was shown in [31] that these complex waveforms did not impact performance and that hydrogen production follows the average value of the waveform. It could be interesting to experimentally verify the initial testing at NREL and continue the analysis to verify that the overpotentials (i.e., losses) are a function of the rms value of the waveform.

Electrochemical Compression

The intrinsic ability of PEME to electrochemically compress hydrogen product is a clear advantage of this technology over alkaline systems. While electrolyzers that utilize alkaline technology raise the pressure of both the anode and cathode, it comes with the potential risk of the system containing high-pressure oxygen which could accelerate

the combustion of nearly all materials including textiles, rubber, oils and even metal [52]. Experimental results could help verify models intended to quantify the benefits of electrochemical compression.

Remaining System issues

Back-Pressure Regulator

The back-pressure regulator of the UND system seems to be operating suspiciously. During the initial testing, a system pressure of 200 psig was attempted however, the regulator was unable to reach greater than 160 psig while maintaining the $\sim 1 \text{ Nm}^3 \text{ hr}^{-1}$ hydrogen flow. During system set-up, the hydrogen system pressure transducer and mass flow meter are monitored while the back-pressure regulator is adjusted. Adjusting the regulator clock-wise increases system pressure. It was found that above ~ 160 psig the mass flow sensor would see reduced flow down to $\sim 0.3 \text{ Nm}^3 \text{ hr}^{-1}$ and not recover. It is normal to see a reduced mass flow when increasing system pressure but once the set-point pressure within the regulator is reached hydrogen flow should recover to $\sim 1 \text{ Nm}^3 \text{ hr}^{-1}$ when operating the stack at 140 A. It should be confirmed that the regulator is operating properly and can achieve the desired system pressure of 200 psig and hydrogen flow rate.

Desiccant Tubes

It is possible that one or both of the desiccant tubes have been jeopardized and may have become wet. In this case PES recommends running the system at ~ 15 A and 200 psig for at least 8 hours to help dry the desiccant. Based on conversations with PES, running the system at low current and high pressure will minimize the amount of water vapor into the desiccant tubes while continually purging the tubes with dry hydrogen.

The back-pressure regulator will need to be adjusted to achieve the recommended hydrogen system pressure of 200 psig at 15 A. The orifice in the desiccant system is designed to achieve a flow of $\sim 0.1 \text{ Nm}^3 \text{ hr}^{-1}$ at this pressure which represents 10 % of the product at full stack current (140 A). Therefore, running at 10 % of the full stack current at 200 psig will produce the desired flow of hydrogen for desiccant drying during this recovery procedure.

Dew Point Sensor

The system dew point sensor has not been verified which may stem from the potentially wetted desiccant explained above. The range of the sensor is 20°C down to -60°C and PES expects the desiccant system to produce hydrogen product near the low-end of this dew point range. However, the preliminary trials witnessed the dew point sensor latched at -80°C which, according to the unit's operating manual, indicates a problem. Verification of sensor power, connectors and data acquisition wiring would be the first step in troubleshooting the problem.

Vent Valve

The normally open solenoid valve on the hydrogen phase separator manifold may be partially blocked. Conversations with PES confirm that the UND system is witnessing slower than normal decay rate of the hydrogen system pressure at shutdown. Small diameter debris was found in the manifold and also near the solenoid valve as shown in Figure 39. A small orifice, located in this manifold, is used to reduce the flow of high-pressure hydrogen upon shutdown and could have become partially blocked by this debris. It is very possible that the debris is desiccant from the drying system that could have found its way to the vent manifold while a tee was located between the desiccant

tube output and a check valve (not shown in Figure 39) on the manifold. PES has since deemed this tee unnecessary and it was removed from the UND system.

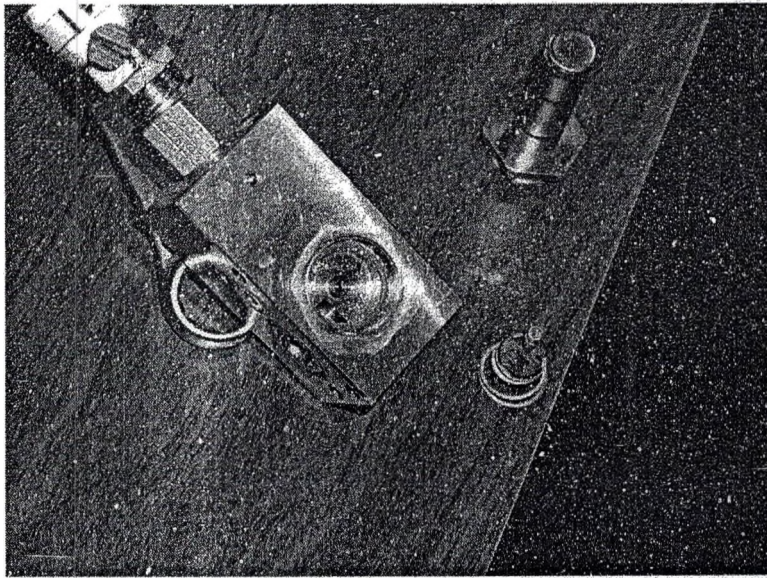


Figure 39. Debris found in hydrogen phase separator that could be partially blocking the vent orifice at shutdown.

APPENDICES

APPENDIX A
Wiring Diagrams

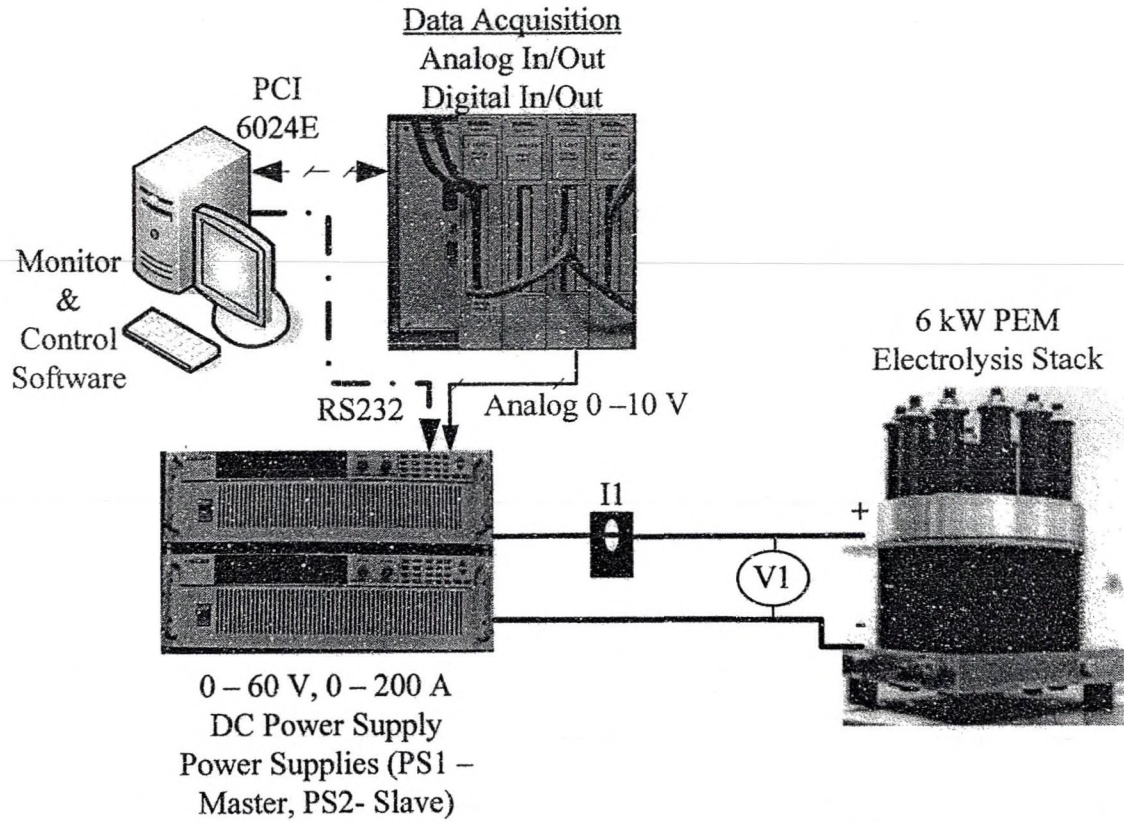


Figure 40. Fundamental components of system monitoring, control and power to PEM stack.

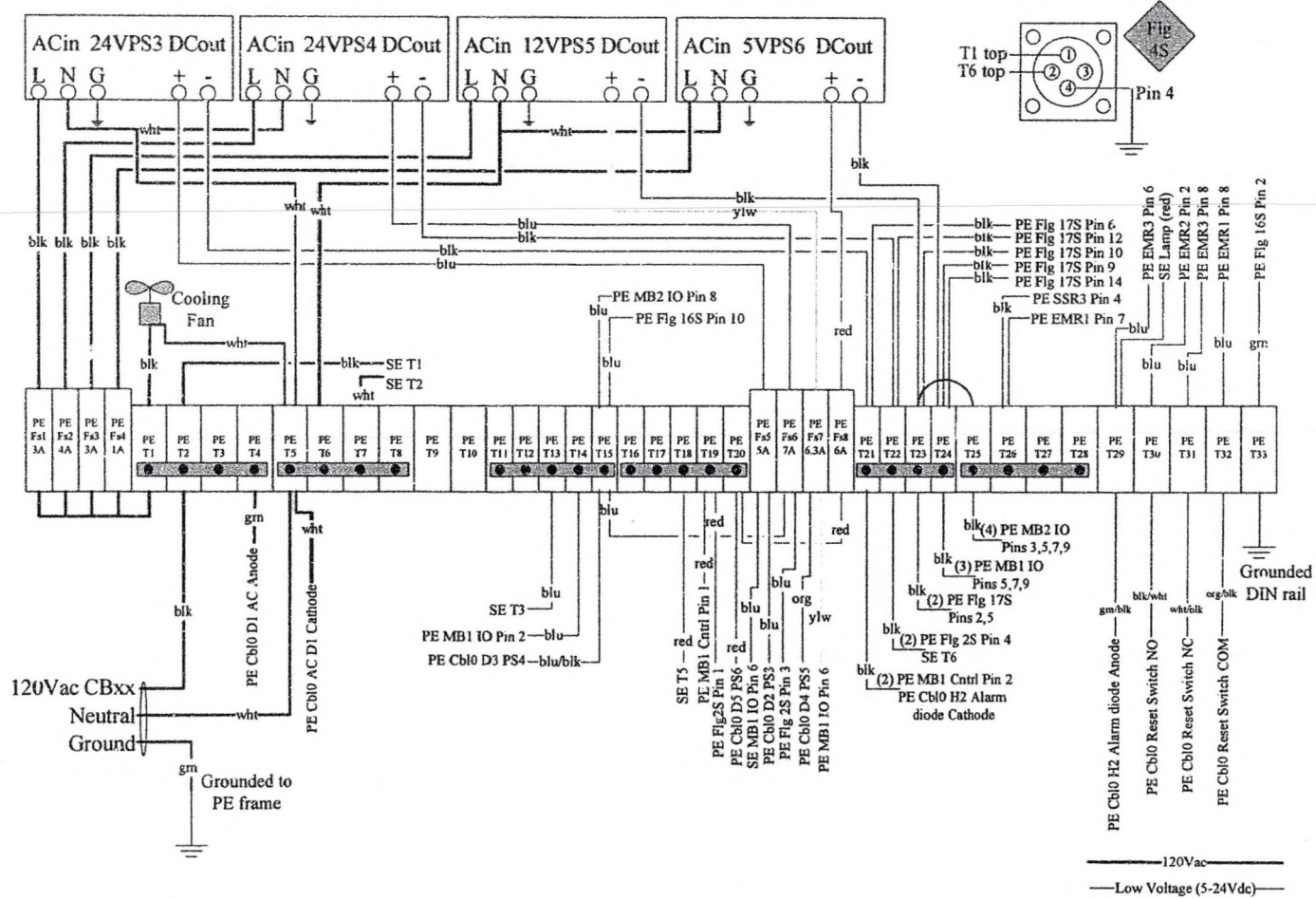


Figure 41. Power enclosure (PE) power supply, terminal and fuse wiring.

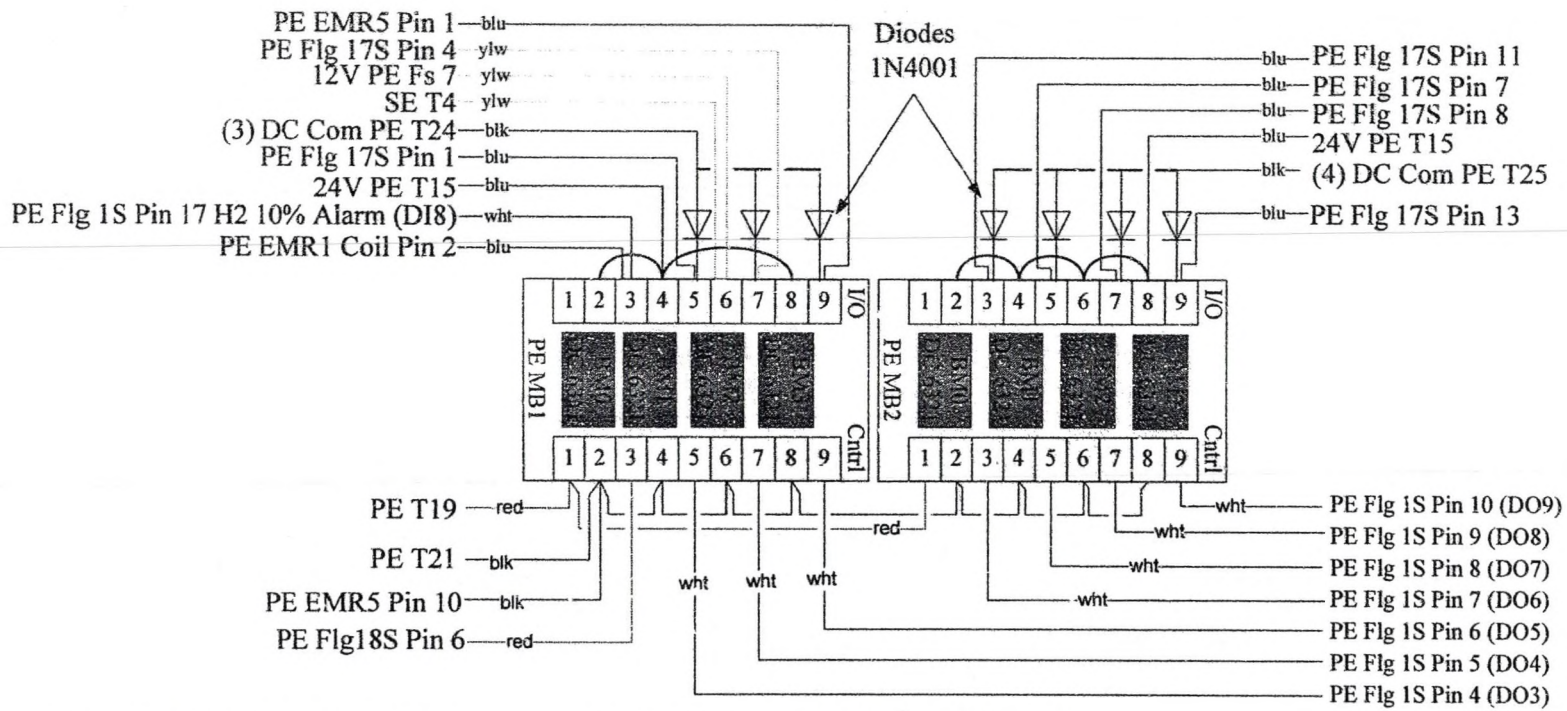


Figure 42. Power enclosure (PE) buffer module (BM) mounting board (MB) wiring.

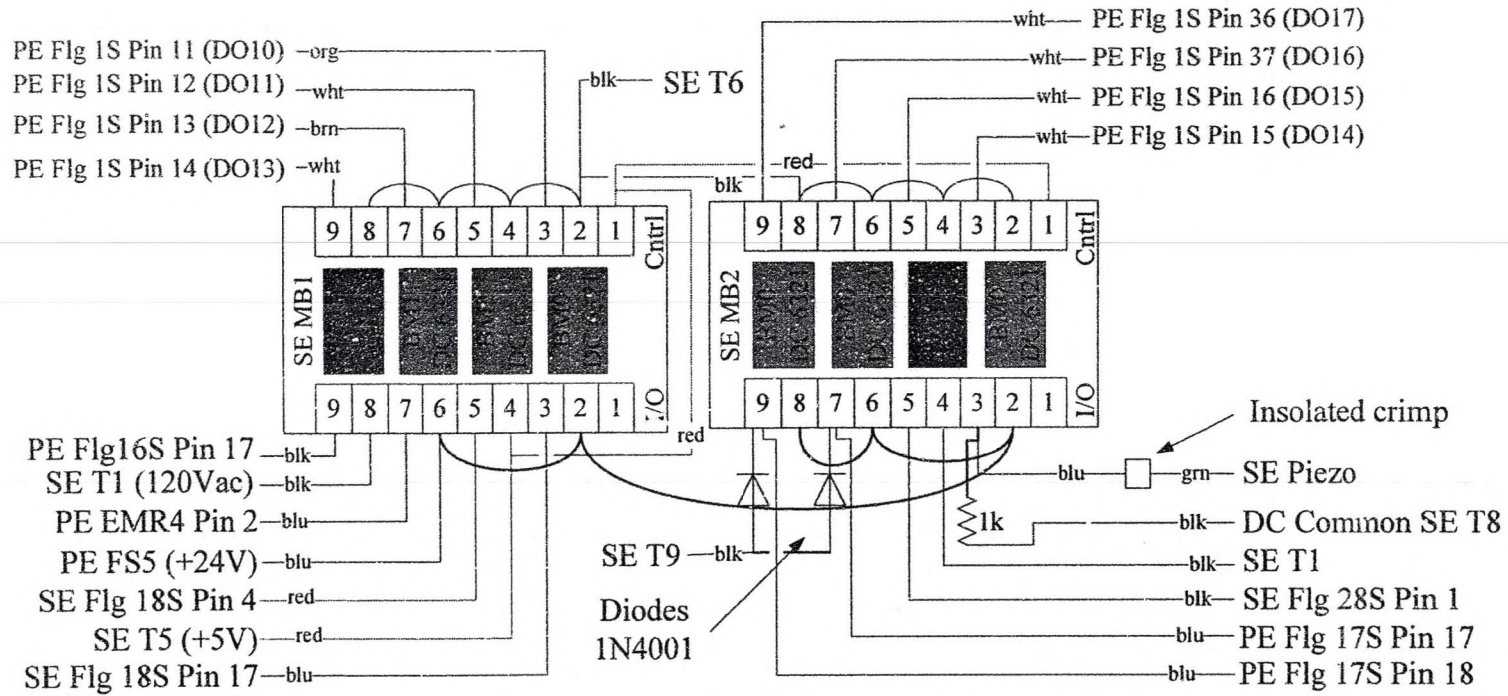
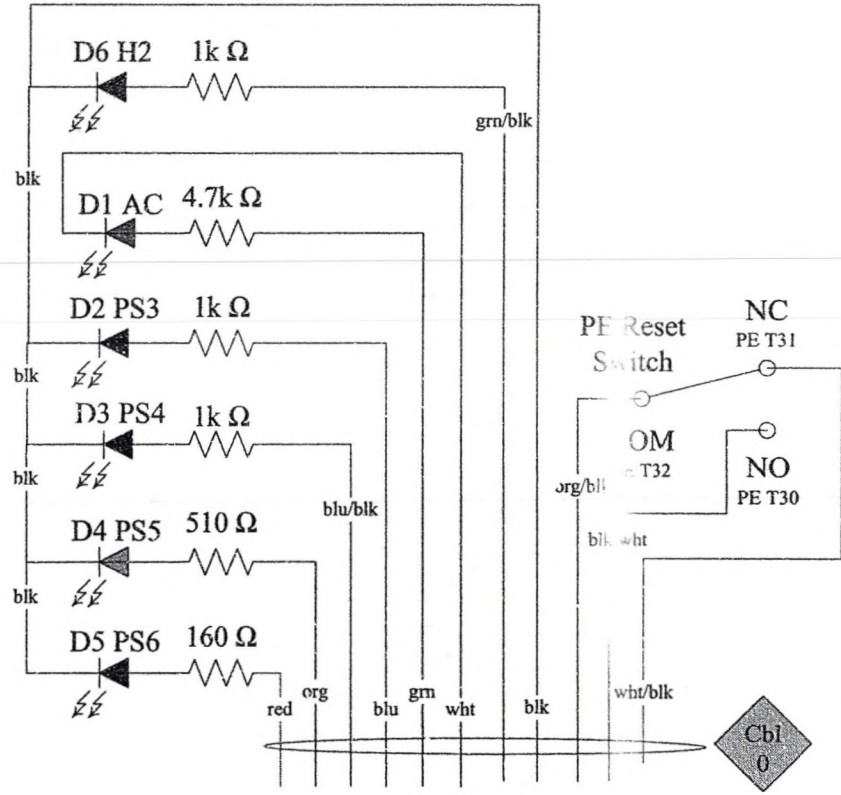
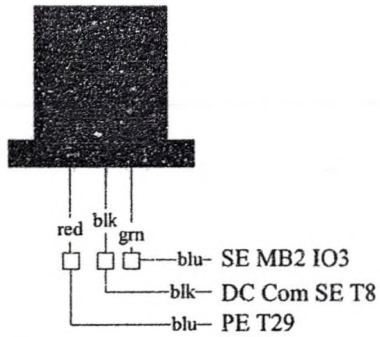
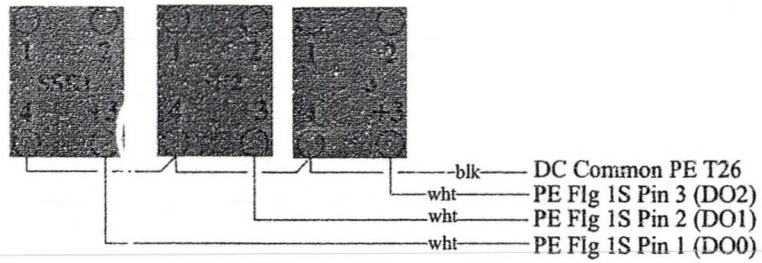


Figure 43. Sensor enclosure (SE) buffer module (BM) mounting board (MB) wiring.



Power Enclosure cable from terminals to door diodes & Reset Switch

Figure 44. Sensor and power enclosure devices.

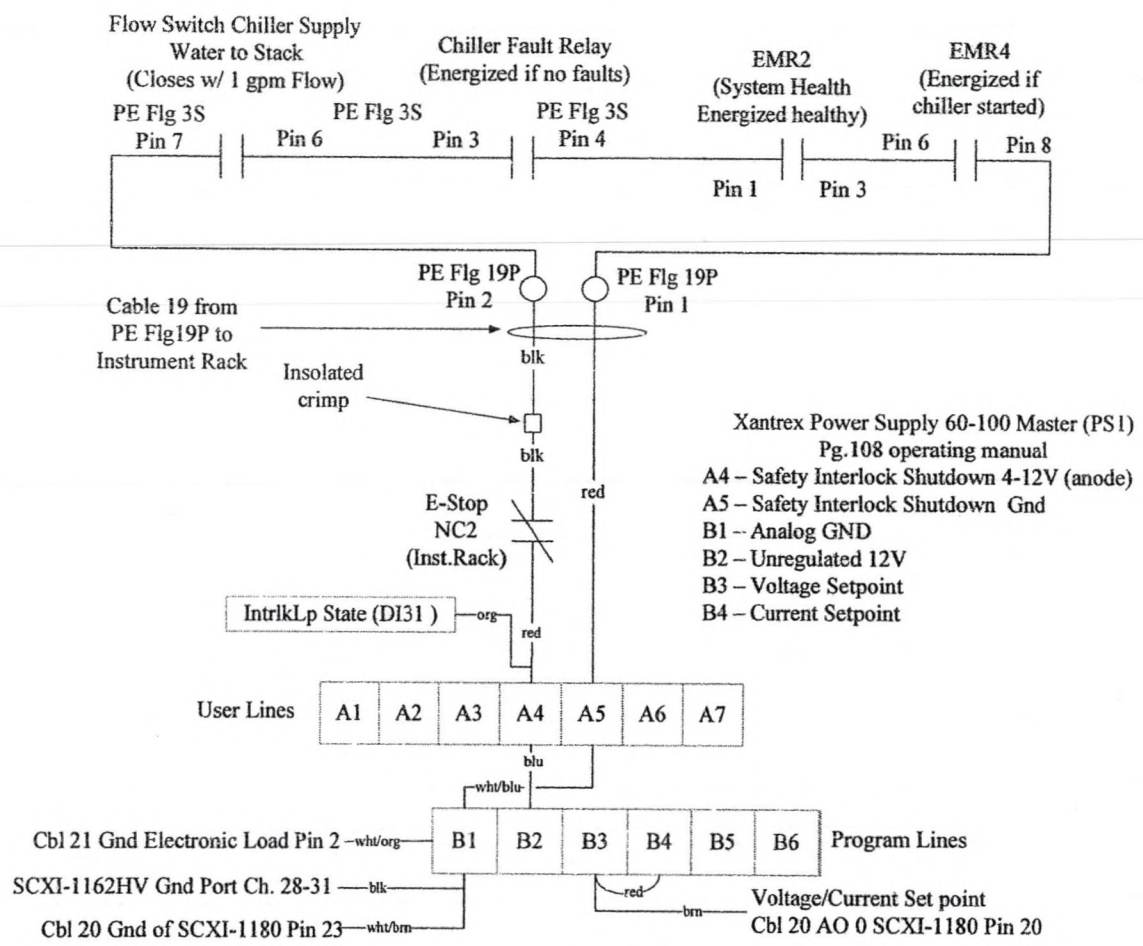


Figure 46. Interlock loop wiring showing user and program lines of PS1.

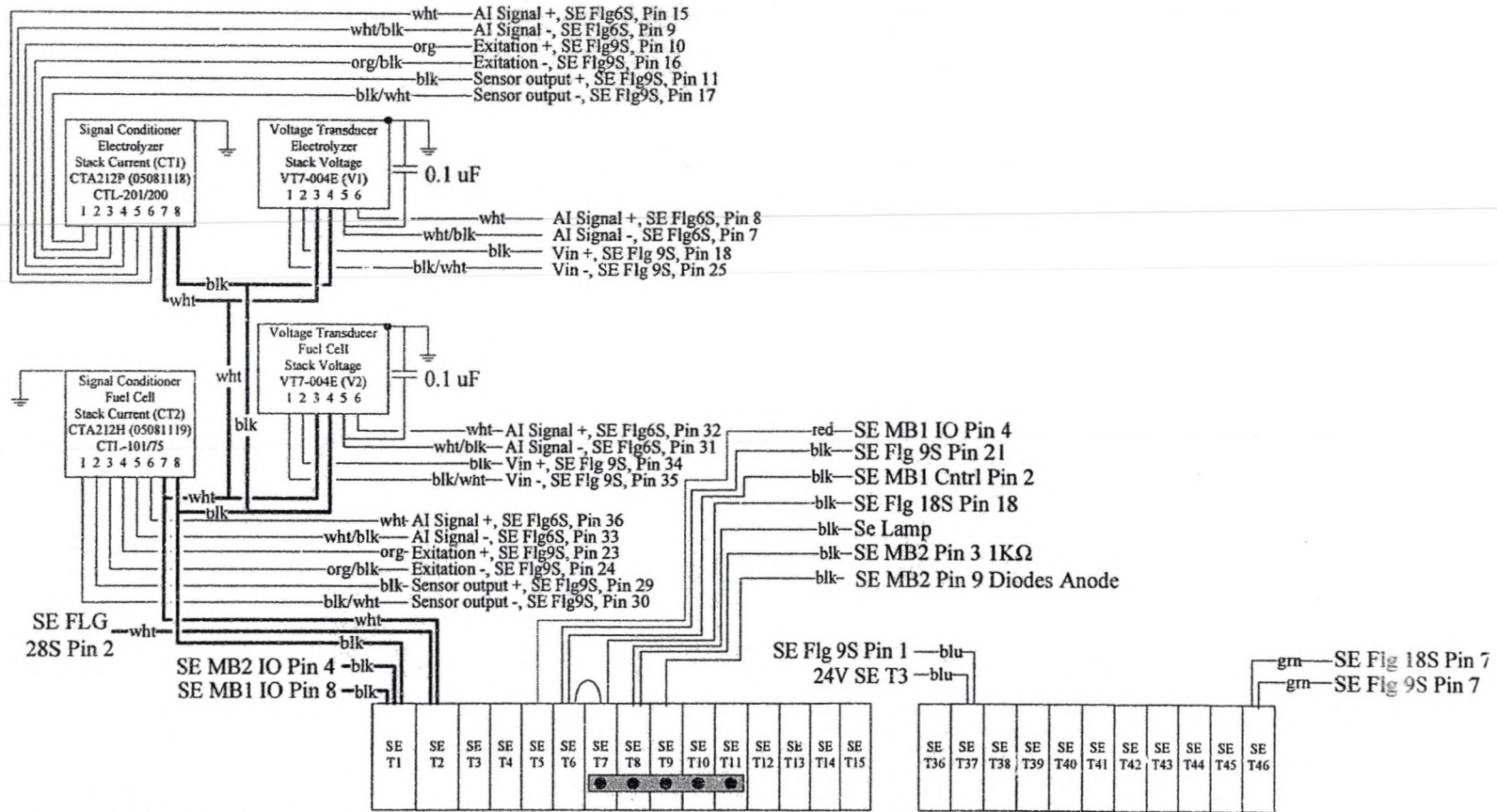


Figure 47. Sensor enclosure (SE) terminal, current and voltage sensor wiring

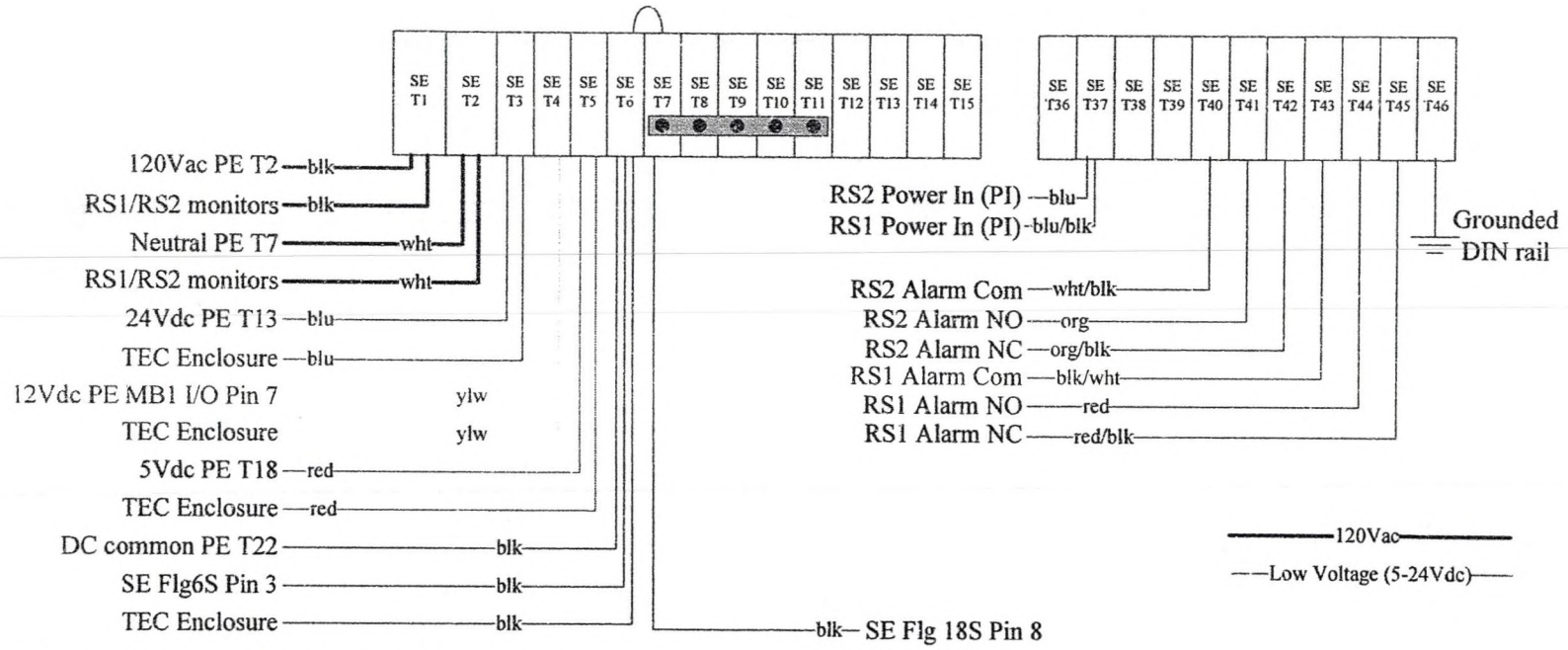


Figure 48. Sensor enclosure (SE) terminal wiring continued.

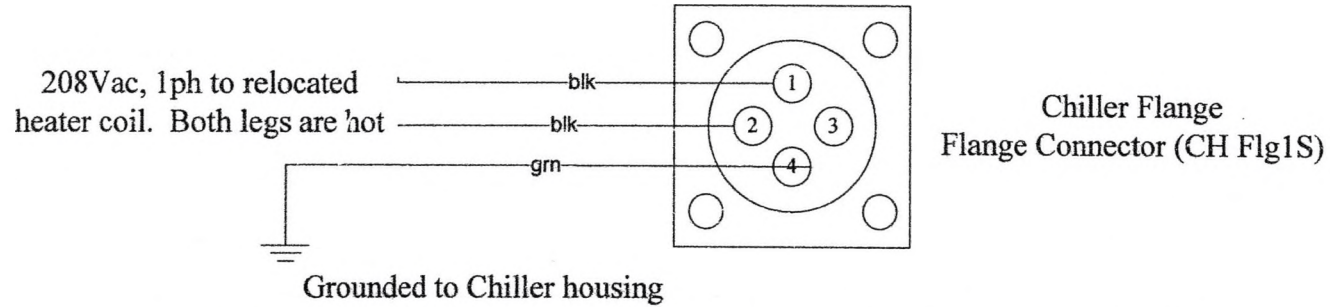
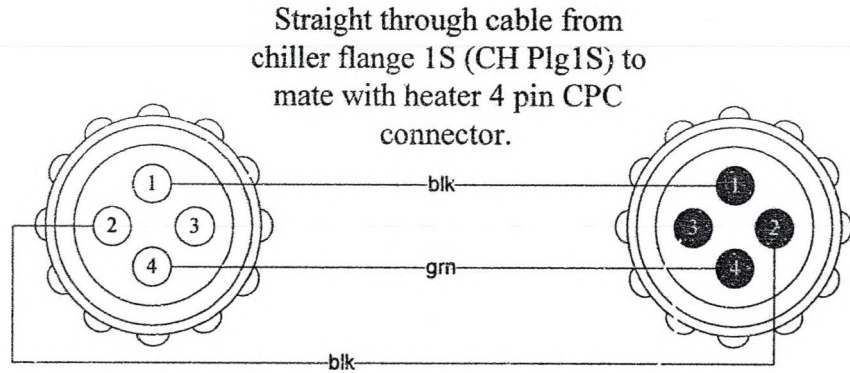
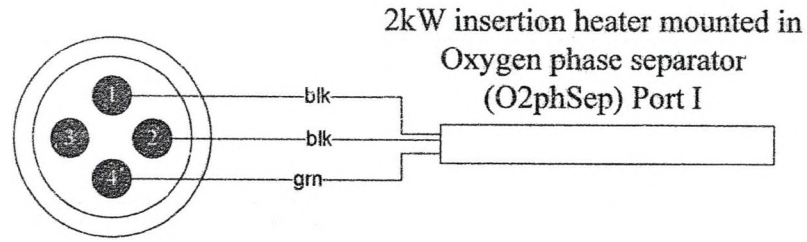


Figure 49. Chiller heater extension wiring to CH Flg 1 to accommodate 2 kW heater relocation.

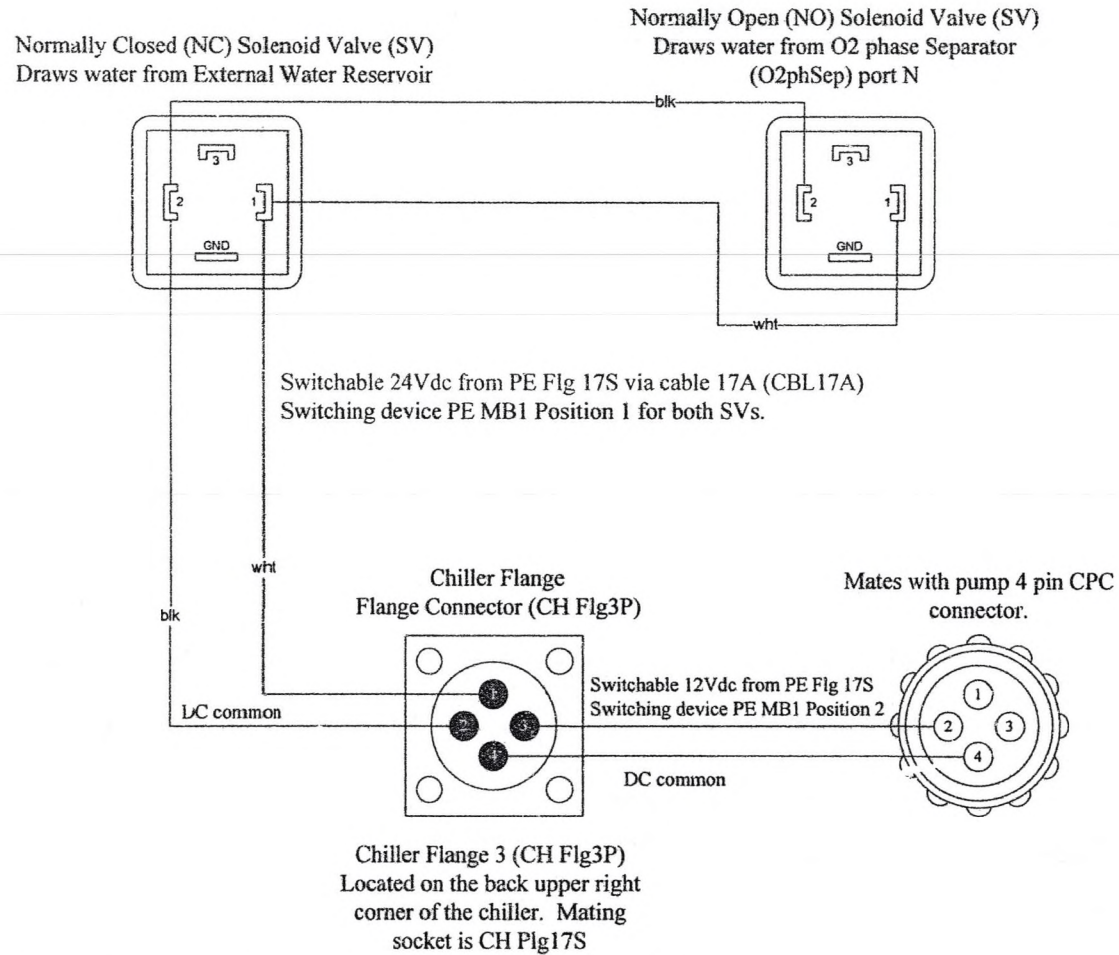


Figure 50. External water loop solenoid valves CH Flg3.

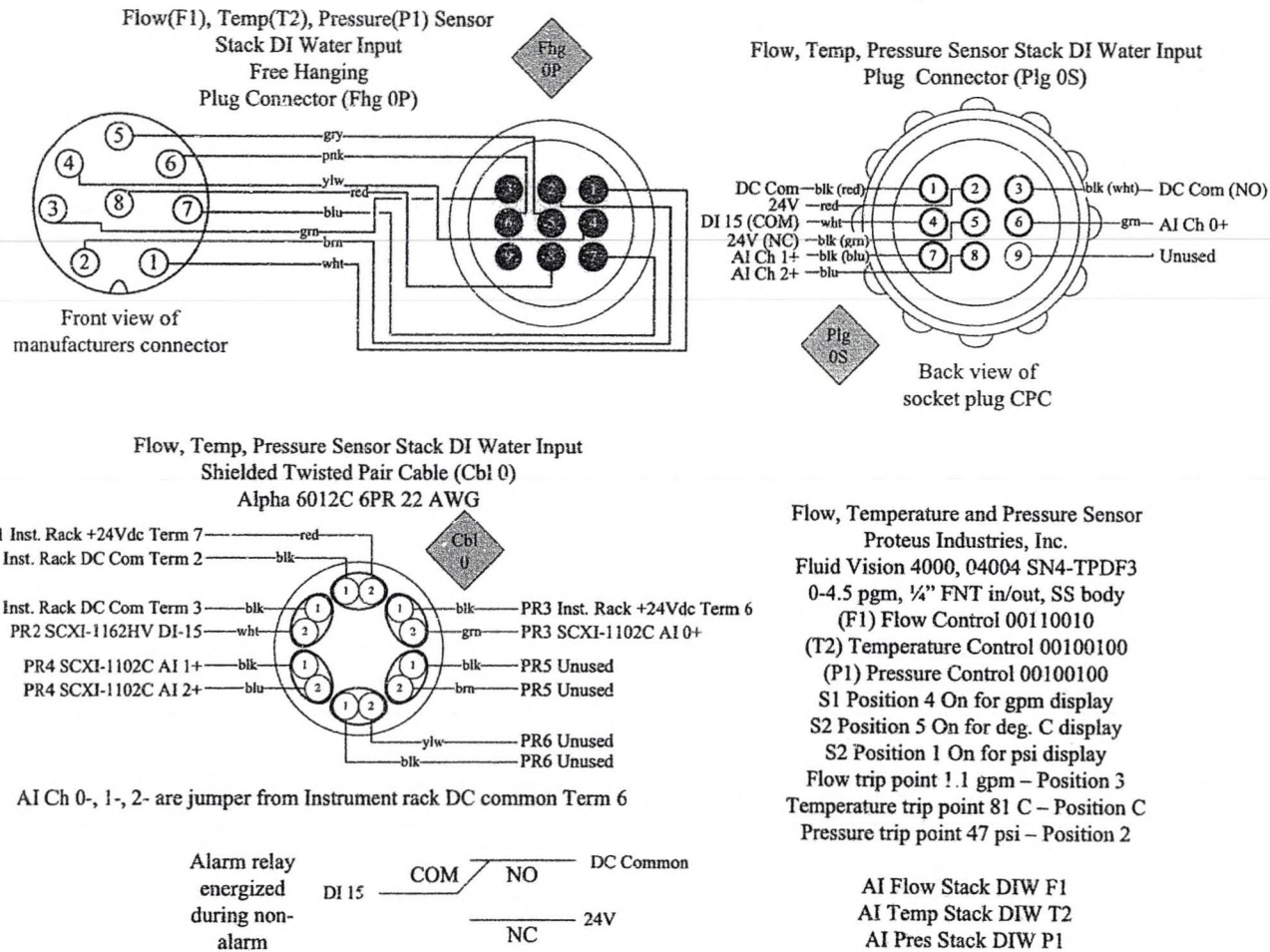
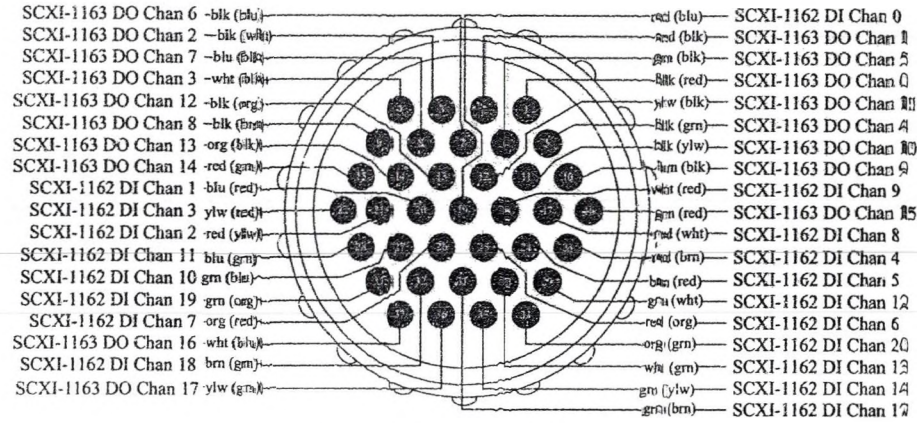
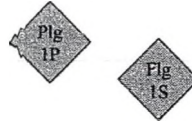


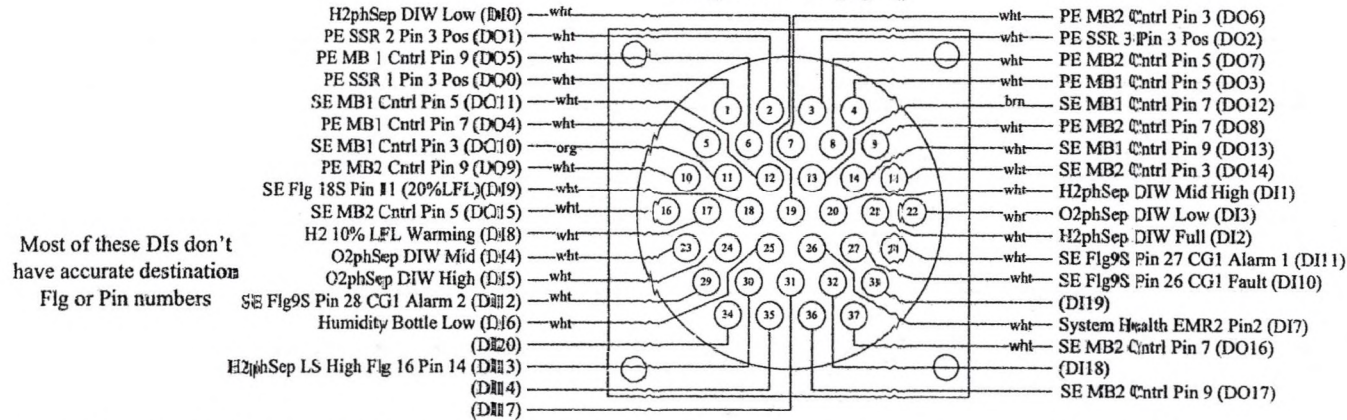
Figure 51. Flow, temperature and pressure sensor cable wiring and configuration.



From Power Enclosure to SCXI-1163/62
Plug Connector (Plg 1P)



Power Enclosure DI / DO
Flange Connector (Flg 1S)



Most of these DIs don't
have accurate destination
Flg or Pin numbers

Figure 52. Analog input cable Flange1 (Flg 1) wiring from power enclosure to instrument rack.



DI/DO Cable to SCXI-1162HV/63
 Unshielded Cable (Cbl 1)
 Belden 9748 19PR 22 AWG

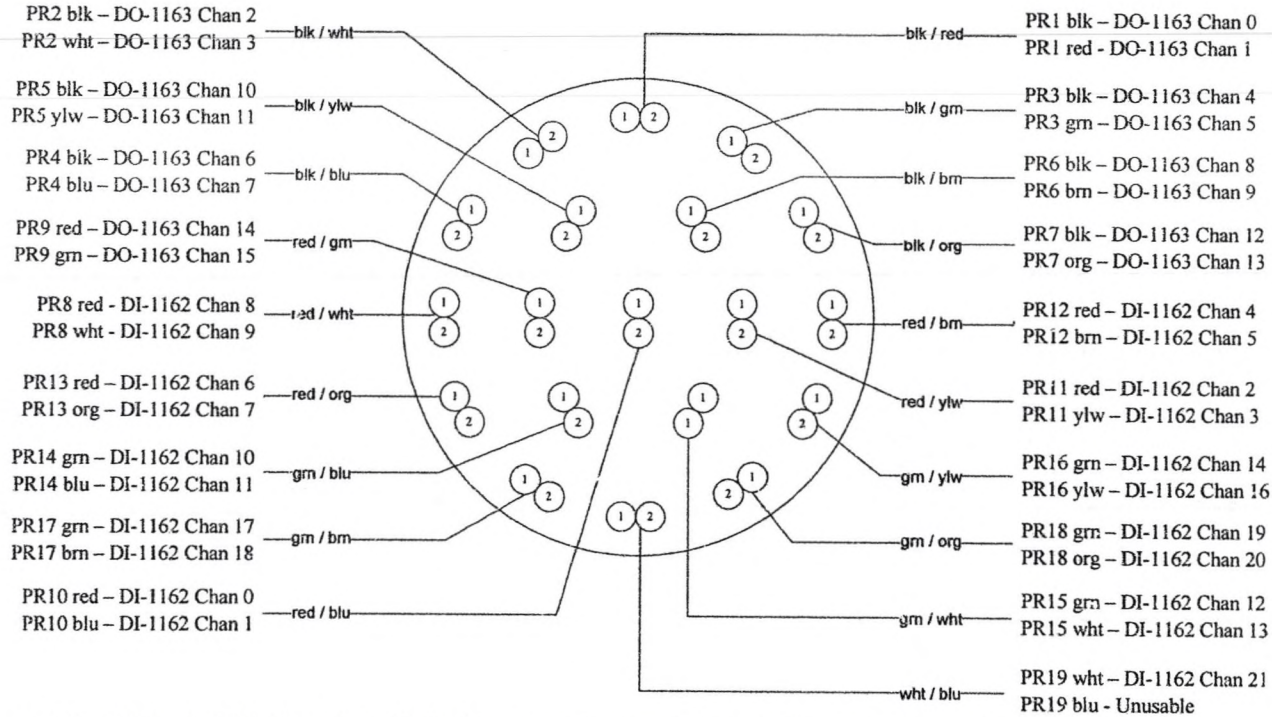


Figure 53. Cable 1 (Cbl 1) carrying digital input and output signals from power enclosure to instrument rack.

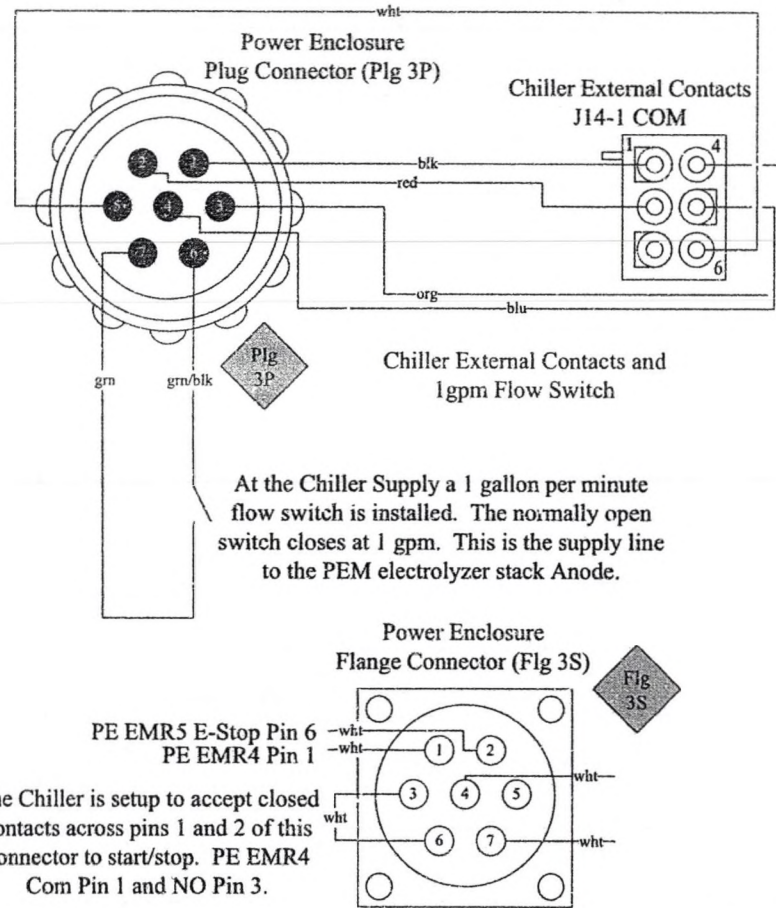
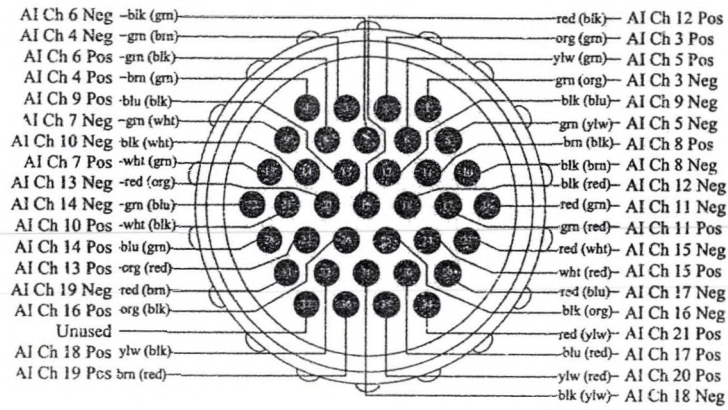


Figure 54. Chiller external contacts and flow switch wiring as part of the interlock loop.



FUTURE: If want to monitor FC regulator out (Anode) pressure. You will have to run individual cable back to SCXI-1102C module. No wires left in SE Flg/Cbl 6 AI signals from SE to SCXI-1102C.



Sensor Enclosure to SCXI-1102C Plug Connector (Plg 6P)

Sensor Enclosure AI signals to SCXI-1102C Flange Connector (Flg 6S)

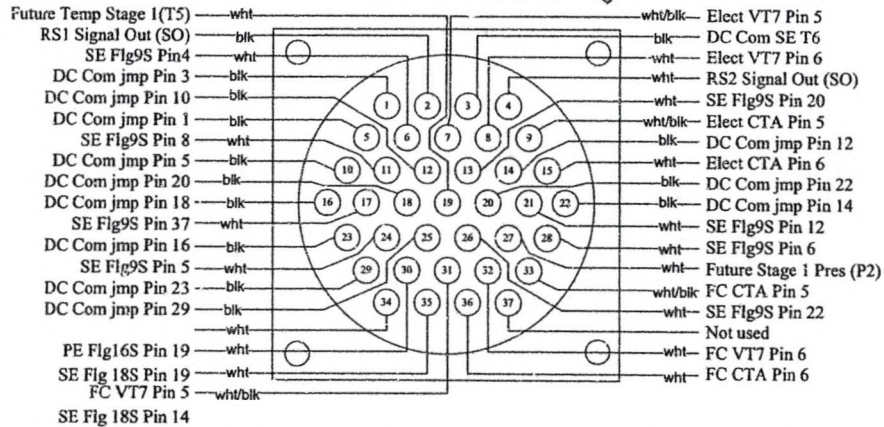


Figure 55. Plug and flange 6 (Plg/Flg 6) wiring assembly. Analog input signals from power enclosure (PE) to instrument rack and internal flange wiring of power enclosure (PE).

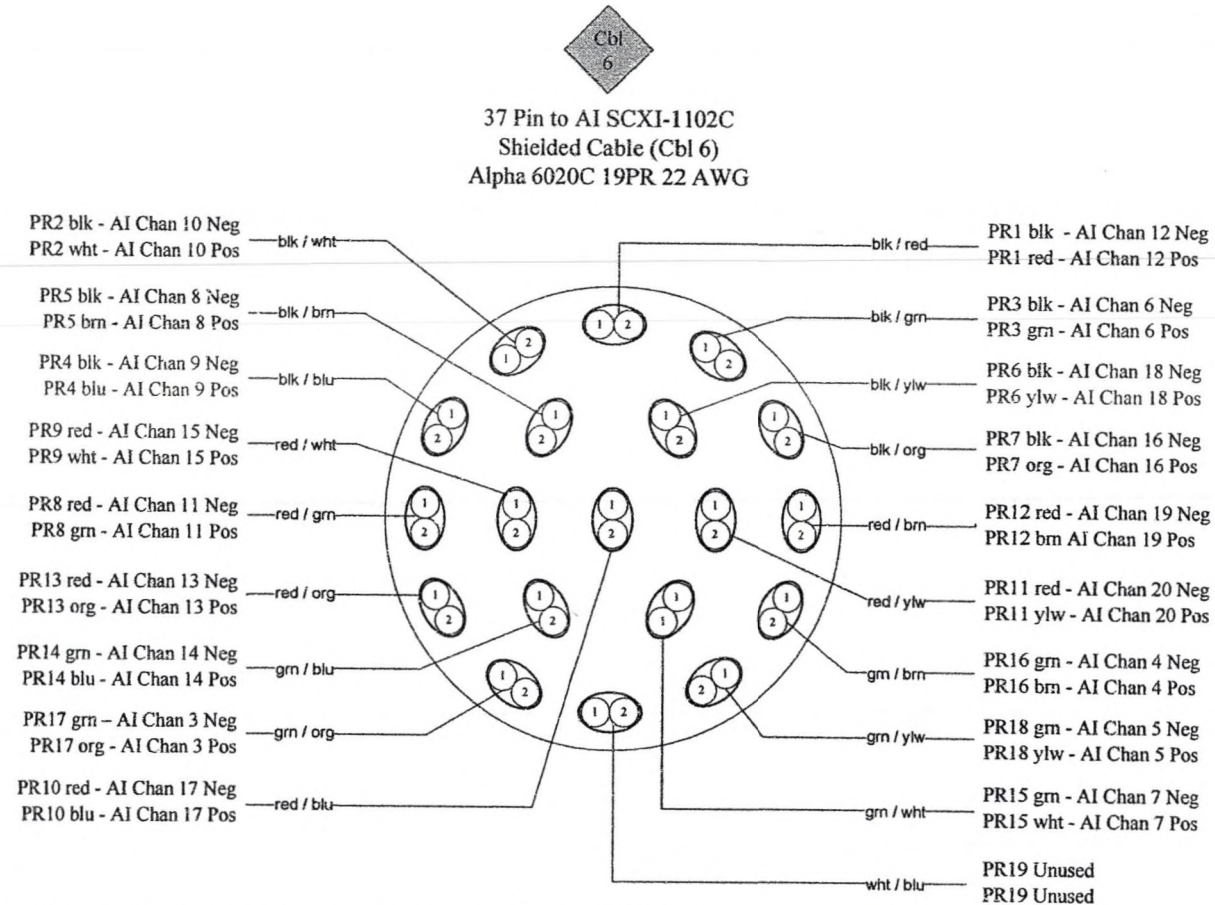


Figure 56. Analog input cable wiring Cable 6 (Cbl 6).

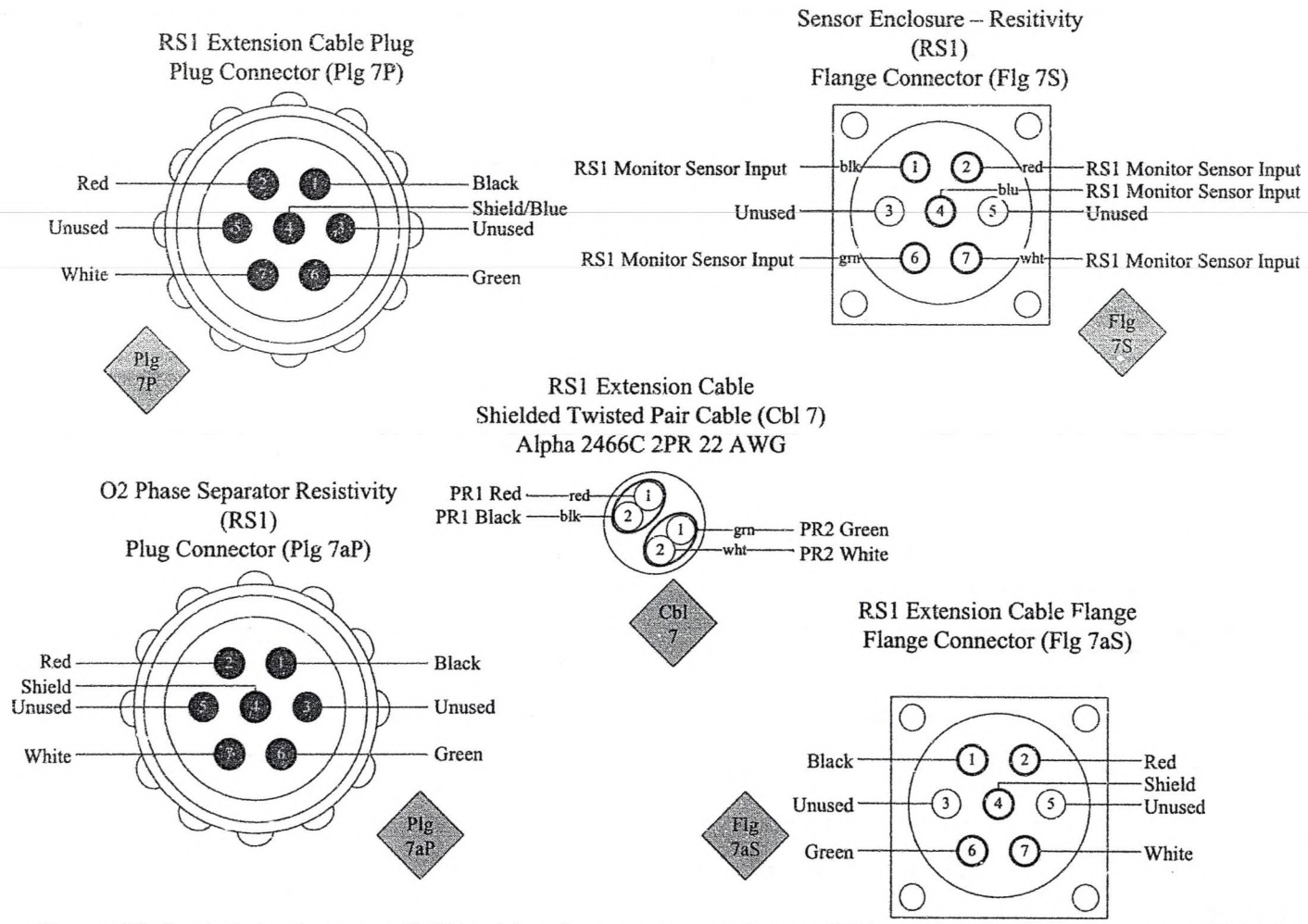


Figure 57. Resistivity 1 sensor (RS1) wiring from sensor enclosure (SE) to oxygen phase separator (O2phSep).

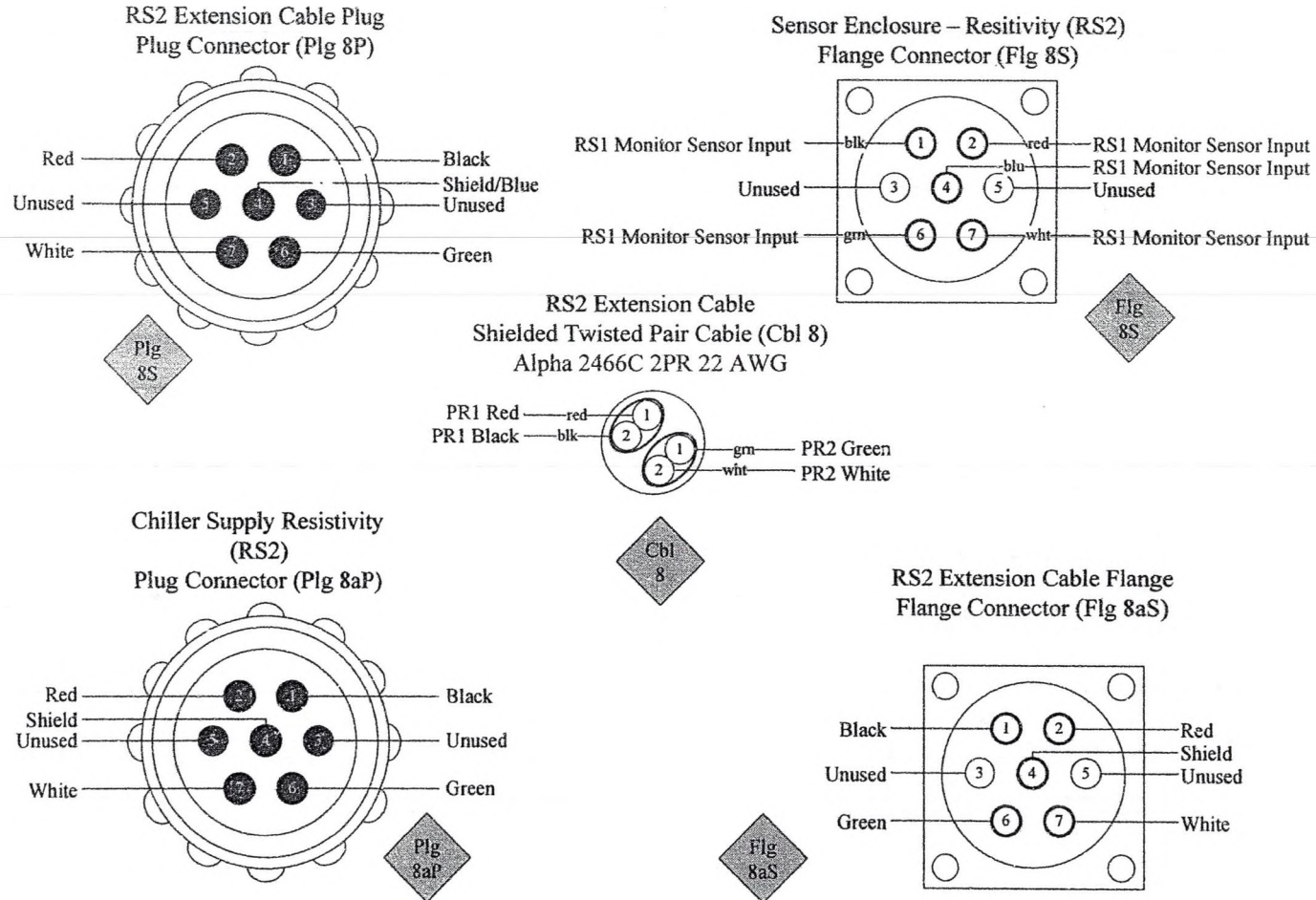
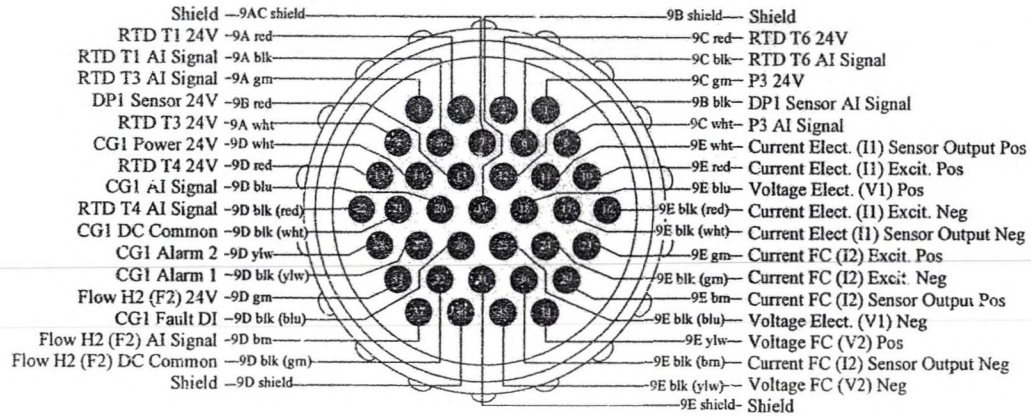


Figure 58. Resistivity 2 sensor (RS2) wiring from sensor enclosure (SE) to oxygen phase separator (O2phSep).



Plg 9P Analog Inputs -Sensor Enclosure Plug Connector (Plg 9P)

Flg 9S Analog Inputs - Sensor Enclosure Flange Connector (SE Flg 9S)

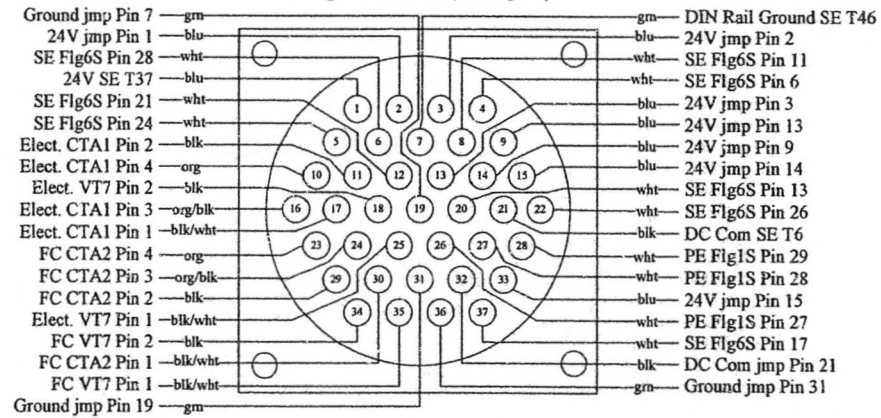
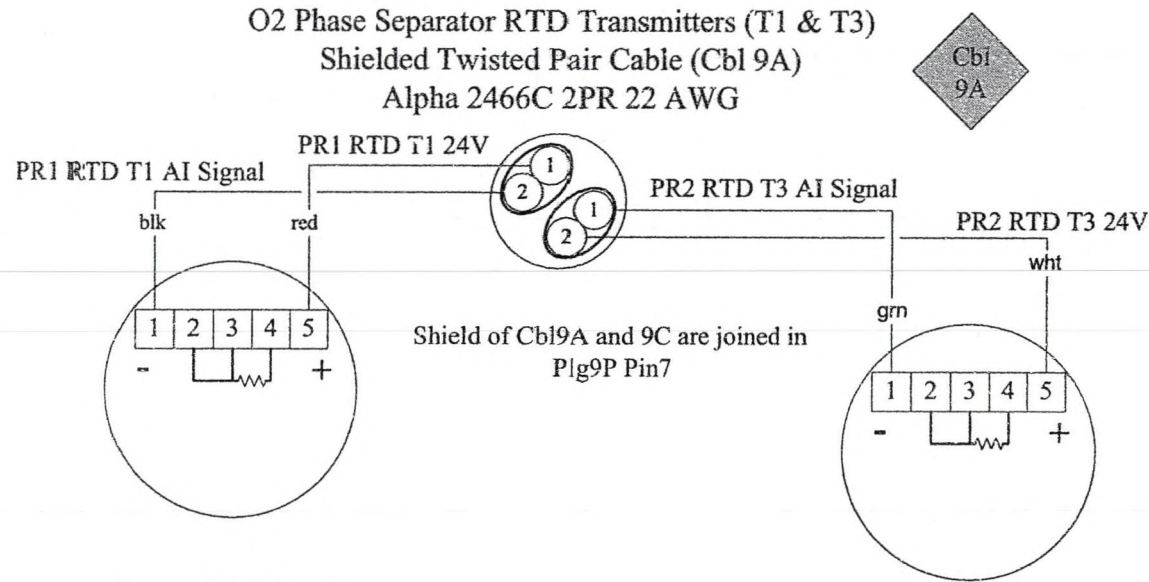


Figure 59. Plug and flange 9 wiring assembly (Plg/Flg 9).



Temp O2phSep T1
 Pt 100Ω ($\alpha=0.00385$) 3-wire RTD Transmitter
 Supply Voltage 10-36V Supply Current 28mA
 Switch settings 100101 (TX254)
 Calibrated 0 to 100°C on March 1, 2006

Temp Stack DIW out T3
 Pt 100Ω ($\alpha=0.00385$) 3-wire RTD Transmitter
 Supply Voltage 10-36V Supply Current 28mA
 Switch settings 100101 (TX254)
 Calibrated 0 to 100°C on March 1, 2006

Figure 60. Oxygen phase separator (O2phSep) temperature sensors (T1, T3) wiring and configuration (Cbl 9A).

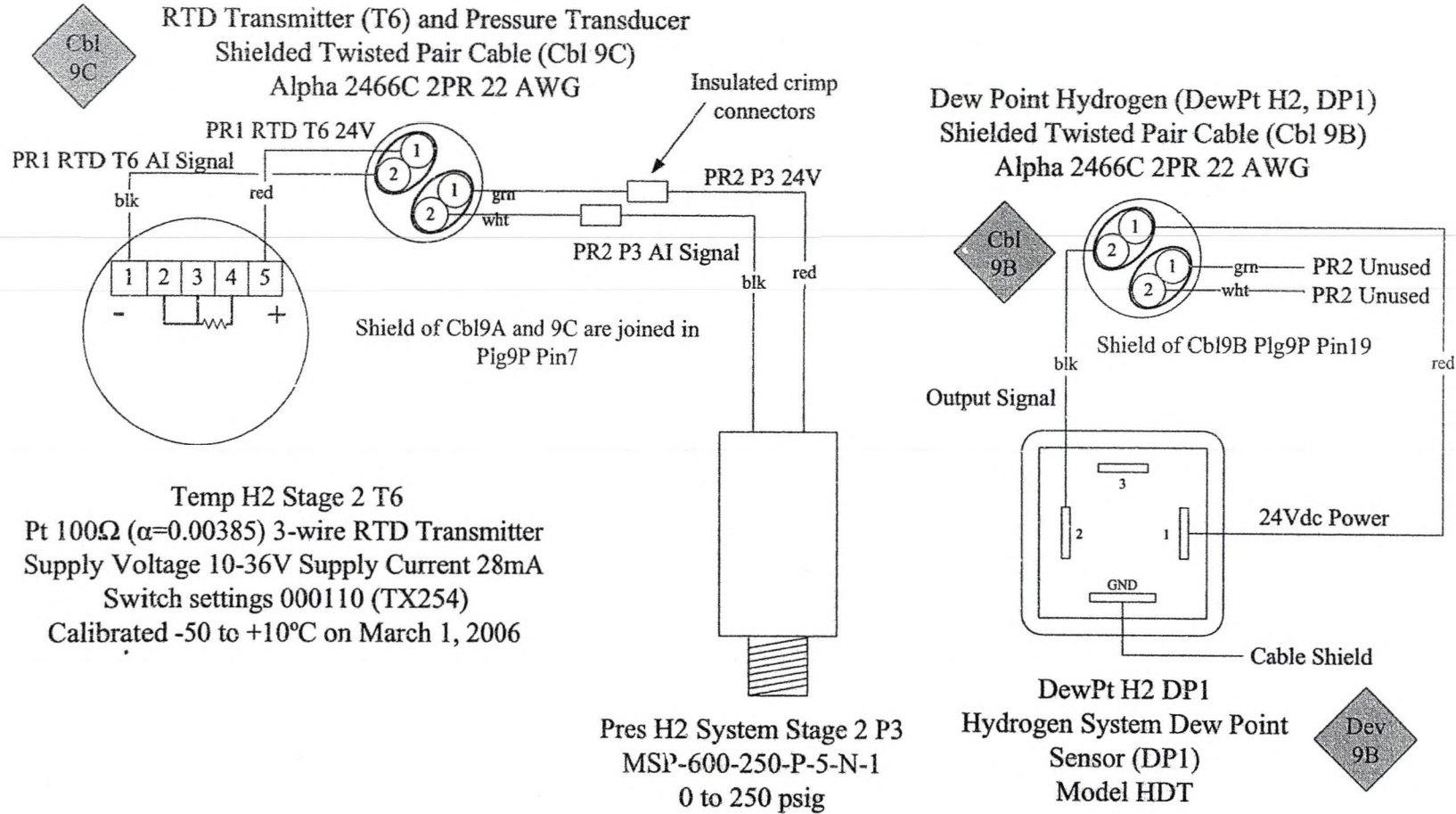
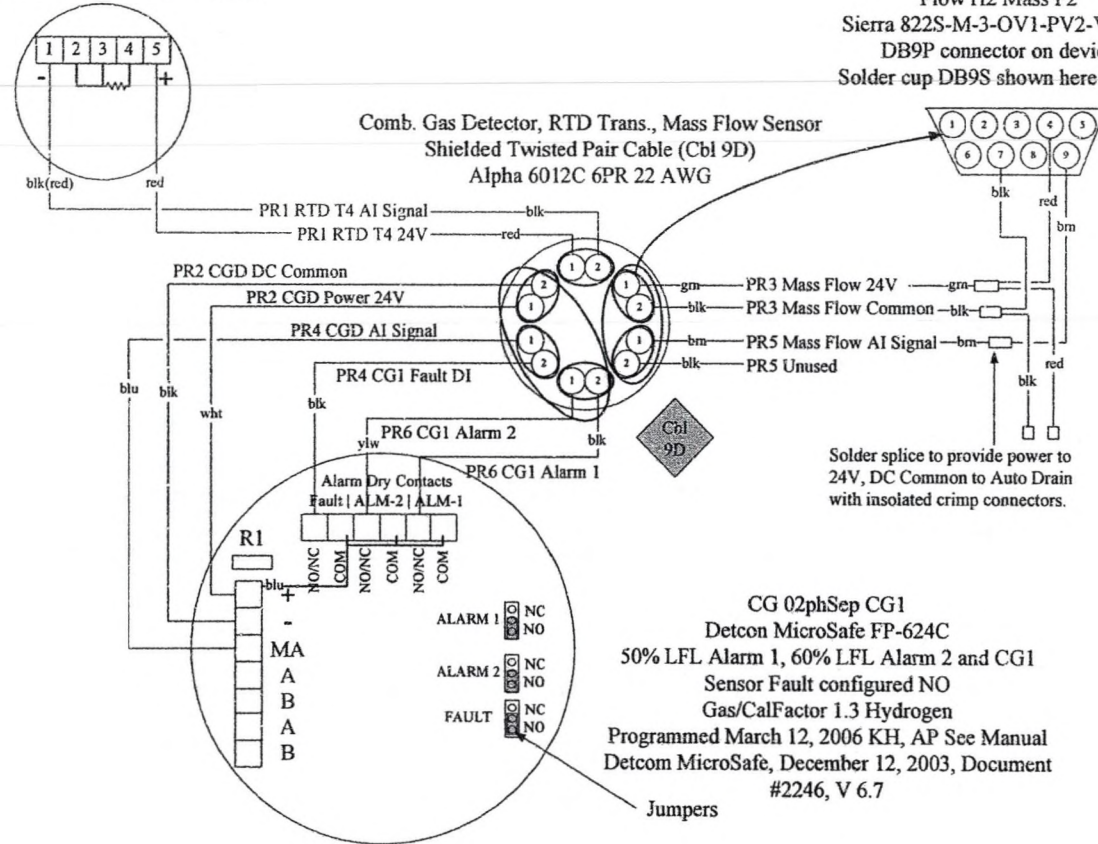


Figure 61. Pressure (P3), temperature (T6), and dew point (DP1) sensor wiring (Cbl 9B,C and Dev 9B).

Temp H2 System T4
 Pt 100Ω ($\alpha=0.00385$) 3-wire RTD Transmitter
 Supply Voltage 10-36V Supply Current 28mA
 Switch settings 100101 (TX254)
 Calibrated 0-100°C on March 1, 2006

Flow H2 Mass F2
 Sierra 822S-M-3-OV1-PV2-V4-HP
 DB9P connector on device
 Solder cup DB9S shown here (back)

Comb. Gas Detector, RTD Trans., Mass Flow Sensor
 Shielded Twisted Pair Cable (Cbl 9D)
 Alpha 6012C 6PR 22 AWG



Solder splice to provide power to 24V, DC Common to Auto Drain with insulated crimp connectors.

CG 02phSep CG1
 Detcon MicroSafe FP-624C
 50% LFL Alarm 1, 60% LFL Alarm 2 and CG1
 Sensor Fault configured NO
 Gas/CalFactor 1.3 Hydrogen
 Programmed March 12, 2006 KH, AP See Manual
 Detcom MicroSafe, December 12, 2003, Document #2246, V 6.7

Figure 62. Temperature (T4), combustible gas detector (CG1) and electrolyzer hydrogen flow (F2) wiring and configuration (Cbl 9D).

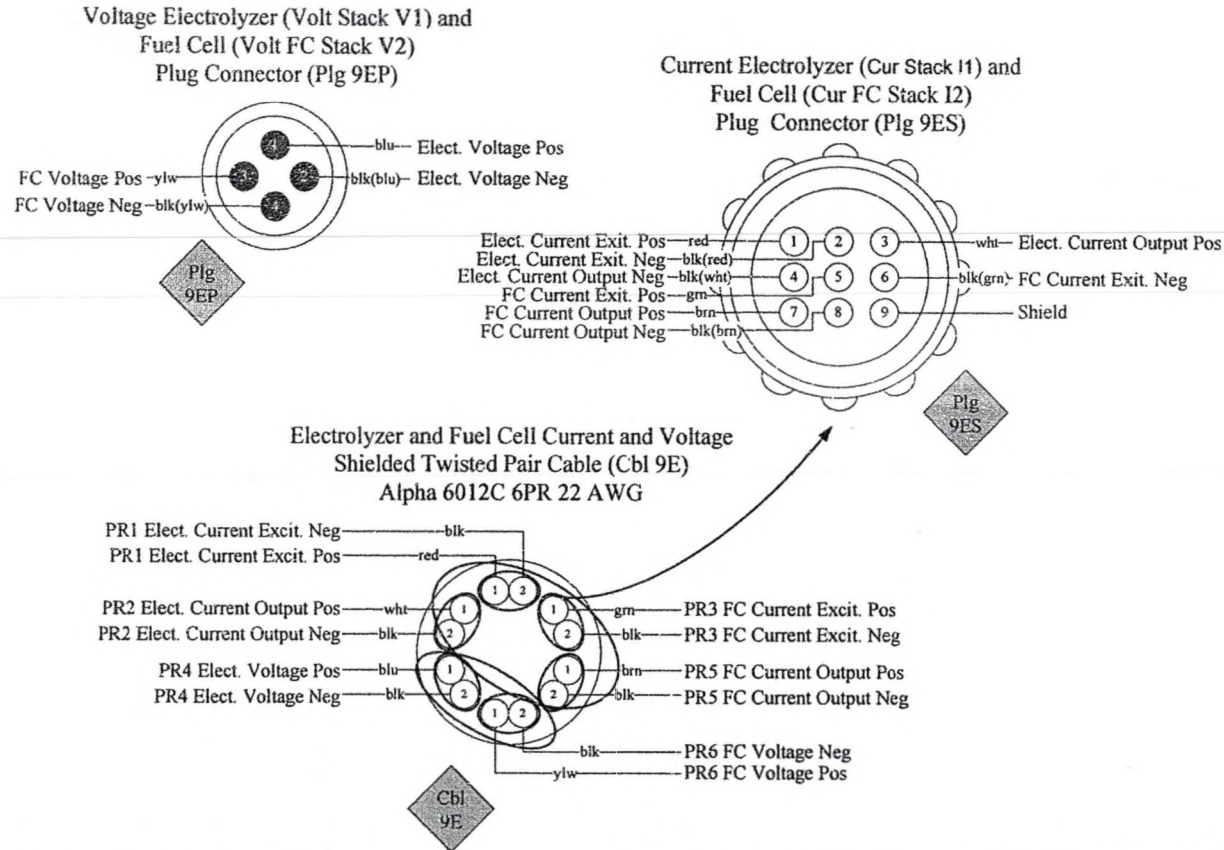


Figure 63. Electrolyzer voltage and current (V1, I1) and fuel cell voltage and current (V2, I2) wiring (Plg9E P/S, Cbl 9E).

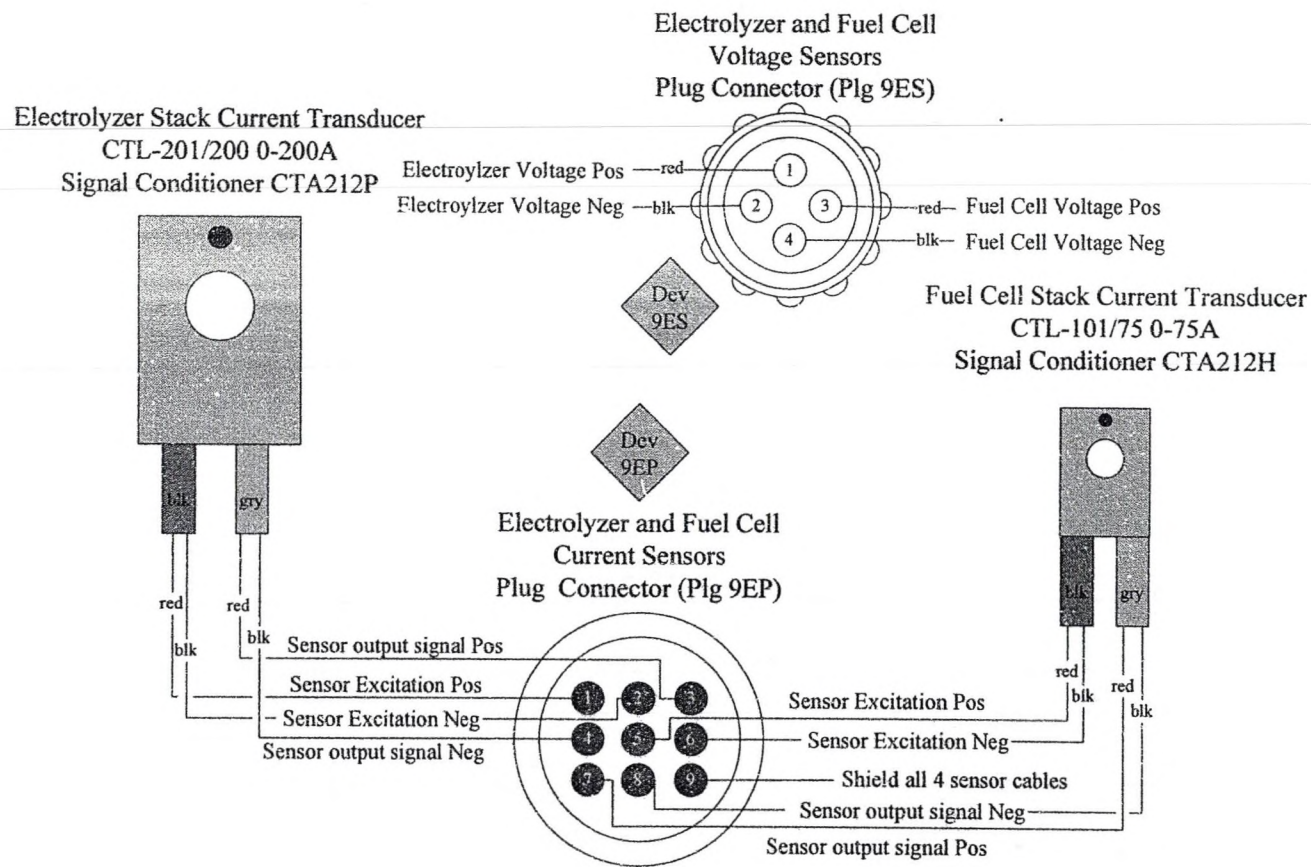


Figure 64. Electrolyzer and fuel cell hall-effect current transducers and voltage device wiring (Plg 9E S/P).

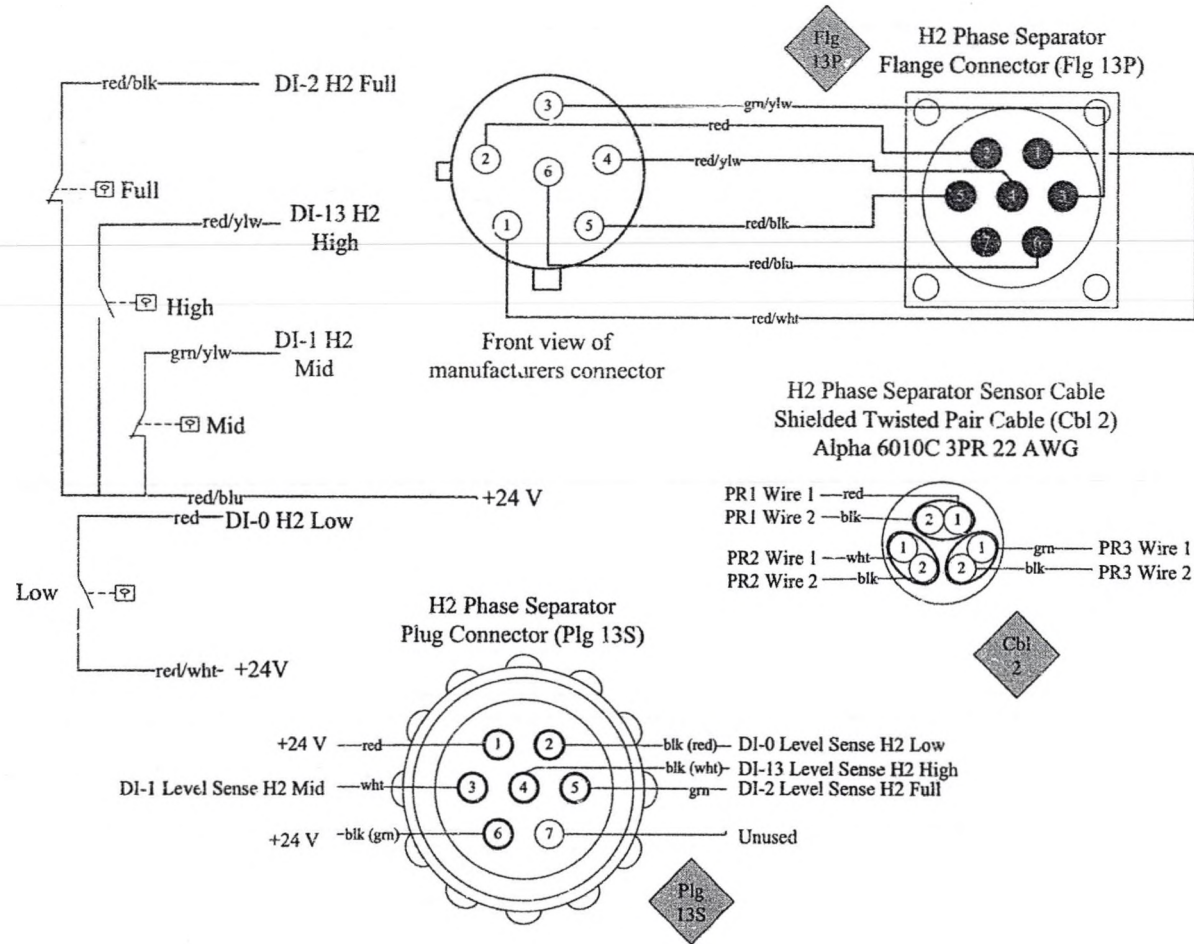


Figure 65. Hydrogen phase separator (H2phSep) level sense wiring and float orientation (Flg/Plg 13, Cbl 2).

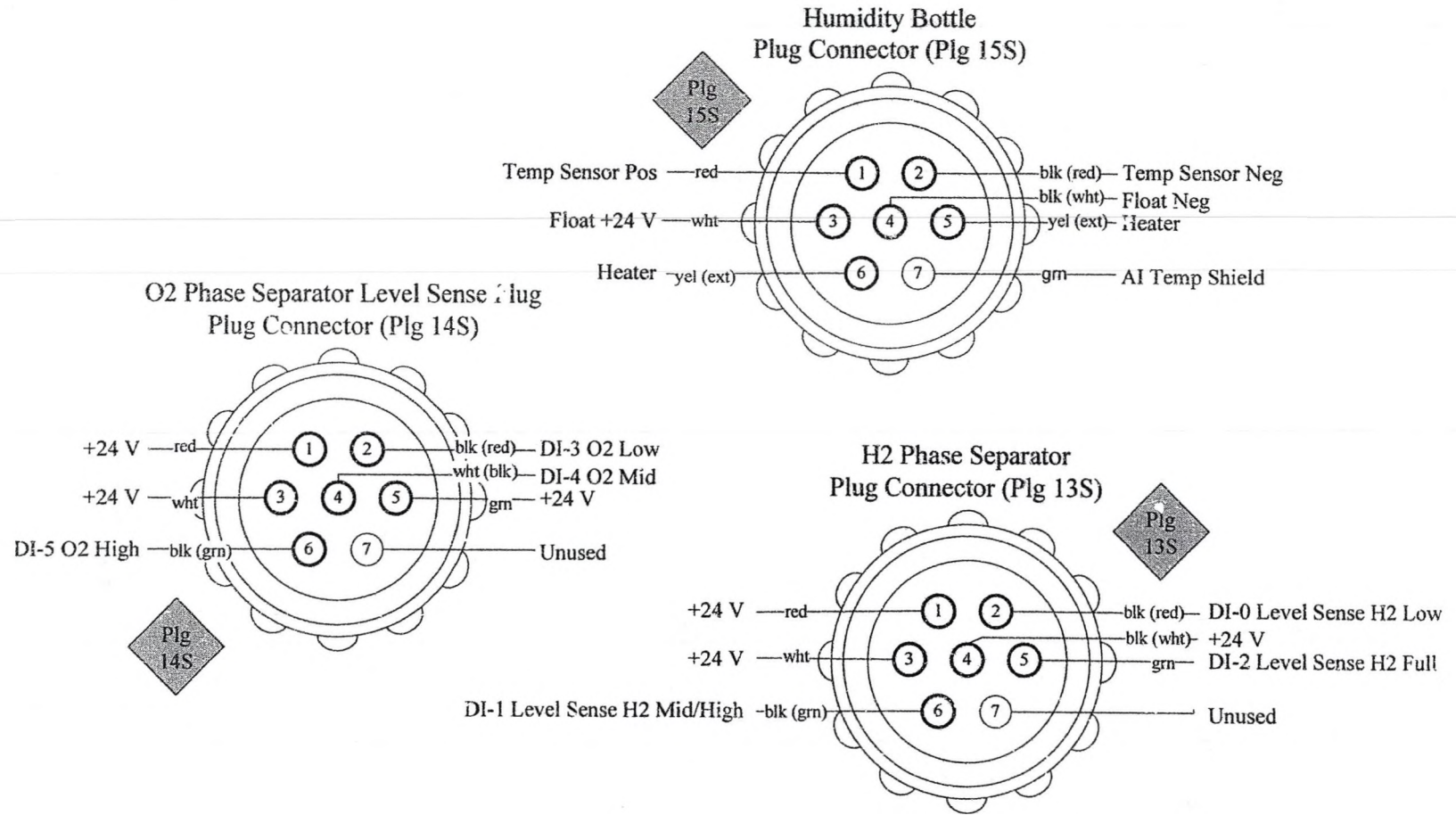


Figure 66. Oxygen phase separator (O2phSep) level sense, hydrogen phase separator and humidity bottle device wiring (Plg13 – 15).

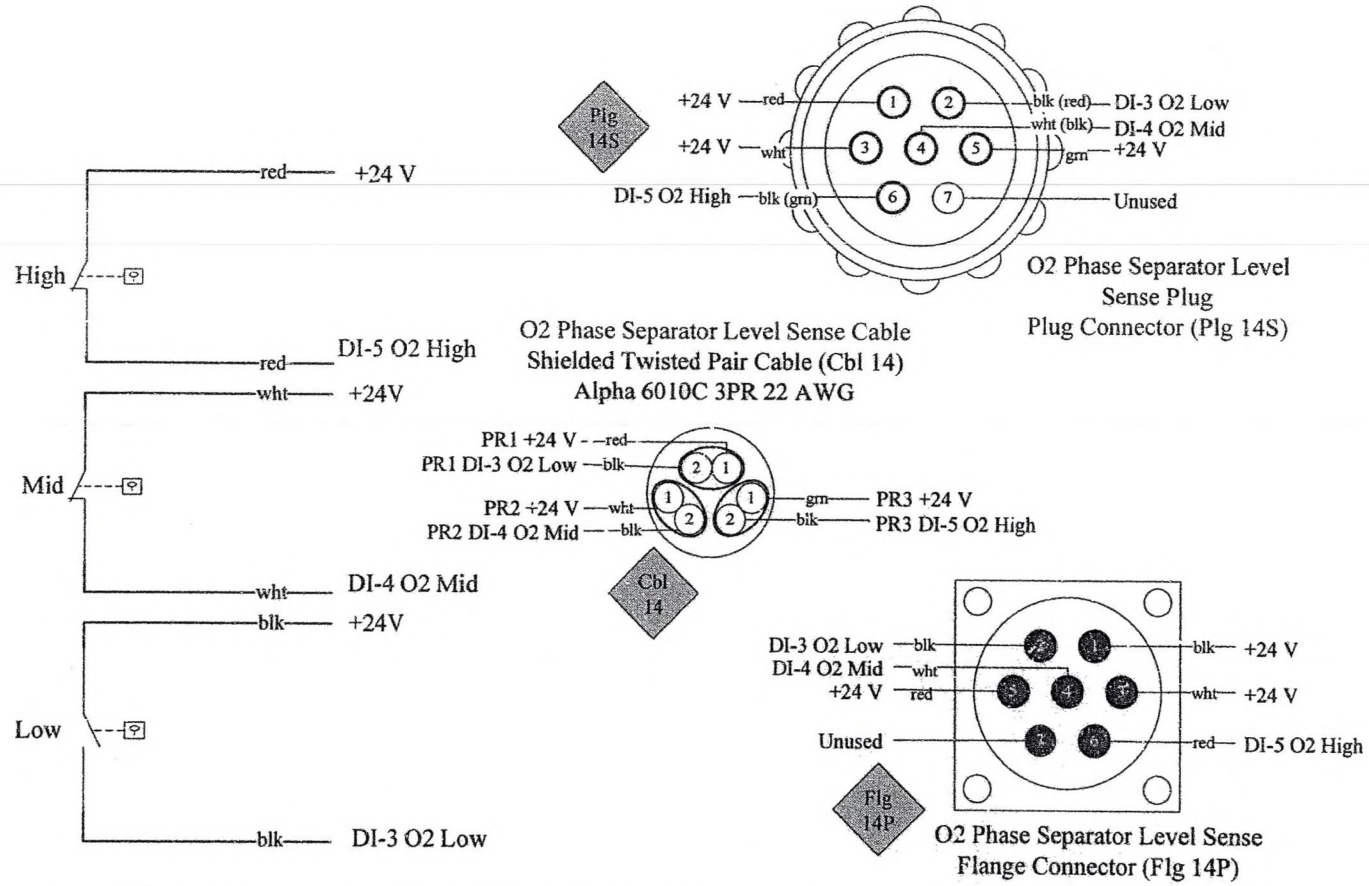


Figure 67. Oxygen phase separator (O2phSep) level sense wiring and float orientation (Flg/Plg/Cbl 14).

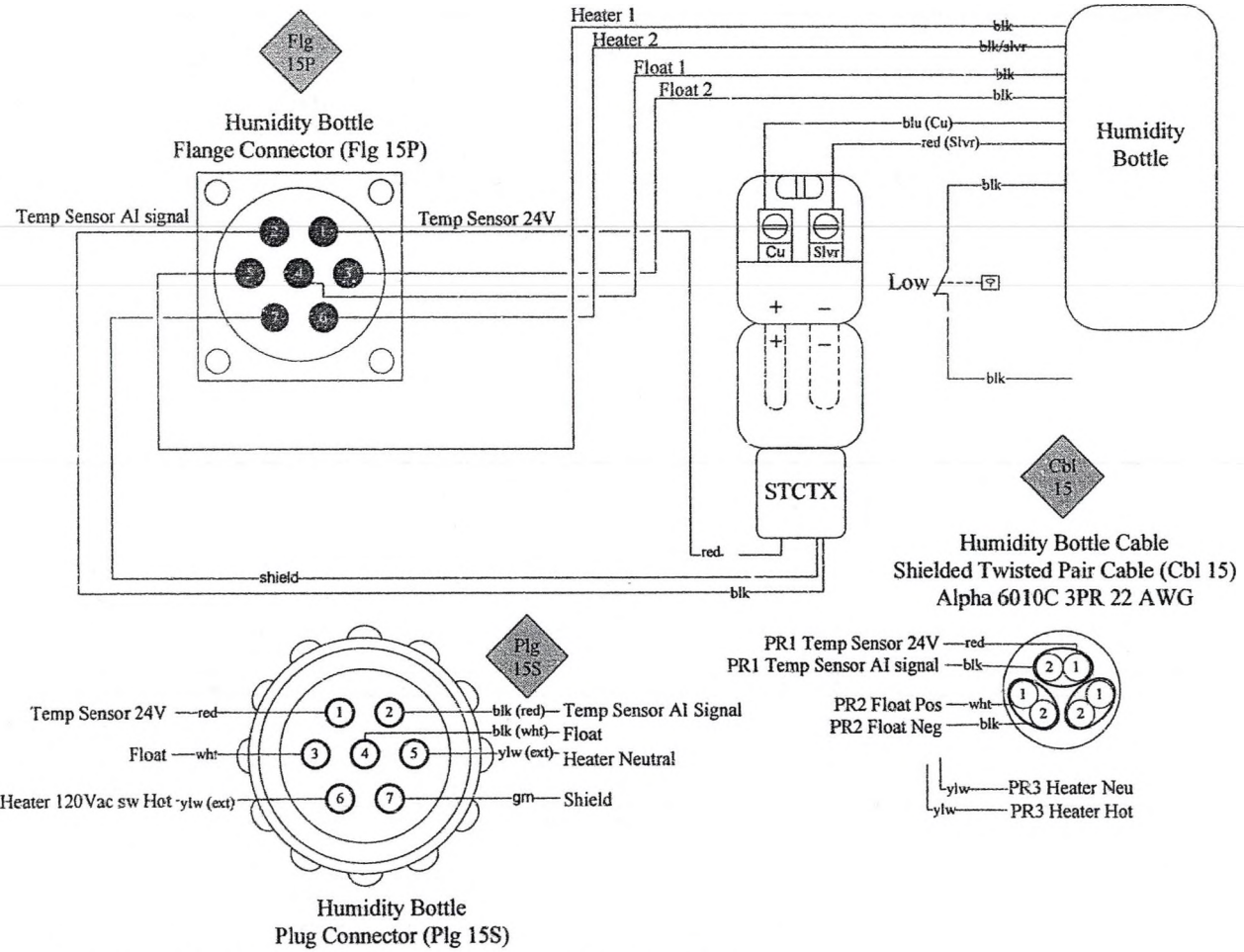


Figure 68. Humidity bottle flange device wiring (Flg/Plg/Cbl 15).

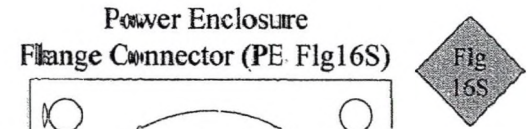
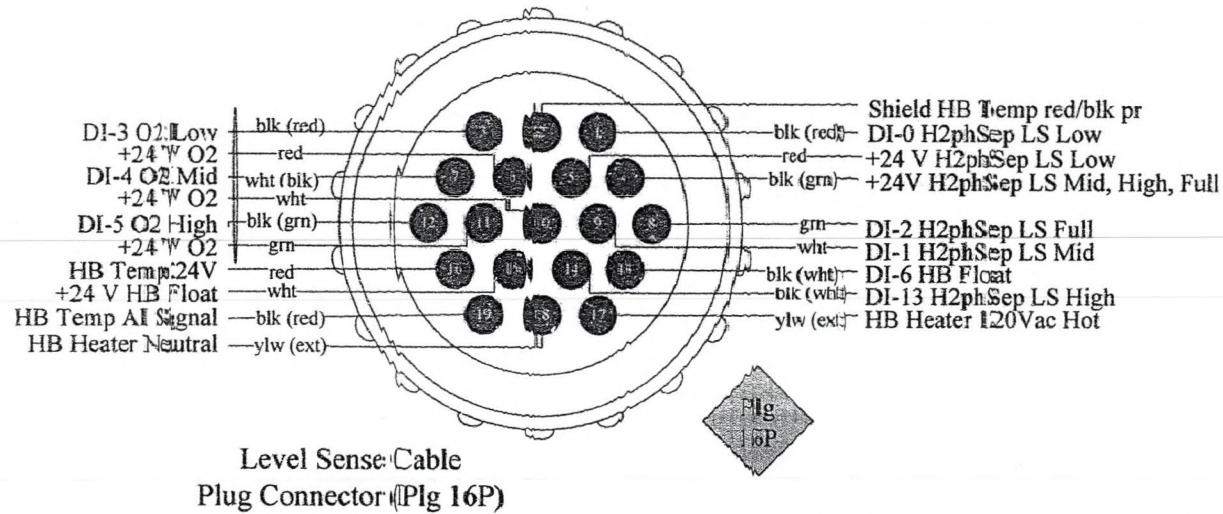


Figure 69. Flange and plug wiring for level sense and humidity bottle (Flg/Plg 16).

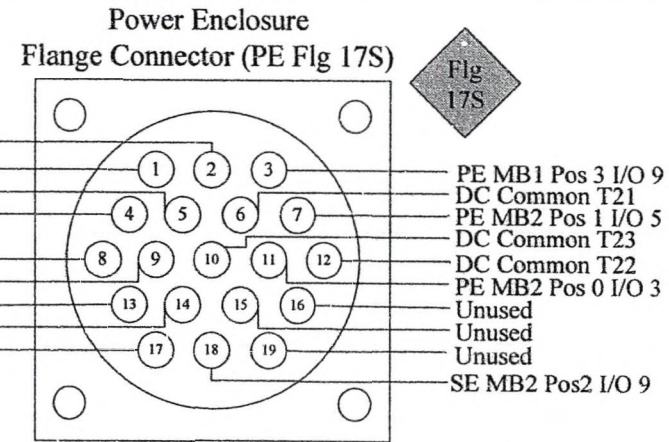
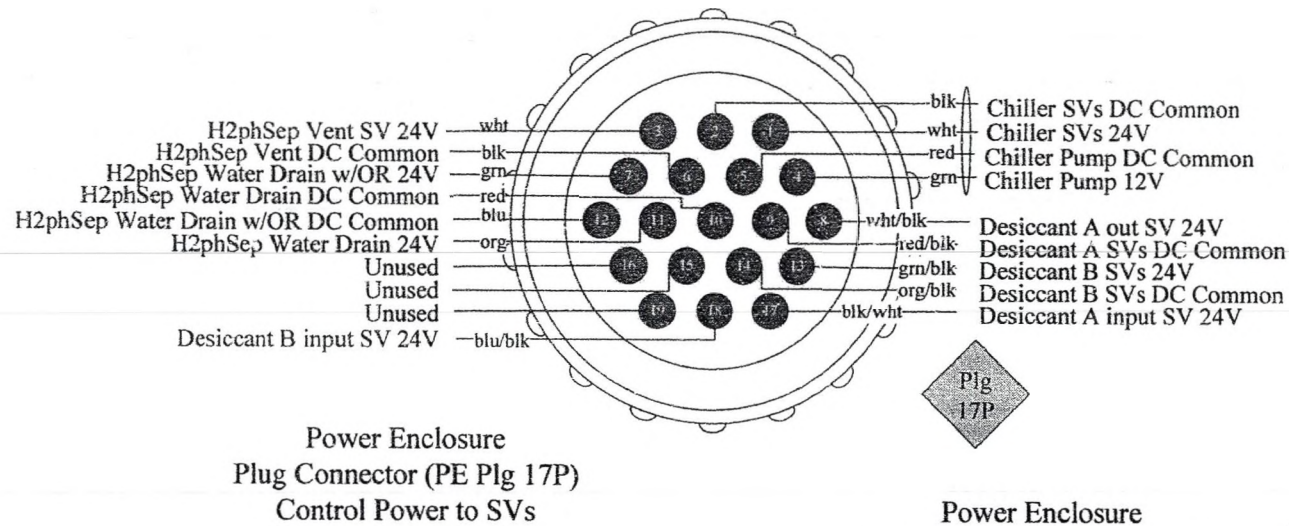


Figure 70. Flange and plug wiring of solenoid valves (Flg/Plg 17).

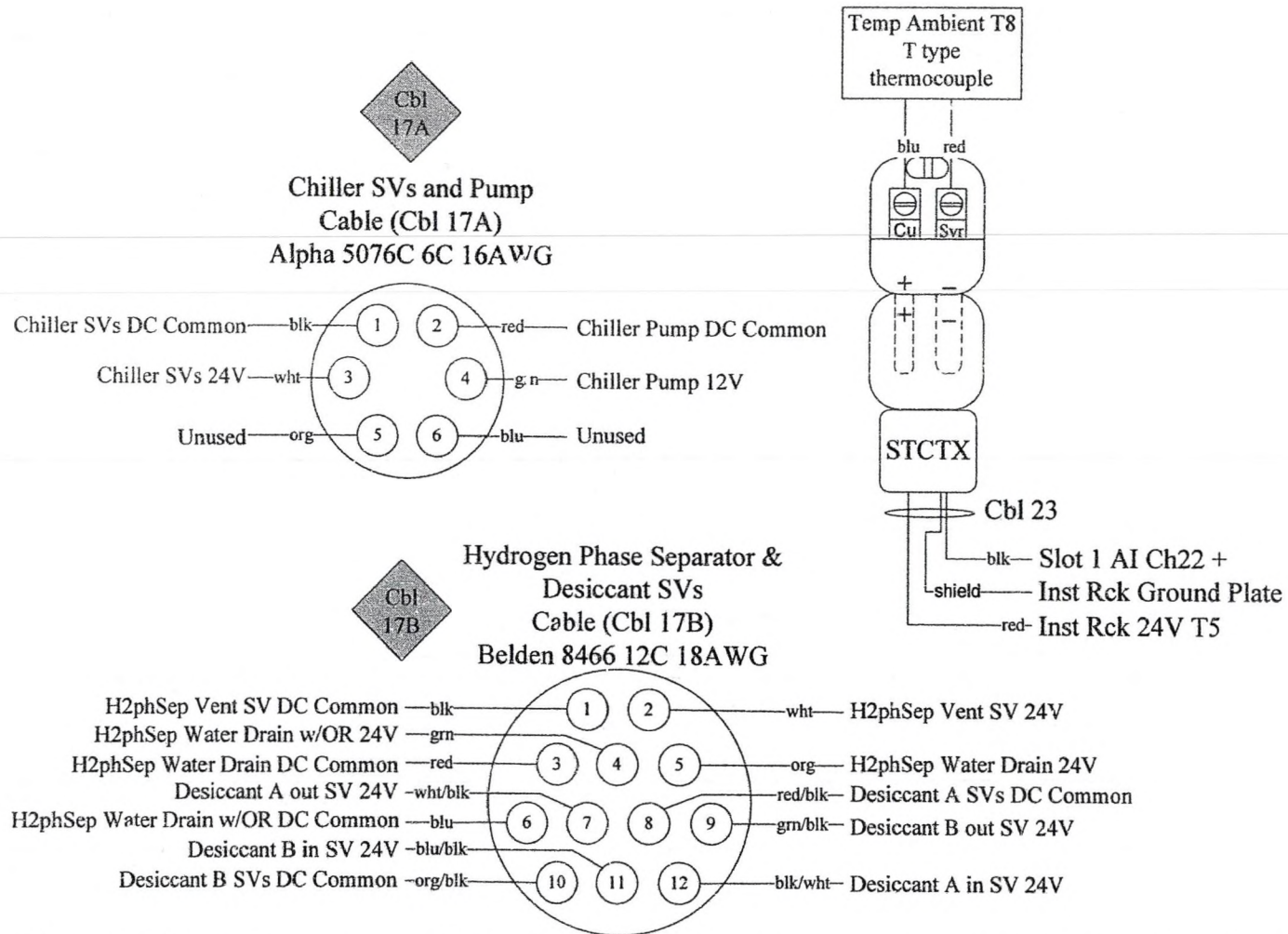


Figure 71. External water pump and solenoid valves. Hydrogen phase separator and desiccant solenoid valves and ambient temperature (T8) wiring (Cbl 17A, B).

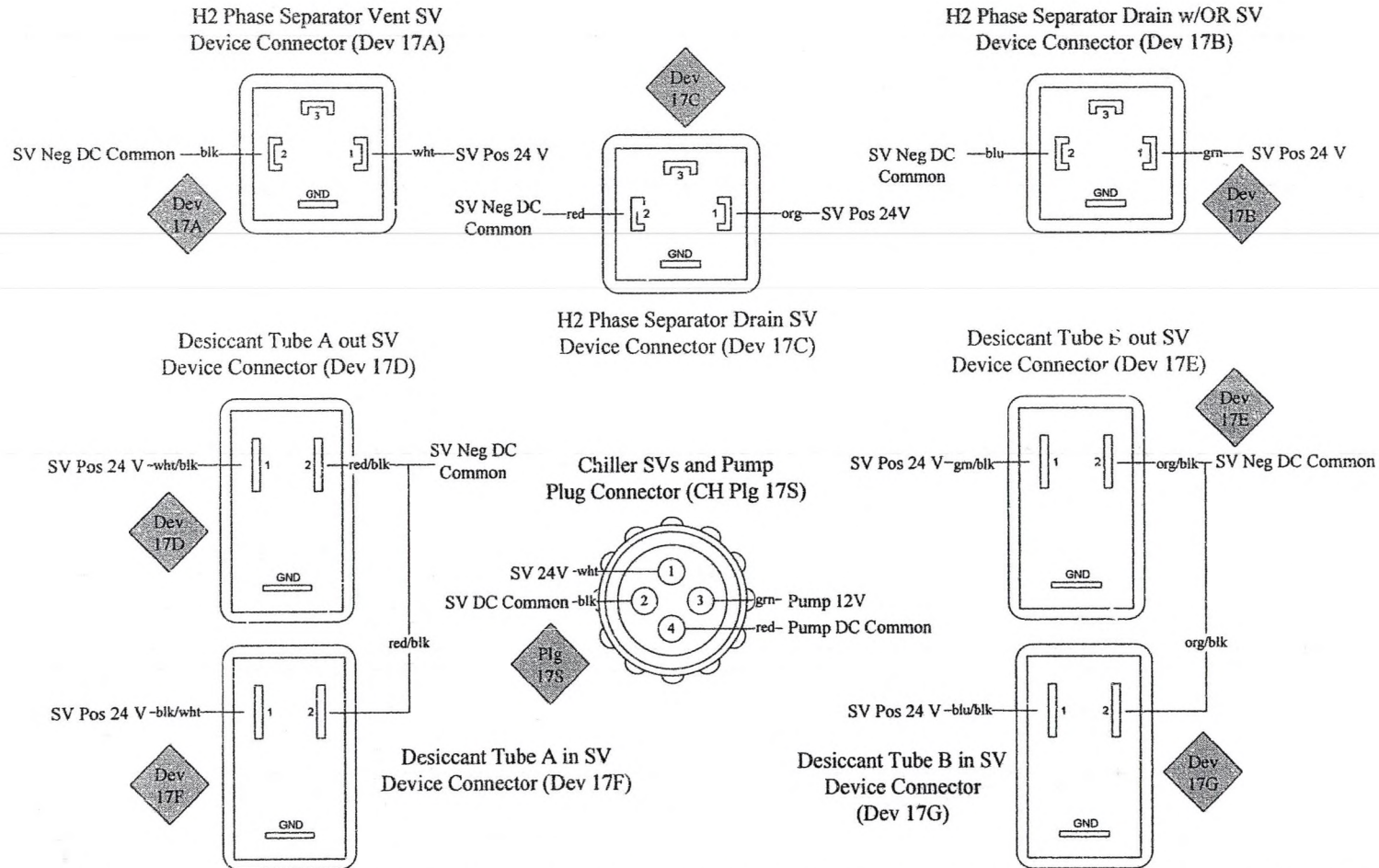


Figure 72. Solenoid valves for chiller (CH Plg17S), hydrogen phase separator and desiccant device wiring (Dev 17x).

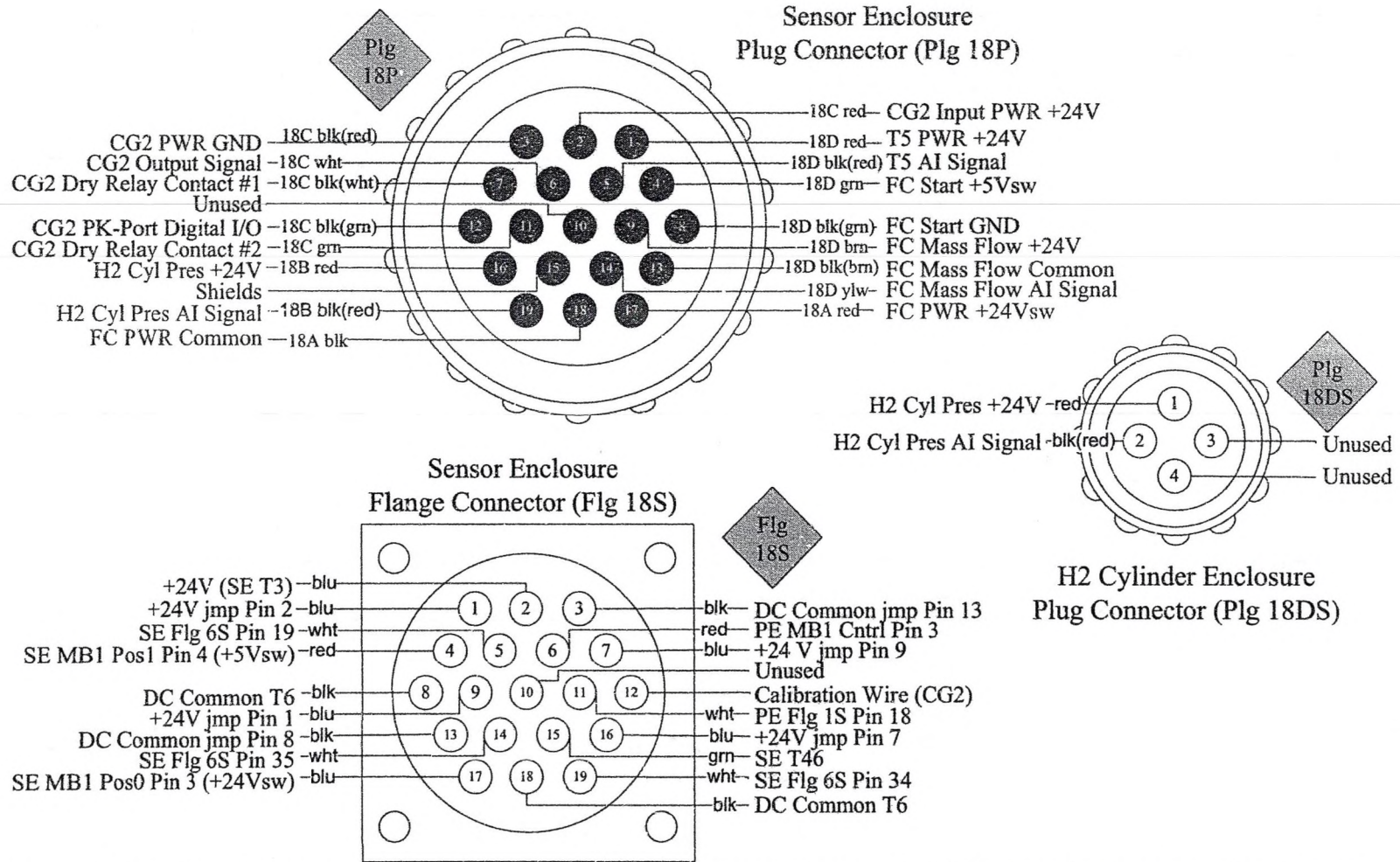
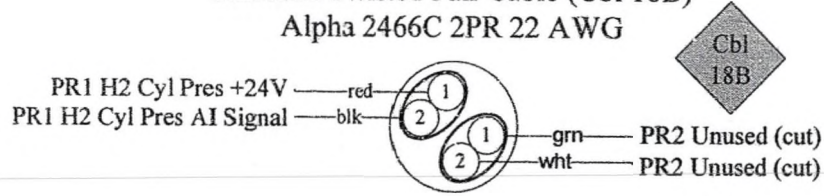


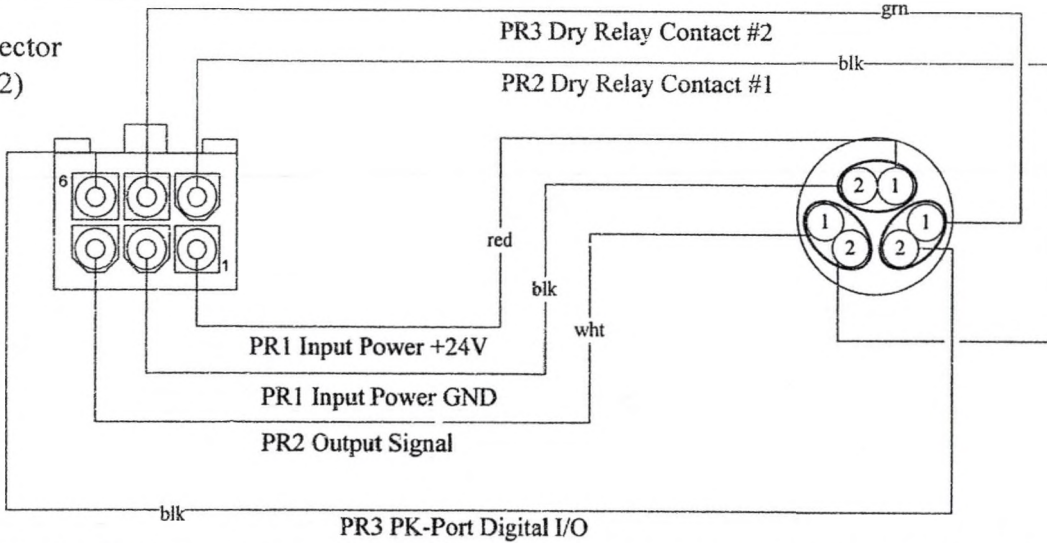
Figure 73. Combustible gas detector (CG2), hydrogen cylinder pressure and fuel cell power and start signal wiring (Flg/Plg 18).

H2 Cylinder Pressure P4
 Shielded Twisted Pair Cable (Cbl 18B)
 Alpha 2466C 2PR 22 AWG



Cbl
18B

H2 Detector
(CG2)



Cbl
18C

Hydrogen Gas Detector (CG2)
 Shielded Twisted Pair Cable (Cbl 18C)
 Alpha 6010C 3PR 22 AWG

158

Figure 74. Hydrogen detector (CG2) and cylinder pressure sensor wiring (Cbl 18 B,C).

Temperature H2 Stage 1 T5
 Pt 100Ω ($\alpha=0.00385$) 3-wire RTD Transmitter
 Supply Voltage 10-36V Supply Current 28mA
 Switch settings 100mV (TX254)
 Calibrated 0-50°C on March 1, 2006

159

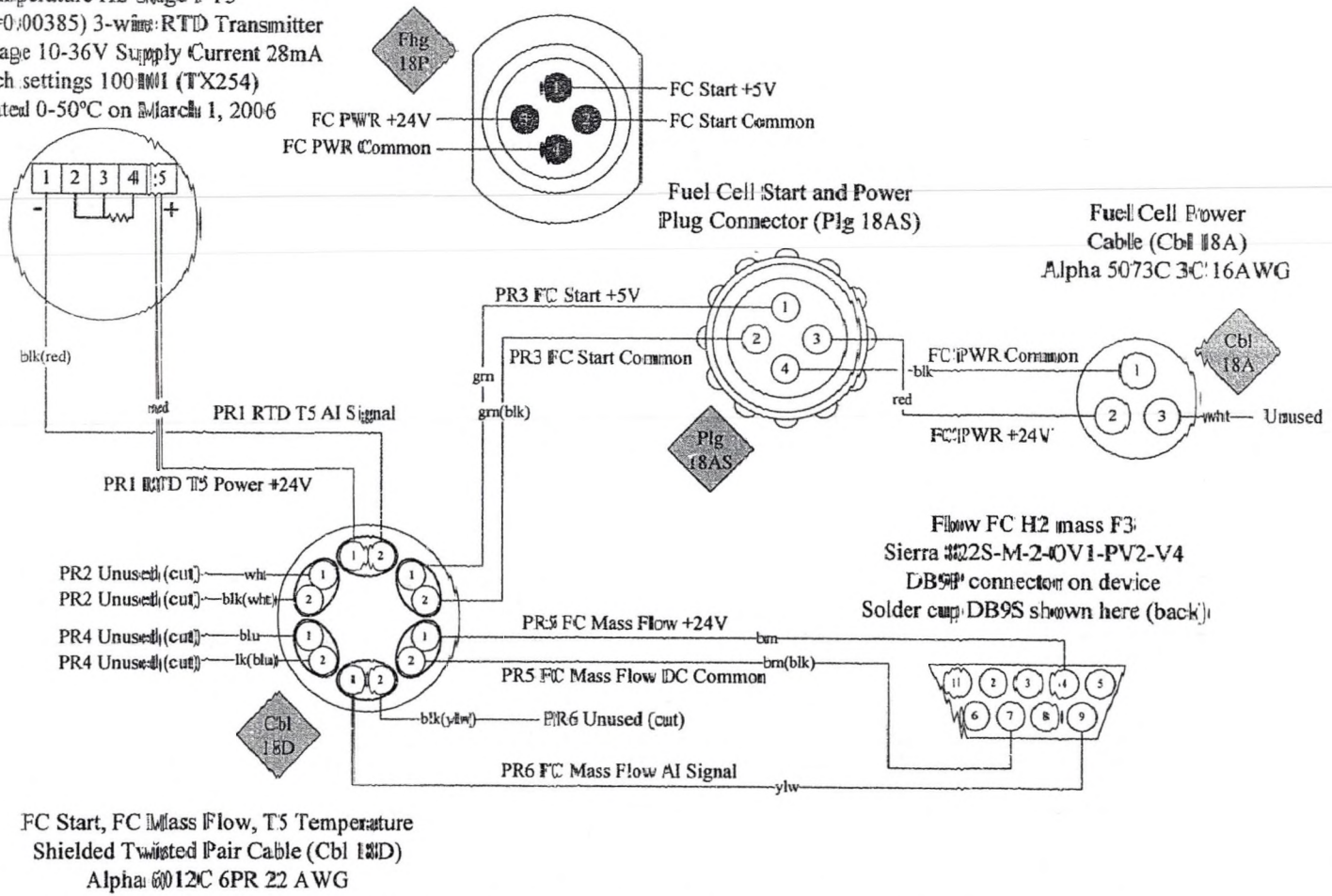


Figure 75. Temperature stage 1 (T5), fuel cell power and start signal and fuel cell mass flow wiring (Fig 18, Plg 18A, Cbl 18A,D).

Interlock Loop and E-Stop
Power Enclosure to Instrument Rack
Shielded Twisted Pair Cable (Cbl 19)
Alpha 2466C 2PR 22 AWG

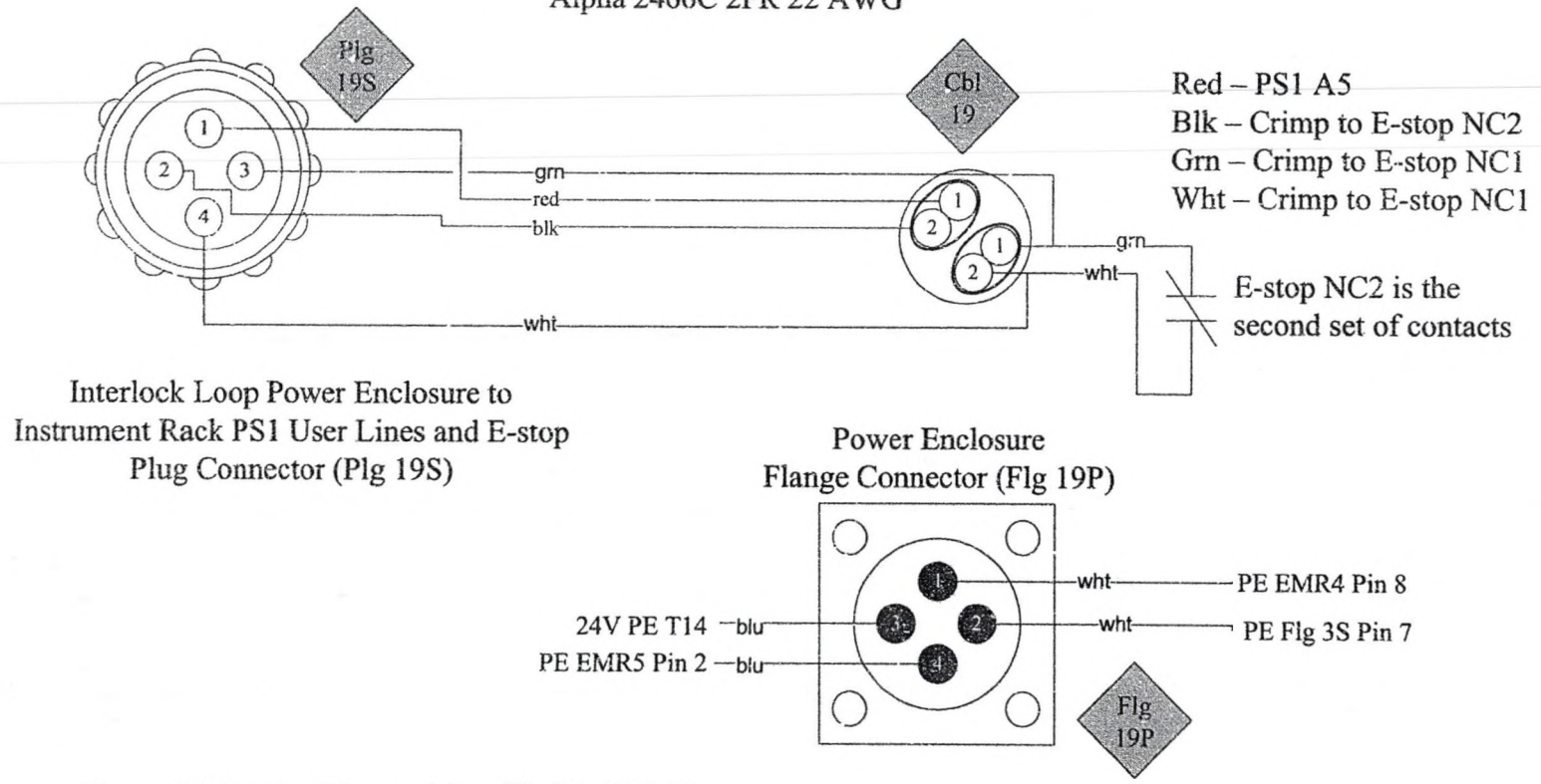


Figure 76. Interlock loop wiring (Flg/Plg/Cbl 19).

Instrument Rack Power Supply 1 (PS1) Master

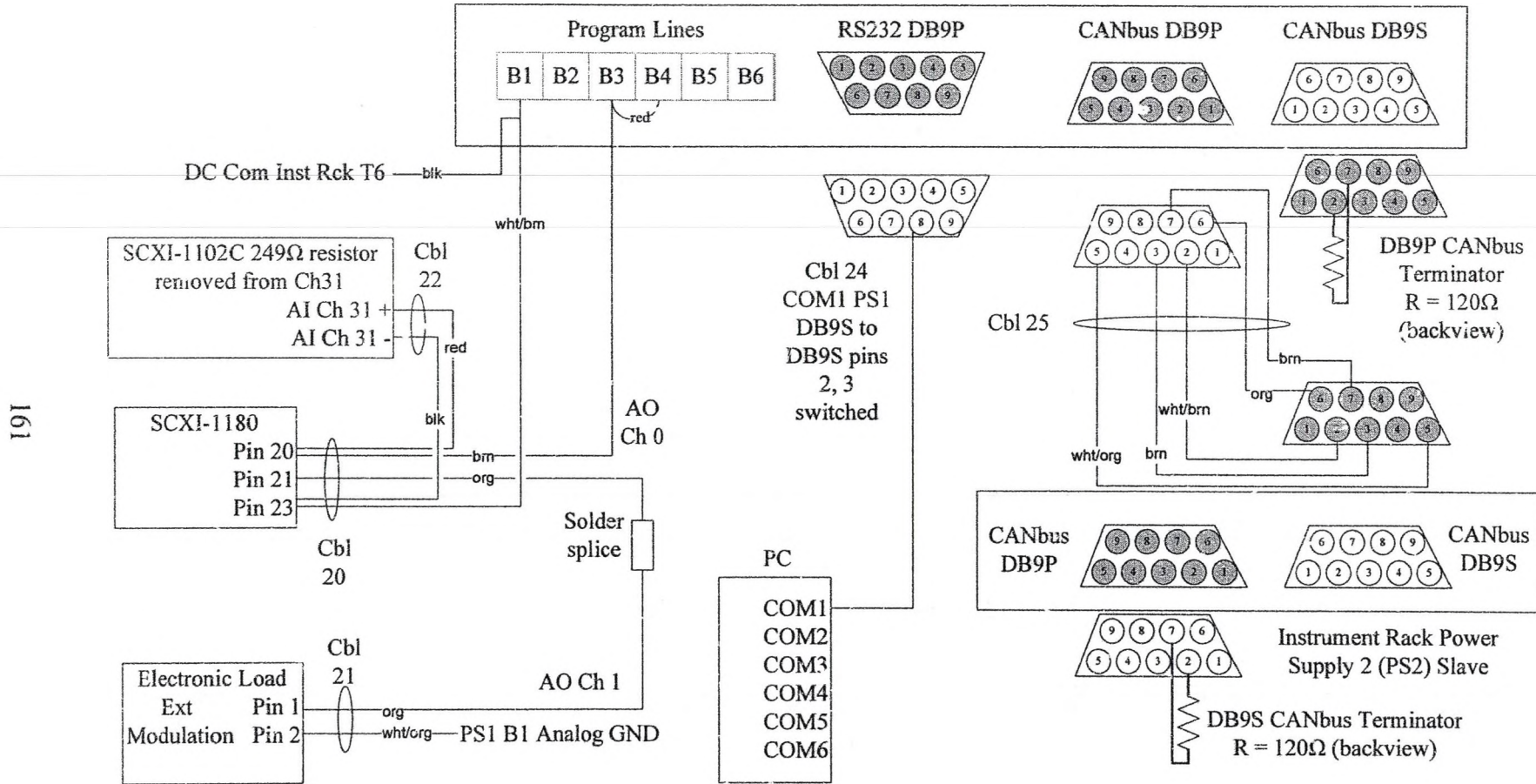


Figure 77. Instrument rack cables. Analog output (AO) to power supplies 1, 2 (PS1, PS2), serial communication cable (COM1) to power supply 1 and CANbus wiring from PS1 to PS2 (Cbl 20 - 25).

SE Flg 28S, Plg 28P, Cbl28 and DEVs 28A, 28B.
 Solenoid valves from Pmp1 (NO) to O2phSep
 and Stack Cathode Flush (NC).

Pump 1 (Ext. water loop, Pmp1) will close during
 shutdown to route water to Cathode Flush SV11 (NC).

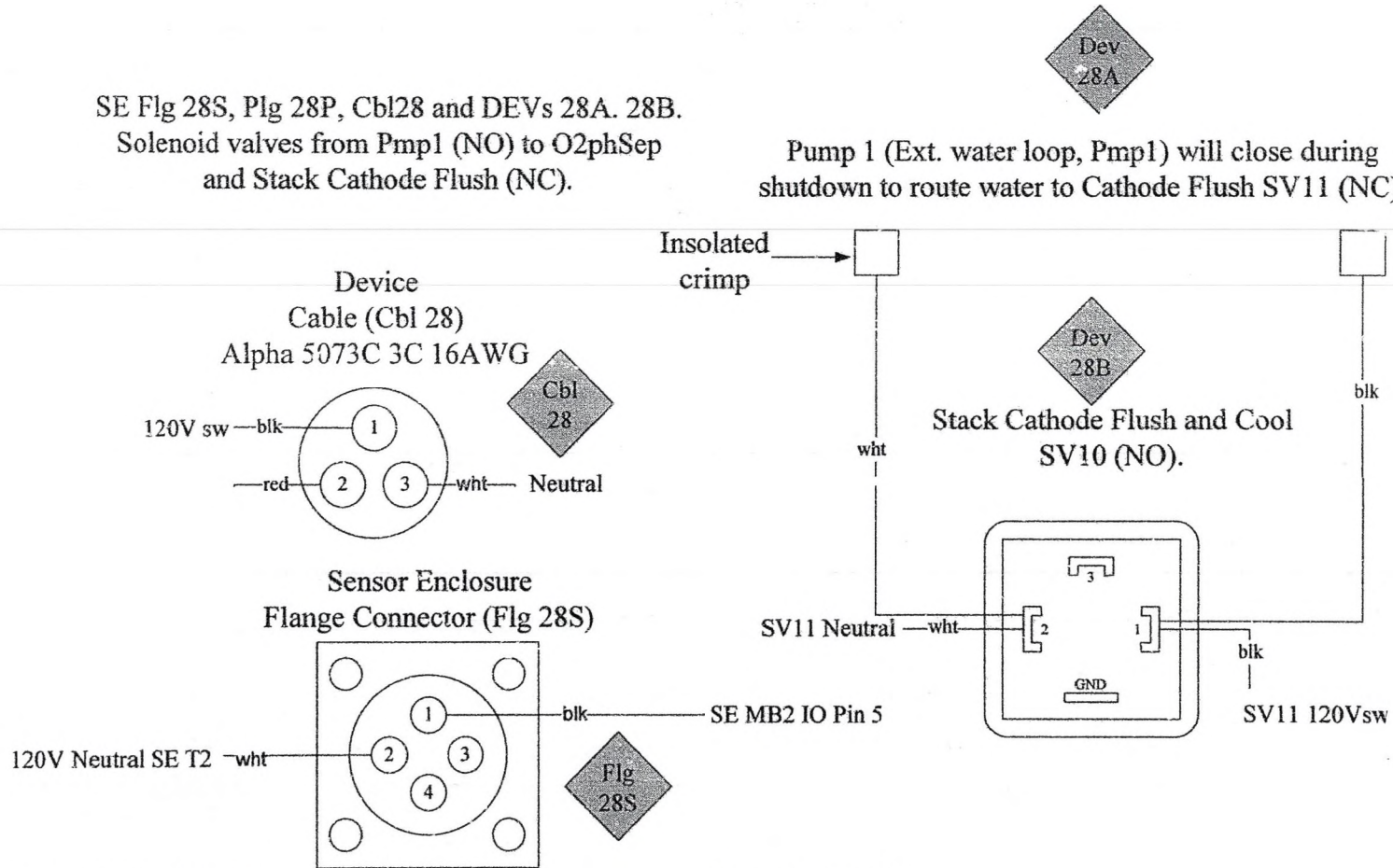


Figure 78. Cathode flush and cool solenoid valve wiring (Flg/Cbl/Dev 28).

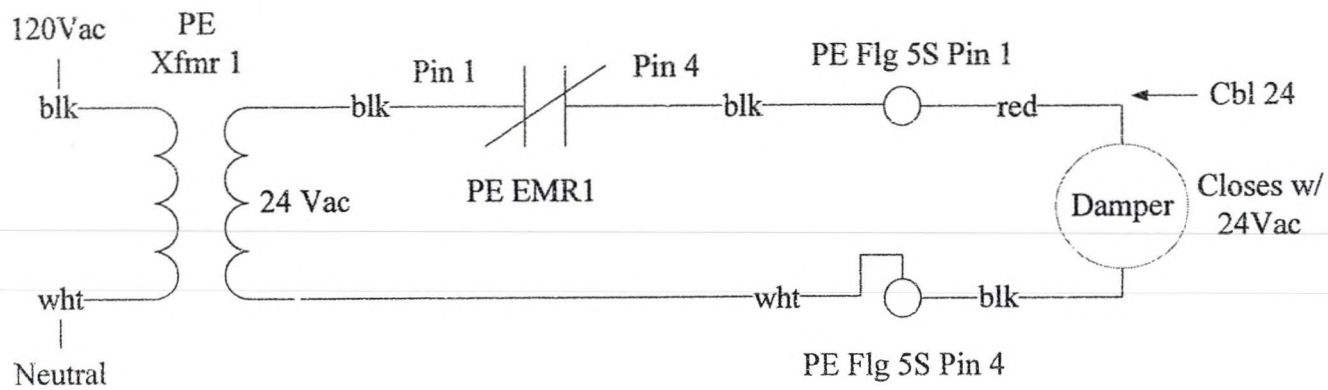


Figure 79. Damper (14 Vac) connection diagram for Harrington hall laboratory 360A.

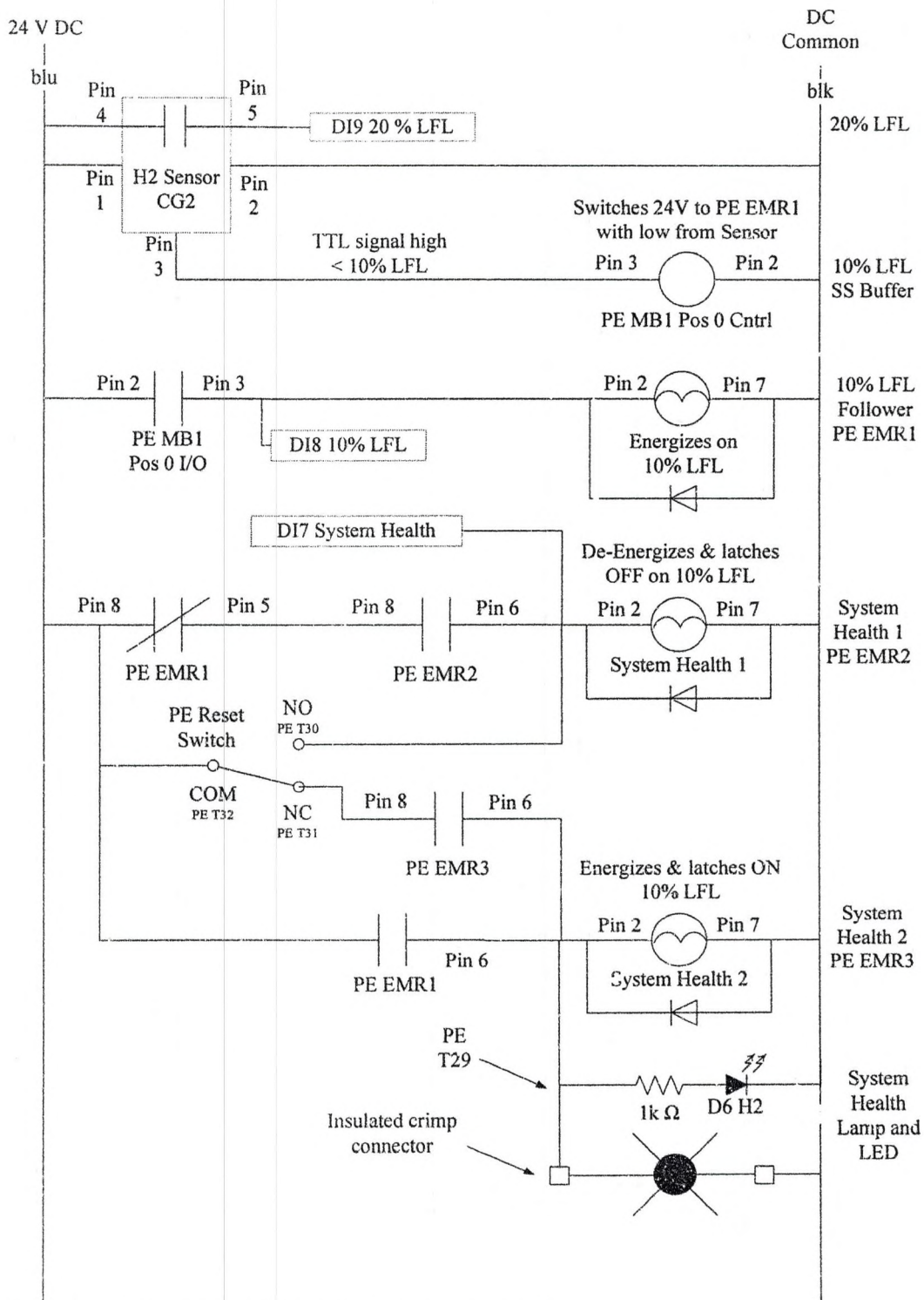


Figure 80. Two line wiring of safety and relay logic.

APPENDIX B
Plumbing Diagrams

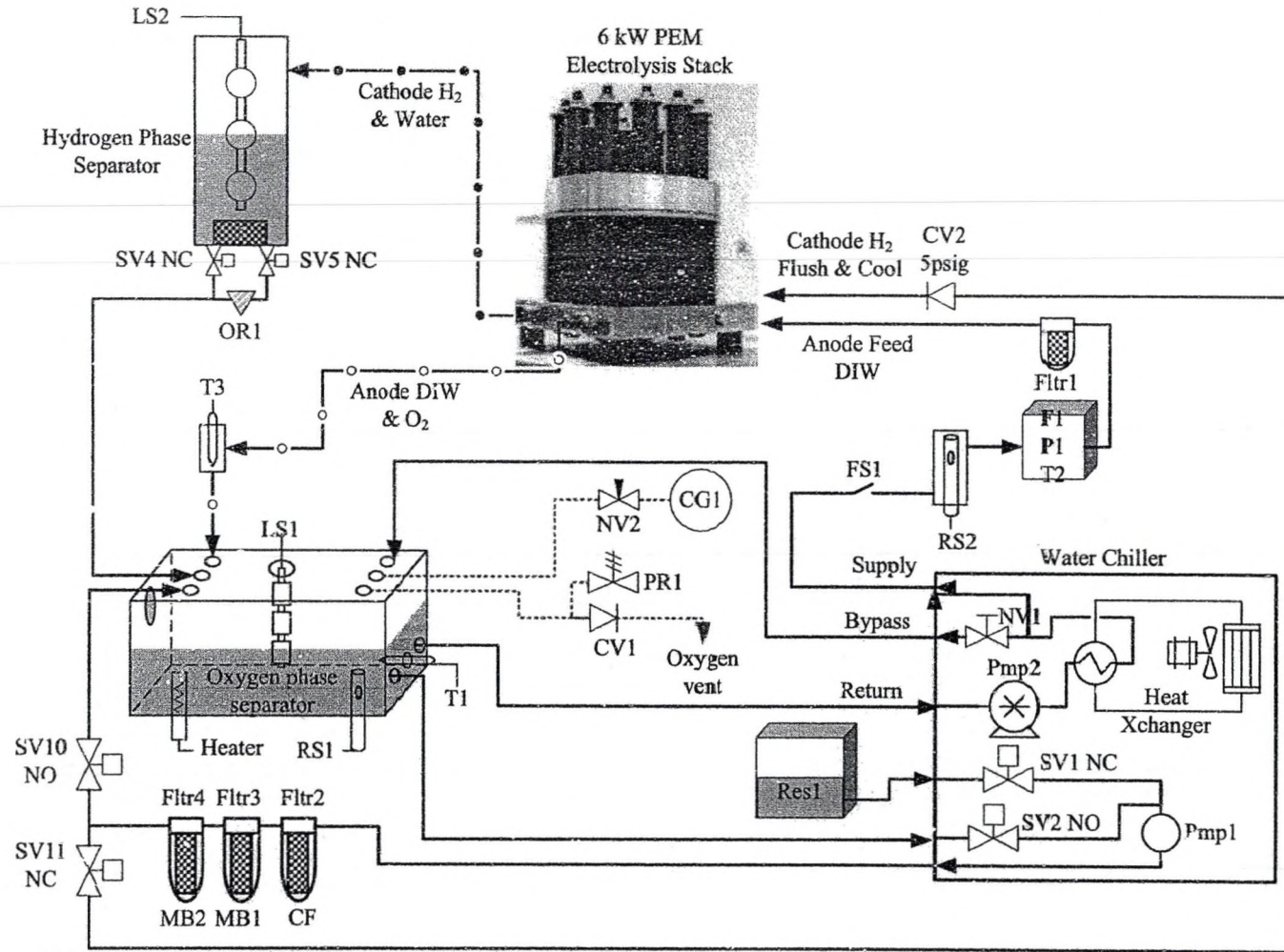


Figure 81. External and deionized water loops with sensors, valves and major components.

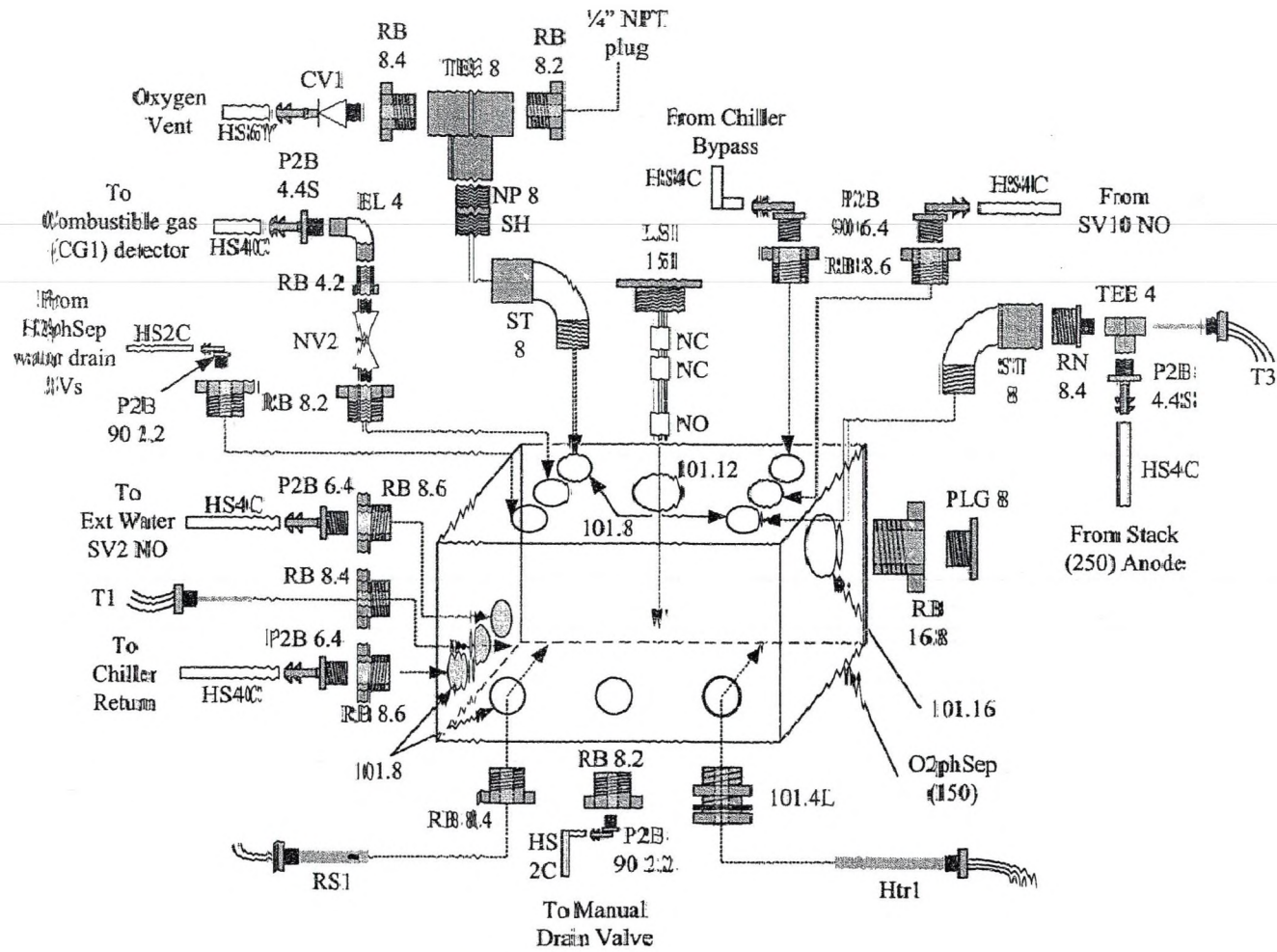


Figure 82. Oxygen phase separator plumbing components.

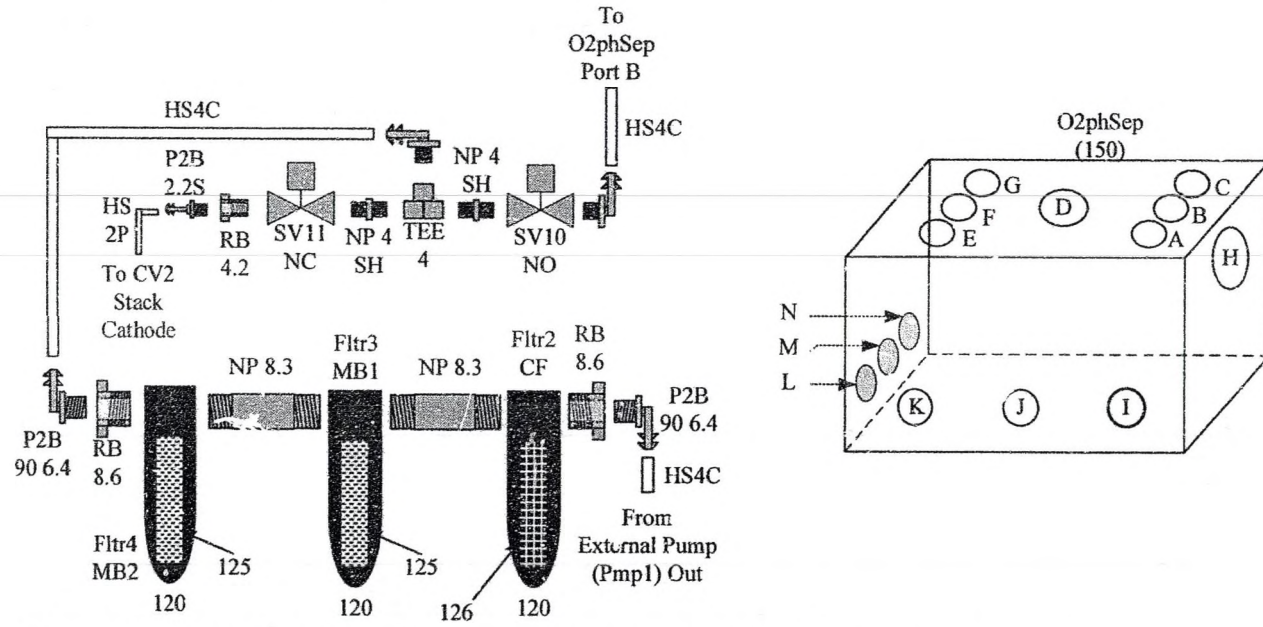


Figure 83. Filter plumbing and oxygen phase separator port designations.

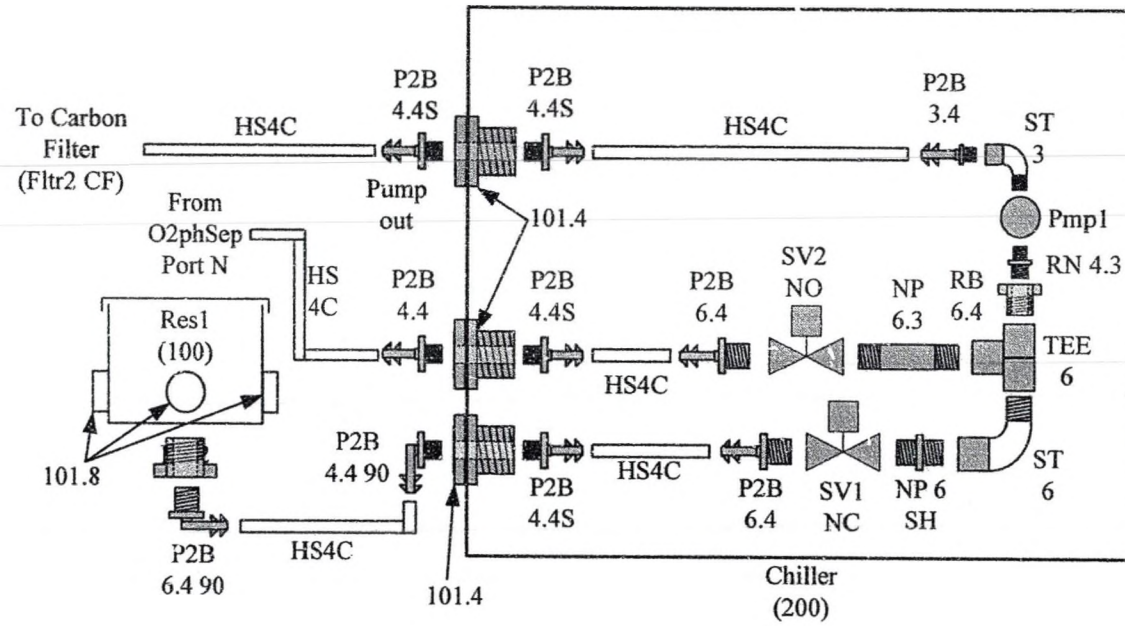


Figure 84. External water loop plumbing components

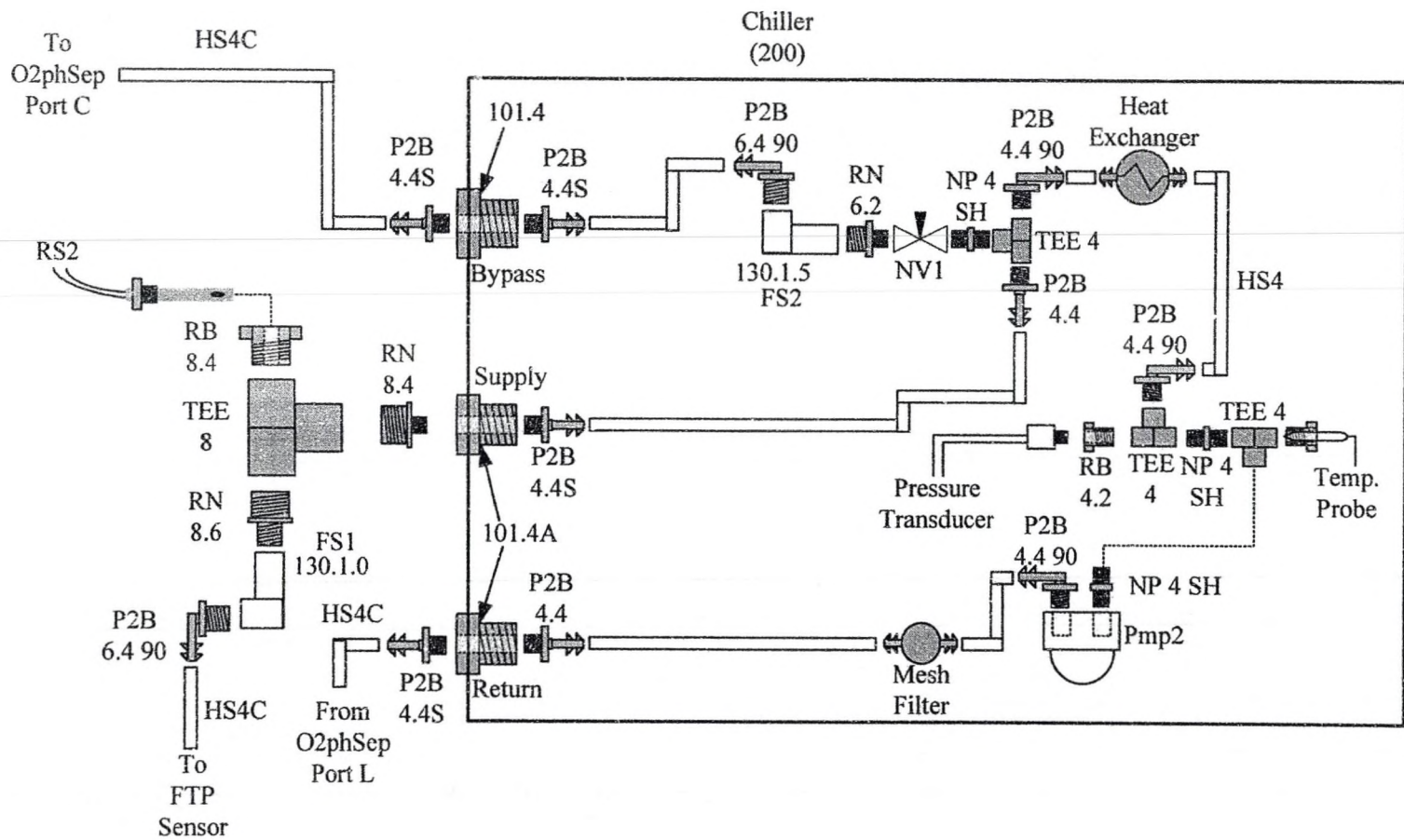


Figure 85. Chiller plumbing components.

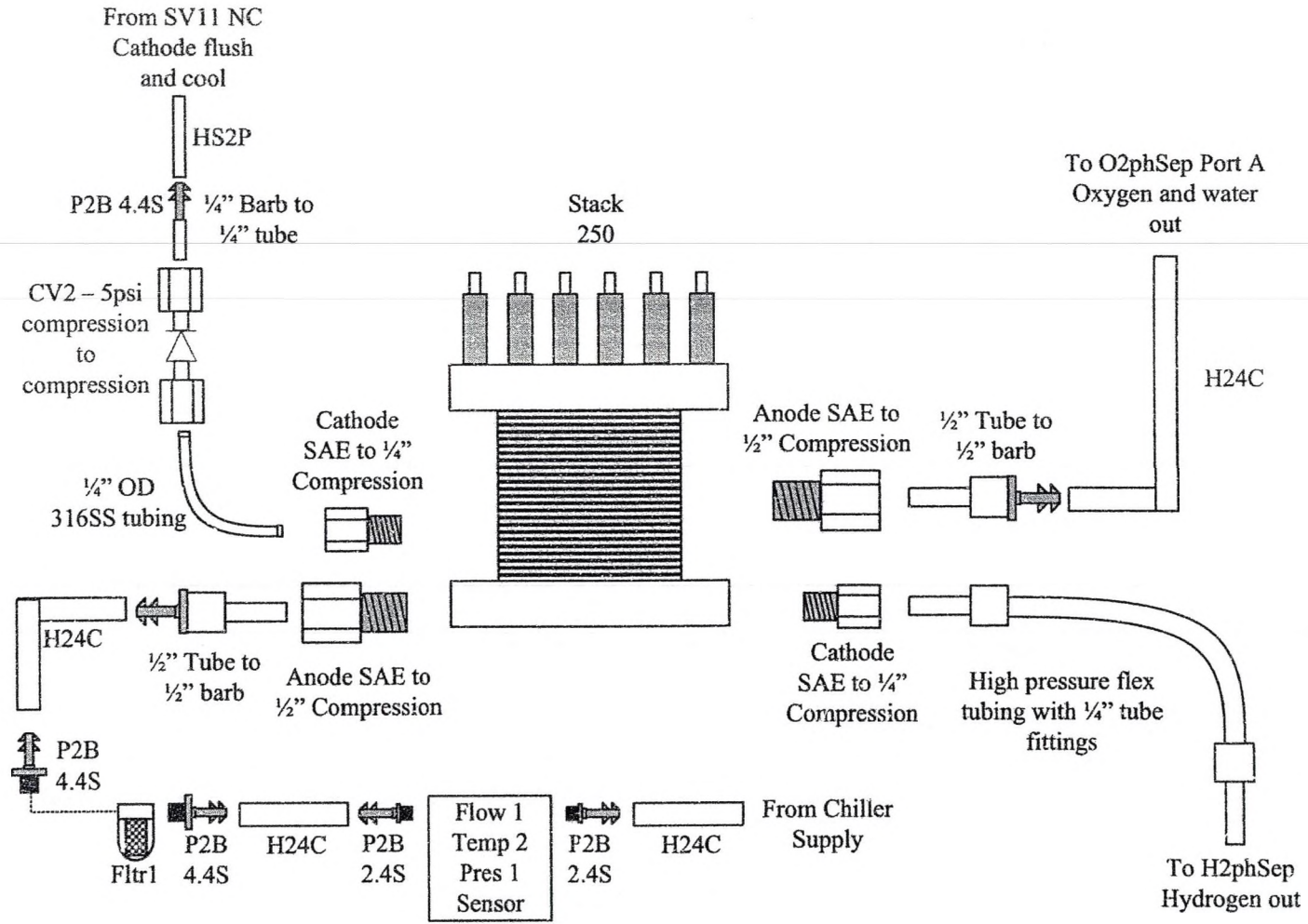


Figure 86. Stack plumbing components.

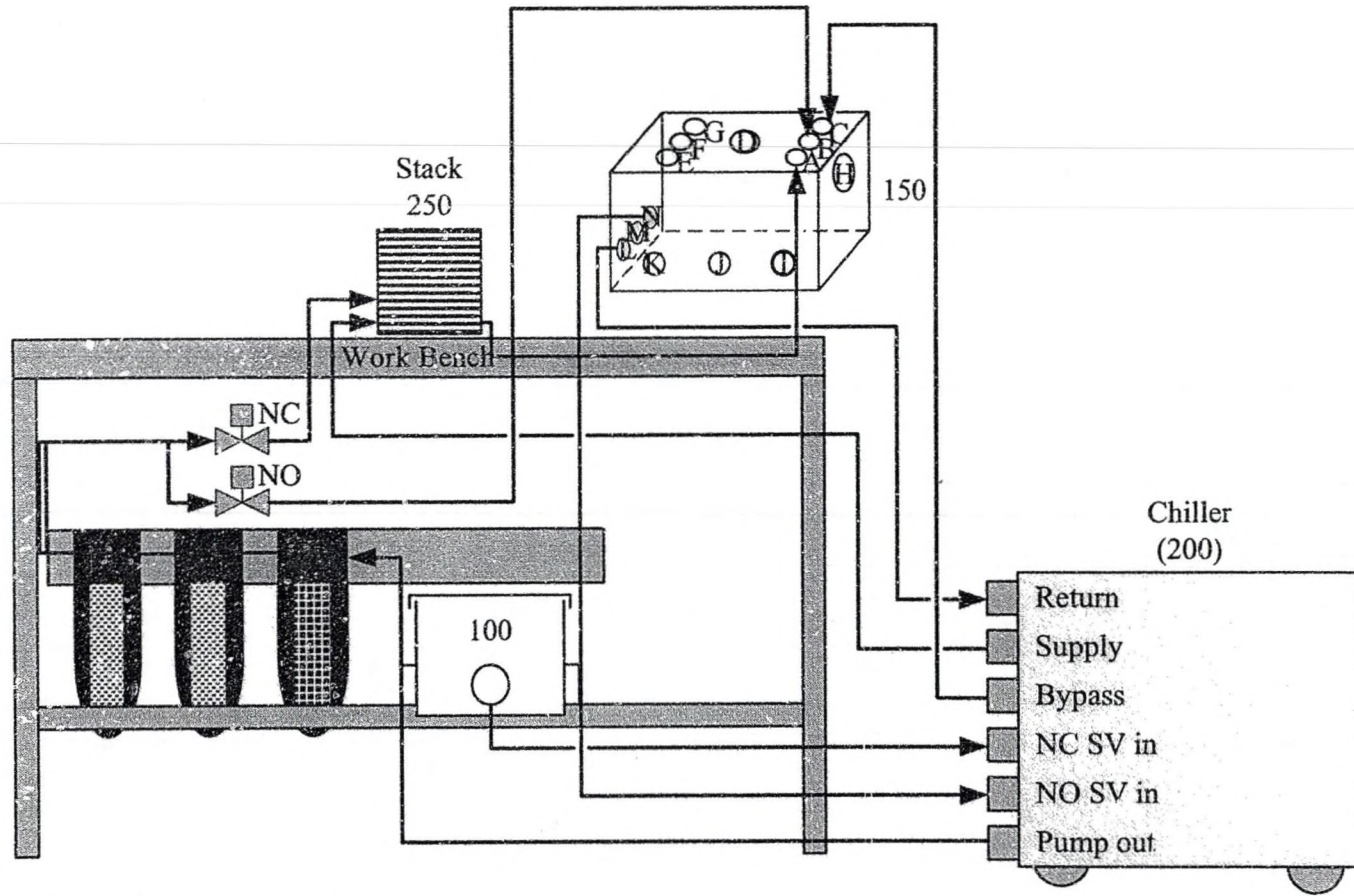


Figure 87. Deionized and external water flow.

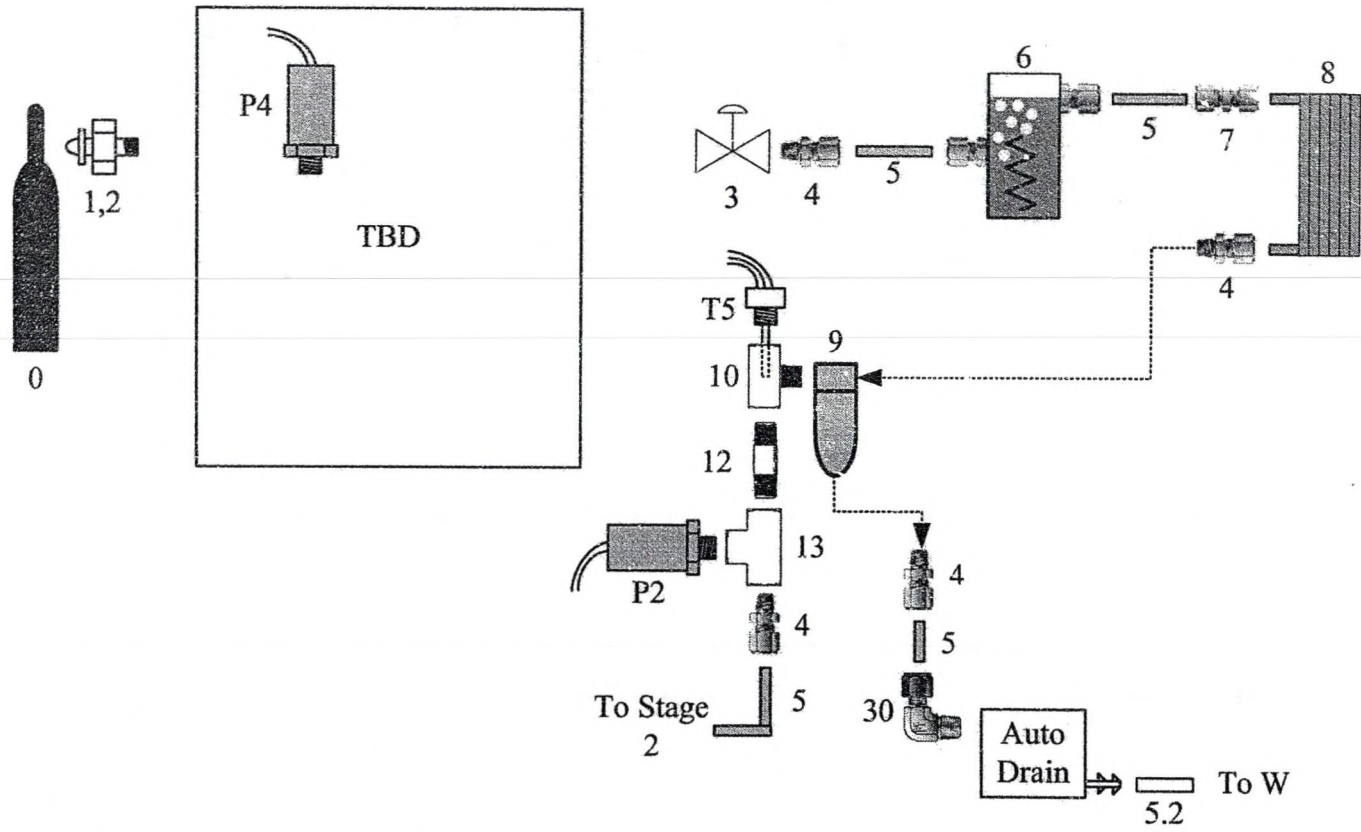


Figure 88. Dew point control detailed fitting plan.

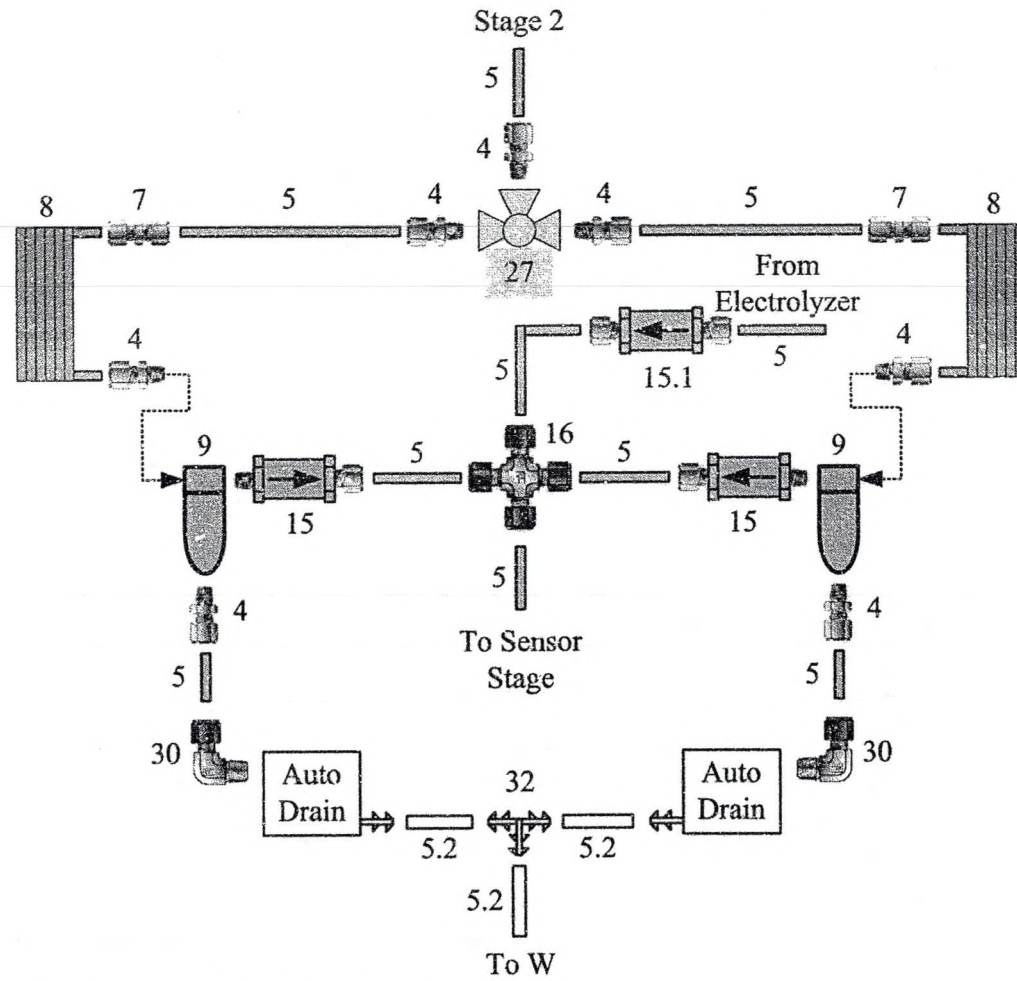


Figure 89. Stage 2 detailed fitting plan.

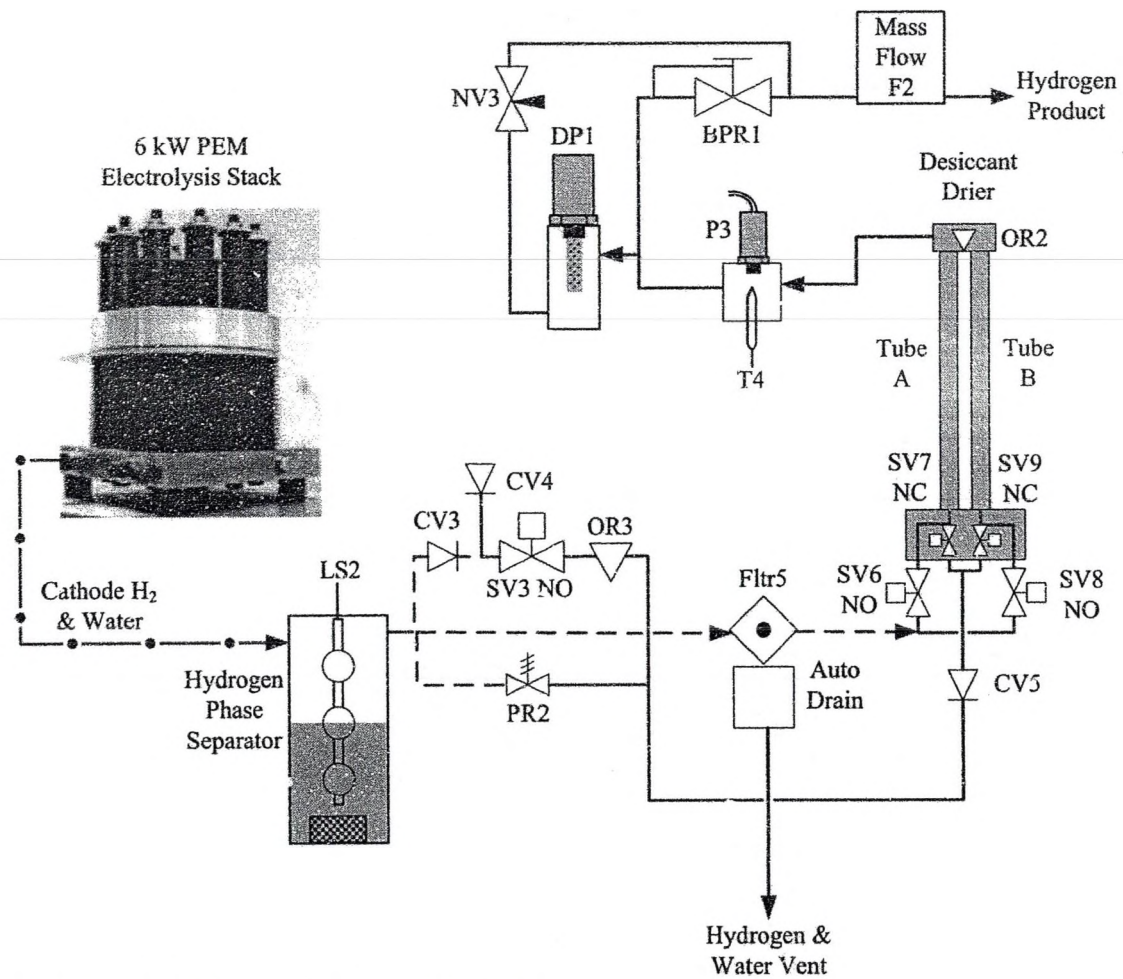


Figure 90. Hydrogen loop line diagram.

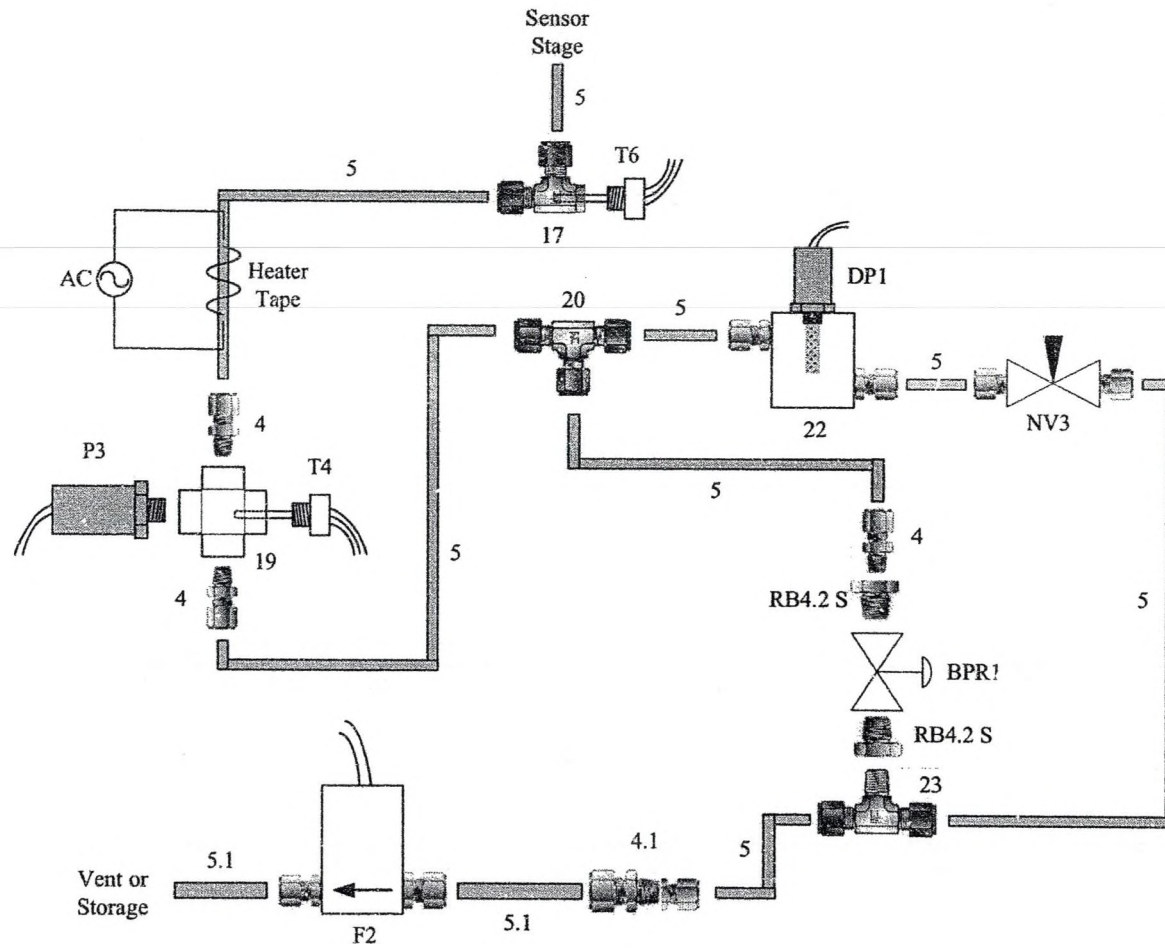


Figure 91. Hydrogen sensor stage for electrolyzer output.

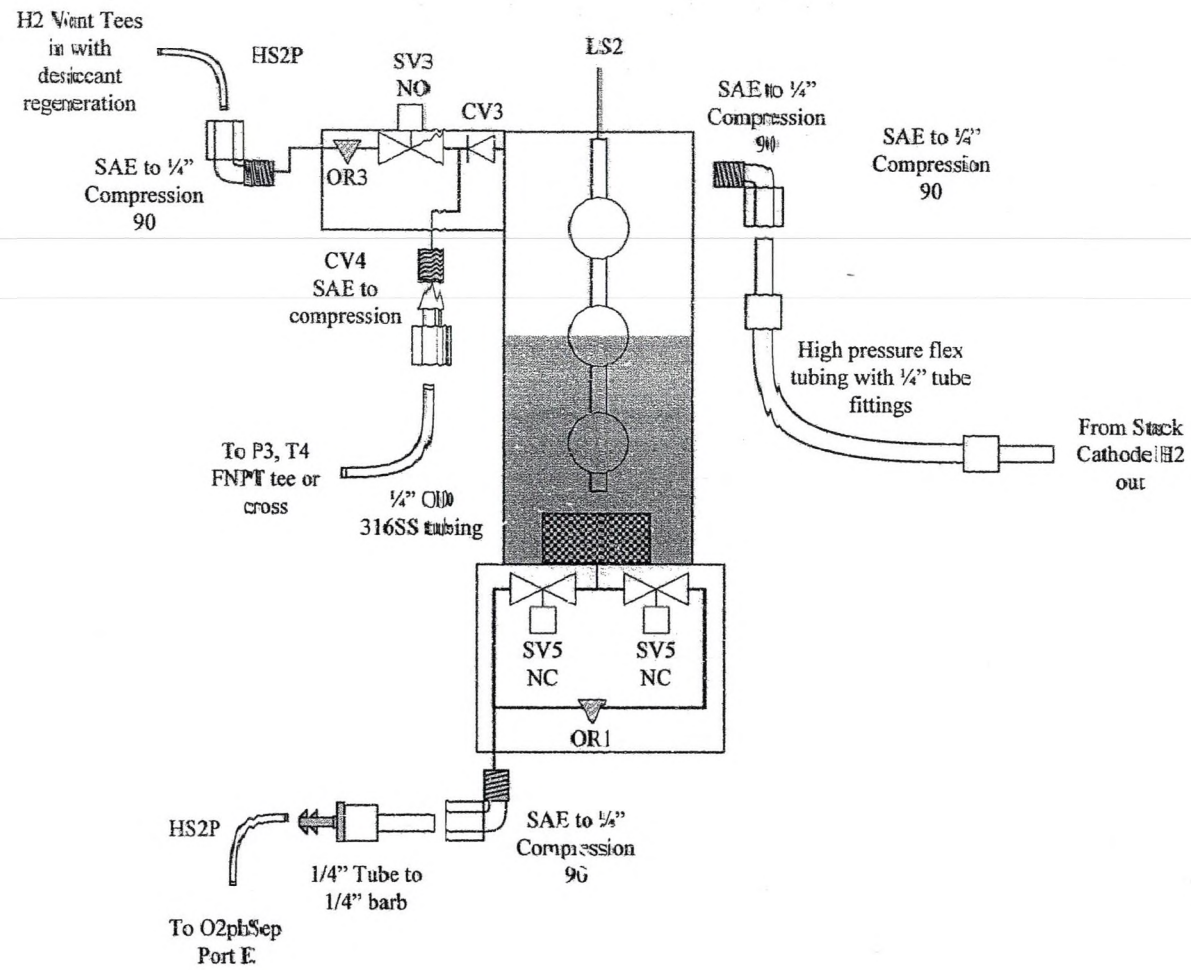


Figure 92. Hydrogen phase separator plumbing components.

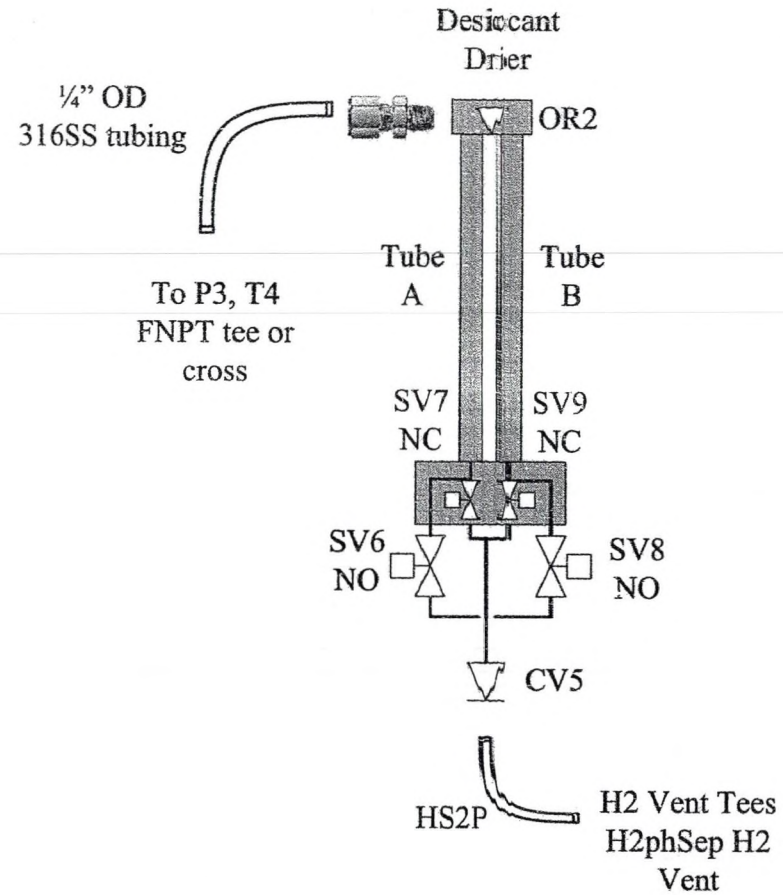
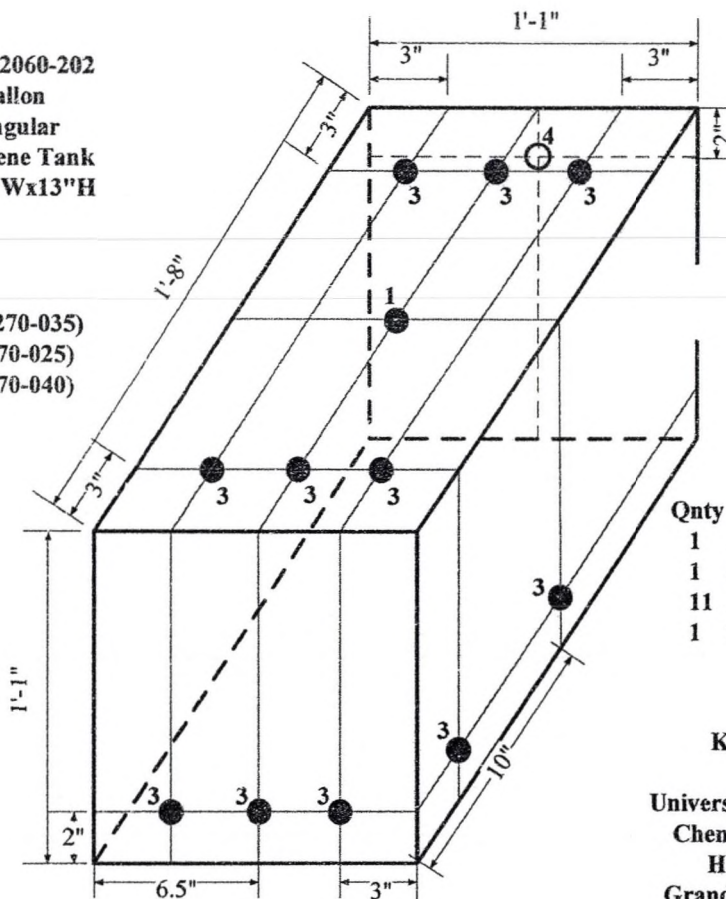


Figure 93. Desiccant plumbing components.

Product #2060-202
 15 Gallon
 Rectangular
 Polyethylene Tank
 20"Lx13"Wx13"H

American Tank
 Company, Inc.
 (877) 655-1100
 AmericanTank.com

- 1 - 1½" FPT (0270-035)
- 3 - 1" FPT (0270-025)
- 4 - 2" FPT (0270-040)



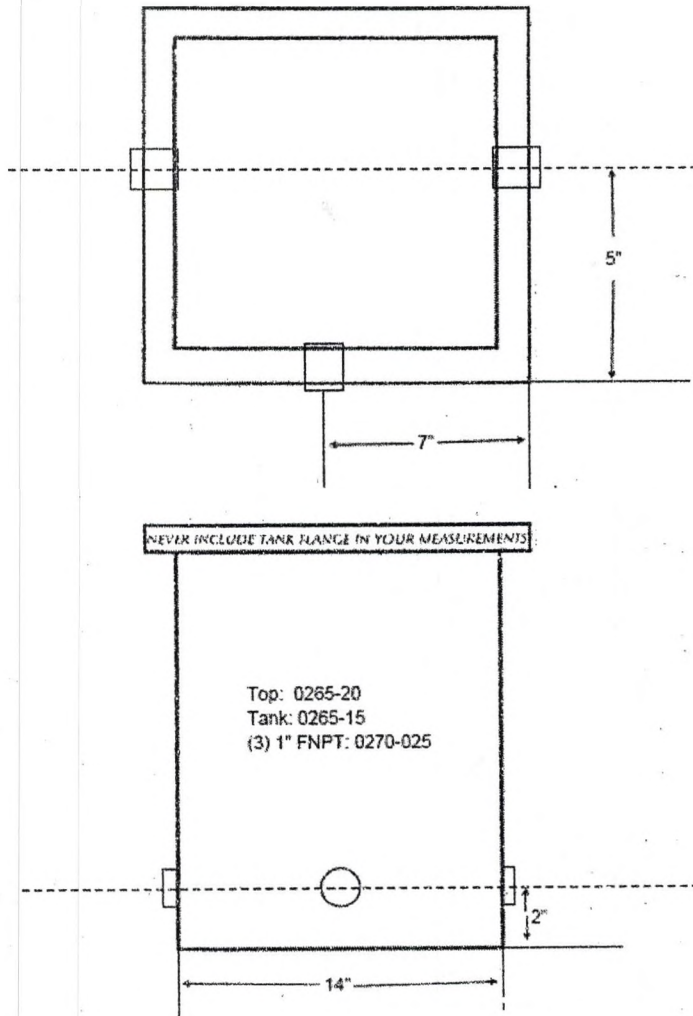
Estimated Price			
Qty	Description	Per Unit	Extended Cost
1	15gal Rect. Poly Tank	\$131.25	\$131.25
1	1½" FPT tank fitting	10.00	10.00
11	1" FPT tank fitting	10.00	110.00
1	2" FPT tank fitting	10.00	10.00

*Total \$261.26
 Does NOT include S&H

Kevin Harrison
 Nilesh Dale
 University of North Dakota
 Chemical Engineering,
 Harrington Hall
 Grand Forks, ND 58202
 (701) 777-2553 Lab
 (218) 340-0253 Kevin Cell

Figure 94. Oxygen phase separator specification to manufacturer.

Fax to: Sandy Eaton, American Tank
 Phone: 707-535-1417
 Fax: 707-535-1487



NOTES:

Attn: Kevin Harrison, kevin.harrison@und.edu

Harrington 109, 701-777-2553

GALLON CAPACITY	5
LENGTH	14
WIDTH	10
HEIGHT	10
TYPE OF MATERIAL TO BE USED	polyethylene spinweld
DATE	November 2, 2005
REFERENCE	

Figure 95. External reservoir (Res1) specification to manufacturer.

APPENDIX C

Facility Layout

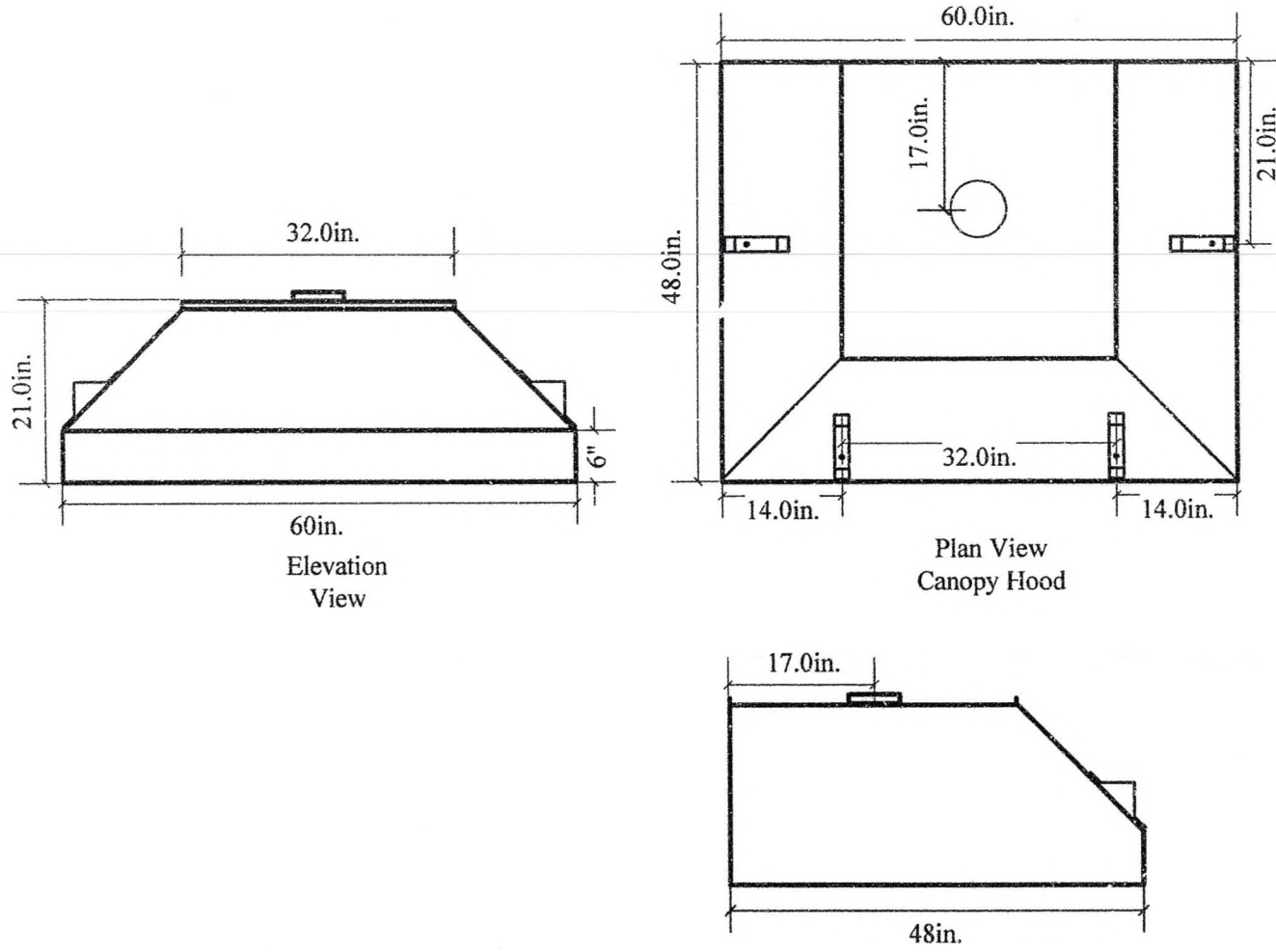


Figure 96. Detailed hood dimensions and views.

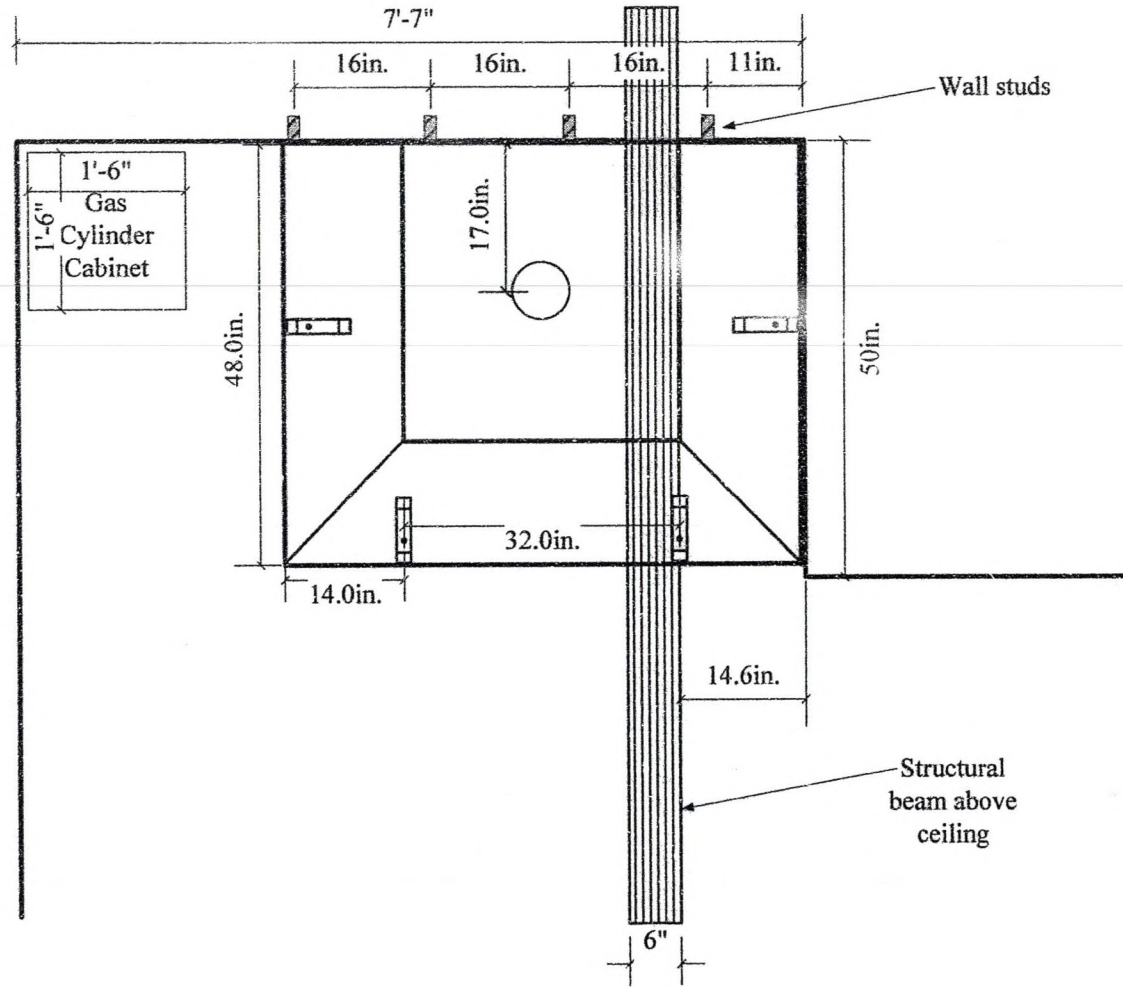


Figure 97. Top view Upson 360A showing structural components with hood

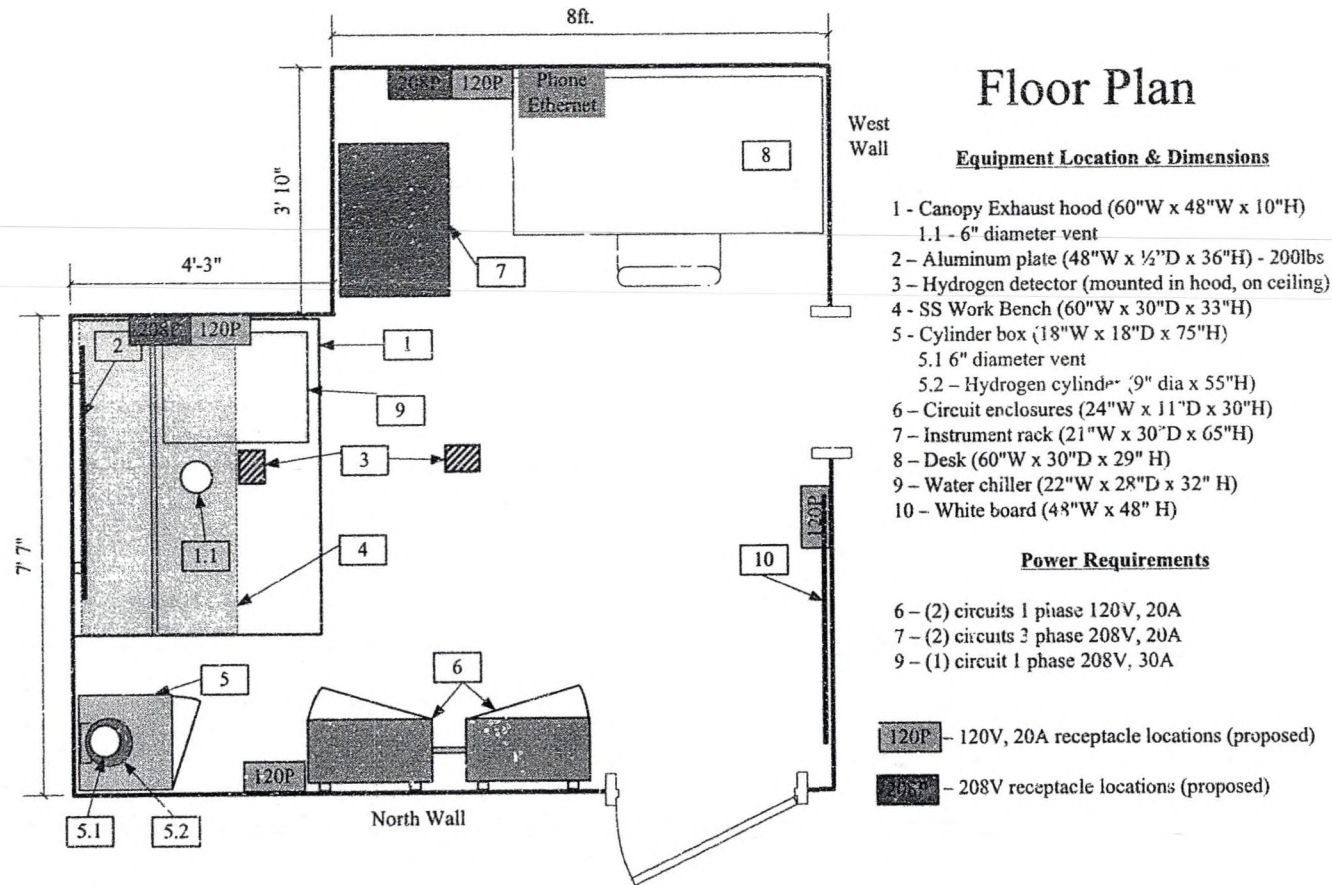


Figure 98. Upson 360A top view floor plan with descriptions.

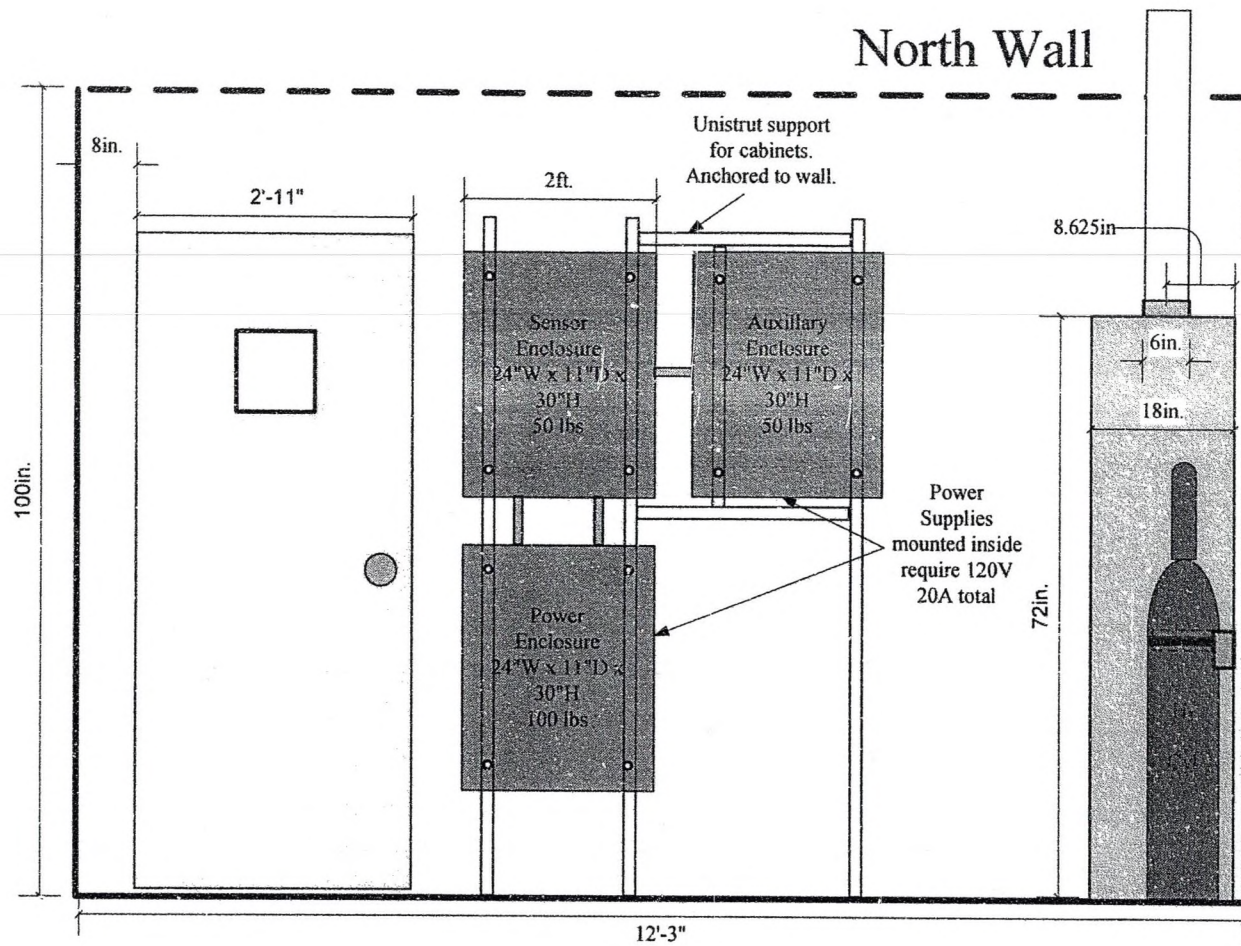


Figure 99. Upson 360A north wall enclosures and cylinder cabinet.

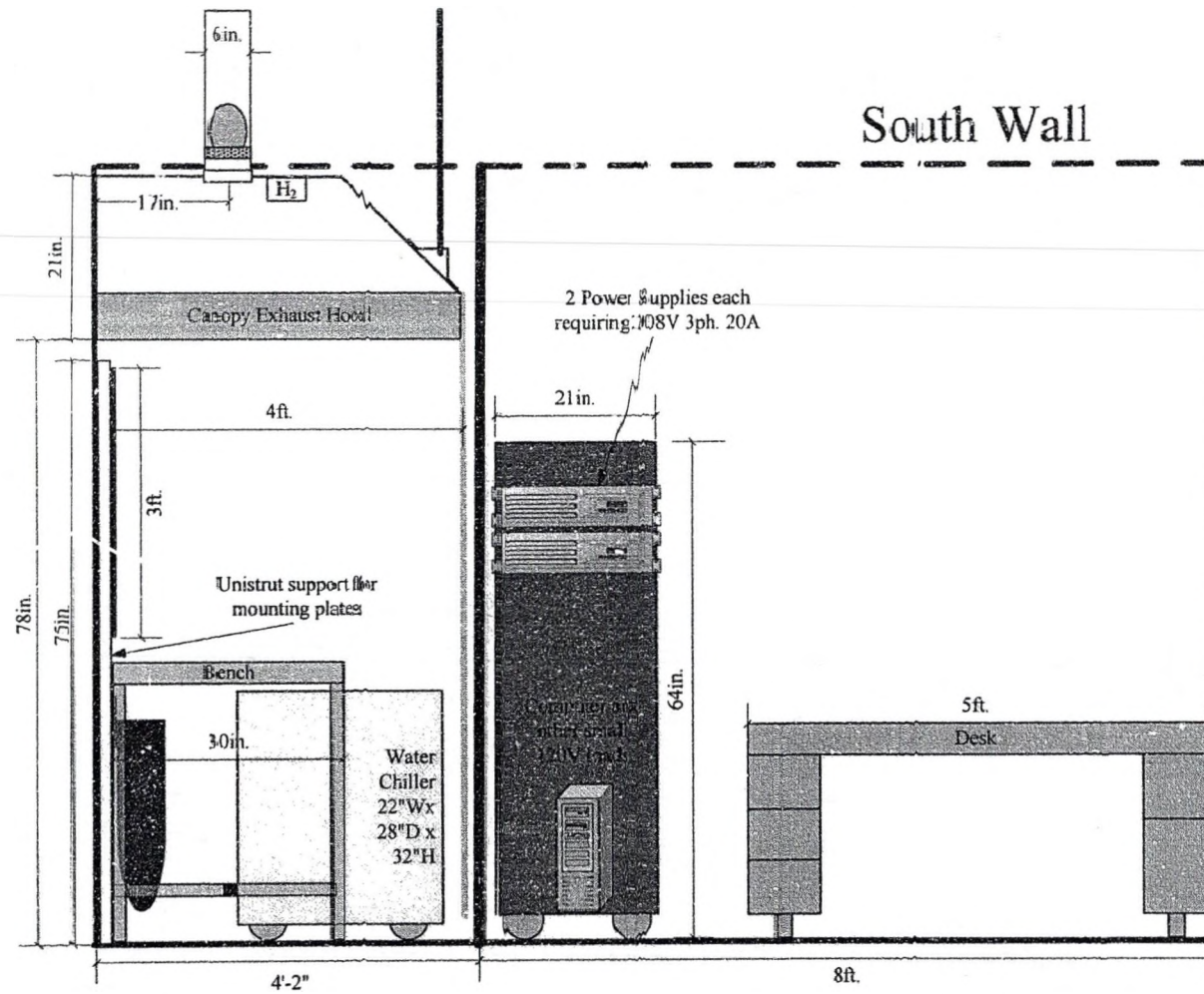


Figure 100. Upson 360A south wall with desk, instrument rack and canopy hood.

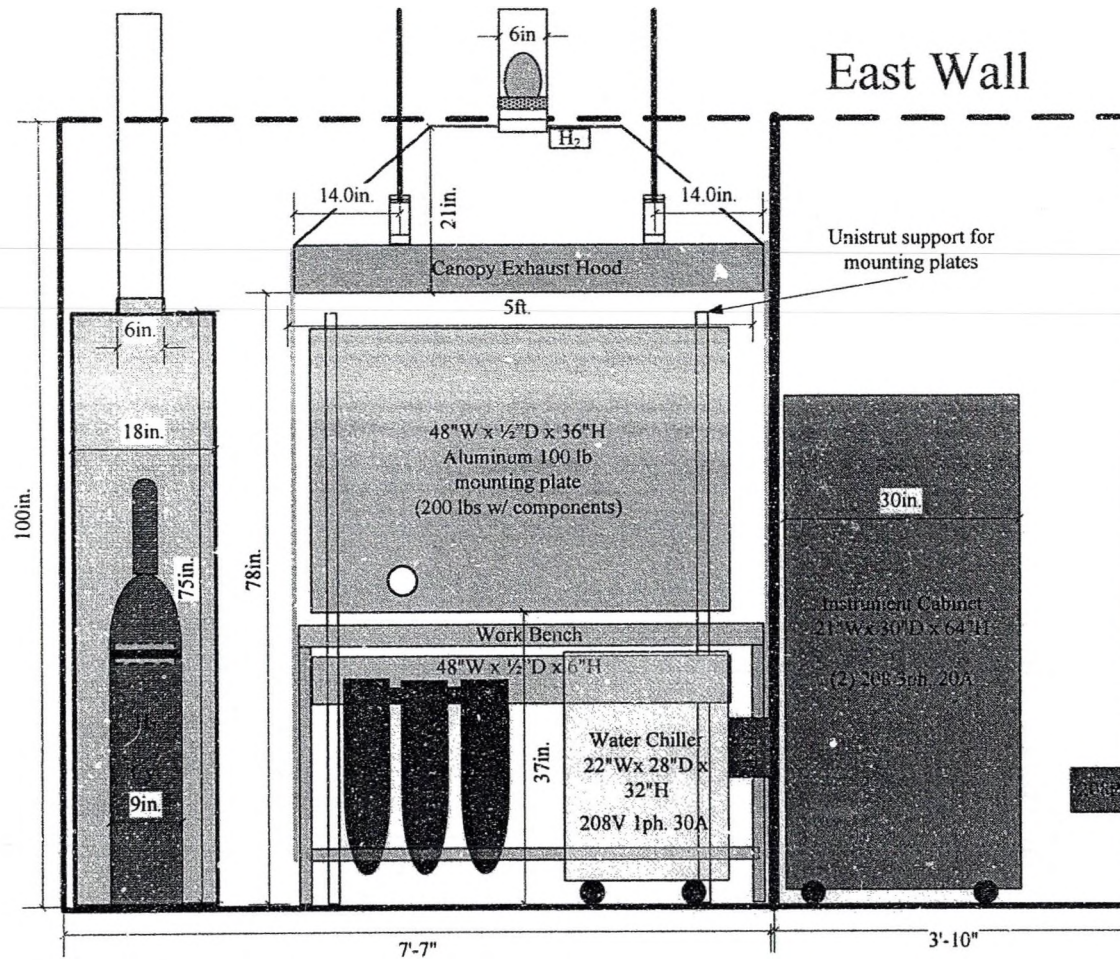


Figure 101. Upson 360A east wall canopy hood, instrument rack, cylinder cabinet and major component locations.

APPENDIX D

Model Code

```
Sub PEMmodel()  
'Kevin W. Harrison, 2006  
'NOTES: Standard enthalpy of formation of water  
'-(measured under standard conditions 25C, 1atm)  
'Total energy associated with splitting h2o into H2 and o2.  
'Produced from reaction but not all will be able to do work (J/kg)  
'Standard Gibbs free energy of formation of water  
'-(measured under standard conditions 25C, 1atm)  
'Del_Go is the practical energy to do work  
'Negative = reaction will proceed without additional energy. Ours are positive  
'Enth_Intgral - specific heat capacity at const pres. and changes w/ Temp.  
'The Avg value of Cp depends on whether you are calculating Enthalpy or Entropy.  
'Nernst potential  
'Use the static function and as Logn(tau) with tau being a double precision floating point  
Dim Row_Start, Col_Iop, Col_Vop, Col_Top, Col_Vpred, Col_Effth, Col_mass, n As  
Integer  
'Initialize Variables  
'-----  
'Specify the start ROW of the data  
Row_Start = 2  
'This program reads the current (Iop) from the column you specify.  
Col_Iop = 1  
'Next reads the operational voltage (Vop) from the column you specify.  
Col_Vop = 2  
'Read the DI water temperature to the stack.  
Col_Top = 3  
Cells(1, 4) = "Blank"  
'The predicted stack voltage will be reported in this column.  
Col_Vpred = 5  
Cells(1, Col_Vpred) = "Model Stack Voltage"  
'Specify what column to report the thermal efficiency in  
Col_Effth = 6  
Cells(1, Col_Effth) = "Model Stack Efficiency"  
'Specify Column to report the calculated mass flow  
Col_mass = 7  
Cells(1, Col_mass) = "Model mass Flow"
```



```

'Specify what column to start debug reporting in
Col_Debug = 10
Cells(1, Col_Debug) = "Debug"
'Specify number of cells in the stack
n = 20
'-----
Dim Tc, Pca, Paa, iao, ico, sigma, Pcp, Pap As Double
'Heat capacities of gases in ideal state. Properties
'Single Temperature calculations
'===== System Variables =====
'Tc = 35          'operating temperature (C)
'Now read Tc from Temperature date in Col_Top
Pcp = 184        'Cathode pressure (psia)  170 psig + 14 psi = psia
Pap = 20         'Anode pressure (psia)
Pca = Pcp / 14.6 'Cathode pressure (1atm = 14.6psia)
Paa = Pap / 14.6 'Anode pressure (atm)
'Anode exchange current density (A/cm^2)
'These constants depend on temperature
'iao = 1.65 * 10 ^ (-8)
'Cathode exchange current density (A/cm^2)
'ico = 0.09
'Membrane Conductivity (S/cm)
'sigma = 0.075
'Constants fitted to experimental data functions of Temp
'=====
'
Dim F As Long          'Faraday's Constant Coulomb per mol
Dim Eo As Double      'Reversible voltage based on Gibbs free energy
Dim p, alpha_a, alpha_c, z As Double 'loop counter
Dim Iop, i, A, Vop, EFFth As Double
Dim VactC, phi, VactA, Vact, Vohm, Vpred, HHV, m As Double
Dim kg_per_day, Nm3, rho, Del_G, H_Int, S_Int As Double
Dim Ah2, Bh2, Ch2, Dh2, Ao2, Bo2, Co2, Do2, Ah2o As Double
Dim Bh2o, Ch2o, Dh2o, Ts, Tk, tau, R As Double
Dim Del_A, Del_B, Del_C, Del_D, Del_Ho, Del_Go As Double
Dim Pw, Ph2, Po2, Vn As Double
'
'-----Constants-----
A = 86.4          'Cell Active area (cm^2)
alpha_c = 0.5    'cathode electron exchange coefficient
alpha_a = 0.5    'anode electron exchange coefficient
p = 2            '# of electrons
pm = 178 * 10 ^ (-4) 'membrane thickness (cm)
F = 96485        'Faraday constant

```

```

R = 8.314           'Universal Gas Constant (J mol-1) K-1)
Ts = 298           'Standard temperature (K)
HHV = 141.86      'kJ/g
rho = 0.08988     'density of H2 kg/Nm3
Ah2 = 3.249
Bh2 = 0.422 * (10 ^ (-3))
Ch2 = 0
Dh2 = 0.083 * (10 ^ 5)
Ao2 = 3.639
Bo2 = 0.506 * (10 ^ (-3))
Co2 = 0
Do2 = -0.227 * (10 ^ 5)
Ah2o = 8.712      'Heat capacity of liquid water
Bh2o = 1.25 * (10 ^ (-3))
Ch2o = -0.18 * (10 ^ (-6))
Dh2o = 0
Del_A = Ah2 + 0.5 * Ao2 - Ah2o
Del_B = Bh2 + 0.5 * Bo2 - Bh2o
Del_C = Ch2 + 0.5 * Co2 - Ch2o
Del_D = Dh2 + 0.5 * Do2 - Dh2o
Del_Ho = 285830
Del_Go = 237129   'p461, 638 Chem Thermo Book
'
z = Row_Start
Do Until (IsEmpty(Cells(z, Col_Iop)))
  Tc = Cells(z, Col_Top)
  iao = 2 * 10 ^ (-6) * (Exp(0.043 * Tc))
  ico = 0.12 * Exp(0.026 * Tc)
  sigma = 0.001 * Tc + 0.03
  Tk = 273 + Tc
  tau = Tk / Ts    'Ratio of T and Ts
  Pw = (610.78 * Exp((Tc / (Tc + 238.3)) * 17.2694)) / 101325 'pressure H2O (atm)
  Ph2 = Pca - Pw   'H2 partial pressure
  Po2 = Paa - Pw   'O2 partial pressure
  H_Int = (1 / Tk) * ((Del_A * Ts * (tau - 1)) + ((Del_B / 2) * (Ts ^ 2) * ((tau ^ 2) - 1)) +
  ((Del_C / 3) * (Ts ^ 3) * ((tau ^ 3) - 1)) + ((Del_D / Ts) * ((tau - 1) / tau)))
  S_Int = Del_A * Log(tau) + (Del_B * Ts + (Del_C * (Ts ^ 2) + (Del_D / ((tau ^ 2) * (Ts
  ^ 2)))) * ((tau + 1) / 2)) * (tau - 1)
  Del_G = R * Tk * (((Del_Go - Del_Ho) / (R * Ts)) + (Del_Ho / (R * Tk)) + H_Int -
  S_Int)
  Eo = Del_G / (2 * F) 'Reversible voltage function of Temperature
  Vn = Eo + (R * Tk) / (2 * F) * Log(Ph2 * Sqr(Po2) / Pw)
  Iop = Cells(z, Col_Iop) 'Read Iop from Col_Iop
  i = Iop / A           'Amps/cm^2

```



```

Vop = Cells(z, Col_Vop)           'Read Vop from Col_Vop
EFFth = 100 * ((Vn * n) / Vop)   'n=# of cells
Cells(z, Col_Effth) = EFFth
'Overpotentials
VactA = ((R * Tk) / (alpha_a * p * F)) * Log(i / iao)
VactC = ((R * Tk) / (alpha_c * p * F)) * Log(i / ico)
Vact = VactA + VactC
Vohm = i * (phi / sigma)
Vpred = (Vn + Vohm + Vact) * n   'per cell * n # of cells
Cells(z, Col_Vpred) = Vpred
Cells(z, Col_Debug) = VactC * n
Cells(z, Col_Debug + 1) = VactA * n
Cells(z, Col_Debug + 2) = Vohm * n
Cells(z, Col_Debug + 3) = Vn * n
'm is the mass flow rate in g/sec
m = (Iop * Vop * (EFFth / 100)) / (HHV * 1000)
Cells(z, Col_mass) = m
z = z + 1
Loop
kg_per_day = (m * 3600 * 24) / 1000 'kg/day
Nm3 = kg_per_day / (24 * rho)
'
End Sub

Sub EoTemp()
'Heat capacities of gases in ideal state. Properties
'Initialize Variables
'-----
'==== System Variables =====
Dim F As Long           'Faraday's Constant Coulomb per mol
Dim Eo, Temp, Temp2, X As Double 'Reversible voltage based on Gibbs free energy
Dim z As Integer       'loop counter
Dim Del_G, H_Int, S_Int As Double
Dim Ah2, Bh2, Ch2, Dh2, Ao2, Bo2, Co2, Do2, Ah2o As Double
Dim Bh2o, Ch2o, Dh2o, Ts, Tk, tau, R As Double
Dim Del_A, Del_B, Del_C, Del_D, Del_Ho, Del_Go As Double
Dim PWA, PHy, POx, Vn As Double
Dim Tc, Pca, Paa, Pcp, Pap As Double
'-----Constants-----
Cells(1, 10) = Log(2.71828284) 'Log is natural log (Ln)
Tc = 0                        'operating temperature (C) assigned in loop
Pca = 184                     'Cathode pressure (psia) 170 + 14
Pap = 20                      'Anode pressure (psia)
Pca = Pcp / 14.6              'Cathode pressure (1atm = 14.6psi)

```


$P_{aa} = P_{ap} / 14.6$ 'Anode pressure (atm)
 $n = 20$ '# of cells in stack

 $F = 96485$ 'Faraday constant
 $R = 8.314$ 'Universal Gas Constant ($J \text{ mol}^{-1} \text{ K}^{-1}$)
 $A_{h2} = 3.249$
 $B_{h2} = 0.422 * (10^{-3})$
 $Ch2 = 0$
 $D_{h2} = 0.083 * (10^5)$
 $A_{o2} = 3.639$
 $B_{o2} = 0.506 * (10^{-3})$
 $Co2 = 0$
 $Do2 = -0.227 * (10^5)$
 $A_{h2o} = 8.712$ 'Heat capacity of liquid water
 $B_{h2o} = 1.25 * (10^{-3})$
 $Ch2o = -0.18 * (10^{-6})$
 $D_{h2o} = 0$
 $Del_A = A_{h2} + 0.5 * A_{o2} - A_{h2o}$
 $Del_B = B_{h2} + 0.5 * B_{o2} - B_{h2o}$
 $Del_C = Ch2 + 0.5 * Co2 - Ch2o$
 $Del_D = Dh2 + 0.5 * Do2 - Dh2o$

 $T_s = 298$ 'Standard temperature (K)
 $Del_H_o = 285830$
 $Del_G_o = 237129$ 'p461, 638 Chem Thermo Book
For $z = 0$ To 70 Step 5 'Set $P_c = 170$ psi since data was taken around this.
 $T_c = z$ 'z is counter for degrees C
 $T_k = 273 + T_c$
 $\tau = T_k / T_s$ 'Ratio of T and T_s
 $P_{Wa} = (610.78 * \text{Exp}((T_c / (T_c + 238.3)) * 17.2694)) / 101325$ 'pressure H2O (atm)
 $P_{Hy} = P_{ca} - P_{Wa}$ 'H2 partial pressure
 $P_{Ox} = P_{aa} - P_{Wa}$ 'O2 partial pressure
 $H_Int = (1 / T_k) * ((Del_A * T_s * (\tau - 1)) + ((Del_B / 2) * (T_s^2) * ((\tau^2) - 1)) + ((Del_C / 3) * (T_s^3) * ((\tau^3) - 1)) + ((Del_D / T_s) * ((\tau - 1) / \tau)))$
 $S_Int = Del_A * \text{Log}(\tau) + (Del_B * T_s + (Del_C * (T_s^2) + (Del_D / ((\tau^2) * (T_s^2)))) * ((\tau + 1) / 2)) * (\tau - 1)$
 $Del_G = R * T_k * (((Del_G_o - Del_H_o) / (R * T_s)) + (Del_H_o / (R * T_k)) + H_Int - S_Int)$
 $E_o = Del_G / (2 * F)$ 'Reversible voltage
 $V_n = (R * T_k) / (2 * F) * \text{Log}((P_{Hy} * \text{Sqr}(P_{Ox})) / P_{Wa}) + E_o$
 $Cells(1, 27) = "T_c"$
 $Row = (z / 5) + 1$
 $Cells(Row, 27) = z$ 'Temperature
 $Cells(1, 28) = "E_o"$

```

Cells(Row, 28) = Eo           'per cell
Cells(1, 29) = "Vn"
Cells(Row, 29) = Vn         'per cell
'Cells(1, 26) = "PWa"
'Cells(Row, 26) = (610.78 * Exp((Tc / (Tc + 238.3)) * 17.2694)) / 101325
'Cells(1, 25) = "POx"
'Cells(Row, 25) = POx
'Cells(1, 24) = "PHy"
'Cells(Row, 24) = PHy
'Cells(1, 23) = "Xout"
'Cells(Row, 23) = PHy * Sqr(POx)
Next
'
End Sub

```

LIST OF REFERENCES

- [1] J. Verne, *The Mysterious Island (1874) – A New Translation*: translated by Jordan Stump, Modern Library, 2001.
- [2] D. Gregory, "A Brief History of the Hydrogen Energy Movement," Symposium Papers: Hydrogen for Energy Distribution, Institute of Gas Technology, Chicago, 1978.
- [3] D. H. Smith, "Industrial Water Electrolysis," in *Industrial Electrochemical Processes*, A. T. Kuhn, Ed.: Elsevier Publishing Company, 1971, pp. 127 - 157.
- [4] D. Gregory, "The Hydrogen Economy," in *Scientific American*, vol. 228, No. 1, 1973, pp. 13 - 21.
- [5] D. Gregory and J. B. Pangborn, "Hydrogen Energy," presented at Hydrogen for Energy Distribution, Institute of Gas Technology, 1978.
- [6] W. E. Winshe, K. C. Hoffman, and F. J. Salzano, "Hydrogen: Its Future Role in the Nation's Energy Economy," in *Science*, vol. 180, 1973, pp. 1325 - 1332.
- [7] J. Levene, B. Kroposki, and G. Sverdrup, "Wind Energy and Production of Hydrogen and Electricity - Opportunities for Renewable Hydrogen," NREL Report No. CP-560-39534, 2006.
- [8] "Comparative Cost of Wind and Other Energy Sources," American Wind Energy Association (AWEA), <http://www.awea.org/pubs/factsheets/Cost2001.PDF>, 2001.
- [9] "The Economics of Wind Energy," American Wind Energy Association, <http://www.awea.org/pubs/factsheets/EconomicsOfWind-Feb2005.pdf>, February 2005.
- [10] R. L. Ottinger, D. Wooley, D. R. Hodas, N. A. Robinson, and S. E. Babb, *Pace University Center for Environmental Legal Studies; Environmental Costs of Electricity*: Oceana Publications, 1990.

- [11] K. Silverstein, "Clean Tech Goes Mainstream," in *EnergyBiz Insider*: http://www.energycentral.com/centers/energybiz/ebi_detail.cfm?id=164, CyberTech Inc., 2006.
- [12] J. C. Bokow, "Fabric, Not Filling, to Blame Hydrogen Exonerated in Hindenburg Disaster," National Hydrogen Association, <http://www.hydrogenus.com/advocate/ad22zepp.htm>, 1997.
- [13] J. R. Petit, et al., "Vostok Ice Core Data for 420,000 Years," NOAA/NCDC Paleoclimatology Program, IGBP PAGES/World Data Center for Paleoclimatology Data Contribution Series #2001-076., Boulder, CO, 2001.
- [14] "Climate Change: New Antarctic Ice Core Data." Retrieved January 6, 2006, from http://www.daviesand.com/Choices/Precautionary_Planning/New_Data/, 2000.
- [15] "Kyoto Protocol - Essential Background," Retrieved on July 6, 2006, from http://unfccc.int/essential_background/items/2877.php, 2006.
- [16] C. G. Schneider, "Death Disease and Dirty Power: Mortality and Health Damage Due to Air Pollution from Power Plants," Clean Air Task Force, <http://www.cleartheair.org/fact/mortality/mortalitylowres.pdf>, Boston, MA, October 2000.
- [17] S. Hock, C. Elam, and D. Sandor, "Can We Get There? Technology advancements could make a hydrogen electric economy viable—and expand opportunities for all renewables," in *Solar Today*, 2004.
- [18] "Proton Energy Manufactures Three Families of HOGEN® Hydrogen Generation Systems," in *Proton Energy Systems - Products - HOGEN H Series, Hogen S Series, Hogen GC*. Retrieved on July 6, 2006, from <http://www.protonenergy.com/products.html>, 2005.
- [19] "Hybrid Wind Energy System," Retrieved on June 26, 2006, from <http://energy.coafes.umn.edu/windenergy>, University of Minnesota, Research and Demonstration Center, 2005.
- [20] "Basin Electric joins pilot project to marry wind, hydrogen," in *Energy Services Bulletin*: Retrieved on May 22, 2006, from <http://www.wapa.gov/es/pubs/esb/2004/December/dec045.htm>, 2006.
- [21] G. Schroeder, "Transition to the Hydrogen Age Transition to the Hydrogen Age: Myths and Realities." Retrieved on June 29, 2006 from <http://fcgov.com/utilities/pdf/eps06-fuel-hydrogen.pdf>, 2006.

- [22] J. Ivy, "Summary of Electrolytic Hydrogen Production: Milestone Completion Report," National Renewable Energy Laboratory, Golden, CO, NREL/MP-560-35948, April 2004.
- [23] A. F. G. Smith and M. Newborough, "Low-Cost Polymer Electrolysers and Electrolyser Implementation Scenarios for Carbon Abatement," Heriot-Watt University, Edinburgh, Report to the Carbon Trust and ITM-Power PLC, November 2004.
- [24] N. Lymberopoulos, "Hydrogen Production from Renewables," Center for Renewable Energy Sources (C.R.E.S), Pikermi Attiki, Project Technical Assistant Framework Contract EESD Contract No: NNE5-PTA-2002-003/1, September 2005.
- [25] "Hemoglobin, From Wikipedia, the Free Encyclopedia." Retrieved on June 22, 2006 from <http://en.wikipedia.org/wiki/Hemoglobin>.
- [26] "DOE Hydrogen Program: President's Hydrogen Fuel Initiative: A Clean and Secure Energy Future," Retrieved on July 6, 2006, from http://www.hydrogen.energy.gov/presidents_initiative.html, 2003.
- [27] "Hydrogen Properties," College of the Desert, http://www.eere.energy.gov/hydrogenandfuelcells/tech_validation/pdfs/fcm01r0.pdf, December 2001.
- [28] "OSH Answers: Compressed Gases - Hazards," Canadian Centre for Occupational Health & Safety (CCOHS), Retrieved on March 25, 2006, from <http://www.ccohs.ca/oshanswers/chemicals/compressed/compress.html>, 2005.
- [29] P. Choi, D. G. Bessarabov, and R. Datta, "A Simple Model for Solid Polymer Electrolyte (SPE) Water Electrolysis," *Solid State Ionics*, vol. 175, pp. 535 - 539, 2004.
- [30] R. W. Larson, "The Right Future? ASES and the renewables community examine renewable hydrogen's potential benefits — and weigh growing concerns.," in *Solar Today*, 2004.
- [31] K. W. Harrison, B. Kroposki, and C. Pink, "Electrolyzer Characterization Report, Proton Energy Systems HOGEN 40RE," NREL, Golden, CO, Technical, In Press 2006.
- [32] J. Speranza, M. Cardin, and O. Chow, "Technical Description and Product Specification, 8 kW Renewable Energy Capable Electrolyzer," Proton Energy Systems, DSP02010 Rev. 2, 2002.

- [33] "Operating Manual for XDC Series Power Supply," <http://www.xantrex.com/web/id/96/docserve.asp>, Release 3.0 (2002-06), 2002.
- [34] "HOGEN® Hydrogen Generation and Stable Flow™ Continuous Hydrogen Injection Improve Performance in Electric Power Generators." Adapted from a presentation by: John Speranza, Proton Energy Systems and Lawrence Dusold, Cetrom, Inc., http://www.protonenergy.com/data/Unsorted/HighPurity_H2_in_ElectPwr_Gens-5.0-17509.pdf, 2005.
- [35] D. White and C. Heinrich, "What is Clean, Dry Air?" Compressed Air and Gas Institute (CAGI), <http://www.cagi.org/pdfs/tap106.pdf>, Technical Article Program (TAP): TAP #106.
- [36] "Technical Specifications, HOGEN Hydrogen Generating Systems." PD-0600-002, Rev. 11.05: Proton Energy Systems (PES), <http://www.protonenergysystems.com/data/Unsorted/hogen-specs-16982.pdf>, 2005.
- [37] "Thermoelectric effect - Wikipedia, the free encyclopedia," Retrieved on July 6, 2006, from http://en.wikipedia.org/wiki/Peltier-Seebeck_effect.
- [38] F. C. McQuiston, J. D. Parker, and J. D. Spitler, *Heating, Ventilation, and Air Conditioning: Analysis and Design*: John Wiley and Sons, Inc., 2005.
- [39] T. Padfield, "Moisture in air, Equations describing the physical properties of moist air," Retrieved on January 9, 2006, from <http://www.natmus.dk/cons/tp/atmcalc/atmoclc1.htm>, 1996.
- [40] H. Vömel, "Saturated Vapor Pressure Formulations." CIRES, University of Colorado, Boulder: Retrieved on January 9, 2006, from <http://cires.colorado.edu/~voemel/vp.html>, 2006.
- [41] M. Williams, "Snow Hydrology (GEOG 4321): Phases of Water," Retrieved on January 9, 2006, from <http://snobear.colorado.edu/Markw/SnowHydro/Phases/phases.html>.
- [42] "Butler-Volmer Equation," Retrieved on April 22, 2006, from http://chem.ch.huji.ac.il/~eugeniik/butler-volmer_equation.htm.
- [43] "Exchange current," Retrieved on July 6, 2006, from <http://www.corrosionsource.com/technicallibrary/corrdoctors/Modules/Kinetics/Exchange.htm>.
- [44] A. J. Bard and L. R. Faulkner, *Electrochemical Methods, Fundamentals and Applications*, 2nd ed: John Wiley & Sons, Inc., 2001.

- [45] T. Berning and N. Djilali, "Three-Dimensional Computational Analysis of Transport Phenomena in a PEM Fuel Cell — A Parametric Study," *Journal of Power Sources*, vol. 106, pp. 284-292, 2003.
- [46] J. M. Smith, H. C. Ness, and M. M. Abbott, *Introduction to Chemical Engineering Thermodynamics*, 6th ed: Mc Graw Hill, 2001.
- [47] J. Larminie and A. Dicks, *Fuel Cell Systems Explained*, 2nd ed: John Wiley and Sons, 2002.
- [48] S. H. Chan, K. A. Khor, and Z. T. Xia, "A complete polarization model of a solid oxide fuel cell and its sensitivity to the change of cell component thickness," *Journal of Power Sources*, vol. 93, pp. 130-140, 2001.
- [49] S. Slade, S. A. Campbell, T. R. Ralph, and F. C. Walshc, "Ionic Conductivity of an Extruded Nafion 1100 EW Series of Membranes," *Journal of The Electrochemical Society*, vol. 149, pp. A1556-A1564, 2002.
- [50] E. Anderson, T. Molter, and F. Mitlitsky, "Recent advances in hydrogen generation using PEM water electrolysis," presented at 201st Electrochemical Society Meeting, Philadelphia, PA, 2002.
- [51] J. B. S. Haldane, "DAEDALUS or Science and the Future." Cambridge, 1923.
- [52] "Take Care with Oxygen, fire and explosive hazards in the use of oxygen," Health and Safety Executive, <http://www.hse.gov.uk/pubns/hse8.pdf>, HSE8(rev2) C150 4/00, April 2000.